



Technische Universität Dresden
Fakultät Mathematik und Naturwissenschaften

Analysis of Double Beta Decays in Germanium, Palladium and Argon

Diplomarbeit Physik

vorgelegt von

Björn Lehnert

geboren am
07. September 1982
in Halle-Saale

Erstgutachter: **Prof. Dr. Kai Zuber**
Zweitgutachter: **Jun.-Prof. Dr. Arno Straessner**
Betreuer: **Prof. Dr. Kai Zuber**

Abgabedatum: 14. Februar 2011

(Update 1: 15. March 2011)

Dedicated to *Alexander Lankau*

Abstract

Neutrinoless double beta decay experiments are an important contribution to fathom neutrino characteristics and therewith the fundamental processes in particle physics and cosmology. This decay mode is the gold plated channel for investigating the Dirac or Majorana type of neutrinos and can additionally constrain or fix the neutrino mass scale. Nuclear models are required in order to calculate an effective Majorana neutrino mass out of a measured half-life. These calculations benefit from additional experimental input such as double beta decays into excited states which is the main topic in this thesis.

Four different double beta decay transitions were investigated with data from the GERDA experiment, the Felsenkeller laboratory and with various MC simulations. The $2\nu\beta^-\beta^-$ decay of ^{76}Ge into the first excited 0^+ state of ^{76}Se was studied for the GERDA Phase I setup and a promising preliminary signal over background excess of 10 is expected. The $2\nu\beta^-\beta^-$ and the $2\nu\text{ECEC}$ transition of ^{110}Pd and ^{102}Pd into the first excited 0^+ state of ^{110}Cd and ^{102}Ru respectively were analyzed with $13\text{ kg}\cdot\text{d}$ exposure which resulted in new best lower half-life limits of $2.54\cdot 10^{19}\text{ yr}$ and $2.54\cdot 10^{18}\text{ yr}$ (95% CL) for the respective nuclides. Limits for the decays into the first excited 2^+ states were set to $2.14\cdot 10^{19}\text{ yr}$ for ^{110}Pd and $1.73\cdot 10^{18}\text{ yr}$ for ^{102}Pd . All these limits are also valid for the respective 0ν decay modes. Another analysis was done for the radiative $0\nu\text{ECEC}$ decay of ^{36}Ar with $96,500\text{ kg}\cdot\text{d}$ exposure of the first GERDA test data which yielded a preliminary lower half-life limit of $7.32\cdot 10^{20}\text{ yr}$ (95% CL) and is two orders of magnitude better than the prior limit. Additionally, the important $^{42}\text{Ar}/^{42}\text{K}$ background component of the GERDA experiment was studied which offered hints of an inhomogeneous ^{42}K distribution and contributes to the ongoing investigation of the GERDA collaboration.

Autorenreferat

Experimente zum neutrinolosen doppelten Betazerfall sind ein wesentlicher Bestandteil um grundlegende Neutrinoeigenschaften zu entschlüsseln und damit fundamentale Prozesse in der Teilchenphysik und der Kosmologie zu verstehen. Diese Experimente sind die am Besten geeignete Methode um zwischen der Dirac- oder Majorananatur der Neutrinos zu unterscheiden und können zusätzlich die Neutrinomassenskala einschränken oder fixieren. Es werden hierfür theoretische Kernmodelle benötigt, um aus einer gemessenen Halbwertszeit die effektive Majorananeutrinomasse zu berechnen. Diese Berechnungen profitieren von zusätzlichen experimentellen Daten, wie z. B. von den ähnlichen neutrinobeleiteten doppelten Betazerfällen in angeregte Zustände. Die Untersuchung solcher Zerfälle ist der Hauptbestandteil dieser Arbeit.

Es wurden vier verschiedene doppelte Betazerfälle mit Daten des GERDA Experiments, aus dem Niederniveau Messlabor Felsenkeller und mit Hilfe von MC Simulationen untersucht. Der $2\nu\beta^-\beta^-$ Zerfall von ^{76}Ge in den ersten angeregten 0^+ Zustand von ^{76}Se wurde für die Phase I des GERDA Experiments analysiert. Hierbei wird ein Signal-zu-Untergrund-Verhältniss von 10 vorhergesagt. Der $2\nu\beta^-\beta^-$ und der $2\nu\text{ECEC}$ Zerfall von ^{110}Pd und ^{102}Pd in die ersten angeregten 0^+ Zustände von ^{110}Cd und ^{102}Ru wurden mit $13\text{ kg}\cdot\text{d}$ Daten aus dem Felsenkeller analysiert und ergeben neue höchste untere Halbwertszeitgrenzen von $2,54\cdot 10^{19}\text{ yr}$ und $2,54\cdot 10^{18}\text{ yr}$ (95% CL) für die entsprechenden Zerfallsmodi. Die unteren Grenzen für Zerfälle in die ersten 2^+ Zustände wurden auf $2,14\cdot 10^{19}\text{ yr}$ für ^{110}Pd und $1,73\cdot 10^{18}\text{ yr}$ für ^{102}Pd gesetzt. All diese unteren Halbwertszeitgrenzen gelten auch für die 0ν Zerfallsmodi. Eine weitere Analyse betrachtete den γ -emittierenden $0\nu\text{ECEC}$ Zerfall von ^{36}Ar mit $96500\text{ kg}\cdot\text{d}$ von den ersten GERDA Testdaten, was eine vorläufigen unteren Halbwertszeitgrenze von $7,32\cdot 10^{20}\text{ yr}$ mit 95% CL ergab. Dies ist zwei Größenordnungen besser als die vorher bekannte untere Grenze. Des Weiteren wurde der dominante Untergrundbeitrag von $^{42}\text{Ar}/^{42}\text{K}$ im GERDA experiment analysiert, was Hinweise darauf liefert, dass die ^{42}K -Verteilung im flüssigen Argon inhomogen ist und zu der andauernden Untersuchung der GERDA Kollaboration beiträgt.

Contents

1	Introduction	1
2	Theoretical Considerations	5
2.1	The Neutrino	6
2.1.1	Neutrinos in the Standard Model	6
2.1.2	Dirac versus Majorana Particles	7
2.1.3	Neutrino Masses & See-Saw Mechanism	8
2.2	Approaches to Determine Neutrino Characteristics	9
2.2.1	Neutrino Oscillation Experiments	9
2.2.2	Beta Decay Experiments	11
2.2.3	Neutrinoless Double Beta Decay Experiments	12
2.2.4	Cosmological Constraints on Neutrinos	13
2.3	Double Beta Decays	14
2.3.1	Neutrino Accompanied DBD's	14
2.3.2	Neutrinoless DBD's	16
2.4	From $T_{1/2}$ to $ m_{ee} $	16
2.4.1	Nuclear Matrix Element	17
2.4.2	Phase Space Factor	18
2.5	Importance of DBD for Neutrino Physics	18
3	Experimental Considerations	21
3.1	Current Experiments	22
3.1.1	Different Experimental Approaches	23
3.1.2	Comparison of Experiments	24
3.2	Underground Laboratories	25
3.2.1	Laboratori Nazionali del Gran Sasso (LNGS)	26
3.2.2	Niederniveaumesslabor Felsenkeller	27
3.3	Background Sources in Low Background Experiments	28
3.3.1	Direct Cosmic Radiation	28
3.3.2	Cosmic Activation	30
3.3.3	Primordial Decay Chains	30
3.3.4	Anthropogenic Radioactivity	31
3.4	From Spectral Data to Half-Lives	32
3.4.1	Calculating Half-Lives	32
3.4.2	Statistical Methods for Low Count Rates	32
3.4.3	Bayesian versus Frequentist	33
3.4.4	Unified Approach: Feldman-Cousins	34
3.4.5	Profiled Likelihood	35
3.4.6	Binned Analysis	38

4	The GERDA Experiment	41
4.1	Experimental Goals	42
4.2	GERDA Design & Concept	42
4.2.1	Detector Array	43
4.2.2	Cryostat	45
4.2.3	Water Tank & Muon Veto	45
4.2.4	Superstructure, Cleanroom & Lock	46
4.3	Monte Carlo Simulations	47
4.4	Data Acquisition & Processing Chain	48
5	GERDA Coincidence Analysis	49
5.1	Introduction	50
5.2	Analysis Workflow	51
5.3	Background Model	52
5.3.1	Cosmic Activation and Internal Background	53
5.3.2	Primordial Decay Chains and External Background	54
5.3.3	Phase I Background	55
5.4	Monte Carlo Results	57
5.4.1	Energy Spectra	57
5.4.2	Cut Analysis	61
5.5	Conclusions & Perspectives	65
6	GERDA ^{42}Ar Study	67
6.1	Situation in GERDA	68
6.2	Production of ^{42}Ar	69
6.3	Monte Carlo Study	70
6.3.1	Workflow	70
6.3.2	Prestudy of ^{42}K decays in the GERDA Cryostat	71
6.3.3	Homogeneous ^{42}K Scenarios	73
6.3.4	Inhomogeneous ^{42}K Scenarios	75
6.3.5	Summary and Scaling of MC Data	76
6.4	Experimental Data	76
6.5	Analysis	79
6.6	Conclusion & Perspectives	83
7	New Limits for DBD's of Pd into Excited States	85
7.1	Introduction	86
7.1.1	Historic Measurements of DBD's in Pd	87
7.1.2	Theoretical Prediction	87
7.2	Measurements & Cleaning	88
7.2.1	Experimental Setup	88
7.2.2	Energy Calibration	89
7.2.3	Calibration of Energy Resolution	90
7.2.4	Efficiency Calibration	90
7.2.5	Correction of Efficiency Calibration	92
7.2.6	Validation Checks	94
7.2.7	Cleaning	96
7.3	Spectral Analysis	98
7.3.1	Background Peak Before and After Cleaning	98
7.3.2	Area around Pd Peaks	98
7.3.3	Background Model	99
7.3.4	Extracting Count Limits	100
7.3.5	Calculating Half-Lives	101
7.4	Conclusion & Perspectives	102

8 GERDA ^{36}Ar Analysis	105
8.1 Introduction	106
8.2 Experimental Data	107
8.3 MC Study of Detection Efficiency	107
8.4 Analysis	109
8.4.1 Background Model	109
8.4.2 Extracting Count Limits	110
8.4.3 Calculating Half-Lives	110
8.5 Conclusions & Perspectives	111
9 Conclusions & Perspectives	113
A General Considerations	A-1
B Example MaGe Macro	B-1
C GERDA Coincidence Analysis	C-1
D Excited States in Palladium	D-1
E List of Acronyms	i
Bibliography	iv
Acknowledgments	xiii

Chapter 1

Introduction

Neutrinos are a fundamental part of our understanding of the underlying processes in nature. They are by far the most elusive particles that are currently detectable and the considerable experimental effort to investigate them created an own branch in modern physics: neutrino physics. The theoretical description of neutrinos is complex and different experimental approaches are necessary in order to fathom the predicted observables; the concept of double beta decay, DBD, is, among others, one of these approaches and is the most promising angle to decide the fundamental question whether neutrinos are Majorana or Dirac type particles, i.e. whether they are their own antiparticles or not.

Wolfgang Pauli postulated the neutrino in 1930 in order to explain the β -decay as a three-body decay and thus to redeem the energy and angular momentum conservation in the light of a continuous β -spectrum. The theoretical description of the weak decay was formulated by Enrico Fermi in 1934 with a massless Dirac neutrino [1] but it took two more decades until neutrinos were directly discovered by Frederick Reines and Clyde L. Cowan in 1956 in a nuclear reactor experiment [2]. The idea of DBD as two consecutive single β -decays, $2\nu\beta\beta$, was formulated by Maria Goeppert-Mayer in 1935 and experimentally confirmed indirectly in geochemical experiments in 1950 with ^{130}Te by Mark G. Inghram and John H. Reynolds [3]; the direct verification in counting experiments was not successful until 1987 with ^{82}Se [4]. Theoretically much more compelling and momentous is the DBD without neutrinos, $0\nu\beta\beta$, which was proposed by Wendell H. Furry in 1939 [5] but remains undiscovered to this day. A hint for evidence was found in 2002 by parts of the Heidelberg-Moscow collaboration but remains debated within the community [6].

Besides the fundamental question of Dirac or Majorana type neutrinos, $0\nu\beta\beta$ experiments can also constrain or fix their absolute mass scale which was established with the observation of neutrino oscillation by the Super-Kamiokande experiment in 1998 [7]. However, theoretically calculated nuclear matrix elements, NME, are necessary in order to convert the measured half-life for a $0\nu\beta\beta$ transition of a specific nuclide into one single effective Majorana neutrino mass. The NME's have different values for different nuclides and depend on nuclear models which have non negligible uncertainties. The $0\nu\beta\beta$ NME calculations can be facilitated with auxiliary experimental data of similar decays as e.g. the $2\nu\beta\beta$ decays into the ground state or into excited states.

DBD's into excited states have been first experimentally observed in ^{100}Mo in 1995 [8] but remain undiscovered for most DBD nuclides. Their experimental signature consists of de-excitation γ 's in the final state and is therefore best suitable for coincidence analysis in multiple detector experiments.

The GERmanium Detector Array, GERDA, is an ionization experiment that uses an array of enriched high purity germanium detectors to investigate the $0\nu\beta\beta$ in ^{76}Ge . It is placed 1400 m underground in the Laboratori Nazionali del Gran Sasso, LNGS, and is designed in two phases to reach a background level of 10^{-2} cts/(kg · yr · keV) for 15 kg · yr in Phase I and 10^{-3} cts/(kg · yr · keV) for more than 100 kg · yr in Phase II.

The aim of this diploma thesis is the investigation of excited states $2\nu\beta\beta$ transitions in ^{76}Ge with the GERDA experiment and in ^{110}Pd and ^{102}Pd with a comparably simple γ -spectrometry setup in the local underground laboratory Felsenkeller. As a study of opportunity, the unexpected large background contribution of $^{42}\text{Ar}/^{42}\text{K}$ was investigated in the first GERDA data which, in turn, was used to perform a preliminary analysis of the radiative $0\nu\text{ECEC}$ transition in ^{36}Ar .

The content of this thesis is outlined in three preceding considerations for theoretical motivation and implications, for experimental techniques and challenges and for the presentation of the GERDA experiment. The theory of neutrinos in the standard model of particle physics and for a non-zero neutrino rest mass, the principle of neutrino oscillation and the fundamental different approaches of fixing the neutrino mass scale, the characteristics of $2\nu\beta\beta$ and $0\nu\beta\beta$ decays, the problem of calculating the effective Majorana neutrino mass

out of a measured half-life and a summation of the importance of DBD for neutrino physics is presented in Chap. 2. Chap. 3 compares different experimental approaches and current DBD experiments, motivates and compares the use of different underground laboratories, presents different background contributions and reduction techniques in a low background environment and outlines the path of retrieving a half-life out of a measured energy spectrum with different statistical methods for different experimental conditions. The GERDA experiment including the physics reach, the setup and the Monte Carlo, MC, framework MaGe is presented in detail in Chap. 4.

The main body with the four different, mainly independent studies presents in, Chap. 5, a coincidence analysis of $2\nu\beta\beta$ excited state transitions in ^{76}Ge in the GERDA Phase I setup. This study includes the construction of an elaborate background model and the development and performance testing of various multi detector cuts. A MC study for the $^{42}\text{Ar}/^{42}\text{K}$ background contribution in the experimental data of the GERDA experiment is performed in Chap. 6. The first data taking runs are presented and MC and experimental data are compared and briefly discussed. Chap. 7 contains an analysis of DBD excited state transitions in ^{102}Pd and ^{110}Pd . It presents the detailed path from the measured count spectrum, to detector calibration, over in situ tests of the calibration towards the extraction of new half-life limits for these decay modes with the two Frequentist methods of Feldman and Cousins and the profiled likelihood. Chap. 8 presents a brief preliminary analysis of the radiative $0\nu\text{ECEC}$ decay in ^{36}Ar with the first GERDA data.

The thesis is concluded with the posterior presentation of perspectives for all four different analyses and studies in Chap. 9.

Chapter 2

Theoretical Considerations

2.1 The Neutrino

Neutrinos (ν_e, ν_μ, ν_τ) are an essential part in the Standard Model, SM, of particles and are yet still the least known. Their only weakly interacting nature made them elusive for many experiments and major advances were only possible in recent years. New evidence points to theoretical models that are beyond established SM physics and open a gate to explain so far unanswered questions of particle physics and cosmology.

2.1.1 Neutrinos in the Standard Model

In the Standard Model, neutrinos were introduced as massless fermions¹ as part of the electroweak theory which was developed by Glashow, Salam and Weinberg in 1961 [9]. They are only subject to the weak interaction which does not act upon right-handed fermions and left-handed antifermions since there are only left-handed weak charge currents². If fermions have a zero rest mass, their helicity³ is conserved and has the same eigenvalues as the chirality which means that right-handed fermions or left-handed antifermions cannot be created by weak interactions in the SM and that the fermionic and antifermionic spin projections are always negative and positive respectively.

Fermions are grouped into left-handed doublets and right-handed singlets according to the electroweak theory⁴ as shown Tab. 2.1. The same is true for antifermions with opposite chirality.

Table 2.1 Fermionic doublets and singlets in the electroweak theory.

Quarks			Leptons		
$\begin{pmatrix} u \\ d' \end{pmatrix}_L$	$\begin{pmatrix} c \\ s' \end{pmatrix}_L$	$\begin{pmatrix} t \\ b' \end{pmatrix}_L$	$\begin{pmatrix} e \\ \nu_e \end{pmatrix}_L$	$\begin{pmatrix} \mu \\ \nu_\mu \end{pmatrix}_L$	$\begin{pmatrix} \tau \\ \nu_\tau \end{pmatrix}_L$
$(u)_R, (d)_R$	$(c)_R, (s)_R$	$(t)_R, (b)_R$	$(e)_R$	$(\mu)_R$	$(\tau)_R$

The three quarks d' , s' and b' are weak flavor eigenstates mixed out of the quark mass eigenstates d and u , s and c , and b and t respectively according to the CKM Matrix⁵. This mixing violates the baryon flavor and breaks CP symmetry⁶. The right-handed singlets do not mix since they do not couple to the weak interaction. There is only one right-handed lepton singlet per family because right-handed neutrinos cannot interact weakly, thus, cannot interact at all and are not present as particles in the SM. The lepton flavor is conserved in contrast to baryon flavor although neutrino oscillation experiments already disproved this assumption (Sec. 2.2.1); however, the total baryon and lepton number is conserved with the best constraints coming from p -decay and $0\nu\beta\beta$ experiments respectively⁷. The amount of three light neutrino flavors according to the three lepton families was established in 1989 by measurements of the Z^0 boson width⁸ with the LEP experiment [10].

¹Spin $\frac{1}{2}$ particles.

²The handedness or chirality is the chiral projection of a spinor ψ by the projection operators: $\psi_{L/R} = (1 \mp \gamma^5)\psi$. The weak interaction includes a projection operator, which is a consequence of maximal parity violation, and hence, does not act upon a particle spinor $\psi_R = (1 + \gamma^5)\psi$ or on antiparticle spinor $\psi_L = (1 - \gamma^5)\psi$.

³Helicity is the sign of the projection of the spin vector, $\boldsymbol{\sigma}$, onto the direction of momentum, $\frac{\mathbf{p}}{|\mathbf{p}|}$: $\mathcal{H} = \frac{\boldsymbol{\sigma} \cdot \mathbf{p}}{|\mathbf{p}|}$. Helicity is only conserved by massless particles when there is no reference frame in which the direction of momentum can turn around. Then, helicity is identical to chirality.

⁴The quantum number of the weak interaction is the weak isospin, T , which is $1/2$ for left-handed fermions and groups them into doublets with $T_3 = \pm 1/2$. Right-handed fermions have no weak isospin charge ($T = 0$) and are thus singlets.

⁵Cabibbo-Kobayashi-Maskawa mixing matrix for the quark sector.

⁶Charge and Parity symmetry.

⁷There is no theoretical reason, i.e. no symmetry according to the Noether's-theorem, that makes baryon and lepton flavor conservation, as well as their number conservation imperative in the SM.

⁸Light in this case means lighter than $1/2$ of the Z^0 mass.

The small cross sections⁹ of neutrinos are inherent to their only weak interacting nature. The calculation of electroweak matrix elements always includes a propagator term with the heavy Z^0 (91.1876 ± 0.0021 GeV) and W^\pm (80.399 ± 0.023 GeV) bosons [12] in its denominator. This severely reduces the interaction probability of neutrinos at energies below the weak mass scale of 100 GeV. The observation of rare and short-ranged interaction even led to the historic assumption of a four-point interaction without a propagator by Fermi in 1934 [1].

2.1.2 Dirac versus Majorana Particles

Fermions are called Dirac particles if the particle and antiparticle are different states: $f \neq \bar{f}$; they are called Majorana particles if the particle and the antiparticle are identical: $f = \bar{f}$. In the latter case, all their additive quantum numbers, e.g. electric charge, baryon number, lepton number etc., have to be neutral which is only possible for neutrinos¹⁰. With this argument, Dirac neutrinos could have a static magnetic and electric dipole whereas Majorana neutrinos cannot since it would be required to be equal for neutrinos and antineutrinos. Neutrinos are embedded in the SM as Dirac particles which can be described as four-component spinors by the Dirac equation in quantum field theories. Their non-zero spin of $1/2$ allows for two chiral projection for each particle and antiparticle respectively: $\nu_L^D, \nu_R^D, \bar{\nu}_L^D$ and $\bar{\nu}_R^D$. The Majorana spinor only needs two components in contrast: $\nu_L^M = \bar{\nu}_L^M$ and $\bar{\nu}_R^M = \nu_R^M$. The different Dirac and Majorana states are summarized in Tab. 2.2 including their interaction probability with charged fermions. The massless Dirac (anti-)neutrino only interacts with negatively charged fermions if it is left-handed and with positively charged anti-fermions if it is right-handed. Hence, only two Dirac states are experimentally accessible and the distinction between Dirac and Majorana neutrinos is impossible. The right-handed projection of a massive Dirac neutrino can, however, also interact with negatively charged fermions with the probability, P , of [13]

$$P = \frac{1}{2} \left(1 - \frac{v}{c}\right) \approx \left(\frac{m_\nu}{2E}\right)^2. \quad (2.1)$$

Equally, massless left-handed Majorana neutrinos cannot interact with anti-fermions whereas massive Majorana neutrinos can with the probability P .

Table 2.2 States of Dirac and Majorana Neutrinos. $p(l^-)$ and $p(l^+)$ denote the probability to produce a lepton of the respective charge.

	notation	chirality	$p(l^-)$	$p(l^+)$
Dirac ν	ν_L^D	L	$1 - \left(\frac{m_\nu}{2E}\right)^2$	0
	ν_R^D	R	$\left(\frac{m_\nu}{2E}\right)^2$	0
Dirac $\bar{\nu}$	$\bar{\nu}_L^D$	L	0	$\left(\frac{m_\nu}{2E}\right)^2$
	$\bar{\nu}_R^D$	R	0	$1 - \left(\frac{m_\nu}{2E}\right)^2$
Majorana ν	$\nu_L^M = \bar{\nu}_L^M$	L	$1 - \left(\frac{m_\nu}{2E}\right)^2$	$\left(\frac{m_\nu}{2E}\right)^2$
Majorana $\bar{\nu}$	$\bar{\nu}_R^M = \nu_R^M$	R	$\left(\frac{m_\nu}{2E}\right)^2$	$1 - \left(\frac{m_\nu}{2E}\right)^2$

For massive neutrinos, all four Dirac states can interact with charged fermions and a distinction between the Dirac and Majorana nature is possible; however, with neutrino masses converting to zero, the distinction becomes continuously more minute and can only be detected by very sensitive experiments. This is the reason why it remains an unanswered question so far and only the latest $0\nu\beta\beta$ experiments have a chance to answer that question.

⁹The average neutrino cross section for the reactor neutrino experiment by Reines and Cowan [2] is approximately 10^{-43} cm² [11].

¹⁰A meson's example for a Majorana particle is e.g. the π^0

2.1.3 Neutrino Masses & See-Saw Mechanism

The observation of neutrino oscillation (Sec. 2.2.1) requires the neutrino to have a non-zero rest mass which has to be inserted in the SM. Consequently, also neutrino singlets, $(\nu_e)_R$, $(\nu_\mu)_R$ and $(\nu_\tau)_R$, which are not present in the definition of the SM¹¹ have to be inserted to create Dirac masses (see Tab. 2.1).

A straight forward approach is the introduction of a Dirac mass term into the Lagrangian¹² with which leptons acquire mass by coupling to the higgs field¹³ [11]:

$$\mathcal{L}^D = -\mathcal{M}_D \nu \bar{\nu} = -\mathcal{M}_D [\bar{\nu}_R \nu_L + \bar{\nu}_L \nu_R]. \quad (2.2)$$

In this equation, \mathcal{M}_D^ν is the coupling strength to the higgs field, i.e. the neutrino mass and ν and $\bar{\nu}$ the four-component neutrino spinors that can be separated into their chiral projections ν_R and ν_L . It becomes apparent that there cannot be a Dirac mass term without right-handed neutrinos, ν_R , and left-handed antineutrinos, $\bar{\nu}_L$.

The ν and $\bar{\nu}$ can be seen as creation and annihilation operators that have to come in pairs on order to conserve quantum numbers e.g. electric charge or lepton number. The electric charge is conserved since neutrinos are neutral and with abandoning the lepton number conservation, in principle there can be two more mass terms which are precisely the Majorana mass terms:

$$\mathcal{L}^M = -\frac{1}{2} \mathcal{M}_{M_L} [(\bar{\nu}_L)^c \nu_L + \bar{\nu}_L \nu_L^c] - \frac{1}{2} \mathcal{M}_{M_R} [(\bar{\nu}_R)^c \nu_R + \bar{\nu}_R \nu_R^c]. \quad (2.3)$$

Here, the mass is created with the coupling of a field to its charge conjugated field which is denoted by the superscript c (see [11]). Generally all three mass terms, \mathcal{M}_D , \mathcal{M}_{M_L} and \mathcal{M}_{M_R} , could coexist and can be rewritten in a form of a 2×2 -matrix:

$$\mathcal{L}^M = -\frac{1}{2} \cdot ((\bar{\nu}_L)^c, \bar{\nu}_R) \cdot \mathcal{M} \cdot \begin{pmatrix} \nu_L \\ \nu_R^c \end{pmatrix}, \quad \mathcal{M} = \begin{pmatrix} \mathcal{M}_{M_L} & \mathcal{M}_D^T \\ \mathcal{M}_D & \mathcal{M}_{M_R} \end{pmatrix}. \quad (2.4)$$

The mass matrix, \mathcal{M} , can be diagonalized resulting in generally two non-degenerated eigenvalues, \mathcal{M}_1 and \mathcal{M}_2 . With the simplifying assumption that $\mathcal{M}_{M_R} \gg m_e$, $\mathcal{M}_{M_L} \approx 0$ and $\mathcal{M}_D \approx m_e$ the equation solves to

$$\mathcal{M}_1 = \frac{\mathcal{M}_D^2}{\mathcal{M}_{M_R}} \ll \mathcal{M}_D \quad (2.5)$$

$$\mathcal{M}_2 = \mathcal{M}_{M_R} \left(1 + \frac{\mathcal{M}_D}{\mathcal{M}_{M_R}} \right) \approx \mathcal{M}_{M_R} \gg \mathcal{M}_D, \quad (2.6)$$

which is called the see-saw mechanism. This mechanism provides an elegant way of explaining a light neutrino mass, \mathcal{M}_1 , of orders of magnitude lower than that of Dirac leptons if one assumes that the Dirac neutrino coupling to the higgs field, \mathcal{M}_D , is similar to the one of other Dirac leptons as the one for e , μ or τ . Additionally, a heavy neutrino, \mathcal{M}_2 , is postulated that could serve as a dark matter candidate. The Majorana mass terms and the see-saw mechanism are only possible if the neutrino is in fact a Majorana particle which remains to be proven.

¹¹Depending on how one defines the Standard Model, massive neutrinos can be described by it or not. If by definition the SM is merely the combination of the $U(1) \times SU(2) \times SU(3)$ symmetry groups, then new particles can be incorporated i.e. neutrino singlets. If the SM is defined by the symmetry group and the fermions in Tab. 2.1, then massive neutrinos are physics beyond the standard model.

¹²Fundamental physical description of a dynamic system that is used in quantum field theories to derive equations of motion. See e.g. [14]

¹³A so far hypothetical field that is believed to interact with SM fields and generate observable mass terms.

2.2 Approaches to Determine Neutrino Characteristics

Since the discovery of neutrino oscillations by Super-Kamiokande [7], we know that at least two neutrino mass eigenstates have a non-zero rest mass, that their mass eigenstates and weak eigenstates are different, that they oscillate between those states and that they violate lepton flavor. This will be explained in more detail in Sec. 2.2.1. What neutrino oscillation experiments cannot determine is the absolute mass scale which can be measured by β -decay experiments (Sec. 2.2.2), $0\nu\beta\beta$ experiments (Sec. 2.2.3) and with cosmological constraints (Sec. 2.2.4). However, all these experiments measure a different combination of mass eigenstates and are difficult to compare especially since $0\nu\beta\beta$ experiments and cosmological constraints are model dependent in retrieving a neutrino mass.

2.2.1 Neutrino Oscillation Experiments

The idea of neutrinos mixing, analogous to the quark sector, was introduced by Maki, Nakagawa and Sakata in 1962 [15], but the first connection to possible neutrino oscillations was not till seven years later by Gribov and Pontecorvo in 1969 [16]. They introduced the idea of massive neutrinos that allows for neutrino oscillation and the violation of the lepton flavor conservation analogously to quark mixing according to the CKM matrix. This section is only a brief summary of the physical consequences of neutrino oscillation; a more detailed description can be found in [17], [18] and [11] among others. The basic assumption for neutrino oscillation is that the neutrino weak flavor eigenstates are not identical with their mass eigenstates and hence are a superposition of the latter and vice versa. Mathematically this is expressed as

$$|\nu_\alpha\rangle = \sum_i U_{\alpha i}^* |\nu_i\rangle \quad \text{and} \quad |\nu_i\rangle = \sum_\alpha U_{\alpha i} |\nu_\alpha\rangle \quad (2.7)$$

in which $\alpha = e, \mu, \tau$ are the weak eigenstates, $i = 1, 2, 3$ are the mass eigenstates and $U_{\alpha i}$ are the matrix elements of the PMNS matrix¹⁴ [15]. In its most general form the PMNS matrix can be parametrized as

$$U = \begin{pmatrix} 1 & 0 & 0 \\ 0 & c_{23} & s_{23} \\ 0 & -s_{23} & c_{23} \end{pmatrix} \cdot \begin{pmatrix} c_{13} & 0 & s_{13}e^{-i\delta} \\ 0 & 1 & 0 \\ -s_{13}e^{i\delta} & 0 & c_{13} \end{pmatrix} \quad (2.8)$$

$$\cdot \begin{pmatrix} c_{12} & s_{12} & 0 \\ -s_{12} & c_{12} & 0 \\ 0 & 0 & 1 \end{pmatrix} \cdot \begin{pmatrix} e^{i\alpha_1/2} & 0 & 0 \\ 0 & e^{i\alpha_2/2} & 0 \\ 0 & 0 & 1 \end{pmatrix} \quad (2.9)$$

in which s and c denote sine and cosine of the mixing angles ij respectively and δ , α_1 and α_2 are CP violating phases [11]. Specifically α_1 and α_2 are Majorana phases which are only important if neutrinos prove to be Majorana particles. The observable oscillation, however, does not change in this case.

Neutrino oscillation essentially means that neutrinos are produced in their respective weak eigenstate which is a quantummechanical superposition of mass eigenstates, then propagate as one specific mass eigenstate, which in turn is a superposition of weak eigenstates, and finally interact as one of these weak eigenstates. The formula to describe the probability of a neutrino being created with flavor α to interact as a neutrino with flavor β is [12]

¹⁴Pontecorvo-Maki-Nakagawa-Sakata mixing matrix for the lepton sector.

$$P_{\alpha \rightarrow \beta} = |\langle \nu_\beta(t) | \nu_\alpha \rangle|^2 \quad (2.10)$$

$$= \left| \sum_i U_{\alpha i}^* U_{\beta i} \cdot e^{-im_i^2 L/2E} \right|^2 \quad (2.11)$$

$$= \delta_{\alpha\beta} - 4 \sum_{i=1}^2 \sum_{j=i+1}^3 \mathcal{R}e(U_{\alpha i}^* U_{\beta i} U_{\alpha j} U_{\beta j}^*) \sin^2 \left(\Delta m_{ij}^2 \frac{L}{4E} \right) \quad (2.12)$$

$$+ 2 \sum_{i=1}^2 \sum_{j=i+1}^3 \mathcal{I}m(U_{\alpha i}^* U_{\beta i} U_{\alpha j} U_{\beta j}^*) \sin \left(\Delta m_{ij}^2 \frac{L}{2E} \right). \quad (2.13)$$

Here, Δm_{ij}^2 is the squared mass difference between the mass eigenstates i and j , ($m_i^2 - m_j^2$), E is the approximated energy of massless neutrinos and L is the propagated distance of the neutrino. It can be seen that the oscillation properties depend on E , L and Δm_{ij}^2 whereas the maximal mixing at $\sin^2 \left(\Delta m_{ij}^2 \frac{L}{4E} \right) = 1$ depends solely on the mixing angles encoded in the PMNS matrix. In order to determine the unknown Δm_{ij}^2 , an experiment has to know precisely E and L of the neutrinos; however, at larger distances, L , e.g. solar scale, the mixing will average, the oscillation wash out and only the mixing angles, θ_{ij} , can be determined. Δm_{ij}^2 is investigated with artificial neutrino sources¹⁵ at comparably smaller L that probe the first periods of $P_{\alpha \rightarrow \beta}$.



Figure 2.1 Two different scenarios of neutrino mass patterns deduced from oscillation experiments. Left: normal mass hierarchy; right: inverted mass hierarchy. The flavor composition of neutrino mass eigenstates is illustrated with red for the e part, with yellow for the μ part and with blue for the τ part. From [17].

In general, Δm_{ij}^2 and specifically Δm_{23}^2 can be positive or negative which leads to a scenario referred to as normal or inverted mass hierarchy and is shown in Fig. 2.1. This illustration shows both hierarchy scenarios and the composition of each neutrino mass eigenstate. The hierarchy scenario cannot be decided by neutrino oscillation experiments with artificial beams¹⁶ and the absolute mass scale remains unfathomed since Δm_{ij}^2 denotes only the mass difference.

As a conclusion for neutrino masses, we know from oscillation experiments that at least two neutrino mass eigenstates are different from zero and with the knowledge about mixing, that all neutrino weak eigenstates have an effective non zero rest mass. In addition, we can use limits on the effective ν_e mass¹⁷ in combination with the Δm_{ij}^2 as upper mass limits for ν_μ and ν_τ which were formerly quite loosely constrained by kinematic decay experiments. As

¹⁵e.g. Nuclear reactors or neutrino beams in short and long baseline experiments.

¹⁶However, one expects to be able to constrain the hierarchy with solar neutrinos using the difference in oscillation at night (traversing the earth) and during the day (no traversing of the earth) [19].

¹⁷Every weak eigenstate has three different masses. The effective mass of a weak eigenstate is the average mass of mass eigenstates of which the weak eigenstate is composed.

a result, this makes it e.g. possible to use a better constrained limit for the sum of neutrino masses in cosmology.

2.2.2 Beta Decay Experiments

Beta decay experiments investigate the endpoint of a beta spectrum in order to see whether the spectrum reaches up to the Q-value¹⁸. In case of massless neutrinos there would be some decays in which the neutrino has practically no momentum and hence leaves the electron with all the available energy; for massive neutrinos this cannot be the case since there would always be some energy taken by the neutrino rest mass. This effect is quite minute and needs low Q-value nuclides in order to be sensitive e.g. tritium with 18.59 keV used in MAINZ [20] and TROITSK [21] and will be used in KATRIN [22], or ¹⁸⁷Re with the lowest known Q-value of a beta emitter with 2.66 keV which will be used in MARE [23]. The measured mass is the incoherent sum of a real neutrino or the effective electron neutrino mass

$$\langle m_{\nu_e} \rangle = \sqrt{\sum_i m_i^2 |U_{ei}|^2} \quad (2.14)$$

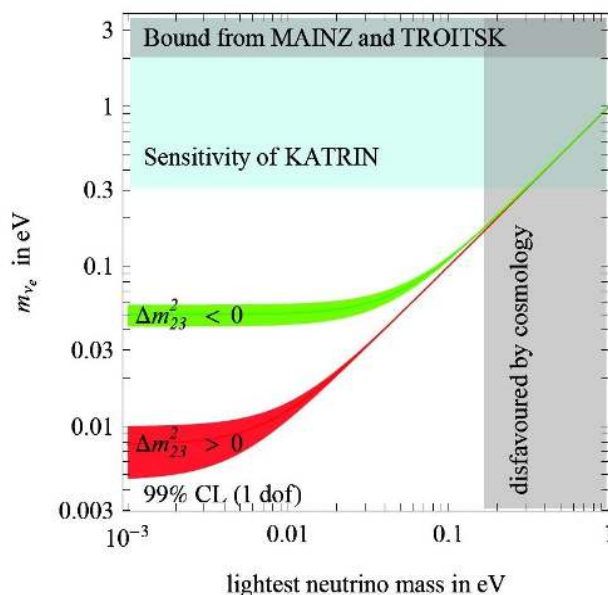


Figure 2.2 Effective electron neutrino mass, m_{ν_e} , as a function of the lightest mass eigenstate. Red denotes the normal hierarchy and green the inverted one. From [17].

with the current limit of $\langle m_{\nu_e} \rangle < 2.0$ eV set by MAINZ and TROITSK [17]. KATRIN and MARE expect a sensitivity of ≈ 0.2 eV. Fig. 2.2 shows the allowed parameter space of m_{ν_e} as a function of the lightest neutrino mass eigenstate for the normal hierarchy, red, and for the inverted hierarchy, green. It is constrained by cosmology with an upper limit for the lightest mass eigenstate and by β -decay experiments with an upper limit for m_{ν_e} . If ν_1 is the lightest neutrino eigenstate (normal hierarchy) which has the biggest contribution to ν_e , it will not be possible to probe the parameter space by currently running or planned experiments. If, on the other hand, the lightest mass eigenstate proves to be quite heavy, then the difference between the hierarchy scenarios becomes insignificant; this is called the almost degenerated scenario.

¹⁸The energy available for the transition.

2.2.3 Neutrinoless Double Beta Decay Experiments

The $0\nu\beta\beta$ decay will be extensively introduced in Sec. 2.3. This decay mode measures the coherent sum of a virtual neutrino¹⁹ or the effective Majorana mass:

$$|m_{ee}| = \left| \sum_i m_i U_{ei}^2 \right| \quad (2.15)$$

$$= \left| m_1 |U_{e1}|^2 + m_2 |U_{e2}|^2 e^{i(\alpha_2 - \alpha_1)} + m_3 |U_{e3}|^2 e^{-i(\alpha_1 + 2\delta)} \right|. \quad (2.16)$$

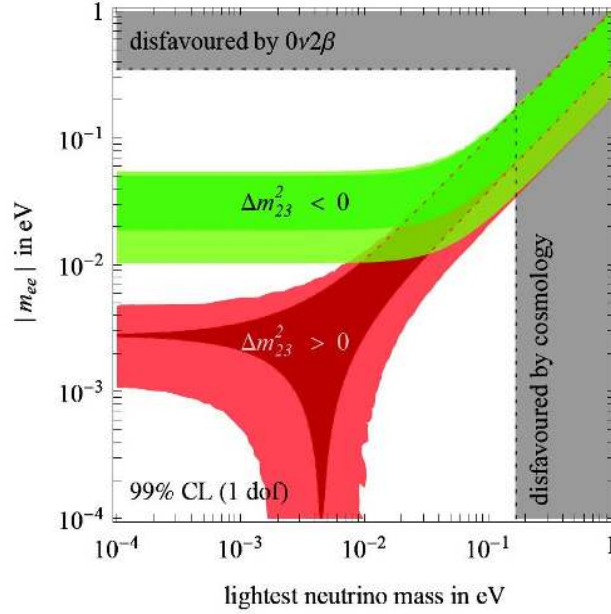


Figure 2.3 Effective Majorana mass, $|m_{ee}|$, as a function of the lightest mass eigenstate. Red denotes the normal hierarchy and green the inverted one. From [17].

Fig. 2.3 shows the parameter space of $|m_{ee}|$ and the lightest neutrino mass eigenstate. Current constraints are given by former $0\nu\beta\beta$ experiments and cosmology. The so far only evidence for $0\nu\beta\beta$ is claimed by a subgroup of the Heidelberg-Moscow collaboration, HDM, around Klapdor-Kleingrothaus starting with a 2.3σ evidence in 2002 [6] and enforcing it to a larger than 6σ evidence in 2006 [24]. The best value for the half-life is $2.23^{+0.44}_{-0.31} \cdot 10^{25}$ yr which translates to a $|m_{ee}|$ of $(0.11..0.56)$ eV depending on the nuclear matrix element, NME. This claim would favor the degenerated scenario (Fig. 2.3) and could not yet been tested by other experiments as can be seen in Fig. 2.4. The plot shows the expected half-lives, T , of $0\nu\beta\beta$ nuclides if the Klapdor claim holds by comparing the NME's and the phase space factors to the ones of ^{76}Ge . With the current data, IGEX and CUORICINO came closest but could not test the claim.

Currently constructed experiments as GERDA are designed to test the claim, i.e. the degenerated scenario, and even to probe the inverted hierarchy (green) in a second step. It needs, however, much more sensitive experiments in the far future to probe the normal hierarchy case shown in red. There is also the possibility that the phases in Eq. 2.15 cancel each other in a way that no Majorana mass will be discoverable. This is illustrated in Fig. 2.3 for the normal hierarchy and a lightest neutrino mass eigenstate of $5 \cdot 10^{-3}$ eV.

¹⁹A virtual particle or propagator is not part of the initial or final state of a process and is hence not observable. This makes it e.g. possible to violate energy-momentum conservation.

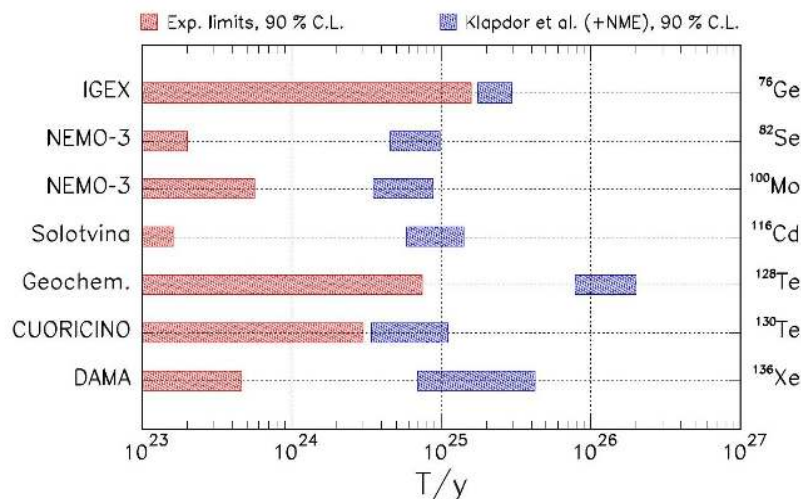


Figure 2.4 Illustration of the status on testing the Klapdor claim with currently running or recently finished experiments. The plot shows the expected half-lives, T , of $0\nu\beta\beta$ nuclides if the Klapdor claim holds by comparing the NME's and the phase space factors to the ones of ^{76}Ge . From [25].

2.2.4 Cosmological Constraints on Neutrinos

There is a multitude of cosmological mechanisms that are effected by neutrinos. The study of those mechanisms can give constraints to neutrino characteristics. However, most of these cosmological mechanisms are not very well known and described by various models which, in turn, makes cosmological constraints dependend of these models. The main information from cosmology used for neutrino physics is data from the Cosmic Microwave Background, CMB, and from Large-Scale Structures, LSS.

Besides photons, neutrinos are the most abundant particles in the universe and have a low energy omnipresent background field much like the CMB. Depending on their rest mass, they contribute to the overall energy density of the universe²⁰, Ω , which influences the CMB.

Another major influence of neutrinos is on the inhomogeneity of the early universe which led to the large-scale structures today. Initial small density fluctuations may have been washed out by freely propagating neutrinos, carrying energy out of areas with higher density. This smoothing effect depends on the mass of neutrinos.

These two effects give constraints on the simple sum of neutrino masses:

$$m_{\text{cosmo}} = \sum_i m_i. \quad (2.17)$$

Fig. 2.5 shows the parameter space of m_{cosmo} and the lightest neutrino mass eigenstate for the normal hierarchy (red) and the inverted hierarchy (green). So far, m_{cosmo} is constrained to be lower than 0.5 eV mainly by WMAP data (see [17] and references therein). The currently running PLANCK mission [26] is expected to probe the inverted hierarchy scale.

²⁰The overall energy density of the universe, Ω , is normalized to the critical density and consists mainly of the energy densities of dark energy Ω_Λ , dark matter Ω_{DM} , baryons Ω_B , photons Ω_γ and neutrinos Ω_ν .

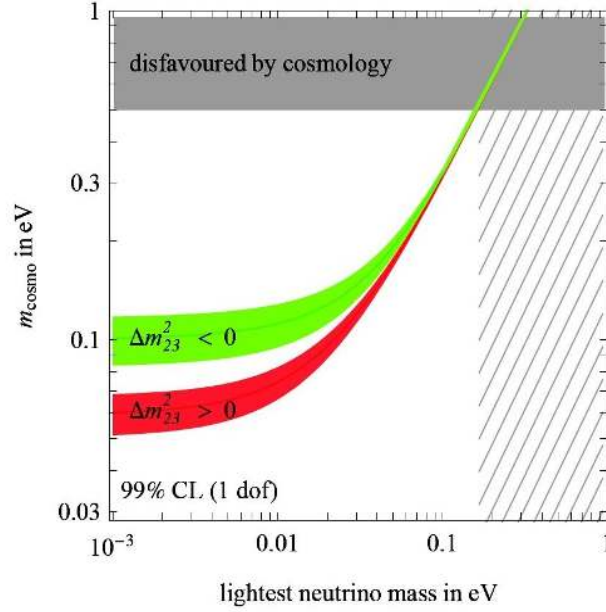


Figure 2.5 Sum of neutrino masses, m_{cosmo} , as a function of the lightest mass eigenstate. Red denotes the normal hierarchy and green the inverted one. From [17].

2.3 Double Beta Decays

DBD's are nuclear transitions with the conservation of the atomic mass, A , and the change of the charge, Z , by two unit charges. They are second order, weak processes that are very rare and usually experimentally concealed in the background of the competing two single beta decays. The observation becomes possible if the transition to the intermediate nucleus is either energetically forbidden or highly suppressed. The first case occurs in even-even nuclei²¹ that have a stronger binding than the intermediate odd-odd nuclei as exemplary shown with the mass parabola of $A = 76$ in Fig. 2.6. The latter case occurs if the difference in angular momentum between the initial state and intermediate state is sufficiently high, which is e.g. true for ^{48}Ca and ^{96}Zr . This leads to 69 known DBD nuclides which are presented in Tab. A.4 and A.6 in the Appendix.

2.3.1 Neutrino Accompanied DBD's

$2\nu\beta\beta$ decays come in four different forms depending on the nucleus and their surroundings in the chart of nuclides:

$$2\nu\beta^-\beta^- : \quad (Z, A) \rightarrow (Z + 2, A) + e_1^- + e_2^- + \bar{\nu}_{e_1} + \bar{\nu}_{e_2}, \quad (2.18)$$

$$2\nu\text{ECEC} : \quad (Z, A) + e_1^- + e_2^- \rightarrow (Z - 2, A) + \nu_{e_1} + \nu_{e_2}, \quad (2.19)$$

$$2\nu\text{EC}\beta^+ : \quad (Z, A) + e^- \rightarrow (Z - 2, A) + e^+ + \nu_{e_1} + \nu_{e_2}, \quad (2.20)$$

$$2\nu\beta^+\beta^+ : \quad (Z, A) \rightarrow (Z - 2, A) + e_1^+ + e_2^+ + \nu_{e_1} + \nu_{e_2}, \quad (2.21)$$

in which EC denotes the Electron Capture²².

The $2\nu\beta^-\beta^-$ decay is experimentally established and found in a variety of nuclides [28]. The form of the differential energy spectrum resembles the one of the single β -decay and is described by [11]:

²¹Even-even nuclei have an even number of protons and an even number of neutrons whereas odd-odd nuclei have respectively odd numbers of either nucleon flavor.

²²In order to avoid semantic confusion about EC being a decay or not: In this thesis, decay is meant as a transition with the release of energy from a bound state, not the increased amount of free final state particles compared to the amount of initial state particles.

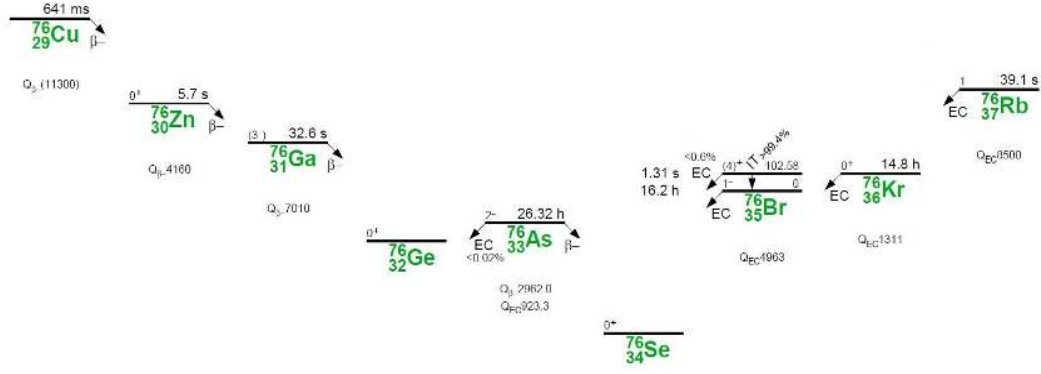


Figure 2.6 Illustration of the mass parabola for isobars with $A = 76$ and the DBD. The x-axis indicates increasing neutron numbers and the y-axis the binding energy. The β^- -decay of ^{76}Ge into ^{76}Ar is energetically forbidden and enables the observation of the DBD into ^{76}Se . From [27].

$$\frac{dN}{dE} \approx E(Q - E)^5 [E^4 + 10E^3 + 40E^2 + 60E + 30], \quad (2.22)$$

in which E is the energy and Q the Q-value of the decay. This is illustrated with an MC simulated spectra in Fig. C.1 in the Appendix. The corresponding Kurie plot²³ is

$$C(Q - E) = \sqrt[5]{\frac{N}{E[E^4 + 10E^3 + 40E^2 + 60E + 30]}}. \quad (2.23)$$

The crossing of the linear function of E with the x-axis is precisely the endpoint of the $\beta^- \beta^-$ -spectrum. An illustration of the $2\nu\beta\beta$ and $0\nu\beta\beta$ spectrum can be seen in Fig. 2.7 which has been convoluted with 5% detector resolution.

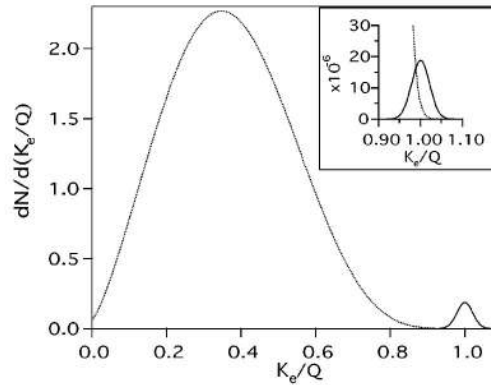


Figure 2.7 Illustrated spectra of $2\nu\beta\beta$ decay (dotted line) and $0\nu\beta\beta$ beta decay (solid line) convoluted with 5% detector resolution. K_e is the electron energy and Q the Q-value of the decay. The ratio between $2\nu\beta\beta$ and $0\nu\beta\beta$ entries is 10^2 in the big plot and 10^6 in the small plot. From [29].

The $2\nu\text{ECEC}$, $2\nu\text{EC}\beta^+$ and $2\nu\beta^+\beta^+$ decays are experimentally difficult to detect. In the double electron capture, the energy is carried away by two neutrinos and X-rays from the atomic shell, leaving only the low energy X-rays as an experimental signal. The decays

²³The linearization of the $2\nu\beta\beta$ spectrum for better visualization which especially facilitates the investigation of the beta endpoint in β^- -decay experiments (Sec. 2.2.2).

including β^+ have a dominant 511 keV signal but also a reduced phase space since one β^+ requires an energy of $2m_e$. That amounts to 2044 keV for the $\beta^+\beta^+$ decay which leaves only six known isotopes with a Q-value high enough [30]. In addition, they always compete with the EC decays and have, with the reduced phase space, a longer half-life.

All those decays, Eq. 2.18-2.21, can also occur into excited states of the daughter nuclide. This is experimentally interesting since the de-excitation γ 's are easily detectable. The disadvantage is a reduced phase space which increases the half-lives of those decay modes. Excited states can include 0^+ and 2^+ states²⁴ with a suppression of the latter due to the less propable spin alignment of all β 's and ν 's in the final state. Decays into excited states also prove very useful as auxiliary information for theoretical NME calculations. Having the same initial state and a similar Hamiltonian to the one of DBD's into the ground state, one can investigate the final state influences and check and tune ones calculations (see Sec. 2.4.1).

So far, excited state transitions have only been observed in ^{100}Mo [8] and ^{150}Nd [31]. The investigation of DBD's into excited states is the main topic of this thesis and is done for ^{76}Ge in Chap. 5 and for ^{102}Pd and ^{110}Pd in Chap. 7.

2.3.2 Neutrinoless DBD's

$0\nu\beta\beta$ decays are theoretically possible for all decay modes in Eq. 2.18-2.21. There exist various theories that predict exotic particles emitted instead of neutrinos such as e.g. a majoron, which, however, shall not be issued in the frame of this thesis. The easiest modes are the simple omitting of neutrinos:

$$0\nu\beta^-\beta^- : \quad (Z, A) \rightarrow (Z + 2, A) + e_1^- + e_2^-, \quad (2.24)$$

$$0\nu\text{ECEC} : \quad (Z, A) + e_1^- + e_2^- \rightarrow (Z - 2, A), \quad (2.25)$$

$$0\nu\text{EC}\beta^+ : \quad (Z, A) + e^- \rightarrow (Z - 2, A) + e^+, \quad (2.26)$$

$$0\nu\beta^+\beta^+ : \quad (Z, A) \rightarrow (Z - 2, A) + e_1^+ + e_2^+. \quad (2.27)$$

Since no neutrino can carry energy out of the detector, the particles in the final states, β^\pm , deposit in sum a monoenergetic energy which equals the Q-value. Thus the hunt for the $0\nu\beta\beta$ is a hunt for a monoenergetic signal which is illustrated in Fig. 2.7 with a detector resolution.

In the case of $0\nu\text{ECEC}$, there are no other particles than the daughter nucleus in the final state but the energy has to be released nonetheless. There exist various theoretical models with e.g. e^+e^- pair emission, internal conversion or photons [32]. The latter model is called radiative $0\nu\text{ECEC}$ decay and the mentioned photon results from bremsstrahlung of the captured e^- . Additionally, two X-ray photons are emitted which have to originate from different shells since in total three photons need to account for angular momentum conservation in the $0^+ \rightarrow 0^+$ transition. Thus the most probable signal will consist of three photons, one with a K-shell energy, one with an L-shell energy and one with $E_\gamma = Q - E_K - E_L$.

In this thesis, a radiative $0\nu\text{ECEC}$ decay is investigated for ^{36}Ar in Chap. 8.

2.4 From $T_{1/2}$ to $|m_{ee}|$

Experiments searching for the $0\nu\beta\beta$ decay usually result in an upper half-life limit or, if lucky, in the half-life for the decay of the specific nuclide. Measuring a $0\nu\beta\beta$ half-life has a tremendous impact on its own, but the effective Majorana mass $|m_{ee}|$ (Eq. 2.15) is the important outcome for the big picture in physics. The half-life, $T_{1/2}$, is related to $|m_{ee}|$ with [11]:

²⁴ J^P notation; J is the spin of the nucleus and P the parity.

$$\left[T_{1/2}^{0\nu}(0^+ \rightarrow 0^+)\right]^{-1} = G^{0\nu}(Q, Z) \cdot |\mathcal{M}^{0\nu}|^2 \cdot |m_{ee}|^2, \quad (2.28)$$

in which $G^{0\nu}$ is the phase space factor and $\mathcal{M}^{0\nu}$ the NME for the $0\nu\beta\beta$ decay mode. However, both factors are not straight forward to determine and are based on rather complex theoretical models; different models with different approximations are the reason why the neutrino mass determined with $0\nu\beta\beta$ decays is in fact model dependent.

Methods of statistically determining $T_{1/2}^{0\nu}$ is described in Sec. 3.4, $|m_{ee}|$ is explained in Sec. 2.2.3 and $\mathcal{M}^{0\nu}$ and $G^{0\nu}$ are outlined in the following two sections.

2.4.1 Nuclear Matrix Element

The NME's for DBD's can be described as usual matrix elements with $\langle f|H(p)|i\rangle$ in which $|i\rangle$ is the initial state (ground state of the parent), $\langle f|$ the final state (ground state of the daughter) and $H(p)$ the Hamiltonian which includes all possible excited states of the intermediate nucleus. Since DBD nuclides have a particle number from 36 onwards (^{36}Ar), they cannot be calculated precisely and various approximations have to be applied. Different models for determining $\mathcal{M}^{0\nu}$ use different approximations that try to describe the excitation schemes of the respective nuclides.

The NME's can be separated into a Fermi and a Gamow-Teller contribution²⁵ [11]

$$\mathcal{M}^{0\nu} = \mathcal{M}_{GT}^{0\nu} - \frac{g_V^2}{g_A^2} \mathcal{M}_F^{0\nu}. \quad (2.29)$$

The Gamow-Teller term, $\mathcal{M}_{GT}^{0\nu}$, includes transitions over multiple excited states in the intermediate nucleus whereas the Fermi term, $\mathcal{M}_F^{0\nu}$, only includes 0^+ states; $2\nu\beta\beta$ decays have only a Gamow-Teller contribution since only the 1^+ states are allowed in the intermediate nucleus²⁶.

The two main approaches are called QRPA (Quasiparticle Random Phase Approximation) and ISM (Interactive Shell Model) (see e.g. [29] for an overview) but there exist many more acronyms for variations of those and for different approaches: e.g. IBM (Interacting Boson Model), HFB (Hartree-Fock Bogoljubov), EDF (Energy Density Functional), RQRPA (Renormalized QRPA) and more. Simply put, the QRPA uses particle-hole and particle-particle interactions to determine the NME whereas the ISM uses single valence particle states that interact with an effective nucleon. All theories have advantages and disadvantages and are the subject of intense ongoing research and debate.

Fig. 2.8 shows a compilation of $\mathcal{M}^{0\nu}$ for different nuclides calculated by different models. It is difficult to determine the theoretical uncertainties in NME calculations but, although not justifiable, one can use the spread of different models to gain an estimate. One should note that a difference of three in $\mathcal{M}^{0\nu}$ gives a difference of nine in $T_{1/2}$ (Eq. 2.28).

Yet another source of uncertainty is the axial nucleon coupling, g_A , which is measured as $g_A = 1.25$ in the vacuum but could as well be $g_A \approx 1$ inside a nucleus, taking quenching into account; quotations of NME values are often accompanied with the corresponding value of g_A .

²⁵A Fermi transition denotes a vector coupling without the exchange of spin; a Gamow-Teller transition denotes an axial-vector coupling with the exchange of spin.

²⁶Similar to a simple beta decay, the e^- and $\bar{\nu}$ carry away a total spin of 1. This spin is used in the 0^+ ground state of the parent to turn the spin of an initial proton into the opposite spin of the final neutron, leaving the final nucleus in a 1^+ state.

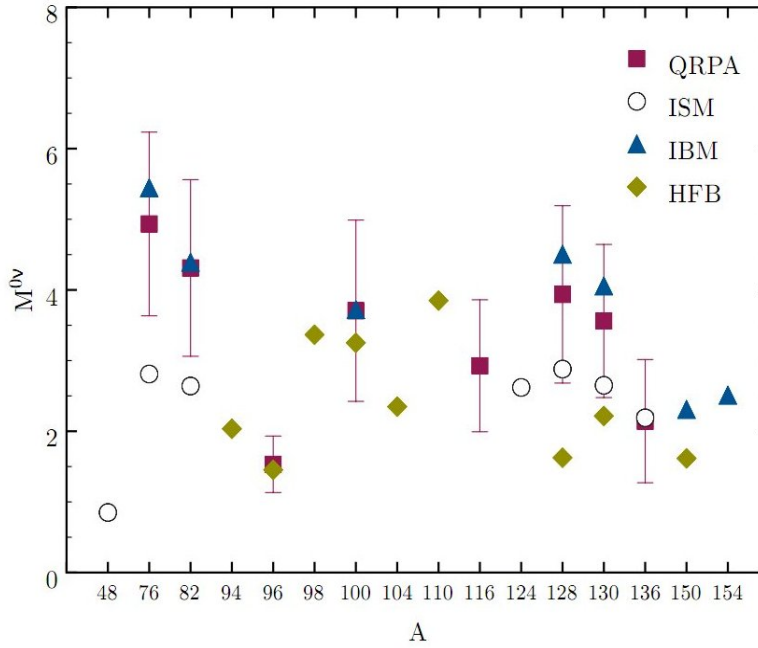


Figure 2.8 Illustration of the difference in NME calculations for $0\nu\beta\beta$ in different theoretical models and different DBD nuclides. From [33].

2.4.2 Phase Space Factor

The phase space factor is much more under control than the NME's. It depends mainly on the Q-value of the decay and the nucleus charge, Z , but needs some simplifying assumptions:

$$G^{0\nu} = \frac{F(Q_{\beta\beta}, Z)}{4R} \quad \text{with} \quad R = 1.2A^{1/3}(\text{fm}). \quad (2.30)$$

Here, F is the Fermi function, R the radius of the nucleus which is approximated with the atomic mass number A . Uncertainties are induced by the radius calculation which changes for some deformed nuclides and the Fermi function that is often approximated non-relativistically and usually does not include contributions from the electron shell.

$G^{0\nu}$ scales with Q^5 whereas $G^{2\nu}$ scales with Q^{11} which is explained in detail in [11]. Fig. 2.9 shows $G^{0\nu}$ for a variety of $0\nu\beta\beta$ candidates used in experiments.

In conclusion, the value of the phase space factors is as important for $0\nu\beta\beta$ experiments as the values of NME's which becomes apparent in Eq. 2.28.

2.5 Importance of DBD for Neutrino Physics

Experiments of all kinds set out to investigate the hierarchy structure resulting from oscillation experiments. KATRIN and MARE with β -decays, GERDA, Majorana, and many more with $0\nu\beta\beta$ decays and the PLANCK mission with new CMB data. Even oscillation experiments as e.g. SNO+ [35] will try to determine the hierarchy with oscillation effects inside the earth [19]. Neutrinos are complex particles concealing three mixing angles, three mass eigenstates one CP violating phase and possibly two Majorana phases which makes it difficult to constrain them. All experimental approaches are necessary in order to unveil the full picture of characteristics.

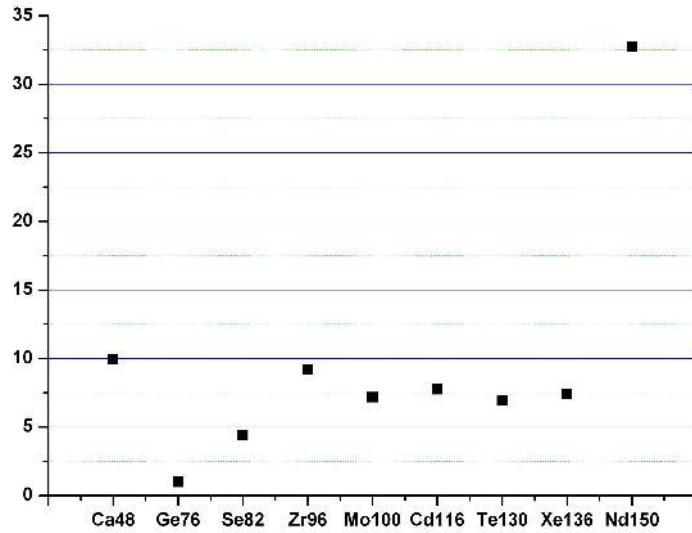


Figure 2.9 Phase space factors compared for some promising $0\nu\beta\beta$ candidates. Values are normed to ^{76}Ge . From [34].

However, only $0\nu\beta\beta$ experiments can probe the Majorana nature of neutrinos and determine possible Majorana phases. These experiments are now at the brink of validating or disproving the so far only claim of evidence for $0\nu\beta\beta$ and probing the inverted hierarchy in a next step. However, due to the intrinsic uncertainty of a signal being the $0\nu\beta\beta$ decay or an unknown background isotope, it will need more than one positive experimental results with different nuclides in order to accept a $0\nu\beta\beta$ discovery and all its implications by the community. This makes $0\nu\beta\beta$ experiments one of the most interesting and exciting neutrino experiments of our time.

Chapter 3

Experimental Considerations

Since the proposal of $0\nu\beta\beta$ decay by W.H. Furry in 1939 [5], quite a few experiments set out to find it. So far there is only a controversial claim of evidence by parts of the HDM with a half-life of $2.23_{-0.31}^{+0.44} \cdot 10^{25}$ yr in ^{76}Ge . A new generation of experiments of similar type is now being built to verify this claim and some might reach the requested sensitivity within two years.

This chapter gives a brief overview of current $0\nu\beta\beta$ experiments and their different approaches in Sec. 3.1, followed by a comparison of the underground facilities especially the Laboratori Nazionali del Gran Sasso and the Niederniveaumesslabor Felsenkeller in which the experiments for this thesis are set up in Sec. 3.2. The main sources of background that remain in a low background environment will be described in Sec. 3.3 and the statistical approaches to derive a half-life limit from measured spectra in Sec. 3.4.

3.1 Current Experiments

Current experiments use different experimental techniques and nuclides to test the $0\nu\beta\beta$ decay. The former will be explained in Sec. 3.1.1. The DBD nuclides, which are listed in Tab. A.4 and A.6 in the Appendix, have to be chosen for suitable characteristics which mainly include:

A high isotopic abundance within their elemental form or the possibility of cost efficient enrichment is needed to increase the target mass and reduce other isotopes as potential background sources at the same time. Enrichment is easiest for noble gases and favors those as candidates.

A high Q-value increases the phase space factor and, more importantly, reduces the background in the signal range. A Q-value above 2615 keV immediately decreases the background of an experiment by 1.2 orders of magnitude¹ [36].

A high NME is needed in order to be competitive at the $|m_{ee}|$ level (see Eq. 2.28); a lower $T_{1/2}$ is experimentally easier to measure.

A high phase space factor has the same argument as a high NME.

A good resolution should be available with experimental techniques that are suited for the specific element e.g. solid state detector, TPC's², etc.

Slowness of the $2\nu\beta\beta$ decay is important to avoid large background contributions in the $0\nu\beta\beta$ area for experiments with poor resolution.

A good radiopurity of the peripheral isotopes or chemically similar elements is needed to reduce the background index, BI³, in the region of interest, ROI. Especially the cosmic activation of all isotopes within the elemental composition is an issue and demands careful logistics and low neutron cross sections.

A low cost of the specific nuclide or element is important to be able to purchase a large target mass being compatible with funding.

Fig. 2.8 shows that there is no DBD nuclide that excels with an especially high NME. ^{150}Nd has a higher than average phase space factor (Fig. 2.9) but the combined difference between DBD nuclides is smaller than a factor of 5 [37] so that there is no canonical $0\nu\beta\beta$ candidate in terms of theoretical consideration.

Experimentally interesting nuclides are ^{76}Ge with the use of good resolution High Purity Germanium, HPGe, detector, ^{48}Ca , ^{150}Nd , ^{116}Cd , ^{100}Mo and ^{82}Se with a Q-value above

¹The highest occurring γ -line from natural primordial decay chain nuclides comes from ^{208}Tl with 2614.53 keV (see Tab. A.1, A.2 and A.3 in the Appendix).

²TPC - Time Projection Chamber

³The BI around the signal is often quoted in $\text{cts}/(\text{kg} \cdot \text{yr} \cdot \text{keV})$.

the natural γ -background, ^{136}Xe with easy handling and enrichment and ^{130}Te with a high natural isotopic abundance. Those are nuclides that are currently used or planned to be used in $0\nu\beta\beta$ experiments. So far many of these experiments are in a similar league of sensitivity which does not give prominence for a single $0\nu\beta\beta$ candidate with experimental considerations.

A list of experiments that are currently running or being constructed can be found in Tab. 3.1. It features the name, the $0\nu\beta\beta$ candidate, the experimental method, the isotopic mass, the resolution in FWHM⁴, the background events per year and kilogram in the FWHM, the location and a reference. The different experimental techniques will be briefly discussed in Sec. 3.1.1 and the different underground sites will be presented in Sec. 3.2. The experiments are ordered according to four different states of progress and alphabetically within each state. Numbers are taken from [38], [33] and [37] and are expectations for not yet running experiments; naturally they become more speculative in earlier states.

Table 3.1 Overview of current experiments in different stages of process with data from [38], [33], [37] and references therein. The columns denote the experiment, the DBD nuclide, the experimental technique, the isotopic mass of the DBD nuclide, the energy resolution in keV at the Q-value of the DBD nuclide, the background counts per kg and year in within the energy resolution, the location of the experiment and a reference. The underground laboratories are presented in Tab. 3.2.

Name	$0\nu\beta\beta$ nuclide	Method	Isotopic mass	FWHM [keV]	Bg [$\frac{\text{cts}}{\text{kg}\cdot\text{yr}\cdot\text{FWHM}}$]	Location	Ref.
Running & recently completed experiments							
CUORICINO NEMO-3	^{130}Te	bolom.	10.4 kg	7.9	0.18	LNGS	[39]
	$^{100}\text{Mo}/^{82}\text{Se}$	track.	6.9/0.9 kg	240	0.1	LSM	[40]
Experiments with construction funding							
CUORE	^{130}Te	bolom.	200 kg	5	0.05	LNGS	[41]
EXO-200	^{136}Xe	liq. TPC	160 kg	50	0.95	WIPP	[42]
GERDA I/II	^{76}Ge	ioni.	35 kg	4	0.04/0.004	LNGS	[43]
KamLAND-Zen	^{136}Xe	scint.	400 kg	230	0.1	Kamioka	[44]
Majorana	^{76}Ge	ioni.	26 kg	4	0.003	DUSEL	[45]
SNO+	^{150}Nd	scint.	56 kg	200	N/A	SNOLab	[35]
Experiments with R&D funding / prototyping							
CANDLES	^{48}Ca	scint.	350 g	N/A	N/A	Kamioka	[46]
C0BRA	$^{116}\text{Cd}/^{130}\text{Te}$	ioni.	40 g	30	0.3	LNGS	[47]
NEXT	^{136}Xe	gas TPC	80 kg	17	0.003	LSC	[48]
SuperNemo	$^{82}\text{Se}/^{150}\text{Nd}$	track	100 kg	100	0.01	LSM	[49]
R&D and/or conceptual design							
CARVEL	^{48}Ca	scint.	N/A	N/A	N/A	Slotvina	[50]
DCBA	^{150}Nd	drift ch.	N/A	N/A	N/A	Kamioka	[51]
EXO gas	^{136}Xe	gas TPC	N/A	N/A	N/A	SNOLab	[42]
MOON	^{100}Mo	track.	N/A	N/A	N/A	OTO	[52]

3.1.1 Different Experimental Approaches

There are two very basic different approaches for $0\nu\beta\beta$ experiments: On-source detectors in which the detector partly consists of the target nuclides and off-source detectors in which the target nuclides reside next to the detector. Both approaches have their advantages and disadvantages.

⁴Full Width at Half Maximum.

The on-source detector approach allows a variety of different techniques. It is possible to accumulate large target masses very easily as e.g. in KamLAND-Zen. One can achieve high resolution with proper detectors as e.g. in GERDA and Majorana and one can use TPC's to reconstruct the event topology as in e.g. NEXT. However, all these advantages are difficult to combine and on-source detector experiments have a limited choice of $0\nu\beta\beta$ nuclides that are suitable to be combined with detector technologies.

The off-source detector approach has the main advantage that basically every $0\nu\beta\beta$ nuclide can be investigated since it is entirely independent of the detector as e.g. in NEMO. The event reconstruction and signal efficiency is usually rather high compared to on-source experiments since the detectors technology is practically free of choice. This even allows to measure angular correlation of the two β in $2\nu\beta\beta$ and possibly in $0\nu\beta\beta$ decays. The main disadvantage is the difficulty to increase the target mass since that requires an equal increase of detectors which stresses the costs and increases the background.

The kind of detector technology which can be used for event reconstruction depends on the nuclide. There are normal, even commercially available, ionization based detectors possible with germanium in e.g. GERDA and Majorana or CdZnTe in COBRA. This can be combined with detectors working in large anti-coincidence arrays to reject background events as proposed in COBRA. There are gaseous, liquid or even solid TPCs in which the event can be reconstructed on a coordinate level e.g. in NEXT, EXO or one of the COBRA approaches. There are bolometric measurements that can use multiple axis thermal and solid state excitations (phonons) as experimental signature as in e.g. CUORICINO and CUORE and there are scintillation detectors that allow large scales as in SNO+ or KamLAND-ZEN. All these techniques have their own advantages in radioactive purity, background rejection, signal efficiency and resolution.

This thesis uses data from GERDA, an anti-coincidence on-source HPGe detector array which is thoroughly described in Chap. 4 and data from a comparably simple off-source HPGe detector setup which is described in Sec. 7.2.1.

3.1.2 Comparison of Experiments

Comparing the sensitivity⁵ of experiments is a debated endeavor since experimental techniques are quite distinct and NME calculations are uncertain. Concentrating on the experimental challenges and leaving the theoretical NME's and phase space factors aside, a good estimate of an experiment's sensitivity is the expected measurable half-life, $T_{1/2}$. It depends linear on the target mass, M , the measuring time, t , the isotopic abundance, α , and the detection efficiency, η , in the case of no background in the ROI:

$$[T_{1/2}]^{-1} \propto \alpha \cdot \eta \cdot M \cdot t. \quad (3.1)$$

A more realistic assumption of a non-zero background in the ROI changes the dependency of $T_{1/2}$ to the square root of M and t :

$$[T_{1/2}]^{-1} \propto \alpha \cdot \eta \cdot \sqrt{\frac{M \cdot t}{B \cdot \Delta E}}. \quad (3.2)$$

The product of the background, B , and the energy resolution, ΔE , is the total amount of background events in the ROI. It summarizes most of the technical difficulties and is a good figure of merit for comparing different technologies. The product $M \cdot t$ is the exposure and the least challenging in a physical point of view since it is mainly constrained by funding. However, the final effective Majorana mass $|m_{\beta\beta}|$ only depends on $M \cdot t$ with the power of $1/4$ as can be seen in Eq. 2.28.

⁵The half-life corresponding to the minimum detectable number of events over background at a given confidence level.

Even with no alien background there remains the intrinsic $2\nu\beta\beta$ background that can distribute into the ROI in experiments with poor ΔE and makes it important to either have a good ΔE or a slow $2\nu\beta\beta$ decaying nuclide.

To predict the near future physics reach and compare the current and proposed experiments, one thus needs to include the background situation, the energy resolution, the nuclide properties and non physical characteristics as the status or probability of funding. This is naturally difficult and controversial but done in e.g. [38], [33], [37]. Fig. 3.1 gives an overview of assorted past experiments (green circles) and future experiments with a reference scenario (blue squares) and an optimistic scenario⁶ (red diamonds). The background index, BI, in $\text{cts}/(\text{kg} \cdot \text{yr} \cdot \text{keV})$ is plotted versus the energy resolution in FWHM in keV whose product is the crucial factor in Eq. 3.2; the diagonal lines denote a similar product $B \cdot \Delta E$, i.e. a similar background count per exposure. Hence, the best experiments are in the lower left corner of the plot. Future experiments aim to enhance their background by up to two orders of magnitude compared to the best experiments in the past.

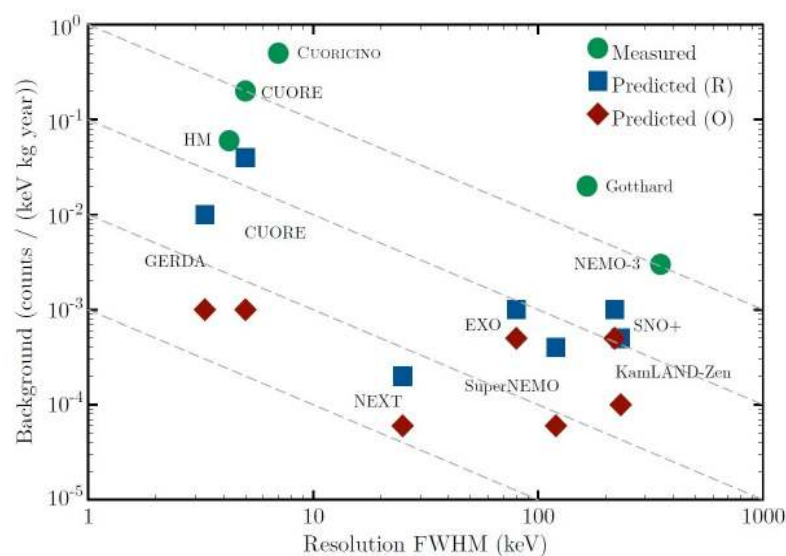


Figure 3.1 Comparison of past and future DBD experiments with past experiments in green circles and future experiments in blue squares in the reference scenario and in red diamonds in an optimistic scenario. The BI in $\text{cts}/(\text{kg} \cdot \text{yr} \cdot \text{keV})$ is plotted versus the FWHM in keV and the diagonal lines denote an equal product $B \cdot \Delta E$. Plot taken from [33] with an idea from [53].

3.2 Underground Laboratories

A variety of underground laboratories exists world wide of which most are the remains of abandoned mines or mine galleries and only few were built specifically for scientific purposes. Those purposes are not only to provide a low background environment for the actual experiments but also to provide storage capacity for materials in order to prevent them from cosmic activation and for production chains of low background materials as e.g. the fabrication of electro-formed Cu parts for the Majorana experiment in the DUSEL mine [54]. With respect to low background physics, there are some categories of comparison for underground sites:

The depth or overburden is crucial to reduce cosmic radiation. For the three contributions of p , n and μ , there are different thresholds that change the composition of the

⁶The reference scenario consists of rather conservative assumptions for B and ΔE compared to the optimistic scenario.

cosmic radiation significantly. The overburden is often scaled to a water equivalent, w.e., in order to compare different underground sites; 1000 m of w.e. is roughly 300 m of standard rock [36].

The stone composition is important for scaling the overburden to a water equivalent. It also determine the radioactivity in terms of primordial decay chains that contribute to the background of n , γ and Rn in the laboratory⁷.

The accessibility and the size of the cavities determines its use for future large scale experiments, the effort of constructing large structures and the possibility to support on-site scientific staff.

A comparison of the main underground sites world wide can be seen in Tab. 3.2 which includes the two laboratories which were used for data taking in this thesis: the LNGS and the Felsenkeller.

Table 3.2 Overview of underground facilities world wide with data taken from [55]. Name acronyms and abbreviations denote: BNO - Baksan Neutrino Observatory, BUL - Boulby Palmer Laboratory, CJPL - China JinPing Deep Underground Laboratory, CuPP - Centre for Underground Physics at Pyhäsalmi, LNGS - Laboratorio Nazionale del Gran Sasso, LSC - Laboratorio Subterráneo de Canfranc, LSM - Laboratoire Subterrain de Modane, SUL - Soudan Underground Laboratory, Kamioka - Kamioka Observatory, OTO - OTO-Cosmo Observatory, Y2L - Yang Yang Underground Laboratory, SNOlab - VALE's Creighton Inc. mine, SUL - Soudan Underground Laboratory, and DUSEL - Deep Underground Science and Engineering Laboratory. The values for n and μ are total fluxes unless an energy range is given in parenthesis, the values for Rn activities are at experimental sites and include counter measures as e.g. ventilation.

Name	Country	Depth [m w.e.]	n -flux (ΔE) [$\text{m}^{-2}\text{s}^{-1}(\text{MeV})$]	μ -flux [$\text{m}^{-2}\text{s}^{-1}$]	Rn in air [Bq/m ³]
BNO	Russia	4700	$1.4 \cdot 10^{-3}(> 1)$	$(3.03 \pm 0.19) \cdot 10^{-5}$	40
BUL	UK	2800	$1.7 \cdot 10^{-2}(> 0.5)$	N/A	N/A
CJPL	China	2500 rock	N/A	N/A	N/A
CUPP	Finland	1400 rock	N/A	N/A	N/A
LNGS	Italy	3200	$3.78 \cdot 10^{-2}$	$3 \cdot 10^{-4}$	50..120
LSC	Spain	2400	$2 \cdot 10^{-2}$	$(2.4) \cdot 10^{-3}$	50..80
LSM	France	4800	$5.6 \cdot 10^{-2}$	$4.7 \cdot 10^{-5}$	15
SUL	Ukraine	1000	$< 2.7 \cdot 10^{-2}$	$1.7 \cdot 10^{-2}$	33
Kamioka	Japan	2700	$2 \cdot 10^{-1}$	$3 \cdot 10^{-3}$	N/A
OTO-Cosmo	Japan	1400	$4 \cdot 10^{-2}$	$4 \cdot 10^{-3}$	10
Y2L	Korea	2000	$8 \cdot 10^{-3}(1.5..6)$	$2.7 \cdot 10^{-3}$	40..80
INO	India	3500	N/A	N/A	N/A
SNOlab	Canada	6010	$9.3 \cdot 10^{-2}$	$3 \cdot 10^{-6}$	120
SUL	USA	2000	N/A	$2 \cdot 10^{-3}$	300..700
DUSEL	USA	7200	N/A	N/A	N/A
Felsenkeller	Germany	120	6	$< 1.4 \cdot 10^{-4}$	50..60

3.2.1 Laboratori Nazionali del Gran Sasso (LNGS)

The LNGS [56] is part of the Italian Istituto Nazionale di Fisica Nucleare, INFN, and is the largest underground facility world wide with respect to size and scientific community. It was proposed in 1979 as a side gallery to a highway tunnel crossing the Apennine mountains close to L'Aquila in order to substantially reduce the costs. It was approved in 1982, completed in

⁷The activities of ²³⁸U, ²³⁵U, ⁴²K in e.g. granite is 60, 80, 1000 Bq/kg whereas it is in limestone 30, 70, 90 Bq/kg [36].

1987 and operated as an international laboratory since then. Three main halls and ancillary tunnels provide a space of 17300 m² or 180000 m³ for experiments (see Fig. 3.2) that are chosen by an international Scientific Committee [55]. Experiments include the main physics topics of dark matter, double beta decay, solar neutrinos, supernova neutrinos, nuclear astrophysics, neutrino oscillation and some other. 1400 m of overburden (3200 m w.e.) reduce the μ -flux to $3 \cdot 10^{-4} \text{ m}^{-2}\text{s}^{-1}$. The total n -flux is measured with $3.78 \cdot 10^{-2} \text{ m}^{-2}\text{s}^{-1}$ and separates into $1.08 \cdot 10^{-2} \text{ m}^{-2}\text{s}^{-1}$ for $E < 0.05 \text{ eV}$, $1.84 \cdot 10^{-2} \text{ m}^{-2}\text{s}^{-1}$ for $E = 0.05..1000 \text{ eV}$, $0.54 \cdot 10^{-2} \text{ m}^{-2}\text{s}^{-1}$ for $E = 1..2500 \text{ keV}$ and $0.32 \cdot 10^{-2} \text{ m}^{-2}\text{s}^{-1}$ for $E > 2.5 \text{ MeV}$. The Rn activity in the air is 50..120 Bq/m³ [55].



Figure 3.2 Illustration of the LNGS underground laboratory and the surrounding landscape.

The LNGS is the site of the GERDA experiment which provided data that is analyzed in Chap. 6 and 8.

3.2.2 Niederniveaumesslabor Felsenkeller

The Niederniveaumesslabor⁸ Felsenkeller [57] was built in 1982 and is run by the VKTA Rossendorf e.V.⁹ since 1991 with the purposes of decommissioning the old nuclear facilities in Rossendorf, fissile material and waste management, environmental and radiation protection and commercial analytical services. The laboratory itself is situated outside Dresden in the storage gallery of an old brewery with 47 m of Monzonite rock overburden which translates into 120 m w.e. and is easily accessible. Up to ten experimental setups are placed inside two chambers which are enforced with up to 35 cm of composite shielding. A n -flux of smaller than $1.4 \cdot 10^{-4} \text{ m}^{-2}\text{s}^{-1}$ and a μ -flux of $6 \text{ m}^{-2}\text{s}^{-1}$ is present inside the chambers. The Rn activity is roughly 150 Bq/m³ in the gallery and 50..60 Bq/m³ inside the measuring chambers. The laboratory is small compared to others in Tab. 3.2 and operations are maintained by two permanent staff members.

In this thesis, the Felsenkeller was used for the data taking of palladium spectra in Chap. 7.

⁸German: Laboratory for low level background measurements

⁹Verein fuer Kernverfahrenstechnik und Analytik, German: Nuclear Engineering and Analysis Rossendorf Inc.



Figure 3.3 Illustration of the Felsenkeller underground laboratory and the surrounding landscape.

3.3 Background Sources in Low Background Experiments

For $0\nu\beta\beta$ experiments it is imperative to reduce the background in the ROI as much as possible (Sec. 3.1.2). This requires the understanding and counteracting of various background sources. In addition, the statistical methods used to derive a half-life from a low count spectrum makes it essential to have a good knowledge of the remaining background composition in order to build an accurate background model. Background levels of 0.1 cts/(kg · yr · keV) are the best achieved so far in the HDM experiment and levels of 0.01 cts/(kg · yr · keV) are aimed for in current experiments such as GERDA to probe the degenerated scenario. For probing the inverted hierarchy, a background level of 0.001 cts/(kg · yr · keV) will become necessary and for the normal hierarchy, in addition to large target masses, background levels as low as 0.0001 cts/(kg · yr · keV) [53]. The advance to lower background levels changes significantly the background composition and challenges experiments with yet unknown and unconsidered influences as e.g. the recently discovered ^{42}Ar in GERDA as a dominating component.

The main background contributions in state of the art $0\nu\beta\beta$ experiments are due to cosmic muons penetrating the site's overburden (Sec. 3.3.1), cosmic activation of the actual detectors and material (Sec. 3.3.2) and primordial decay chains in the surrounding rock and material (Sec. 3.3.3).

A rather exhaustive description of background influences can be found in [36] of which most values in the following sections are cited if not marked differently. Information on cosmic radiation on sea-level can be found in e.g. [58].

3.3.1 Direct Cosmic Radiation

Primary cosmic radiation can be separated in a high energy flux from galactic sources and in a low energy flux from solar winds. The latter, with typical particle energies up to 100 keV, has proven to influence the cosmic radiation at sea-level only up to 1% in normal conditions, i.e. at non extreme solar activities [58]. Primary particles from galactic sources hit the atmosphere with an approximate flux of $100,000 \text{ m}^{-2}\text{s}^{-1}$ and are composed of 92% p , 6% α and 2% heavy nuclei. The spectral shape resembles a power law with an index of -2.7 for $E < 10^{15} \text{ eV}$ and -3 for $E > 10^{15} \text{ eV}$ [11]. These primary particles interact with atmospheric nuclei and produce showers of secondary particles that result in an average composition of 0.6% p , 15.1% e^- , 21.3% n and 63.0% μ at sea-level. This composition highly depends on local parameters such as the local magnetic field, the atmospheric density and humidity, i.e.

the weather conditions and on building material in the vicinity; especially the p and n -fluxes are highly variable. Primary cosmic γ -radiation is sparse and contributes less than 1% to the overall γ -flux which is dominated by primordial decay chains.

The μ -flux is the largest and most stable cosmic flux on sea-level with $1.44 \cdot 10^2 \text{ m}^{-2} \text{ s}^{-1}$ [59] and can penetrate into multiple kilometers of rock¹⁰. For flat overburdens, the flux scales approximately exponentially with the depth but is difficult to estimate for mountainous surfaces as Kamioka or Gran Sasso due to the complicated angular dependence. The shape of the muon spectrum shifts towards higher energies with increasing depth due to the more effective absorption of low energy muons via ionization. Some fluxes at different depth can be seen in Tab. 3.2. Neutrons have an attenuation length of one order of magnitude lower than that of muons and are absorbed almost entirely after some meters of rock by inelastic scattering. Protons are stopped within centimeters due to their additional electromagnetic interaction.

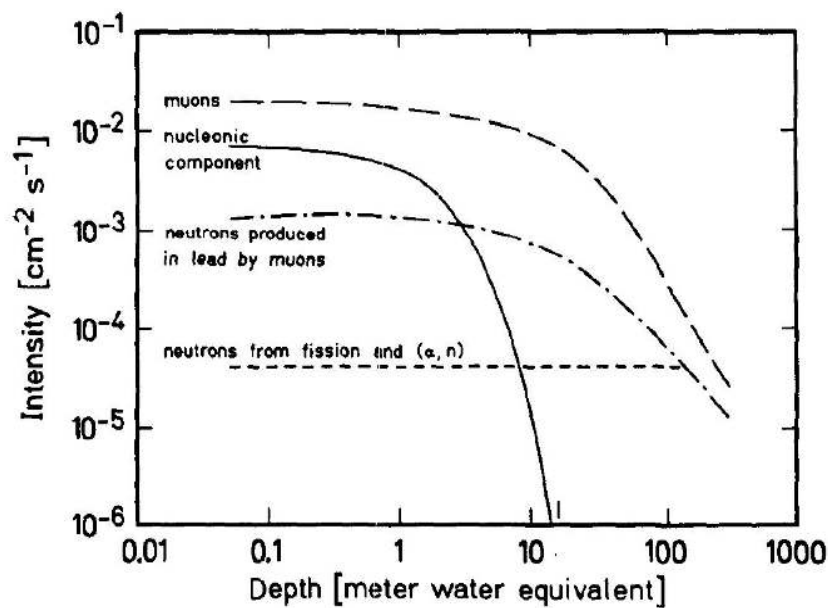


Figure 3.4 Fluxes of different secondary cosmic particles as a function of depth in m w.e. From [36].

Fig. 3.4 shows the intensity of different cosmic radiation components for different thicknesses of shielding in m w.e. The atmospheric μ -flux is compared to the nucleonic flux of p and n and to the flux of muon induced secondary neutrons. The depth independent flux of neutrons from fission and (α, n) reactions in primordial decay chains is also presented. It becomes apparent that after 20 m w.e. the primary nucleonic component becomes insignificant and secondary neutrons and neutrons from primordial decay chains dominate. After a depth of approximately 100 m w.e., the constant contribution of neutrons from primordial decay chains becomes the dominant element.

Despite that dominant constant contribution it is worthwhile to go to higher depth since it is easy to shield against low energy primordial decay chain contributions. It is also easy to reject primary muons with muon anti vetoes, so the biggest threat are neutrons being induced by high energy cosmic muons just outside the muon veto; those fast neutrons with

¹⁰The μ -flux is defined as the amount of particles that traverse a plain unit area. The integrated or omnidirectional μ -flux is the amount of particles that traverse a sphere with a unit area surface. At sea-level it is $1.92 \cdot 10^2 \text{ m}^{-2} \text{ s}^{-1}$.

energies up to GeV can easily penetrate active and passive shielding¹¹. Fluxes of induced neutrons are usually 3.4 orders of magnitude lower than the total n -fluxes but contribute to the background through in-situ activation inside the detectors; this activation might even cause delayed decays which are almost impossible to discriminate. Going to higher depth reduces this kind of background significantly.

3.3.2 Cosmic Activation

The n and p radiation on sea-level activates detector material and infrastructure material and can produce instable nuclides. This becomes especially troublesome if those nuclides have long half-lives¹² and large fractions remain at the time of commissioning of the experiment.

The straightforward approach to reduce cosmic activation is to limit the exposure to cosmic radiation. This is done by reducing transport ways, transport times, avoiding the transportation at high altitudes, shielding the material during transport, storing material underground or even producing material underground.

The prevention of cosmic activation is important but the quantitative estimation is equally imperative for constructing a solid background model. This is described in e.g. [60]. The total production rate, R_{tot} , is the sum of all productions due to n and p activations and the sum of all target nuclides in the material. R_{tot} depends on the amount of nuclei per nuclide in the material, N_i , the energy dependent n and p cross sections of all of those nuclides, $\sigma(E)$, and the n and p spectral fluxes, $\phi(E)$, as:

$$R_{\text{tot}} = \sum_{n,p} \sum_i N_i \cdot \int \sigma(E)_{i,n/p} \cdot \phi(E)_{n/p} \cdot dE. \quad (3.3)$$

The cross sections are often not well known and only numerically estimated. This is especially difficult for neutrons due to the occurrence of resonances at thermal energies. The n and p -fluxes are location dependent and intrinsically erroneous. Thus, an accurate calculation of R_{tot} is difficult and often not more than a ballpark figure.

With improving experimental shielding underground, the cosmic activation becomes the biggest background contribution in state of the art experiments as in GERDA and is extensively considered in Sec. 5.3.

3.3.3 Primordial Decay Chains

Primordial decay chains include a variety of radioactive nuclides undergoing mainly α and β -decays with accompanying γ emission. Apart from short ranged α 's and β 's with energies up to 10 MeV, their most energetic γ -line is at 2615 keV of ^{208}Tl . All decay chain nuclides are fed by merely four long living nuclides, ^{238}U , ^{232}Th , ^{235}U and ^{40}K , that have been produced in supernovae explosions and remain at significant quantities today¹³. A list of all associated nuclides with their decay characteristics can be seen in Tab. A.1, A.2 and A.3 in the Appendix. Chemically, they are placed between the elements of uranium and lead, with the exception of potassium, and are omnipresent in natural rock and chemically similar material. Typical activities in the continental upper crust are 425 Bq/kg for ^{40}K , 44 Bq/kg for the ^{232}Th chain and 20 Bq/kg for the ^{238}U chain which accounts for a sea-level γ -flux of $10^5 \text{ m}^{-2}\text{s}^{-1}$ and renders all other primordial isotopes insignificant.

In modern experiments, it is rather easy to shield against α 's, β 's, γ 's and secondary n 's from the surrounding rock with lead, copper or water. The real trouble lies in primordial

¹¹The passive shielding, e.g. PE or water, is designed to absorb less energetic neutrons from thermal to MeV energies coming from fission and (α, n) reactions.

¹²Here, long is a time frame in the order of the construction time or run time of an experiment.

¹³To be precise, ^{42}K has no decay chain and is simply a long-living nuclide. It can also be produced in advanced stellar states prior to a supernova.

decay chain impurities in materials close to the detectors and in the detectors itself. Especially standard lead has high activities of up to 2.5..50 kBq/kg due to ^{210}Pb which is part of the ^{238}U decay chain; specially manufactured lead is more expensive but can be purified up to 0.4 Bq/kg. Additionally to intrinsic impurities, lead has X-ray lines up to 80 keV which can disturb low energy γ -ray spectroscopy as in dark matter experiments and ECEC decay experiments. The strategy for passive shielding is often a composite approach out of a cheap main body of standard lead and an inner layer of purified lead to shield against intrinsic activities. An innermost layer of copper can then shield against lead X-rays.

Primordial decay chains in natural deposits are in secular equilibrium¹⁴ which takes a few half-lives of the nuclides to be reached. Material processing often breaks secular equilibrium with changing the nuclide ratios and only subsets of the decay chains with short half-life nuclides reestablish equilibrium within the time frame of experiments. This has to be considered for the screening of building material and for the calculation of internal primordial background contributions.

Radon is another major issue with ^{222}Rn ($T_{1/2} = 3.82\text{ d}$) and ^{220}Rn ($T_{1/2} = 55.6\text{ s}$) being volatile noble gas nuclides in the ^{238}U and ^{232}Th chain respectively. ^{222}Rn is emitted from surfaces containing primordial decay chains so that e.g. 1300 Bq/(m² · d) accumulates in the air coming from the continental crust [36]; this accounts for an activity of around 10..20 Bq/m³ in the atmosphere [55]. In confined cavities as underground laboratories this concentration can get larger by two orders of magnitude. Typical Rn activities in underground facilities can be seen in Tab. 3.2 where ventilation already reduces the activity compared to standing air. If Rn can propagate freely, its often charged decay products can stick to surfaces and induce high energy background through β 's and α 's. Approaches to reduce this background are the physical hindrance of air movements, sealing experiments from the common mine air, flushing experimental interiors with e.g. nitrogen, reducing primordial decay chain impurified material inside the experiments and avoiding airborne impurities to come close to the detectors with cleanrooms.

3.3.4 Anthropogenic Radioactivity

The main origins of anthropogenic radioactivity are nuclear bomb tests, the Chernobyl accident and nuclear fuel reprocessing which mainly increase the concentration of ^3H ($T_{1/2} = 12.33\text{ yr}$), ^{14}C ($T_{1/2} = 5730\text{ yr}$), ^{85}Kr ($T_{1/2} = 10.76\text{ yr}$), ^{90}Sr ($T_{1/2} = 28.79\text{ yr}$) and ^{137}Cs ($T_{1/2} = 30.07\text{ yr}$) in the atmosphere. Their concentrations vary heavily and are dependent on the location.

A danger for low background experiments exists when these nuclides get into production chains and find their way into the experimental interior. A more direct anthropogenic impurification in e.g. stainless steel results from ^{60}Co ($T_{1/2} = 5.27\text{ yr}$) which is used in steel works to measure and control the attrition of walls. Since the second world war, most steel products have a troublesome activity for low background environments due to these ^{60}Co sources and require extra considerations [36].

Another specific danger originates from less concentrated anthropogenic radioactive nuclides in the atmosphere as e.g. ^{42}Ar ($T_{1/2} = 32.9\text{ yr}$) which, beside other processes, can be produced by double neutron capture in nuclear explosions. A normally undetectable increase in concentration in the atmosphere can materialize as a severe danger to low background experiments that use huge amounts of natural argon extracted from air as e.g. in GERDA. This specific issue is intensively dealt with in Chap. 6.

¹⁴A decay chain is in secular equilibrium if the ratio of nuclides remains constant, i.e. the feeding by parental nuclides is equal to the decay of the nuclide.

3.4 From Spectral Data to Half-Lives

This section presents the general strategy starting with a measured energy spectrum over the determination of a value or the limit of a signal strength to the calculation of a corresponding half-life. The outline of the strategy is presented backwards and started in Sec. 2.4 with the calculation of the effective Majorana neutrino mass from $T_{1/2}$. In this sense, the calculation of $T_{1/2}$ out of a signal strength is presented in Sec. 3.4.1. The extraction of a signal strength or its upper limit is a more complicated endeavor. The difficulties in case of low count rates and two different philosophical approaches are addressed in Sec. 3.4.2 and 3.4.3. Two distinct Frequentist methods to derive Confidence Intervals, CI, of a parameter, e.g. the signal strength, and their application in ROOT [61] are presented in Sec. 3.4.4, for the Unified Approach of Feldman and Cousins, and in Sec. 3.4.5, for the profiled Likelihood method. The extrapolation of these methods to a count spectrum with a Gaussian signal form that covers multiple bins is done in Sec. 3.4.6.

3.4.1 Calculating Half-Lives

The calculation of a half-life out of a signal strength can be derived straight forward with the decay law. For counting experiments, the signal strength is simply the background corrected amount of signal counts in the ROI, N_{cts} . For long half-lives or slow changing source masses, the decay law can be approximated to a linear time dependency:

$$T_{1/2} = \ln 2 \cdot \frac{N_0^{\text{iso}} \cdot \epsilon_{\text{line}}}{N_{\text{cts}} \cdot \eta^{-1}} \cdot T. \quad (3.4)$$

In this equation, N_{cts} denotes the amount of signal counts which is extracted with statistical methods out of the total counts registered in the detector in the ROI which includes signal and background counts simultaneously. N_{cts} translates with the detection efficiency, η , to the total amount of decays in the source material within the measuring time, T . ϵ_{line} denotes the γ -line efficiency and N_0^{iso} the total amount of source nuclei which can be calculated from the source mass, M , the average elemental atomic mass¹⁵, A , in kg and the isotopic abundance, f^{iso} , according to

$$N_0^{\text{iso}} = \frac{M}{A} \cdot f^{\text{iso}}. \quad (3.5)$$

3.4.2 Statistical Methods for Low Count Rates

The outcome of an experiment should yield the value of a parameter, μ , and its error or confidence interval, i.e. the lower and upper limit $[\mu_l, \mu_u]$ for a specific confidence level, CL. For half-life calculations, μ is the signal strength or the signal counts N_{cts} that enters Eq. 3.4. In the ROI one expects to find signal events, s , and background events, b , which result in the measured quantity of n . The expectation value, E , of this observable is

$$E[n] = \mu s + b_{\text{tot}}. \quad (3.6)$$

In its most general form, s is a normalized probability density function, pdf, that denotes the signal form. In γ -spectroscopy that would be a Gaussian centered around the peak energy with the σ of the detector resolution. The pdf of the background is b_{tot} which has to be known to some extend prior to the calculation of μ . Unlike μ , b_{tot} is not normalized to one but to the actual amount of background events in the ROI.

There are two distinct techniques to model the expected background: An elaborate campaign of material screening and MC simulations can be used to build a background model from scratch. This requires the identification and simulation of each significant background component and later the tuning of the background model to the experimental data. Another, rather simple, approach is the fitting of the observed data in a sideband of the ROI with a suitable function. The function itself, e.g. an exponential, a linear or a constant, is to

¹⁵The atomic mass is usually quoted in atomic units u. $1 \text{ u} = 1.660538782 \cdot 10^{-27} \text{ kg}$.

some extent empirical and not theoretically motivated. In case of a MC constructed background model, b_{tot} is the superposed total background shape of all considered background processes whereas in case of a simple background fit it is the shape of the fitting function in the ROI. In HPGe γ -spectroscopy with high resolution and narrow peaks, it is often feasible to approximate the background as a constant inside the ROI. In a background only case, μ would be zero.

The distribution of s and b_{tot} need to be taken into account if the experiment is able to measure a distribution of n and is e.g. true for binned data if the energy resolution is larger than the binning. This is discussed in Sec. 3.4.6. For simplicity, s , b_{tot} and n are assumed to be simple one dimensional values in this section which is equivalent to a scenario where one bin covers the whole ROI.

In a low count rate experiment, n is quite small and can be best described by a Poisson distribution which is used to construct the Likelihood function, \mathcal{L} :

$$\mathcal{L}(\mu) = \frac{(\mu s + b_{\text{tot}})^n}{n!} e^{-(\mu s + b_{\text{tot}})}. \quad (3.7)$$

This Likelihood function denotes the probability to have measured n events with $\mu s + b_{\text{tot}}$ expected events. The maximization of $\mathcal{L}(\mu)$ with respect to μ results in the maximum likelihood estimate, MLE, for μ , $\hat{\mu}$. The background is assumed to be known with negligible uncertainty in Eq. 3.7, which is not always the case. The construction of a multi-dimensional $\mathcal{L}(\mu, \mathbf{b})$, in which \mathbf{b} can be a vector of multiple background contributions is discussed in Sec. 3.4.5.

There is the chance that a low count rate experiment does not yield a good $\hat{\mu}$ and the experimental result will be the upper limit of the parameter, μ_u . This is the case if the measured counts, n , are smaller than the expected background b_{tot} and the MLE or $\hat{\mu}$ would be unphysical i.e. smaller than zero. There are a variety of statistical methods addressing this problem which perform differently well, especially in extreme cases where even μ_u would be calculated to be smaller than zero with standard procedures.

3.4.3 Bayesian versus Frequentist

The choice of proceeding after the construction of the Likelihood function is a question of faith. There are two distinct systems of theories that differ in the very definition of probability itself: The classical or Frequentist interpretation and the Bayesian interpretation. The battleground of these theories is beyond the scope of this thesis, but a short introduction and definition of CI and CL for both theories is useful in order to properly distinguish and understand the results in this thesis.

Bayesian methods yield the posterior pdf according to Bayes' Theorem [62] and [63]:

$$P(\mu_t | n) = \mathcal{L}(n | \mu) \frac{P(\mu)}{P(n)}. \quad (3.8)$$

The nomenclature reads: The probability of the true parameter, μ_t , given the data, n , equals the Likelihood function (Eq. 3.7) times a prior pdf, $P(\mu)$, and divided by a normalization constant, $P(n)$. The Bayesian "CI" is rather called a credible interval than a Frequentist confidence interval and is calculated by integrating the posterior pdf between μ_l and μ_u until the required CL is reached:

$$\int_{\mu_l}^{\mu_u} P(\mu_t | n) d\mu_t = \text{CL}_B = \alpha_B. \quad (3.9)$$

The lower boundary, μ_l , can be chosen in order to yield a central interval or an upper limit. The subscript B in CL_B and α_B ought to indicate that the interpretation of the Bayesian confidence level is distinct from the Frequentist one. The controversial issue of a Bayesian

analysis is the introduction of a physically unmotivated or guessed prior, $P(\mu)$, that could be subjective¹⁶. A possible prior could be e.g. a Θ -function¹⁷ in case of an \mathcal{L} with its MLE below zero. The resulting posterior would be the \mathcal{L} cut at zero and Eq. 3.9 would integrate the remains up to the aspired CL to yield μ_u . In a Bayesian sense, the CI is the parameter space which contains the true value μ_t with a $\alpha\%$ probability¹⁸.

The Frequentists construction of the CI is very distinct and less intuitive. There are different methods of which two are discussed in the next sections. The Frequentist definition of a CI at a CL of $\alpha\%$ is the parameter space that includes the true parameter, μ_t , $\alpha\%$ of the times if the experiment was repeated. In other words, μ_l and μ_u are functions of n and if they fulfill the equation

$$P(\mu \in [\mu_l, \mu_u]) = \text{CL}_F = \alpha_F. \quad (3.10)$$

for an ensemble of fixed μ , then the interval contains μ_t in a fraction of α experiments.

The distinction extends to the definition of probability: The Bayesian understanding of CL_B is the degree of believe that μ_t is within $[\mu_l, \mu_u]_B$ whereas the Frequentist understanding of CL_F is the amount of times $[\mu_l, \mu_u]_F$ would include or cover μ_t . In other words with the nomenclature of Eq. 3.8, the Bayesian outcome is the probability of the true value μ_t given the data n ($P(\mu_t|n)$), whereas the Frequentist outcome is the probability of the data given the true value, $P(n|\mu_t)$.

A benchmark for statistical methods is the coverage, C , for different values of μ which is not necessarily the same as the stated CL. A method is called overcover if C is higher than the stated CL for at least one μ and it is called to undercover if C is lower than the stated CL for one μ . The first case is called conservative if the method does not undercover for any μ and leads to less powerful testing of a hypothesis, whereas the latter might lead to serious missinterpretations and should be avoided.

The methods used in this thesis are all Frequentist ones and are discussed in the next two sections.

3.4.4 Unified Approach: Feldman-Cousins

A classical and well established Frequentist approach to determine parameter limits from a likelihood function is the so called $(\ln \mathcal{L} + \frac{1}{2})$ -method which will be explained in more detail in Sec. 3.4.5. Another method is the use of information from the second derivative of \mathcal{L} . Both methods are not well defined in cases of small μ or in scenarios in which less events are observed than expected from background. This is why Feldman and Cousins [63] developed a novel method with better coverage in these situations in 1998. The procedure is called the Unified Approach or the Feldman-Cousins method and became the standard procedure for determining Frequentist CI for small event numbers.

Feldman and Cousins use the Neyman construction [64] to construct a confidence belt and find a CI for μ . The general idea is illustrated in Fig. 3.5 and involves the calculation of $P(n|\mu)$ for every μ . An interval $[n_1, n_2]$, called acceptance region, is selected which is shown in Fig. 3.5 as the horizontal lines¹⁹. The method of selecting $[n_1, n_2]$ is in principle free of choice and determines for instance whether the CI is a two-sided central interval or a single-sided upper confidence limit. A description for the latter is e.g. [33]:

¹⁶Frequentists argue, that a prior always introduces a form of belief which is epistemology connected with the analyst. This argument is countered with e.g. "ignorant" priors such as linear functions. A starting point of that discussion is e.g. [63] and references therein.

¹⁷Step function with $\Theta = 1 : x > 0$ and $\Theta = 0 : x < 0$.

¹⁸ α is defined differently in the literature. Here it is equal to the CL (Eq. 3.9) but also $\text{CL} = 100(1 - \alpha)\%$ definitions are found.

¹⁹Note that Fig. 3.5 illustrates the confidence belt of a continuous variable x instead of the discrete example of n in this section. Otherwise, n and x are the same measured quantities.

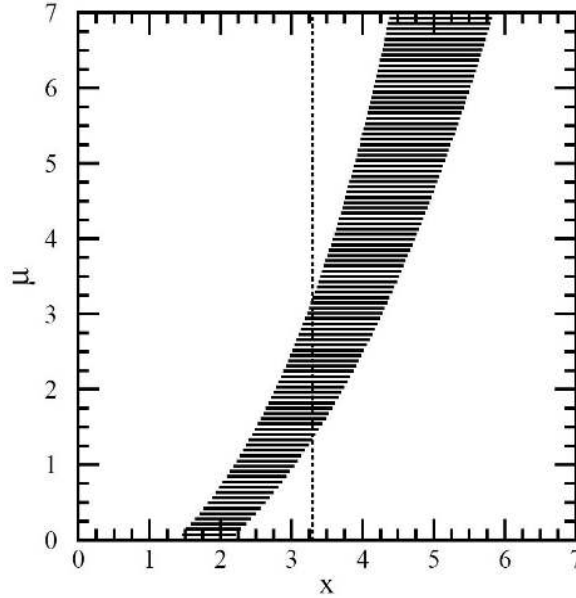


Figure 3.5 Illustration of the construction of a Frequentist confidence belt. The horizontal lines are the acceptance intervals $[n_1, n_2]$ as explained in the text. Note that x is a continuous measurement as the illustration is for a Gaussian distribution. It is, however, otherwise identical to the measured Poisson n in the text. The final CI, $[\mu_l, \mu_u]$, for a measured x/n can be extracted as illustrated with the vertical dashed line. From [63].

$$\sum_{n=n_1}^{n_2} P(n|\mu) \geq \text{CL}. \quad (3.11)$$

The CI, $[\mu_l, \mu_u]$, for a specific measured n can be extracted after the construction of the confidence belt. The difference between the classical method and the Unified Approach is the selection of $[n_1, n_2]$. At a fixed μ , Feldman and Cousins use an ordering principle for the discrete n , which is based on likelihood ratios. This procedure is quite complex and extensively described in the original paper [63] and more comprehensively explained in e.g. the appendix in [33].

The different ordering principle of the Unified Approach distorts the confidence belt of Fig. 3.5 in a way that guarantees that μ_u is never below zero and that the CI is never the empty set as illustrated in Fig. 3.6 for a Poisson signal at 90% CL with a background of $b = 3$. In this scenario, the CI is single-sided up to a measurement of $n = 5$ and becomes a double-sided central CI at higher n . The limits are discrete functions of n due to the Poisson distribution of the measurement.

The Feldman-Cousins method is implemented in the `TFeldmanCousins` ROOT class [65].

3.4.5 Profiled Likelihood

The Unified Approach gives a better coverage at low count rates than the classical method but cannot include uncertainties in nuisance parameters as e.g. the background or the efficiency; however, this can be easily done with the classical method which becomes interesting at high background uncertainties. A method to reduce multi-dimensional Likelihood functions to an \mathcal{L} that only depends on the parameter of interest is called profiled likelihood method and is extensively explained in [66] and [67].

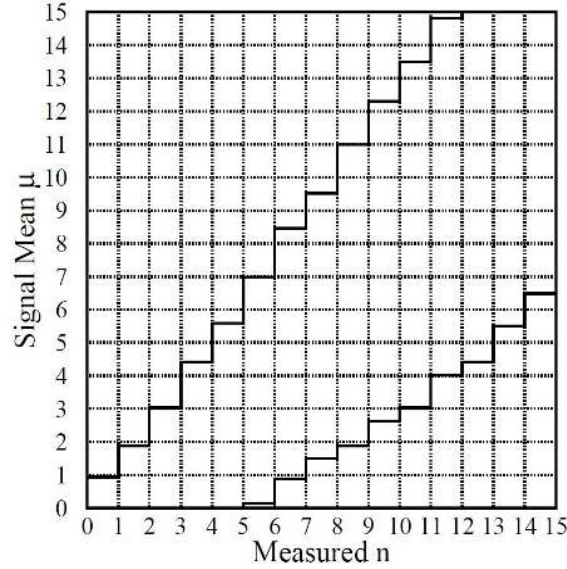


Figure 3.6 Example construction of 90 % CL central CI for a Poisson signal with $b = 3$ with the Feldman and Cousins method. From [63].

The example in this section stays close to the requirements in this thesis, namely, the nuisance parameter being the background, b , distributed according to a Poisson. However, the profiled likelihood method allows a general description with multiple nuisance parameters with different possible distributions. The \mathcal{L} in Eq. 3.7 can be extended to accommodate the background uncertainty in the following way:

$$\mathcal{L}(\mu, b) = \frac{(\mu s + b)^n}{n!} e^{-(\mu s + b)} \cdot \frac{b^m}{m!} e^{-b}. \quad (3.12)$$

$\mathcal{L}(\mu, b)$ is a two-dimensional function and can be reduced to the likelihood ratio

$$\lambda(\mu_0) = \frac{\sup\{\mathcal{L}(\mu_0, b); b\}}{\sup\{\mathcal{L}(\mu, b); \mu, b\}} \quad (3.13)$$

in which the denominator is the supremum over the whole parameter space of μ and b , i.e. one value, and the numerator only over the subspace at a fixed $\mu = \mu_0$, i.e. a function of μ_0 . Hence, the profiled likelihood function, $\lambda(\mu_0)$, only depends on the parameter of interest μ_0 . The computational difficulty of this method is to find $\sup\{\mathcal{L}(\mu, b); \mu, b\}$ in a distorted multi-dimensional parameter space.

λ is often transformed into $-2 \ln \lambda$ for mathematical simplification and can then be treated in the classical way with the $(\ln \mathcal{L} + \frac{1}{2})$ -method which is described in standard text books, e.g. [62]. The starting point is the minimum of $-2 \ln \lambda$, i.e. the MLE of which one goes to either side until $-2 \ln \lambda$ has increased by a specific amount according to the aspired CL. The underlying theory is that, at a large sample size, \mathcal{L} approximates a χ^2 pdf which is e.g. shown in [68]. For a 90 % CL, $-2 \ln \lambda$ has to raise by 2.706 [66]. The procedure is illustrated in the left panel of Fig. 3.7 which shows a scenario with 8 measured counts and 3 expected background counts. The MLE is 5 and the two bounded 95 % CI is [0.28, 12.02].

However, the classical issue remains that the method becomes weak with the breakdown of its premise of a large sample size. Especially if there are much less events observed than expected from the background, the MLE yields an unphysical negative μ and $-2 \ln \lambda$ might not even rise to yield a positive μ_u . The case of a small negative MLE is illustrated in the right panel of Fig. 3.7 for a scenario with $n = 2$ and $b = 3$ where $-2 \ln \lambda$ is cut and the new MLE is set to zero. This yields a 95 % upper limit of 3.6 in contrast to the 3.35 which

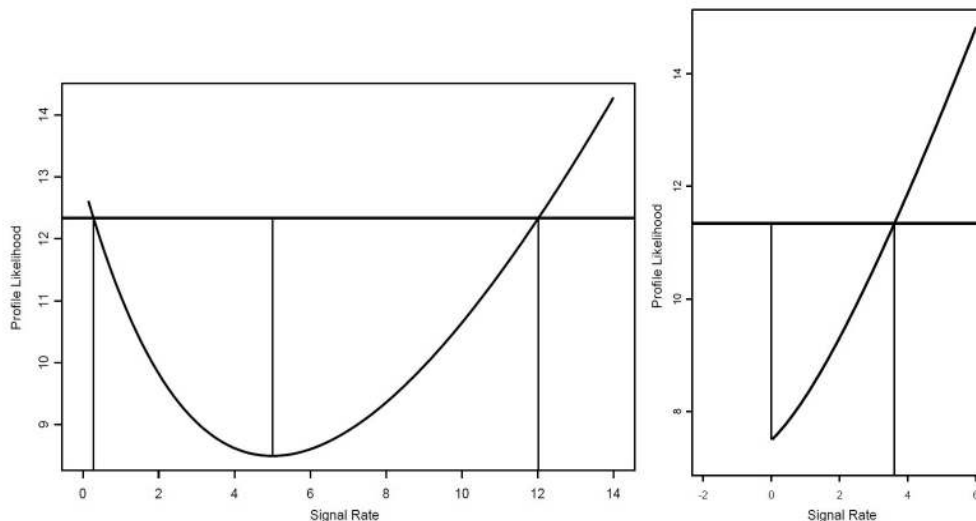


Figure 3.7 Illustration of the $(\ln \mathcal{L} + \frac{1}{2})$ -method for extracting a Frequentist CI. Left: Standard construction of a two-sided interval with $n = 8$, $b = 3$ and a MLE of 5 resulting in a CI of $[0.28, 12.02]$ at 95 % CL. Right: Construction of one-sided upper limit in case of $b > n$ at a scenario with $n = 2$, $b = 3$ and an MLE of -1 . The setting of the MLE to zero results in an upper limit of 3.6. From [66].

would be extracted with the original negative MLE at $\mu = -1$. For very large negative MLE's, Rolke et al. [66] proposes ad-hoc adjustments in order to counter the issue with e.g. artificially increasing the value of n in steps of 1 until the upper limit becomes positive. This is quite troublesome and has absolutely no theoretical justification other than increasing the coverage and not decreasing it; however, there is no method available that deals uniformly with all situations in a good way.

The profiled likelihood method is implemented in the `TRolke` ROOT class [69] for up to two nuisance parameters, background and efficiency, with Poisson, Gaussian or binomial distributions.

The two implementations in ROOT of `TRolke` and `TFeldmanCousins` are compared in Fig. 3.8. It shows a $n = 5$ and $b = 6$ scenario with the detection efficiency $z = 0.5$ as an additional nuisance parameter. The uncertainty of z , σ_e , is Gaussian and fixed to 0.1 and the uncertainty of b is Gaussian and running from 0.0 to 1.0. The profiled likelihood is plotted as squares and considers all uncertainties, whereas the Feldman and Cousins method is plotted as the triangle and ignores uncertainties, i.e. it has only one data point at $\sigma_b = 0$. The calculation of the upper limits show that in this scenario the profiled likelihood yields more conservative results with increasing upper limits at increasing background uncertainties. In a more difficult scenario ($n < b$) and without considering σ_e the Feldman and Cousins method would reveal its power and result initially in a higher μ_u at $\sigma_b = 0$ but gets overtaken at higher σ_b .

The conclusion for this thesis is to use the profiled likelihood method in case of significant uncertainty in the background model and the Feldman and Cousins method in case of negligible uncertainties. The former was applied in an in-situ background fit of low count rate data as in the Pd analysis in Chap. 7 and in the ^{36}Ar analysis in Chap. 8. The Feldman and Cousins method would be of use in case of a background model construction from scratch with MC simulations where the background uncertainty is selectable by computing power as done in the ^{76}Ge coincidence analysis in Chap. 5. In either case, with the simple implementation in ROOT, it is feasible to extract upper limits with both methods and quote them for comparison.

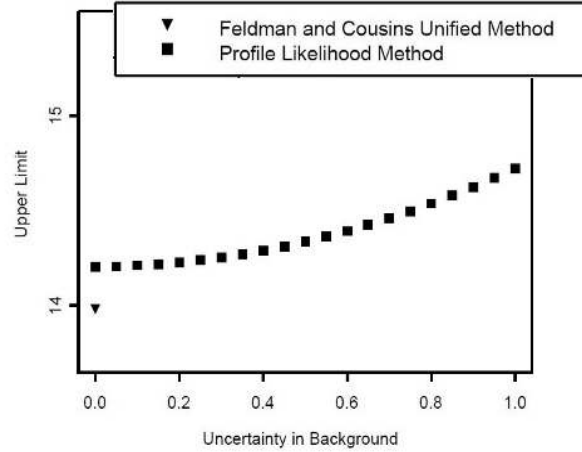


Figure 3.8 Comparison of the TRolke (squares) and the TFeldmanCousins implementations (triangle) in ROOT with the plot of the upper limit over the background uncertainty. The calculations are done in a $n = 5$ and $b = 6$ scenario with a detection efficiency of $z = 0.5$. The profiled likelihood method has a fixed Gaussian detection efficiency uncertainty of $\sigma_e = 0.1$ and a running Gaussian background uncertainty from 0.0 to 1.0. The Unified Approach considers no uncertainties and has only one data point at $\sigma_b = 0$. From [66].

3.4.6 Binned Analysis

In γ -spectroscopy data can be handled in binned or unbinned form depending on the hardware; the energy of data taken with a Multichannel Analyzer, MCA, will be binned according to the analog digital converter, ADC, whereas the energy of data taken with fast ADC's, FADC, is determined for each event with float or double size precision²⁰ and can be considered continuous. In this thesis, MCA data was taken for the Pd analysis in Chap. 7, whereas FADC data is used in the GERDA experiment in Chap. 5, 6 and 8. FADC data, however, can always be binned into a histogram after the data taking which reduces its size and makes it easier to handle but also reduces its information and statistical significance.

The statistical methods described in Sec. 3.4.4 and 3.4.5 are formulated for one data point only. If the signal extends over multiple bins this has to be taken into account. The matter has already been addressed in Eq. 3.6 in which s and b are pdf's $s(x)$ and $b(x)$ with x being e.g. the energy in an energy spectrum. A straight forward approach is to extend the likelihood function in Eq. 3.7 to the product over all N bins in the ROI with the weighting of each bin according to its fraction of s and b , s_i and b_i , [62] and [70]:

$$\mathcal{L}(\mu) = \prod_{i=1}^N \frac{(\mu s_i + b_i)^{n_i}}{n_i!} e^{-(\mu s_i + b_i)}. \quad (3.14)$$

The s_i and b_i , can be simply computed by the integral of s and b over the bin size,

$$s_i = \int_{\text{Bin}_i} s(x) dx \approx s(x_i) \cdot \Delta x_i \quad (3.15)$$

and

$$b_i = \int_{\text{Bin}_i} b(x) dx \approx b(x_i) \cdot \Delta x_i, \quad (3.16)$$

which can be approximated to the product of the value of s / b at the center of the i th bin, $s(x_i) / b(x_i)$, times its width Δx_i in keV. $s(x_i)$ is normalized to one but in case of an insufficient coverage of the signal form by the N bins, it needs to be re-normalized with the

²⁰Standard data type with 4 and 8 bytes respectively.

fraction of the coverage. As mentioned in Sec. 3.4.2, b is not normalized and denotes the absolute background counts per bin.

The binned likelihood function of Eq. 3.14 can now be used as Eq. 3.7 in all statistical methods. However, a simple recipe with the ROOT implementations of `TFeldmanCousins` and `TRolke` is to apply them to each bin individually, retrieve an upper limit μ_u^i for each bin and calculate the weighted sum of the upper limit according to the signal expectation s_i in the i th bin:

$$\mu_u = \sum_{i=1}^N s_i \cdot \mu_u^i. \quad (3.17)$$

Special care has to be taken with the bin width. If there is no additional scaling of the data histogram, the μ_u^i will be in counts per bin and the sum of the upper count limits, μ_u , will have to be divided by the bin width²¹.

The use of a normalization factor can be avoided by considering sufficient bins. For a Gaussian $s(x)$ with the uncertainty of a HPGe detector resolution and a binning of two to three bins per keV, this can easily be achieved with roughly 15 bins. However, the method yields stable results for an excessive use of bins since the outer bins at the tails of the Gaussian $s(x)$ will have an exponentially decreasing weight.

The method of weighting the individual upper limits of each bin and combining them into one upper limit is somehow troublesome since it is usually bad practice to combine limits; they are expected to be more conservative²². It is better to combine the data or MLE's and to calculate a single new limit. There is no simple approach to apply the statistical methods in Sec. 3.4.5 and 3.4.4 to a binned spectrum with different pdf's for s and b ²³ other than re-implement them with Eq. 3.14. This was beyond the scope of this thesis and the increased conservativeness was accepted.

²¹The signal fraction, s_i , is described in keV (see Eq. 3.15) so that the sum, μ_u , is described in counts/bin·keV.

²²The upper limit has a positive value per definition even in a $n \ll b$ case. The summation of upper limits can only increase the final limit which is not necessarily the same when combining MLE's. This can lead to an overestimation of μ_u and hence to a more conservative result for the stated CL.

²³The simple fit of the data with a Gaussian plus background and using the peak area as input for the statistical methods reduced the problem to one bin. This, however, ignores the fact of different expectation values for s and b in each bin.

Chapter 4

The GERDA Experiment

The GERmanium Detector Array [43], GERDA, is an experiment and collaboration founded to investigate the $0\nu\beta\beta$ decay of ^{76}Ge (Sec. 2.3.2). The experiment was designed and built by 18 institutes in seven countries and was finished to be installed in Hall A at the Laboratori Nazionali del Gran Sasso (Sec. 3.2.1) in early 2010. GERDA is an on-source ionization experiment (Sec. 3.1.1) that uses an array of HPGe detectors for anti-coincidence cuts and combines various improvements to previous experiments that are intended to reduce the BI in the ROI by a factor of 100 [71]. The main new feature is the operation of bare HPGe detectors directly in a cryogenic liquid. Currently, a first subset of detectors is operating and producing test data, which is partly analyzed in this thesis.

The scientific reach will be presented in Sec. 4.1 followed by the general concept and design in Sec. 4.2. The last two sections contain rather specific but thesis related topics: Monte Carlo simulations in Sec. 4.3 and data acquisition, DAQ, in Sec. 4.4.

4.1 Experimental Goals

GERDA is planned to run in two phases: The main purpose of Phase I is to validate or disprove the claim of evidence for $0\nu\beta\beta$ by a subset of the HDM collaboration [6] and to test the degenerated mass scale scenario (Sec. 2.2.3). When GERDA was first proposed in 2004 [71], Phase I was planned to consist of a 14 detector array with eight enriched and six normal detectors and to achieve an exposure of $15 \text{ kg} \cdot \text{yr}$ at $10^{-2} \text{ cts}/(\text{kg} \cdot \text{yr} \cdot \text{keV})$ in the ROI. After one year of data taking with the nominal 14-detector setup and without seeing an event, the HDM claim would be ruled out with 99.6% CL [71]. However, due to technical problems with the holding structure, only 12 detectors can be deployed.

For Phase II, it is intended to build additional enriched detectors and accumulate $100 \text{ kg} \cdot \text{yr}$ in 2.3 yr at a BI of $10^{-3} \text{ cts}/(\text{kg} \cdot \text{yr} \cdot \text{keV})$. The lower BI was planned to be achieved with segmented detectors that have better single-site event, SSE, versus multi-site event, MSE, discrimination¹. However, recently it was decided to use commercially available Broad Energy Germanium, BEGe, detectors that favor pulse shape analysis in order to distinguish SSE and MSE. The stated Phase II setup and exposure translates into a half-life sensitivity of $0\nu\beta\beta$ of $T_{1/2} > 2 \cdot 10^{26} \text{ yr}$ (see Eq. 3.2) and an effective neutrino mass of $|m_{ee}| = (0.09..0.29) \text{ eV}$ depending on the matrix element [71] (Sec. 2.4).

There is a multitude of other scientifically valuable investigations possible with the GERDA setup and the associated GERDA Underground Detector Laboratory, GDL; some of which are part of this thesis and will be thoroughly discussed in later chapters.

The $2\nu\beta\beta$ decay into excited states of ^{76}Se [72] is only feasible to be investigated with a sufficiently large detector array that accounts for a good detection efficiency of the de-excitation γ 's in the final state. This will be addressed in Chap. 5.

The large amount of liquid argon, LAr, that envelopes the bare HPGe detectors can be used to examine possible ECEC decays in argon. The candidate nuclide is ^{36}Ar for which an analysis is done in Chap. 8. Furthermore, a variety of nuclides contributing to the background can be investigated which is especially done for ^{42}Ar in Chap. 6.

4.2 GERDA Design & Concept

The following section describes the GERDA setup: The general GERDA design consists of a Ge detector array submersed in a cryostat filled with LAr as a cryogenic liquid. The cryostat itself is enveloped by a water tank which is supported by a superstructure that also holds various working rooms and a cleanroom on top of the experiment. Fig. 4.1 shows an

¹ $0\nu\beta\beta$ is a pure SSE. See discussion in Chap. 5

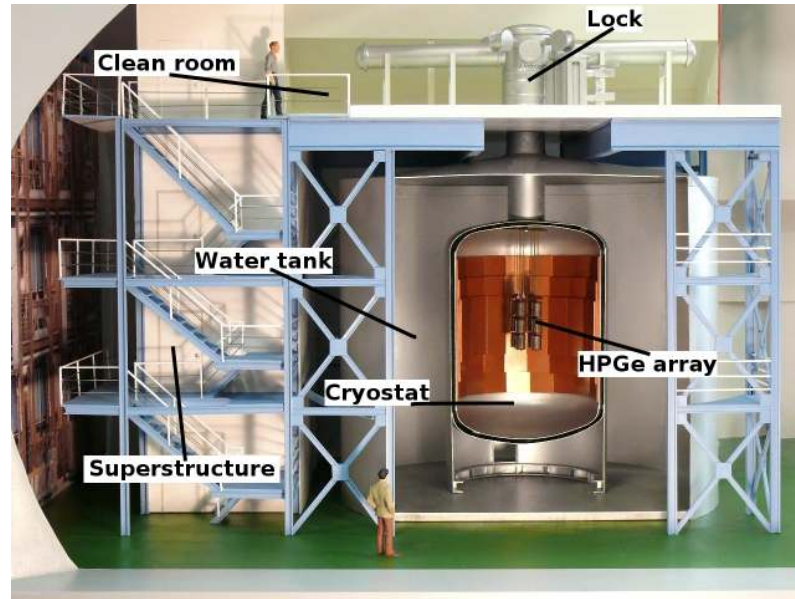


Figure 4.1 A model view of the GERDA experiment illustrating the superstructure, the cleanroom, the lock, the water tank, the cryostat and the detector array. All components apart from the latter are to scale. From [43].

overview of the GERDA superstructure with the various components.

The basic concept is meant to provide a multi layer shielding in order to counter the different kinds of background contributions. Being underground, with an overburden of roughly 3200m of water equivalent, reduces the contribution of primary cosmic ray protons and neutrons entirely; the cosmic ray μ -flux is reduced by a factor of 10^6 . The water tank is large enough to significantly reduce γ 's and n 's from the surrounding rock and also serves as an active muon veto. The LAr around the detector array is the final shielding against photons and reduces the amount of high Z material in the vicinity of the detectors which should result in a lower background from primordial decay chains and cosmic activation. Finally, the cleanroom, with two physical locks, prevents Rd and other airborne impurities to sneak into the experimental interior.

4.2.1 Detector Array

GERDA is designed as a detector array in order to use anti-coincidence cuts as background rejection for the $0\nu\beta\beta$ decays. Therefore, the actual positions of the detectors in the array are very well chosen. It is aimed to pack them as tight as possible for increased coincidence efficiency and to shield each other as good as possible from outside radiation. On the other hand, all 14 dedicated Phase I detectors have individual shapes, sizes, exposure histories and enrichment levels which makes some of them less radiopure compared to others and might lead to a deployment further away from the rest of the array. This is true for the six non-enriched GENIUS² Test Facility, GTF, [73] detectors. A thorough estimation of the intrinsic background of Phase I detectors, combining exposure history, mass and enrichment is done in Sec. 5.3. In Tab. 4.1, only a basic sample of detector characteristics is shown.

The knowledge of individual properties for each detector and the overall deployment scheme is supportive for anti-coincidence cuts for $0\nu\beta\beta$ investigation but becomes absolutely vital for coincidence analysis as is done Chap. 5. This is why different detector deployment schemes are presented in greater detail. Fig. 4.2 shows the GERDA enumeration system for detector

²GERmanium in liquid NITrogen Underground Setup

Table 4.1 Basic properties of Phase I detectors. The first three columns denote different detector names in order to avoid confusion reading different publications and the fourth column the enumeration scheme in MaGe for the Phase I array. The next columns contain the mass in g, the ^{76}Ge abundance in % and the detector origin (HMD: Heidelberg-Moscow, IGEX: International Germanium EXperiment [74] and GTF: GENIUS Test Facility [73]).

Working name	Production name [75][76]	MaGe name [75]	MaGe no. PI	Mass [g] [77]	^{76}Ge abund. [%] [76]	Det. origin
ANG1	89002	ANG1	6	958	85.92	HDM
ANG2	P40239A	ANG2	12	2833	86.44	HDM
ANG3	P40270A	ANG3	13	2391	88.15	HDM
ANG4	P40368A	ANG4	7	2372	86.30	HDM
ANG5	P40496A	ANG5	11	2746	85.60	HDM
RG1	28005-S	RGI	9	2110	87.43	IGEX
RG2	28006-S	RGII	10	2166	87.43	IGEX
RG3	28007-S	RGIII	8	2087	87.43	IGEX
GTF45	P41045A	GTF1	5	2332	7.76	GTF
GTF44	P41044A	GTF2	3	2465	7.76	GTF
GTF32	P41032A	GTF3	2	2321	7.76	GTF
GTF112	P41112A	GTF4	1	2965	7.76	GTF
GTF110	P41110A	GTF5	4	3046	7.76	GTF
GTF42	P41042A	GTF6	0	2467	7.76	GTF

strings; it allows up to 19 strings of which each can hold 3 detectors in Phase I and up to five detectors in Phase II.

Nominal Phase I The original Phase I scheme is already ruled out as an option since the expected lock was changed to a commissioning lock which can hold only 12 detectors. However, extended MC simulations have been performed and published with this setup so that it is still used as a reference and for comparison and is the base of the coincidence analysis in Chap. 5. The scheme consists of five detector strings (see Fig. 4.2): String 4 and 5 are populated by the five ANG detectors, string 14 by the three RG detectors and string 0 and 2 by the six non-enriched GTF detectors, which are further away. The Phase I setup is illustrated in Fig. 4.3.

Anticipated Phase I to date The commissioning lock can hold 3 detector strings and hence up to 12 detectors. Up to now there is no final decision neither on the positioning scheme nor on the detectors to use.

Nominal Phase II The nominal Phase II scheme was planned to consist of all Phase I detectors and additional enriched segmented detectors that had to be made out of 35.4 kg of enriched germanium [43]. This is equivalent to 14 additional Phase I size detectors which were proposed to be deployed as in Fig. 4.4. It was recently decided to use commercially manufactured enriched BEGe detectors which is still a work in progress.

Actual Phase 0 The test string, or unofficially titled “Phase 0”, consists of a single string holding three detectors: GTF45, GTF32 and GTF112 from top to bottom. For visualization see Fig. 4.5.

In all deployment schemes, the detectors are framed by low mass copper holders of which an example is shown in Fig. 4.6 on the left and in the middle. The holders and connecting cable strings are potential background sources due to primordial decay chain impurities and

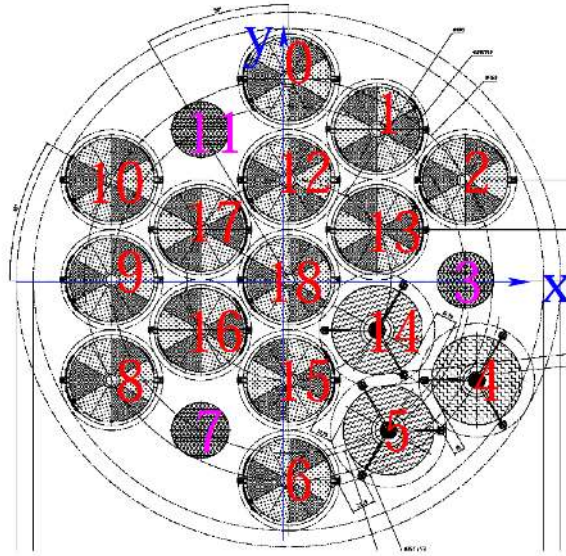


Figure 4.2 Top view onto the detector array illustrating the detector string enumeration. String positions 3, 7 and 11 are reserved for calibration sources; positions 4, 5 and 14 for the enriched Phase I detectors. From [75].

their close vicinity to the detectors. The ANG1 detector is shown as an example in Fig. 4.6 on the right. The HPGe detectors have the p-contact on the outside with a DL³ thickness of 0.8 mm; the n-contact is inside a bore hole and within the inner circle on the detector's top surface with a DL thickness of 0.001 mm. The bore holes are covered by the holder but there are openings for the LAr to enter when the diodes are submerged into the cryostat.

4.2.2 Cryostat

The active cooling of the HPGe detectors is done by 64 m³ of LAr (89.2t) which is easier to purify than solid shielding material. It provides a low enough Z as a direct detector environment and a high enough Z as a good passive shield. The stainless steel cryostat has a height of 7.805 m from bottom to neck and is separated into two walls. The inner wall is 12 mm thick and consists of 8856 kg stainless steel [79]. It is additionally coated on the inside by 16 t of copper plates [80] in order to shield the detector array from background from the cryostat walls. The cooling is done by a separate liquid nitrogen cooling circle in order to conserve LAr. Inside the LAr is a 0.03 mm thick cylindrical Rn shroud with a diameter of 76 cm centered around the detector array for guiding the natural occurring convection in such a way, that Rd contaminated LAr from the sides of the cryostat does not come close to the detectors [81]. For now, the LAr is not instrumented as an active veto; however, recent issues with accumulated ⁴²K close to the detectors may very well make that imperative (see Chap. 6).

4.2.3 Water Tank & Muon Veto

Surrounding the cryostat is a cylindrical water tank with a diameter of 10 m and a height of 8.9 m [82] containing up to 650 m³ of purified water (see Fig. 4.1). It serves as passive shielding against outside radiation, reducing the γ -background contribution to an almost insignificant level and moderating and reducing the n -flux. Sixty photomultipliers, PMT's, with the support of a reflecting foil are used as an active Čerenkov veto [83] against muons traversing the detector setup. Six more PMT's are placed in a volume called pillbox underneath the cryostat and five 200 cm \times 50 cm \times 3 cm scintillator panels [84] on top. With these

³The dead layer, DL, of a HPGe detector is a non active layer on the surface

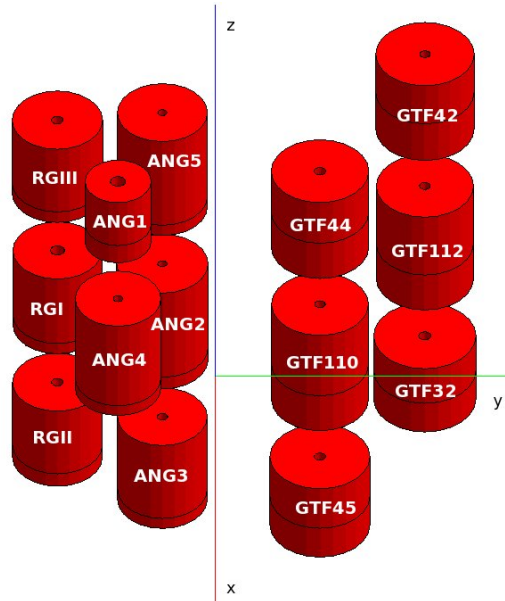


Figure 4.3 Illustrated nominal Phase I geometry.

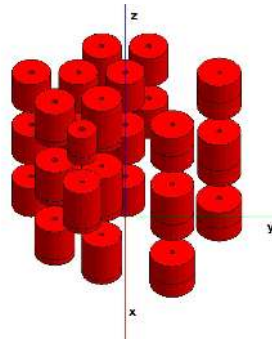


Figure 4.4 Illustrated nominal Phase II geometry.

veto, MC estimations show a better than 99% muon rejection.

4.2.4 Superstructure, Cleanroom & Lock

The superstructure in Hall A provides four levels with various rooms including space for a workshop, the DAQ and the slow control⁴ installations. On top of the water tank is a level 10,000 cleanroom⁵ that provides a first barrier for outside impurities. The air inside is constantly monitored for abnormal Rn concentrations. Inside is a glove box for the detector string assembly which provides another barrier for impurities.

Once assembled step by step in the glove box, the detector strings will be lowered into the cryostat by the lock. The lock is a sophisticated pulley that has to support the detectors weight, has to be able to withstand multiple submersions into a cryogenic liquid, has to guide a multitude of electric wiring and keep the insulation of the cryostat.

⁴Data of environmental properties e.g. HV or temperature

⁵Cleanroom standards are specified by amount and size of airborne particles. A class 10,000 cleanroom may have a concentration of fewer than 352,000 particles per m³ (10,000 particles per ft³) for particles smaller than 5 μm .

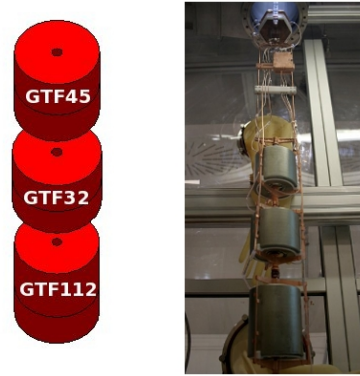


Figure 4.5 Phase 0 geometry illustrated on the left and photographed on the right. Photograph taken from [78].

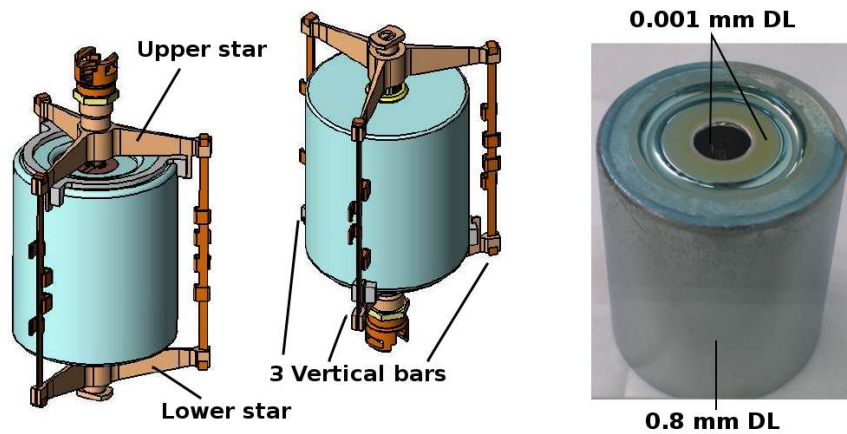


Figure 4.6 From [76]. Technical drawing of the ANG1 holder seen upright (left) and bottom-up (middle) with the three major holder components: The upper star, the lower star and the three vertical bars. A Photograph of ANG1 showing the bore hole and the DL thicknesses is presented on the right.

4.3 Monte Carlo Simulations

Modern experiments need extensive MC studies for research and development (R&D) which often justifies an own MC framework. GERDA is collaborating with the Majorana experiment [45] on a common MC framework, MaGe (MAjorana-GERda) [85], which is based on GEANT4 [86]. MaGe uses object-oriented coding, making it flexible to include new detector geometries, physical processes and output schemes, while the GEANT4 base provides a multitude of event generators, physical models, output and visualization schemes as well as thorough testing in many other experiments. MaGe is tuned to low background physics and underground applications which require precise descriptions of electromagnetic interaction at keV and MeV energies, nuclear decays, nuclear de-excitations, interactions of thermal and fast neutrons, shower developments of cosmic ray muons and α -particle penetration profiles. In addition to R&D, MC simulations are used to develop complex background models which is the main application of MaGe in this thesis.

The MaGe package contains a compiled executable that can be operated interactively or with macro ASCII files. The structure is intuitive and detailed information can be found in [85] and [87]. In the following, a brief sketch of the MaGe input sequence will be presented:

Physics Lists Physics lists are a collection of basic GEANT4 physics processes. Depending on the problem at hand, MaGe provides a preset of various physics lists e.g. specialization for low energy detector effects or high energy shower developments.

Geometries A multitude of different geometries are implemented in MaGe, ranging from the nominal GERDA Phase I/II setups to different supportive experiments such as GDL or detector testing facilities.

Output Various output schemes are implemented providing different details for track recording and detector interaction recording as well as different file formats of the output data. A ROOT output scheme was the one of choice in this thesis.

Event Generator MaGe is able to use GEANT4 native event generators e.g. the General Particle Source, GPS, as well as custom made generators such as DECAY0 [88] which were both used in this thesis. DECAY0 was the generator of choice since it considers angular correlation of cascading γ 's and accounts for higher-order effects in forbidden transitions which have an influence on the shape of the β -spectra. However, only a few selected DBD and background nuclides are implemented in DECAY0 and the GPS was used redundantly. Furthermore, MaGe contains a volume sampler that is able to distribute generated events homogeneously inside a GEANT4 volume e.g. the cryogenic liquid or a single detector.

An example MaGe macro for simulating ^{60}Co decays in the ANG2 detector is shown in Appendix B.

4.4 Data Acquisition & Processing Chain

The GERDA DAQ and analysis stream is separated in different modules and software packages. The package **MGDO** (Majorana-GERDA Data Object) is a software library and forms a standardized framework for analysis tools. It consists of data containers for the various raw data formats and manifold analyzing algorithms such as pulse fitting, energy reconstruction and baseline reconstruction just to name a few. **GELATIO** (GERda LAYout for Input/Output) are two executables designed for a modular analysis: **Raw2MGDO** converts the DAQ raw data into a ROOT file with MGDO n-tuple entries, which is done by designated operators only and provides the ability to blind the data⁶. The MGDO/ROOT files can then be analyzed using another, so far nameless, executable. A GUI or configuration file can be used with this program in order to combine user-defined MGDO modules, e.g. different energy reconstruction algorithms, to process the MGDO/ROOT file into a digested n-tuple ROOT file with different trees for each chosen module. Those trees are connected with a tree friendship. See [61] for information on ROOT.

The processing chain was still under strong development at the time of this thesis and not fully operational for the first test string data. Thus, the data used in this thesis as e.g. in Chap. 6 and 8 do not completely follow the sequence described here (see Sec. 6.4 for more information).

⁶An approach for unbiased analysis.

Chapter 5

GERDA Coincidence Analysis

This chapter presents a MC study for the investigation of the ^{76}Ge $2\nu\beta\beta$ decay into excited states with the GERDA experiment. The array of HPGe detectors proves well suited for coincidence analysis into final states with multiple γ -emissions. An extended simulation and analysis chain was developed in order to facilitate the complex incorporation of up to 14 individual detectors and their geometric deployment scheme into the analysis.

The investigation of DBD's into excited states can help to reduce the theoretical uncertainties in NME calculations. In [72] it is shown that the GERDA experiment provides the facility to test all current theoretically calculated half-life limits up to $3.1 \cdot 10^{23}$ yr with segmented GERDA Phase II detectors. This chapter is the direct preparation for the same analysis with the Phase I array.

The decays of ^{76}Ge into excited states, their theoretical predictions and the current half-life limits are presented in Sec. 5.1. The workflow of MC simulations to construct a background model is described in Sec. 5.2. The specific background model for GERDA Phase I, including various radionuclides produced by cosmic ray spallation and primordial decay chains, is constructed in Sec. 5.3. The results of the study in form of expected detector spectra, the development of a variety of cuts and their performance is presented in Sec. 5.4 and the chapter is concluded in Sec. 5.5.

5.1 Introduction

^{76}Ge can decay via $2\nu\beta\beta$ into the ground state (Q-value of 2039 keV) and excited states of ^{76}Se . The binding energy of $A = 76$ nuclides is shown in Fig. 2.6 and the level scheme of ^{76}Se in Fig. 5.1. Decays into excited states are phase-space suppressed and 0^+ states are preferred over 2^+ states (Sec. 2.3.1). The experimentally most attractive decay mode is the decay into the 1122.3 keV 0_1^+ state with a 916.7 keV β -endpoint and two prompt γ 's with 563.2 keV and 559.1 keV for the $0_1^+ \rightarrow 2_1^+$ and $2_1^+ \rightarrow 0_0^+$ (GS) transition respectively. The study in this chapter is designed for this mode but can be easily adjusted for the other excited states; occasionally, the $2\nu\beta\beta$ excited state signal is compared with the $0\nu\beta\beta$ decay into the ground state.

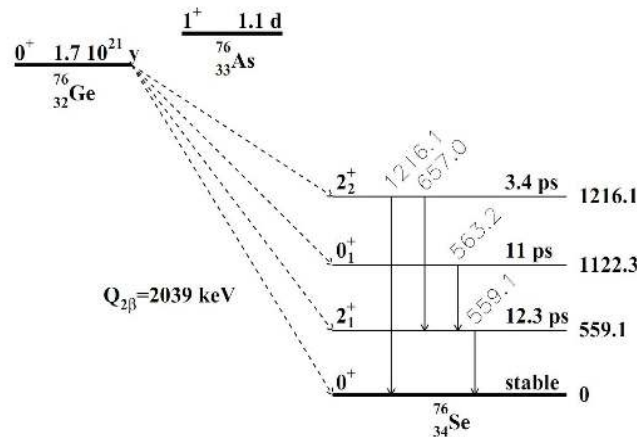


Figure 5.1 Level scheme of ^{76}Ge decays into the ground and excited states of ^{76}Se . From [72] with data from [27].

Theoretically predicted half-lives for decays into the excited states were calculated with various models (see Sec. 2.4.1). No decays into excited states of ^{76}Se were observed and the best experimental limits on the $T_{1/2}$ of each decay mode, together with predictions are shown in Tab. 5.1.

Table 5.1 Experimental and theoretical half-lives for $2\nu\beta\beta$ decays into excited states in ${}^{76}\text{Ge}$. Data taken from [72] and references therein. The theoretical models are the quasi-particle random phase approximation, QRPA, the multiple commutator model, MCM, the Hartree-Fock-Bogoliubov model, HFB, and the shell model, SM (see Sec. 2.4.1).

Decay	$T_{1/2}$ [yr]	Model	Reference
2^+ (559.1 keV)	$> 1.1 \cdot 10^{21}$	Experiment	[89]
	$1.2 \cdot 10^{30}$	SM	[90]
	$5.8 \cdot 10^{23}$	HFB	[91]
	$5.0 \cdot 10^{26}$	QRPA	[92]
	$2.4 \cdot 10^{24}$	QRPA	[93]
	$7.8 \cdot 10^{25}$	MCM	[94]
	$1.0 \cdot 10^{26}$	MCM	[95]
	$(2.4..4.3) \cdot 10^{26}$	QRPA	[96]
0^+ (1122.3 keV)	$> 6.2 \cdot 10^{21}$	Experiment	[97]
	$4.0 \cdot 10^{22}$	QRPA	[92]
	$7.5 \cdot 10^{21}$	MCM	[94]
	$4.5 \cdot 10^{22}$	QRPA	[93]
	$(1.0..3.1) \cdot 10^{23}$	MCM	[95]
2^+ (1216.1 keV)	$> 1.4 \cdot 10^{21}$	Experiment	[89]
	$1.0 \cdot 10^{29}$	QRPA	[92]
	$1.3 \cdot 10^{29}$	MCM	[94]
	$(0.7..2.2) \cdot 10^{28}$	MCM	[95]

The idea to examine $2\nu\beta\beta$ into excited states with the GERDA experiment is based on [72] and [98] which present a similar study for the segmented Phase II of GERDA. This study was done for the nominal Phase I setup with 14 detectors as described in Sec. 4.2.1 and illustrated in Fig. 4.3 with a fictional starting date of 01/07/10 and a run time of one year. The outcome of this study is a background model for each individual detector considering various internal and external background contributions. Based on this background model, various cuts are evaluated in signal and background efficiency for each of the background nuclides.

5.2 Analysis Workflow

The analysis workflow was designed to be as flexible as possible since it was expected that there would be minor changes in geometry and the time frame of the experiment. The basic strategy to construct the background model is the MC simulation of nuclear decays of the respective nuclides in each detector component. This can be either the detectors itself for internal background or the holding structure for external background. The simulation of each component has to be scaled to the expected activity of the respective component and can then be combined to the overall background model.

The MC simulations were done with the MaGe release from 05/07/10. The event generation of decays, i.e. the final state of the decay including all the particle momenta, was done preferably with DECAY0 and with the GEANT4 GPG if the decay was not implemented therein. The homogeneous sampling of the decay inside a GEANT4 volume, i.e. sampling of starting coordinates for the final state particles, was done inside MaGe. See Sec. 4.3 for more information.

There is a fundamental difference in the workflow for internal and external background. For the internal background, each detector has a different exposure history to cosmic rays, a different mass and a different isotopic composition. This means, that independent of their

mass, the individual background components differs for each detector and an independent simulation, with decays sampled in one detector volume at a time, has to be performed. For example, if a total of $14 \cdot 10^6$ decays of a specific nuclide was sampled in all 14 detector volumes at the same time, they would be distributed according to the size of the volume of each detector and it would result in the same activity per volume for each detector, which is not correct. Instead, 10^6 decays are simulated in each of the 14 detectors and scaled to their relative activity to each other later. For the external background this is different since the same holder volumes for the different detectors, even though different in size, are assumed to be equal in material, exposure history and radio impurities. This results in an equal activity per volume and leads automatically to the correct homogeneous distribution of decays by the sampling algorithm.

The simulation of 10^6 decays for each detector and background nuclide results in one ROOT file each, i.e. 14 files for each background nuclide. Each file contains the energy spectra of each active volume (detector) which results in $14^2 = 196$ spectra for each background nuclide. After the simulation, two scaling steps are required: First of all, the relative scaling between all detectors for a specific background nuclide and secondly, the scaling between all background nuclides which is essentially the scaling to the real life activity. The first scaling is done by normalizing the detector with the highest activity to 10^6 simulated decays, i.e. do not alter its simulated decays. For the other detectors, the simulated decays will be reduced to their respective fraction towards the detector with the highest activity with simply throwing away the last recorded decays in the n-tuple ROOT file. The remaining decays are combined in one n-tuple file which now appears like the correctly scaled MC simulation of the whole detector array for that background nuclide with 14 detector spectra. This two step method has the advantage over handling 196 spectra in a single step, that the original simulation output data can be significantly reduced in size from e.g. 30 GB to 150 MB in case of ^{60}Co decays¹. Additionally, the cut based coincidence analysis has to be performed with an n-tuple file which becomes straight forward with one correctly scaled file for the whole array. For the external background, the relative scaling is not necessary and the resulting 14 detector spectra can be scaled to the real life activity straight after the simulation.

The simulated events do not include the detector resolution which has to be convoluted with the simulated energies prior to the analysis. This was done as described in [99] with a Gaussian with the width of

$$\sigma = \frac{\sqrt{A^2 E + B^2}}{\sqrt{\ln 2 \sqrt{8}}} \quad (5.1)$$

in which A is the fano factor of 0.0405, B the electronic noise with 1.31 keV and E the energy in keV. As an example, the 560 keV γ -line of the signal process would be smeared with 1.23σ .

5.3 Background Model

A great deal of manpower and resources is spent in constructing background models for the $0\nu\beta\beta$ in ^{76}Ge by the GERDA collaboration and similar experiments. This decay appears as a monoenergetic single site event at 2039 keV in the detectors and can be furthermore discriminated from background by pulse shape analysis and the segmentation of the detector in arrays and the use of anti-coincidence. The sophisticated and well established background models for $0\nu\beta\beta$, however, can not be used for the $2\nu\beta\beta$ decay into excited states since its main feature are two γ -lines at 563.2 keV and 559.1 keV, which requires the consideration of entirely different background components. Hence, it is imperative to construct an entirely new background model with the emphasis on nuclides with multiple γ 's in the final state which is expected to be the largest background for multi-detector cuts.

¹The reduction is mainly due to the omission of non vital information in the output scheme of MaGe during the copying process.

The contribution of different background components for $0\nu\beta\beta$ is shown in Fig. 5.2 and served as a starting point for constructing the new background model. The detector intrinsic background from ^{68}Ga and ^{60}Co is expected to have the largest impact followed by primordial decay chain nuclides in the detector holders. However, a difference is expected for e.g. ^{68}Ga which is the largest contribution for $0\nu\beta\beta$ but is less critical for this study - in contrast to ^{60}Co . ^{68}Ga has an 8.94% probable GS transition with a 2921.1 keV β -endpoint and no significant γ -line which is an indistinguishable background for $0\nu\beta\beta$ but not for coincidence analysis. ^{60}Co , on the other hand, has two prominent γ -lines with more than 99% probability at 1173.24 keV and 1332.50 keV but only a 318.13 keV β -endpoint which is easily rejectable by pulse-shape analysis and anti-coincidence for $0\nu\beta\beta$ but can equally easily mimic the coincidence signal in this study.

Source	B [10^{-3} cts/(keV kg y)]
Ext. γ from ^{208}Tl (^{232}Th)	$\ll 1$
Ext. neutrons	< 0.05
Ext. muons (veto)	< 0.03
Int. ^{68}Ge ($t_{1/2} = 270$ d)	12
Int. ^{60}Co ($t_{1/2} = 5.27$ y)	2.5
^{222}Rn in LN/LAr	< 0.2
^{208}Tl , ^{238}U in holder	< 1
Surface contam.	< 0.6

Figure 5.2 Expected background components for the $0\nu\beta\beta$ region in GERDA Phase II. From [100].

5.3.1 Cosmic Activation and Internal Background

Cosmic radiation on the earth surface can activate Ge isotopes inside the detectors into unstable nuclides that decay during the run time of the experiment and produce background (Sec. 3.3.2). The calculation of the production rate with Eq. 3.3 is complicated and has to consider all four stable Ge isotopes, ^{70}Ge , ^{72}Ge , ^{73}Ge and ^{74}Ge and the actual DBD isotope ^{76}Ge as targets and the various potential background nuclides as reaction products. Additionally, it has to be distinguished between the natural and the enriched isotopic composition of Ge. The selection of potential background isotopes follows the criteria of a long half-life², a high Q-value³ and prominent γ -lines with high probability and energy.

The production of radionuclides by cosmic ray spallation was extensively investigated by many groups (see e.g. [101]) and the most significantly produced nuclides are presented in Tab. 5.2. It shows the nuclide, the half-life, $T_{1/2}$, the Q-value, the most prominent γ -lines and the production rates, R in $\text{kg}^{-1}\text{d}^{-1}$ for natural and enriched Ge. The latter values are taken from [102] and are a composition of calculations with different codes for different energy ranges. There are no quoted uncertainties, but the production rates differ significantly between publications; however, the cited values are rather conservative in comparison. The first row in Tab. 5.2 is an exception and describes a decay chain; ^{68}Ge is cosmically produced and decays into ^{68}Ga with a half-life of 270.8 d. ^{68}Ge itself is not potentially troublesome, but ^{68}Ga decays with the quoted Q-value of 2921.1 keV and a half-life of 67.63 min.

With the production rates and the exposure history, the amount of background nuclei produced in each detector for each nuclide can be calculated. Their amount will reduce from the time of exposure till the start of the experiments according to their half-life which can easily

²Most activated products have half-lives smaller than a day. In this paradigm, long means in the order of construction and run time of experiments, i.e. more than some month.

³Higher than the $0\nu\beta\beta$ Q-value of ^{76}Ge .

Table 5.2 Important spallation produced radionuclides in Ge. The columns denote the nuclide, the half-life, the Q-value, the most prominent γ -lines and the productions rates in natural and enriched Ge. The first row shows a decay chain in which the $T_{1/2}$ and the production rates are those of the parent and the Q-value and the γ -lines are those of the progeny.

Nuclide	$T_{1/2}$ [d]	Q-value [keV]	γ -lines [keV (eff)]	R_{nat} [$\text{kg}^{-1}\text{d}^{-1}$]	R_{enr} [$\text{kg}^{-1}\text{d}^{-1}$]
$^{68}\text{Ge}/^{68}\text{Ga}$	270.8	2921.1	1077.35 (3.0)	89	13
^{60}Co	1924.06	2823.9	1173.24 (99.97) 1332.50 (99.99)	4.8	6.7
^{65}Zn	244.26	1351.9	1115.55 (50.60)	77	24
^{58}Co	70.86	2307.4	810.78 (99)	14	6.2
^{57}Co	271.79	836.0	14.41 (9.16) 122.06 (85.60) 136.47 (10.68)	9.7	2.3
^{54}Mn	312.3	1377.1	834.85 (99.98)	7.2	5.4

be calculated with the decay law. However, for exposures at different times in history, it is imperative to track the decline of each bunch of produced background nuclei at a different time individually and simply sum up the remains at the starting time of the experiment. The application of the production rates and the exposure history to the specific requirements of Phase I will be done in Sec. 5.3.3.

The recent exposure history dating back to 2006 for each detector, was taken from [76] and is shown in Tab. C.1 in the Appendix. It shows the dates of exposure which are grouped if the dates are in close proximity, the exposure time in days and the elapsed time until the fictional start of the Phase I.

5.3.2 Primordial Decay Chains and External Background

Detector germanium is treated and purified intensively and is expected to have insignificant contaminations of primordial decay chain isotopes which are therefore not considered in this study. This assumption is supported by the results of former Ge DBD experiments as e.g. HDM, that could not see these impurities in their long-term background runs⁴ [103].

Material close to the detectors like the holding cables and the holder frames (Fig. 4.6), however, are expected to contain primordial decay chain impurities. Material screening by the GERDA collaboration shows that plastic-like components as e.g. PTFE have rather high intrinsic activities per unit mass compared to e.g. Cu. The holders mainly consist of pure recycled LENS⁵ Cu in three different main parts, the so called lower star, upper star and vertical bars, illustrated in Fig. 4.6. They are implemented in MaGe with their volume names `LowerStar`, `UpperStar` and `VerticalBar`, where three volumes per holder exist of the latter. These volumes are the only ones used in this study, since the PTFE mass fraction of the holder material is small in comparison and the total activity is thought to be negligible.

The different sized detectors have different sized holders and the mass for each holder component has to be considered. MaGe allows the summation of volumes of the same kind e.g. the sampling of events inside all `LowerStar`'s. This automatically accounts for the right distribution of simulated events between this components of the same kind and requires only their total mass for scaling the MC. The data for the individual masses of the holder volumes was taken from [76] and is presented including the total mass in Tab. 5.3.

⁴The upper activity limits were $0.006 \mu\text{Bq}/\text{kg}$ for ^{228}Th and $0.01 \mu\text{Bq}/\text{kg}$ for ^{226}Ra with 90 % CL.

⁵The LENS experiment, Low Energy Neutrino Spectroscopy [104].

Table 5.3 Masses of the holder components vertical bars, upper stars and lower stars for each detector. The data is taken from [76]. Values for detectors marked * are estimated due to the lack of data sheets. There are three vertical bars per holder which are taken into account in the total sum for each component in the bottom row.

Detector	Vertical bar m [g]	Upper star m [g]	Lower star m [g]
ANG1	3.5	28.0	25.0
ANG2	4.2	32.5	28.3
ANG3	4.0	32.5	28.3
ANG4	4.1	32.5	28.3
ANG5	4.2	32.5	28.3
RGI	3.4	32.5	28.3
RGII	3.8	32.5	28.3
RGIII	3.7	30.0	26.5
GTF32	3.5	35.6	31.0
GTF42*	3.6	35.6	31.0
GTF44*	3.6	35.6	31.0
GTF45	3.6	35.6	31.0
GTF110	4.3	35.6	31.0
GTF112	4.1	35.6	31.0
Sum	160.8	466.6	407.3

Tab. A.1, A.2 and A.3 in the Appendix show all primordial decay chain nuclides of which ^{214}Bi and ^{208}Tl are chosen due to their numerous high energetic and intensity γ -lines. ^{40}K with an 11% 1460.83 keV γ -line is chosen because it is often contained in Cu with higher activities than the primordial decay chains [36]. Additionally, ^{60}Co and ^{137}Cs are considered. ^{60}Co is cosmically produced and ^{137}Cs is a product of the nuclear fuel cycle (see Sec. 3.3.4).

The activity of the holder Cu with respect to each background nuclide has been obtained by personal communication with Hardy Simgen. Measured limits on activities are shown in Tab. 5.4.

Table 5.4 Upper activity limits of important background nuclides in Cu of detector holders in GERDA.

Nuclide	^{262}Ra	^{228}Th	^{40}K	^{60}Co
A [$\mu\text{Bq/kg}$]	< 16	< 19	< 88	< 10

The measured activities for ^{226}Ra and ^{228}Th in the ^{238}U and ^{232}Th decay chains respectively are in secular equilibrium with their progenies (Tab. A.1 and A.2 in the Appendix).

5.3.3 Phase I Background

The background shape and quantity is depending on the time of the experiment compared to the time of exposure. This effect becomes more significant for nuclides with short half-lives. For this study, the Phase I setup was assumed to start taking background data from 01/07/10 for one year ending 30/06/11. It is necessary to calculate the expected number of background events in Phase I for scaling the MC simulations which can easily be done with the decay law.

For spallation produced radionuclides, the previous production calculations were used and the exponentially decaying background nuclei in Phase I are summed up and presented in Tab. 5.5. Additionally to the intrinsic cosmogenically produced background from Sec. 5.3.1, the $2\nu\beta\beta$ ^{76}Ge decay into the ground state is calculated for each detector with the assumed half-life of $1.55 \pm 0.01(\text{stat})_{-0.15}^{+0.19}(\text{syst}) \cdot 10^{21}$ yr [105]. The signal process itself is also calculated for illustration with a fictional $T_{1/2}$ of 10^{23} yr. The uncertainties of the expected decays during Phase I in Tab. 5.5 were not calculated; they are mainly determined by the uncertainties of the production rates which are not known.

The decays in Tab. 5.5 are already the result of the two-step scaling mentioned in Sec. 5.2 and give a more comprehensive idea of the background. For technical details, the first step, i.e. the normalization between the detectors, is presented in Tab. C.2 in the Appendix and the second step, i.e. the scaling of the simulation to real life is shown in Tab. C.3 in the Appendix.

Table 5.5 Background model of intrinsic background nuclides. The ^{76}Ge $2\nu\beta\beta$ decay into the ground state and the signal transition into the first excited 0^+ state with a fictional $T_{1/2}$ of 10^{23} yr are presented in the last two columns respectively. The values denote the expected decays per nuclide and detector within the 1 yr run-time of the fictional GERDA Phase I.

Detector	^{68}Ga	^{60}Co	^{65}Zn	^{58}Co	^{57}Co	^{54}Mn	$^{76}\text{Ge}(\text{GS})$	$^{76}\text{Ge}(\text{Sig})$
GTF42	13.25	5.22	18.11	0.003	2.94	2.88	677.20	10.50
GTF112	27.66	4.24	33.68	0.044	5.14	4.71	813.91	12.62
GTF32	20.99	4.68	25.46	0.034	3.88	3.55	637.13	9.88
GTF44	11.82	4.37	15.98	0.003	2.58	2.51	676.66	10.49
GTF110	24.69	3.95	30.07	0.044	4.59	4.22	836.14	12.96
GTF45	31.86	3.77	37.43	0.061	5.58	4.98	640.15	9.92
ANG1	2.70	2.35	6.56	0.030	0.74	2.06	2912.73	45.15
ANG4	4.04	3.93	10.35	0.022	1.19	3.42	7241.27	112.24
RG3	6.62	6.37	15.82	0.076	1.75	4.80	6454.64	100.05
RG1	3.67	4.33	9.23	0.021	1.05	2.96	6525.77	101.15
RG2	4.09	3.28	10.23	0.024	1.16	3.26	6698.97	103.83
ANG5	4.72	4.63	12.12	0.025	1.40	4.02	8315.02	128.88
ANG2	5.47	5.16	14.01	0.028	1.61	4.61	8662.64	134.27
ANG3	9.91	6.37	23.89	0.095	2.65	7.27	7455.74	115.56
Sum	171.50	62.63	262.93	0.51	36.24	55.25	58547.97	907.49

For the primordial decay chain nuclides it is not necessary to use the exponential decay law since the half-lives of the feeding nuclei are long compared to experimental time frames. The amount of decays per nuclide and volume can simply be calculated by the product of activity and run time and is presented in Tab. 5.6. For ^{137}Cs there was no known upper limit for the activity in holder Cu.

DECAY0 was used as an event generator for the MC simulations (Sec. 4.3) for ^{60}Co , ^{65}Zn , ^{54}Mn , ^{214}Bi , ^{208}Tl , ^{40}K , ^{137}Cs , ^{76}Ge into the ground state and for the signal process ^{76}Ge into the first excited 0^+ state and the GPS was used for ^{68}Ga , ^{58}Co and ^{57}Co .

Table 5.6 Decays in Phase I of external background nuclides in the five holder volumes LowerStar, UpperStar and three times VerticalBar in GERDA Phase I.

Nuclide	Lower star	Upper star	3 × vertical bar
²¹⁴ Bi	205.51	235.44	81.14
²⁰⁸ Tl	231.20	264.86	91.28
⁴⁰ K	1130.33	1294.89	446.25
⁶⁰ Co	128.45	147.15	50.71
¹³⁷ Cs	N/A	N/A	N/A

5.4 Monte Carlo Results

With the background model construction described in Sec. 5.2 and with the data from Sec. 5.3, it is possible to predict the energy spectrum for each detector and how it would appear after a specific time of data taking starting at a specific date. This can include spectra with and without coincidence cuts and is presented in Sec. 5.4.1. Furthermore, it is possible to develop a variety of cuts with the emphasis on rejecting a major fraction of background events but letting pass most of the signal events. If these cuts are applied to simulated background and signal events, it is possible to determine their efficiency and decide which cut to use for future experimental data analysis. An extensive cut analysis is done in Sec. 5.4.2.

5.4.1 Energy Spectra

The spectral shape of decaying background nuclides in GERDA is often not obvious even when knowing the decay properties. Experience of spectral shapes is mostly based on γ -spectroscopy with the radioactive source located outside the detector and with rather low detection efficiency. The GERDA array, however, approaches almost calorimetric properties in which often a large fraction of decay energy is recorded in one or multiple detectors that can be used for a better understanding of the decay. The consideration of internal and external background will also show a distinct difference in spectral shapes which is mainly due to the electron energy being added to the event or not. For all these reasons, the main features of each background nuclide will be briefly discussed in the following.

Fig. 5.3 and Fig. C.1 till C.12 in the Appendix show the spectra of signal and background decays, how it is seen in the example detector ANG2 without a coincidence cut (left side of the plots) and how it is seen in the whole GERDA setup as a sum of all detector energies for one event⁶ (right side of plots). The GERDA plots smear any γ -peak in the presence of a β -spectrum, since the β -energy is always added to the total energy. Decay properties are taken from [106].

Signal Fig. 5.3. The signal decay shows a clear γ -line at 560 keV including the Compton features and a small summation peak at around 1120 keV in the ANG2 spectrum. The difference of 4.1 keV of the two γ -lines is not distinguishable by the assumed detector resolution of 1.23σ at this energy (see Sec. 5.2). The continuum is due to a superposition of the β with one or two γ 's. The GERDA spectrum shows two dents which are due to the escape of one and two γ 's.

⁷⁶Ge (GS) Fig. C.1 Appendix. The DBD into the ground state is seen both by ANG2 and GERDA as described by Eq. 2.22. Events with energies close to the Q-value become statistically less likely and are not well represented by the limited MC.

⁶Note that the spectrum of the sum of energies of all detectors per event is not the same as the sum of spectra.

- ⁶⁸Ga** Fig. C.2 Appendix. ⁶⁸Ga is a β^+ -decay with a Q-value of 2921.1 keV and has significant annihilation lines at 511 keV and 1022 keV as can be seen in the ANG2 spectrum. In the GERDA spectrum, most annihilation γ 's are recorded and only the summation peak is visible; a small "escape dent" is imaginable at 511 keV. The 88.0% β -spectrum with an endpoint of 1899.1 keV is added to the 511 keV γ in the single detector spectrum.
- ⁶⁵Zn** Fig. C.3 Appendix. With a Q-value of 1351.9 keV, ⁶⁵Zn decays by 98% via EC which results in many low-energy X-rays and no continuous β -spectrum. The 50.6% 1115.55 keV γ -line is the main feature in the spectra and there is a summation peak at the Q-value energy. The absence of a β -spectrum results in a similar shape for the ANG2 and GERDA plot.
- ⁵⁸Co** Fig. C.4 Appendix. ⁵⁸Co decays by 85% via EC with a Q-value of 2307.4 keV. The main feature is a 99% 863.96 keV γ -line, a 0.52% 1674.73 keV γ -line and the annihilation peak.
- ⁵⁷Co** Fig. C.5 Appendix. With a Q-value of 836.0 keV, ⁵⁷Co can only decay via EC and has prominent low energy X-rays and a 122.06 keV γ -line.
- ⁵⁴Mn** Fig. C.6 Appendix. ⁵⁴Mn decays only via EC and has one γ -line at the Q-value of 834.85 keV.
- ⁶⁰Co in the detectors** Fig. C.7 Appendix. ⁶⁰Co (2823.9 keV Q-value) has two γ -lines with more than 99% probability at 1173.24 keV and 1332.50 keV and a low 99.9% 318.13 keV β -endpoint which make this decay rather deterministic since there are almost no superpositions of other decay modes. The two γ -lines and their summation peak show some smearing with the low energy β in ANG2 which happens if the γ and the β are detected coincidentally in the same detector. It is much more likely that they are detected coincidentally in the whole GERDA setup which is why the smearing is more significant in the right plot.
- ⁶⁰Co in the holders** Fig. C.8 Appendix. The comparison with ⁶⁰Co decays in the holder shows that the β -tails are gone since they have no chance of propagating into the detector. Here, the ANG2 and GERDA plots look identical which is true for all holder spectra.
- ²¹⁴Bi** Fig. C.9 Appendix. ²¹⁴Bi has a Q-value of 3272 keV and multiple γ -lines dominate the spectra of which the most prominent are listed in Tab. A.1 in the Appendix.
- ²⁰⁸Tl** Fig. C.10 Appendix. ²⁰⁸Tl has a Q-value of 5001 keV and the highest γ -line of the primordial decay chain nuclides at 2614.53 keV with 99%. Summation peaks with lower energetic γ -lines can, however, deposit energy above this natural threshold.
- ⁴⁰K** Fig. C.11 Appendix. ⁴⁰K can decay via β^- -decay (1311.09 keV Q-value) or β^+ -decay and EC (1504.9 keV Q-value) and has a prominent 11% γ -line at 1460.83 keV.
- ¹³⁷Cs** Fig. C.12 Appendix. ¹³⁷Cs has a Q-value of 1175.63 keV and a 85.1% γ -line at 661.66 keV.

Background estimations are often presented in BI in $\text{cts}/(\text{kg} \cdot \text{yr} \cdot \text{keV})$ and have to be scaled accordingly. The two step-scaling of simulation to real life as described in Sec. 5.2 and in Tab. C.2 and C.3 in the Appendix were applied to each spectrum of each detector and background nuclide. The next scaling was done to unit mass, i.e. kg, which has to be done for each detector individually and is essentially the division of the spectrum by the active mass of its detector. The scaling to unit time, i.e. yr, was already done since the background model was developed for one year. The scaling to cts/keV is the adjustment to the bin width of the histograms in which the spectra are presented. Special care has to be taken for the summation of spectra of different detectors since this has to be done prior to the mass scaling.

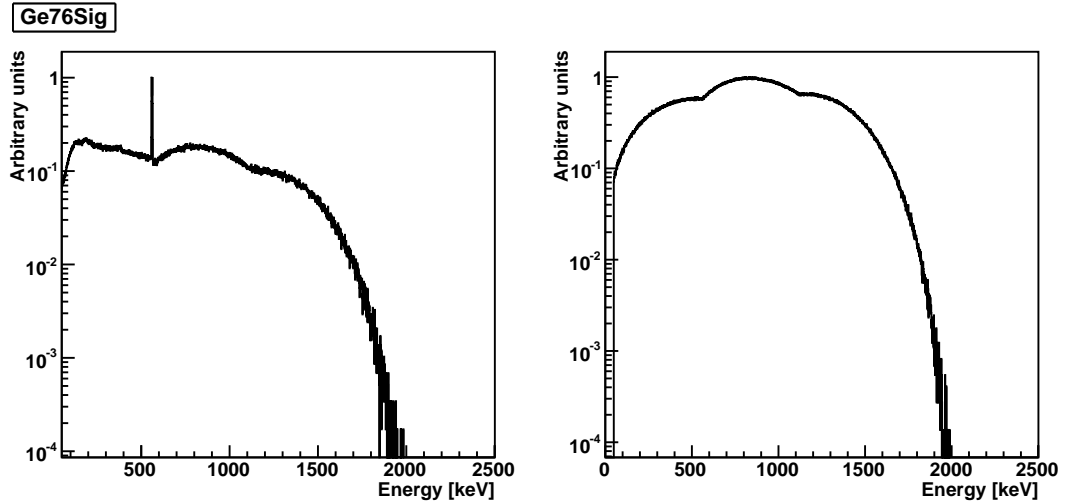


Figure 5.3 Spectral shape of the ^{76}Ge $2\nu\beta\beta$ decay into the first excited 0^+ state as seen in ANG2 without any coincidence cuts (left) and in the whole GERDA Phase I setup, i.e. sum of all detector energies (right). The spectra are shown in arbitrary units normalized to their maximum bin entry.

Fig. 5.4 shows the individual internal background components for all natural detectors and Fig. 5.5 for all enriched detectors. The spectra are scaled to $\text{cts}/(\text{kg} \cdot \text{yr} \cdot \text{keV})$ and the black plots denote the scaled sum spectra over all nuclides and all natural or enriched detectors respectively. The gray plots denote the scaled sum spectra over all nuclides and all detectors and is essentially the weighted average of the black plots from each figure.

These figures illustrate the difference in absolute numbers and shape of background for natural and enriched detectors which is mainly due to different cosmogenic productions in different isotopic compositions (see Tab. 5.2) but also due to different exposure histories and localization in the GERDA Phase I array. The ^{76}Ge (GS) background (blue) is the dominating feature in both figures but one order of magnitude larger in the enriched case which corresponds to the factor of ten of the enrichment of ^{76}Ge . This background, however, does not effect the $0\nu\beta\beta$ ROI at 2039 keV and can be rejected by multi-detector cuts for the excited state signal which makes the other background isotopes more important to consider. ^{68}Ga , which is shown in green, is easier produced in the natural isotopic composition and is the main component for these detectors with roughly $2 \cdot 10^{-3} \text{ cts}/(\text{kg} \cdot \text{yr} \cdot \text{keV})$ in the $0\nu\beta\beta$ ROI; the enriched detectors have a factor of four lower ^{68}Ga background. Here, the ^{60}Co contribution, shown in blue, becomes more significant in time due to the longer $T_{1/2}$ of ^{60}Co compared to other cosmic activated nuclides (see Tab. 5.2).

The difference between isotopic composition and location inside the array is even better illustrated with the expected background spectra for individual detectors. As an example for the enriched detectors, ANG2 was chosen which is in the center of the array, closely cornered by other enriched detectors (see Fig. 4.3). As an example for natural Ge detectors, GTF32 was chosen which is at the outer corner of the array and has a lower mass (see Tab. 4.1). Both spectra are shown in Fig. 5.6. With a higher mass it is expected that the detection efficiency for full energy peaks is increased in ANG2 and that the γ -lines in the spectrum are more prominent. The close embedding in the middle of the array is expected to increase the γ -background coming from other detectors over the continuous β -background from within the detector which again makes the γ -lines more prominent. Furthermore the β -background in enriched detectors is smaller than in natural ones. This can be specifically seen with ^{60}Co (blue) whose γ -lines are significantly more smeared with the β -tail in GTF32 but also in other peaks that have a much lower peak to continuum ratio compared to ANG2. This

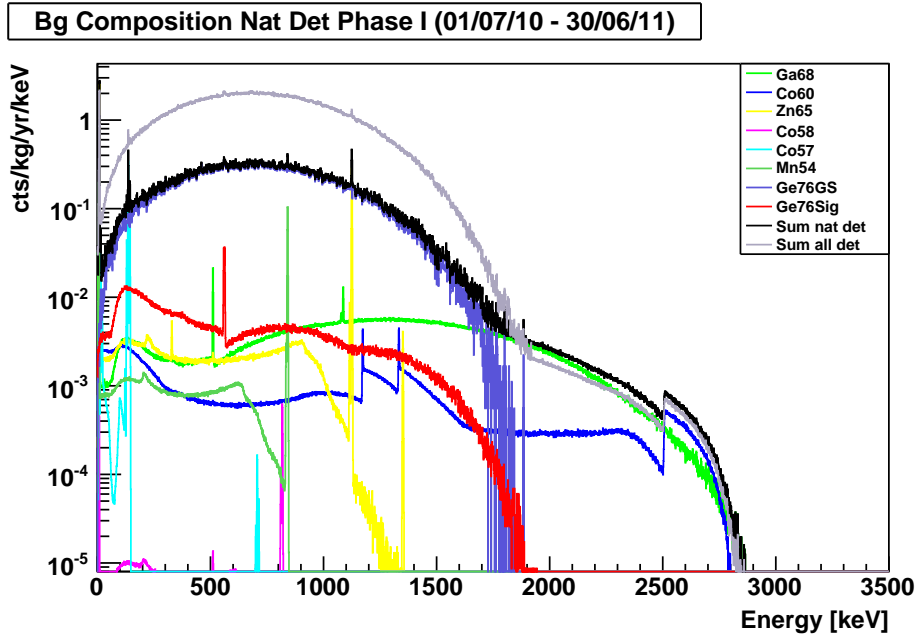


Figure 5.4 GERDA Phase I spectra of internal background nuclides for all natural detectors. The black plot denotes the sum of nuclides and all natural detectors and the gray plot the sum of nuclides and all detectors.

illustrates the significance of the individual detector characteristics for analysis and justifies the cumbersome individual treatment of each detector.

The external background from holders is expected to be mainly independent of the detector and only their mass and geometry changes the detection efficiency of full energy peaks and hence the peak to continuum ratio. The similar size and shape, however, does not result in significant differences which is why this effect is not further investigated and only the GERDA Phase I sum of all detectors shall be presented. This is shown in Fig. 5.7 for all quoted background nuclides in Sec. 5.3.2 apart from ^{137}Cs of which no upper activity limit was known. The plots are the weighted combination of all three different holder components and describe the upper limit of activities and hence a conservative estimation. If no actual values of activities will be measured by material screening, the individual spectra could be fitted to future experimental data with sufficient statistics in order to obtain a better estimate of the respective activities. However, even with these upper limits, the background contribution to the $0\nu\beta\beta$ ROI is below $3 \cdot 10^{-3}$ cts/(kg · yr · keV) with the main contribution coming from ^{208}Tl and it can be expected to be significantly reduced by anti-coincidence cuts and pulse-shape analysis.

The statistical errors of the spectra is statistical fluctuation of counts per bin which is roughly indicated with the thickness of the drawn line in a continuous spectrum; the line thickness is much smaller in sum spectra than in individual detector spectra and at high count values than at low ones. For one detector, roughly 10^6 decays were simulated that all deposit at least some energy in the detector. With a bin width of 1 keV and a continuous spectrum ranging from 0..1,000 keV, 10^3 events per bin are a rough average which would result in a bin error of 3%.

For the evaluation of the $2\nu\beta\beta$ excited state signal, which is shown in red in all plots, these spectra are not very informative since the analysis is based on coincidence. This will be discussed in the next section.

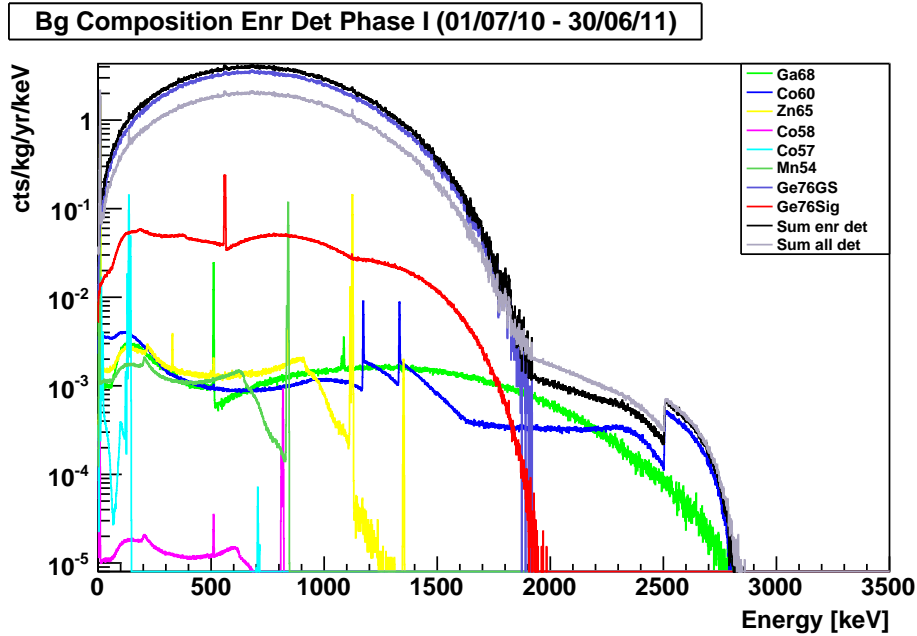


Figure 5.5 GERDA Phase I spectra of internal background nuclides for all enriched detectors. The black plot denotes the sum of nuclides and all enriched detectors and the gray plot the sum of nuclides and all detectors.

5.4.2 Cut Analysis

The GERDA Phase I array with 14 detectors is ideal for coincidence analysis. The signal of interest as presented in Fig. 5.1 consists of three final state particles: two γ 's with discrete energies, E_{γ_1} and E_{γ_2} , and one β with a continuous energy ranging up to E_{β} . The β is expected to be detected inside the detector of the decay whereas a 560 keV γ has an interaction length in Ge of 2.5 cm [72] and can deposit its energy, fully or partly, inside another detector. The most ideal cut for this decay is a 3-detector event in which one detector sees E_{γ_1} , another E_{γ_2} and the third an energy below E_{β} ; however, this is quite restrictive and MC simulations show that only 1,576 decays out of 6,758,674 simulated signal decays (see Tab. C.2 in the Appendix) would pass this cut which is $2.33 \cdot 10^{-2} \%$. Other, less specialized cuts, might have a lower background rejection but allow for more signal statistics. A variety of up to 18 cuts for 2, 3, 4 and 5 detector events was developed for investigation. Their performance with the signal and 12 different background components will be illustrated graphically in signal-background-efficiency ratio plots as exemplary shown for ^{60}Co decaying inside the detectors in Fig. 5.8. All other background components are shown in the Appendix in Fig. C.13 to C.24.

These figures show the signal efficiency in % on the y-axis and the background efficiency⁷ in % on the x-axis which is the probability of an event passing the cut. Every cut can be placed in this parameter space according to its performance; the diagonal lines denote the same signal to background efficiency ratio with the ratio of one (solid line) and a ratio according to 1σ (dotted line), 2σ (dashed line) and 3σ (dash-dotted line)⁸.

The cuts keep their unique color and shape coding in all figures and are defined in the following description. The first number denotes the amount of detectors with an energy deposition above the threshold of 50 keV and the "+" denotes an additional requirement according to the detector energies E_1 , E_2 or E_3 . These energies can be connected with "=" which means a detector equals any energy of the two γ -energies, $E_{\gamma_1} \pm 2.5 \text{ keV}$ OR $E_{\gamma_2} \pm$

⁷This is analog to the signal efficiency: The probability of a background event passing the cut.

⁸Calculated as e.g. for 1σ : $y = \frac{x}{1-0.683}$.

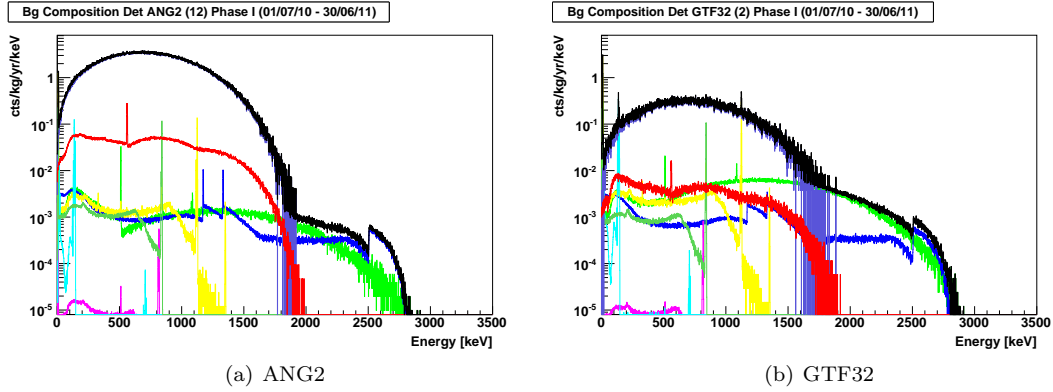


Figure 5.6 GERDA Phase I spectra of internal background nuclides for ANG2 (left) and GTF32 (right). The black plot denotes the sum of nuclides and the other nuclides follow the color coding in Fig. 5.4.

2.5 keV. The connection " $<$ " denotes that the detector energy must be smaller than E_{γ_1} OR E_{γ_2} OR E_{β} minus 2.5 keV, unless one of these energies is already conditioned to another detector energy $E_{\gamma_{1,2,3}}$. A more comprehensible description will be given with the individual cuts:

- 2-Det** Energy is deposited in two detectors above the threshold.
- 2-Det**+ $<$ **E1** Additionally one detector is below 2.5 keV of one of the γ -energies.
- 2-Det**+ $=$ **E1** One detector equals one of the γ -energies ± 2.5 keV.
- 3-Det** Energy is deposited in three detectors.
- 3-Det**+ $<$ **E1** Equivalent to above.
- 3-Det**+ $=$ **E1** Equivalent to above.
- 3-Det**+ $=$ **E1**+ $<$ **E2** One detector equals one of the γ -energies and another detector is below the other γ -energy.
- 3-Det**+ $=$ **E1**+ $=$ **E2** Results in six possible combinations to check.
- 3-Det**+ $=$ **E1**+ $=$ **E2**+ $<$ **E3** Same as above with additional requirement to the third detector which is assumed to be the one with the decay and has hence an energy below the β -endpoint.
- 4-Det** Equivalent to above.
- 4-Det**+ $<$ **E1** Equivalent to above.
- 4-Det**+ $=$ **E1** Equivalent to above.
- 4-Det**+ $=$ **E1**+ $<$ **E2** Equivalent to above.
- 4-Det**+ $=$ (**E1**+**E2**) Two out of four detectors have a combined energy of one of the γ -energies ± 2.5 keV.
- 4-Det**+ $=$ **E1**+ $=$ (**E2**+**E3**) Same as above but with the other γ fully detected in one of the two remaining detector.
- 5-Det** Equivalent to above.
- 5-Det**+ $<$ **E1** Equivalent to above.
- 5-Det**+ $=$ **E1** Equivalent to above.

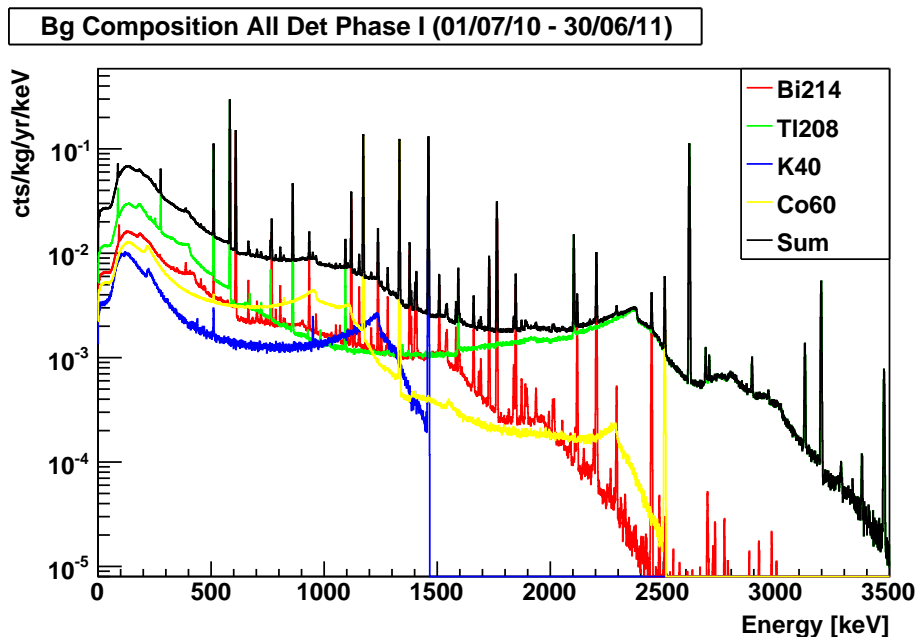


Figure 5.7 GERDA Phase I spectra of external background nuclides in all detectors. The black plot denotes the sum of nuclides and all detectors.

These are all cuts passed by at least one signal event. If none of the simulated background events passes a cut then it is not shown in the plots⁹. The amount of simulated signal and background decays are shown in Tab. C.2 in the Appendix. The percentage of those events that pass the cuts are an indicator for the statistical error of the cut performance. For example, with 10^7 simulated decays and an efficiency of 10^{-3} %, the statistical error, \sqrt{N}/N , would be 10 %.

The example of ^{60}Co decaying inside the detectors (see Fig. 5.8) shows in fact the most difficult considered background spectrum to distinguish from the signal. The plots do not give a quantitative estimation of signal to background ratio which would depend on the total amount of background events, which is known, and on the expected amount of signal events, which is a function of $T_{1/2}$ of the decay mode; they show the probability of an event to be signal or background if it passes a specific cut.

The two cuts with 2-Det and 2-Det+<E1 are only loosely distinguished and are represented close together in the parameter space which makes them often overlap. This is also true for multiple detector events of this kind as e.g. 3-Det and 3-Det<E1 or 3-Det+=E1 and 3-Det+=E1=<E2. The goodness of a cut increases if its data point is close to the upper left corner of the parameter space; however, the signal efficiency needs to be sufficiently high in order to observe signal events at all. The signal efficiency has the same value for one cut in all plots.

Comparing all background nuclides, the rather loose cuts of the form x-Det and x-Det+<E1 are not very decisive for ^{60}Co , ^{68}Ga , ^{58}Co , ^{214}Bi and ^{208}Tl in Fig. 5.8 and Fig. C.13, C.15, C.20 and C.21 in the Appendix respectively. The goodness even decreases with the consideration of higher x for these multi γ nuclides. The best cuts for all nuclides are the 2-Det+=E1, the 3-Det+=E1+<E2 and the initially mentioned 3-Det+=E1+=E2+<E3 cut, of which the first exceeds in more than one order of magnitude in signal efficiency and is clearly the cut of choice. For decays of ^{65}Zn , ^{57}Co , ^{54}Mn , ^{40}K and ^{137}Cs shown in Fig. C.14, C.16, C.17,

⁹Note that these cuts are in fact very efficient and that the absence of a data point in the plots does not demote it.

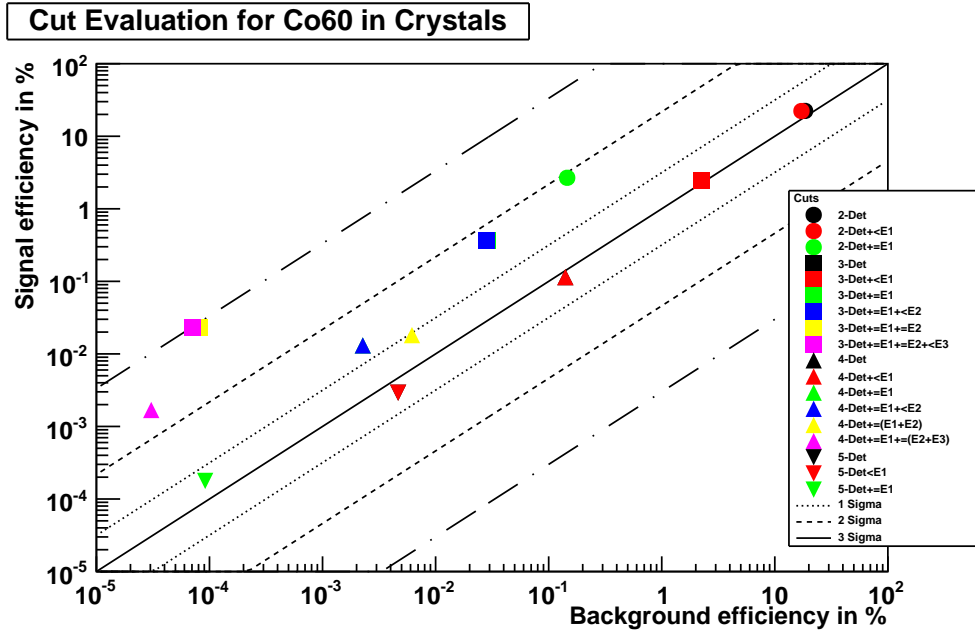


Figure 5.8 Cut evaluation for the signal decay of ^{76}Ge into the first excited 0^+ state compared to the background decay of ^{60}Co inside the detectors. See description in Sec. 5.4.2 for more information on the cuts.

C.23 and C.24 in the Appendix respectively, any of the presented cuts can sufficiently well distinguish them from the signal.

Of special interest is the ^{76}Ge $2\nu\beta\beta$ background into the ground state (Fig. C.18 Appendix) which has no actual γ -line, but can be detected in multiple detectors due to bremsstrahlung being emitted from the two electrons. Additionally it is expected to happen up to three orders of magnitude more often than other background decays and more than 2 orders of magnitude more than the signal decay with the assumed $T_{1/2} = 10^{23}$ yr (see Tab. 5.5). Here, the simple 2-Det and 2-Det+<E1 cuts have a signal identification of two orders of magnitude larger than the ^{76}Ge (GS) background which would not distinguish them very well. The 2-Det+=E1 cut, on the other hand, increases the ratio between signal and background efficiency by a factor ten which makes the signal easier to discriminate.

The entire quantitative prediction of the amount of identified signal events over the amount of falsely identified background events could not be finished in this thesis but was done for the 2-Det+=E1 cut in Tab. 5.7. The cut efficiency for the signal is 2.68% and 24.3 out of 907.5 expected ^{76}Ge excited state events with $T_{1/2} = 10^{23}$ yr would pass this cut. 180,883 simulated events pass the cut, which leads to a statistical error of 0.24% which are ± 0.058 events after the cut for the expected Phase I events. The error contribution of the total simulated events was omitted. The same calculation is done for all considered background nuclides and the total expected sum of background events passing this cut is 2.14. Hence, with the fictional GERDA Phase I array and the assumed run-time, the signal would be clearly distinguishable from the background with a factor 10 excess. This is even a quite conservative estimate since the considered external holder activities are upper limits and might be significantly lower.

The statistical analysis is expected to be done with the Unified Approach of Feldman and Cousins as described in Sec. 3.4.4. The experimental input n would be simply the amount of events that pass a specific cut and the background b the estimated total amount of background events calculated in this chapter.

Table 5.7 Specific evaluation for the 2-Det+=E1 cut. The columns denote the background nuclides, the amount of simulated decays passing the cut for the statistical error estimation, the calculated cut efficiency for the respective nuclide in %, the amount of expected decays of the respective nuclide in GERDA Phase I, the amount of decays that passes the cut with the statistical error. The values for the external background nuclides are the weighted sums of all five holder volumes.

Nuclide	Sim events after cut	Cut eff [%]	Expected decays	Expected events after cut
$^{76}\text{Ge}(\text{Sig})$	180883	2.68	907.49	24.286 ± 0.058
$^{76}\text{Ge}(\text{GS})$	82	$1.21 \cdot 10^{-3}$	58547.97	0.710 ± 0.078
^{68}Ga	3372	$5.59 \cdot 10^{-2}$	171.50	0.096 ± 0.002
$^{60}\text{Co}(\text{Det})$	14325	$1.46 \cdot 10^{-1}$	62.63	0.091 ± 0.001
^{65}Zn	3716	$4.84 \cdot 10^{-2}$	262.93	0.127 ± 0.002
^{58}Co	8656	$1.69 \cdot 10^{-1}$	0.51	0.001 ± 0.001
^{57}Co	8	$1.15 \cdot 10^{-4}$	36.24	0.000 ± 0.001
^{54}Mn	11038	$1.47 \cdot 10^{-1}$	55.25	0.081 ± 0.001
^{214}Bi	11967.56	$5.40 \cdot 10^{-2}$	520.65	0.281 ± 0.003
$^{60}\text{Co}(\text{Holder})$	21084.02	$9.51 \cdot 10^{-2}$	325.41	0.309 ± 0.002
^{208}Tl	14374.34	$6.48 \cdot 10^{-2}$	585.74	0.380 ± 0.003
^{40}K	567.19	$2.56 \cdot 10^{-3}$	2863.60	0.073 ± 0.003
Bg sum				2.15 ± 0.1

The development and performance testing of many, even unrealistic, cuts was done with the intention of combining the experimental data analysis for different cuts. The information on which cut an event passes, could be incorporated into the analysis with a different weight, and hence contribute to a higher sensitivity.

5.5 Conclusions & Perspectives

The individual background model for each detector in the fictional GERDA Phase I, running for one year starting at 01/07/10 was constructed and presented in assorted spectra. Contributions of cosmically produced internal background and various external background sources in the holders were considered which is believed to cover the majority of background components. Phase I, as presented, with a starting date in the past and the 14 detector assumption which is already ruled out, was used because there is yet no updated 12 detector deployment scheme or run schedule for the actual new Phase I. However, the complex framework from MC simulations to analysis is entirely scripted which makes it flexible to adjust for different geometries and background contributions.

Various cuts were developed and evaluated for the excited state signal. The most promising approach for the considered background contributions is a two detector cut with one γ -energy entirely detected in one of the detectors. This, however, is still a work in progress but a preliminary result indicates a factor 10 excess of signal over background for this cut.

In future, the background of the unexpectedly large ^{42}K contribution (see Chap. 6) needs to be incorporated in the background model which is right now the dominant feature in the early experimental data and could very well be the dominant background contribution for coincidence analysis.

The author strongly encourages the proceeding of this work which appears to promise a

discovery within the fictional one year data taking of Phase I if the half-life is within the theoretical predictions. Longer delays, however, will even reduce the background produced by cosmic ray spallation and facilitate the discovery.

Chapter 6

GERDA ^{42}Ar Study

This chapter contains an extensive Monte Carlo study of ^{42}K decays in the LAr of the GERDA setup. It was done to interpret the results of the first data taking with a three detector test string that showed an abnormal ^{42}Ar concentration¹. This issue and its chronological development is presented in Sec. 6.1. The underlying production mechanisms are discussed in Sec. 6.2. In the process of understanding the origin of the ^{42}Ar , a series of background runs with different electric field configurations were done and accompanied by MC studies that are presented in Sec. 6.3. The first experimental GERDA data is presented in Sec. 6.4. Finally, the MC results are scaled to physical parameters and compared to the experimental data in Sec. 6.5. The chapter is concluded in Sec. 6.6.

6.1 Situation in GERDA

After six years of planning and constructing, the GERDA experiment took first data with a three detector test string (see Fig. 4.5) in June 2010 in which only detector GTF32 and GTF112 were operational. Surprisingly, there was an unexpected significant peak growing at around 1525 keV which was quickly identified as coming from ^{42}K .

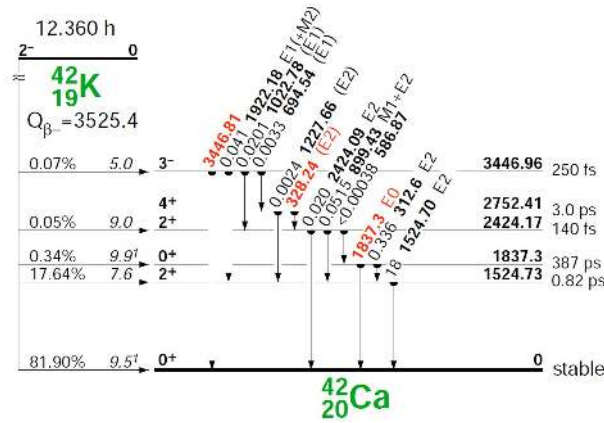


Figure 6.1 Exited states of ^{42}Ca occupied by ^{42}K decays. From [27].

The β -decay scheme of ^{42}K to ^{42}Ca can be seen in Fig. 6.1 and an example spectrum of ^{42}K decays simulated homogeneously inside the LAr in the GERDA setup is illustrated in Fig. 6.2. ^{42}K has a Q-value of 3525.4 keV and is potentially dangerous for the background of GERDA at the ^{76}Ge Q-value of 2039 keV. There is one decay mode with a 2424.09 keV γ -line with 0.02% probability and various modes into higher excited states with cascading γ -lines that could pile up inside one detector. The latter, however, is expected to be less probable and rejectable using pulse shape analysis. The far severer danger are β 's with energies up to the Q-value; the ground state transition is with 81.9% probability by far the most probable with a 3525.4 keV β -endpoint in the final state. Those high energy β 's can easily penetrate the outer DL of the HPGe detectors² and produce a signal similar to the one of $0\nu\beta\beta$. Beside these troublesome modes, the most prominent feature in the ^{42}K spectrum (Fig. 6.2) is the 1524.73 keV γ -line with 18.08% probability.

^{42}K is the daughter nuclide of ^{42}Ar which is expected to be found in low concentrations in LAr. The currently best upper limit for the $^{42}\text{Ar}/^{\text{nat}}\text{Ar}$ concentration is $< 4.3 \cdot 10^{-21}$ g/g with 90% CL from [107]. This translates into an activity of 61.2 $\mu\text{Bq/l}$ or 43.9 $\mu\text{Bq/kg}$. With this limit and the assumption of a homogeneous ^{42}Ar distribution, a BI of $4 \cdot 10^{-5}$ cts/(kg \cdot yr \cdot keV) around the $Q_{\beta\beta}$ was estimated for a single GERDA detector in [71]. More recent estimations with MaGe result in a BI of $1.6 \cdot 10^{-3}$ cts/(kg \cdot yr \cdot keV) for the test string

¹The daughter nuclide of ^{42}Ar is ^{42}K .

²The novel idea of GERDA is to operate the bare detectors in a cryogenic liquid.

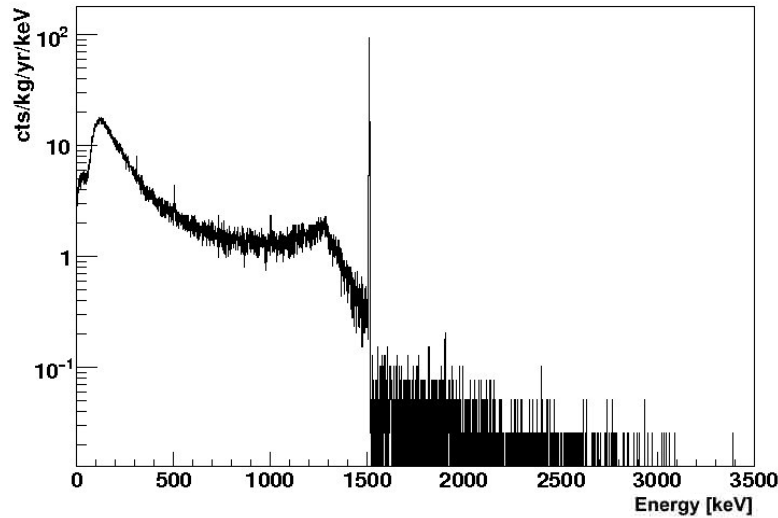


Figure 6.2 MC spectrum that would be seen by GTF32 in the test string geometry with a homogeneous ^{42}K distribution. It is normalized to $\text{cts}/(\text{kg} \cdot \text{yr} \cdot \text{keV})$.

and $1.7 \cdot 10^{-3} \text{ cts}/(\text{kg} \cdot \text{yr} \cdot \text{keV})$ for the Phase I array. The discrepancy between these two MC simulations is mainly due to the additional consideration of β 's in the latter; however, this cannot account for the whole difference and ongoing investigations are being performed.

With a half-life of 12.36 h, ^{42}K is expected to be in equilibrium with ^{42}Ar ; however, the half-life is long enough for charged ^{42}K ions to be mobile in a strong electric field e.g. the high voltage potentials of HPGe detectors. The question of ^{42}K being positively or negatively charged after the ^{42}Ar decay, the extend on the change of its concentration and the possibility to minimize detector close charge collection is currently under investigation in the GERDA collaboration.

6.2 Production of ^{42}Ar

^{42}Ar has a half-life of 32.9 yr and will be in equilibrium with its production within a few half-lives. The main production mechanism is based on natural argon in the atmosphere which consists to $> 99\%$ of ^{40}Ar and includes the reaction $^{40}\text{Ar}(\alpha, 2p)^{42}\text{Ar}$ and the twofold reaction $^{40}\text{Ar}(n, \gamma)^{41}\text{Ar}(n, \gamma)^{42}\text{Ar}$. Elemental argon has a concentration of 0.00934 volume % in air [108].

The $^{40}\text{Ar}(\alpha, 2p)^{42}\text{Ar}$ production could be present in the upper atmosphere with cosmic ^4He nuclei coming from solar winds or galactic sources. It is expected to be the main process for ^{42}Ar production but the resulting concentration is difficult to estimate and requires the knowledge of the energy dependent ^4He -flux, the energy dependent cross section, the ^{40}Ar concentration in the upper atmosphere (see Eq. 3.3 for calculating production rates) and the convection of air in the atmosphere. The ^{42}Ar concentration due to this process has been estimated to be 10^{-20} g/g in [109].

The double n -capture process $^{40}\text{Ar}(n, \gamma)^{41}\text{Ar}(n, \gamma)^{42}\text{Ar}$ requires a high n -flux since the intermediary nuclide ^{41}Ar has a short half-life of 109.34 min. Sufficiently high n -fluxes are only expected in nuclear explosions and the contribution to the ^{42}Ar concentration has been estimated to be less than $1.3 \cdot 10^{-23} \text{ g/g}$ in [110]. The highest uncertainty for calculating the production of ^{42}Ar through this mechanism results from the knowledge of the n -flux in nuclear explosion.

Even the calculation of production rates in the upper atmosphere and at nuclear explosion test sites has to be related to air movements and the location of argon extraction sites; the argon in the GERDA experiment is a mix from different companies that produce at different locations. The complexity of ^{42}Ar production and propagation makes the calculation of ^{42}Ar concentration a difficult endeavor.

6.3 Monte Carlo Study

^{42}K decays are sampled in different volumes homogeneously (Sec. 6.3.3) or at specific locations inhomogeneously (Sec. 6.3.4). The different volumes and positions are illustrated in Fig. 6.3. Descriptions of those volumes and positions and their physical purpose are detailed in the following sections.

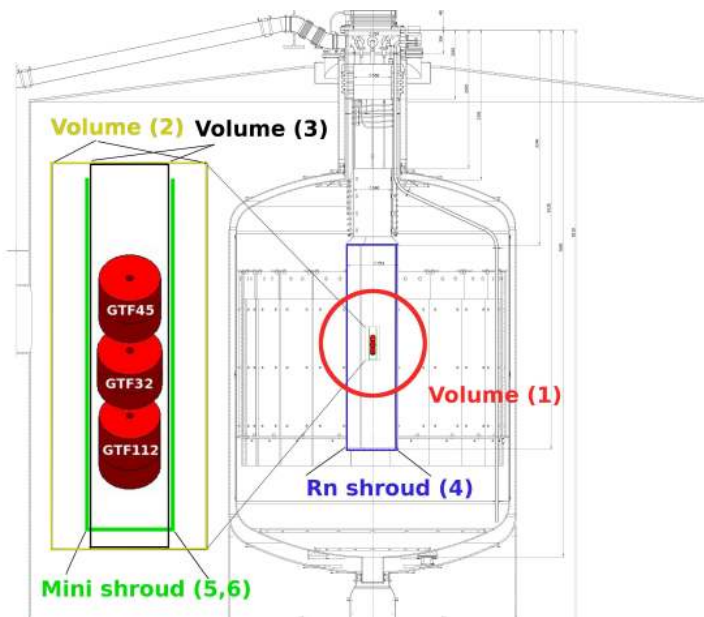


Figure 6.3 Illustration of volumes for ^{42}K MC simulations inside the GERDA cryostat and the water tank. The three detector test string is scaled to size in the whole picture and enlarged on the left for better visibility. For detailed descriptions see Sec. 6.3.3 and 6.3.4 for the MC volumes and Sec. 4.2 for the overall GERDA design.

6.3.1 Workflow

The general workflow contains the event generation, the MC simulation, the output reduction and the analysis. The MC simulations are meant to investigate the effect of ^{42}K on the background around the $Q_{\beta\beta}$ of ^{76}Ge . The low probability of the 2424.09 keV γ -line and short range of β 's in LAr, result in a low detection efficiency for events around $Q_{\beta\beta}$ and a high number of primary events is needed in order to have significant statistics. Therefore, a minimum of 10^9 events are generated with the exception of the Rn shroud scenario in which 10^{10} events are required.

DECAY0 (see Sec. 4.3) is used to generate an event file with 10^7 events that includes all ^{42}K decay modes and higher order corrected β -spectra. The generated events include the amount, the kind and the momentum of primary particles and are the base for all MC simulations. The same 10^7 primary decays are sampled on different positions multiple times to generate the eventual amount of primary decays in the MC. In a result, not all primary decays are statistically independent but the effect is expected to be washed out by the second

randomization of the position sampling.

The MC simulations are done with the MaGe version from 05/07/10 on the Deimos cluster of the ZIH³ at the TU-Dresden and are simply paralleled into independent jobs of 10^7 primary decays. The CPU time and output size of the n-tuple ROOT files differs depending on the MaGe output scheme and the geometry of the simulation, i.e. the amount of detector entries being recorded. The `GerdaArray` and `GerdaArrayWithTrajectory` output schemes are used whereas the latter serves for detailed interpretation of the origin of counts above the 1524.73 keV γ -line. The output size of a MC with 10^9 decay extends up to 750 GB and use a CPU time of 140 h whereas the 10^{10} decay Rn shroud simulation takes a CPU time of 1090 h shared between 1000 CPU's.

After the MC simulation, the n-tuple files are reduced to events with detector entries which decreases the size by a factor of 5 to 500 depending on the geometry. The event entries in these reduced n-tuple files are then convolved with the expected energy resolution (see Eq. 5.1 and values in Sec. 5.2) and further analyzed with ROOT.

In order to compare the MC's with each other and with GERDA data, it is useful to define some comparison categories in form of variables that characterize a low count spectrum in terms of the ^{42}K decay.

Peak count (N_{peak}): The count of events in the prominent 1524.73 keV peak ± 6 keV. It compares the counts of the most prominent peak which can be determined with sufficient statistics in the low count experimental data. This variable is also an indicator for the Compton features below the peak. The N_{peak} rate shall be defined as R_{peak} .

BI counts (N_{BI}): The count of events in between 1990 and 2090 keV which is ± 50 keV around the $Q_{\beta\beta}$ of ^{76}Ge . With this choice it is taken care that the 0.04 % 1922.18 keV γ -line of ^{42}K is not included. This variable is not expected to be of good use for comparison since the statistics in the experimental data will be very poor. However, the N_{BI} is of prime interest for the GERDA experiment and the $0\nu\beta\beta$ decay and is considered to compare different MC scenarios only. The N_{BI} rate is the background index, BI.

Peak / above peak ratio ($R_{\text{p}/>\text{p}}$): The ratio of N_{peak} and events above 1600 keV. Both, N_{peak} and the counts above the peak are expected to have sufficient statistics in experimental data and serve as a good indicator for γ to β contributions to a spectrum.

A summary of these comparison categories for all simulated scenarios can be found in Tab. 6.1. The variables for MC and experimental data are presented in Sec. 6.3.5 and 6.4 respectively and scaled and compared to each other in Sec. 6.5.

6.3.2 Prestudy of ^{42}K decays in the GERDA Cryostat

The GERDA cryostat (Sec. 4.2.2) has a volume of 64 m^3 and can contain 89.2 t of LAr with a density of 1394 kg/m^3 . For efficient use of CPU time it is necessary to restrict the amount of LAr used as a sample volume; this is basically a study to determine the range of 1524.73 keV and 2424.09 keV γ 's in LAr.

In order to choose a volume of LAr for the MC simulations that is large enough to include photons coming from far away⁴ and yet as small as possible for CPU efficiency, different volume sizes are sampled with photons of a specific energy and the detection efficiency in the detectors is compared. Cylindrical volumes, $V(x)$, are parametrized in twenty steps with x going from 0 to 19:

³Zentrum für Informationsdienste und Hochleistungsrechnen, German for: Center for Information Services and High Performance Computing

⁴Contributions from decays far away from the detectors will alter the shape of spectra for their γ -particles are more likely to Compton scatter on their way. This results in a reduction of the full energy peak and a shift towards low energies.

$$V(x) = \pi R(x)^2 H(x) \quad (6.1)$$

$$R(x) = (0.1 + 0.1 \cdot x) \text{ m} \quad (6.2)$$

$$H(x) = (0.5 + 0.2 \cdot x) \text{ m}. \quad (6.3)$$

This parametrization starts with the smallest cylindrical volume of $R(0) = 10$ cm and $H(0) = 50$ cm, incrementing the dimensions in all directions equally and ending with the largest volume of $R(19) = 2$ m and $H(19) = 4.3$ m. 10^8 photons are sampled homogeneously and isotropically in each volume and the counts of the full energy peak, $N_{\text{cts}}(x)$, are recorded. This translates with the simulated photons, N_{sim} , into the detection efficiency, $\eta(x)$:

$$\eta(x) = \frac{N_{\text{cts}}(x)}{N_{\text{sim}}}. \quad (6.4)$$

With constant N_{sim} , $\eta(x)$ decreases with increasing x since there are less simulated events per unit volume. Thus, a better comparison between the $V(x)$ is the ratio between $N_{\text{cts}}(x)$ and the simulated decays per volume, $\eta_{\text{corr}}(x)$:

$$\eta_{\text{corr}}(x) = \frac{N_{\text{cts}}(x)}{N_{\text{sim}}} \cdot \frac{V_{\text{eff}}(x)}{\text{m}^3}, \quad (6.5)$$

in which $V_{\text{eff}}(x)$ is the effective volume ($V(x)$ minus the material that is not LAr e.g. the detectors and the support structures inside $V(x)$), which is calculated by MaGe. $\eta_{\text{corr}}(x)$ should be independent of x if there are no geometrical influences, i.e. the increased volume does only include decays that are not seen by the detectors. The results of $\eta_{\text{corr}}(x)$ are plotted in Fig. 6.4 for 1524.73 keV photons and in Fig. 6.5 for 2424.09 keV photons. The black curve shows the total corrected detection efficiency and the three colored curves show each detector individually. All errors are statistical errors only. At the x at which $\eta_{\text{corr}}(x)$ turns constant is the volume that includes all decays that contribute to the spectrum. Any increase of $V(x)$ will not result in more decays being seen by the detectors. This volume can be used for the actual MC simulation with the confidence that it is large enough. Note that x^3 is proportional to $V(x)$ and $\eta_{\text{corr}}(x)$ is scaled with $V_{\text{eff}}(x)$; if these volumes do not increase proportionally with x^3 i.e. if the increase includes non LAr volumes as cryostat infrastructure or detector holders, $\eta_{\text{corr}}(x)$ would not be constant. This effect is the reason for the small kink at $x = 16$ in both figures.

As a result, $x = 8$ was chosen as the optimal size for MC simulations of both γ -energies which translates into a cylinder with $R(8) = 0.9$ m and $H(2.1) = 2.5$ m and an effective volume of $V_{\text{eff}}(x) = 5,340$ l or a mass of 7.45 t.

Chronologically, this prestudy was not done before the actual MC simulations and did not influence volume choices in this chapter; those were educated guesses with conservative margins. It will be useful for MC's in the future to increase CPU efficiency and justify assumptions. A similar study for 430.8 keV photons is, however, essential for determining the detection efficiency in Chap. 8.

The range of β 's above 0.8 MeV can be estimated with the empiric formula [111]:

$$R[\text{mg}/\text{cm}^2] = 542 \cdot E[\text{MeV}] - 133. \quad (6.6)$$

For β 's with 3525.4 keV this results in a range of 17.6 mm in water, 12.6 mm in LAr and 3.3 mm in germanium. With a maximal range of 3.3 mm in Ge, the β 's can easily penetrate the DL of the detectors and deposit a fraction of their energy and with a range of 12.6 mm in LAr, the collection volume is quite large.

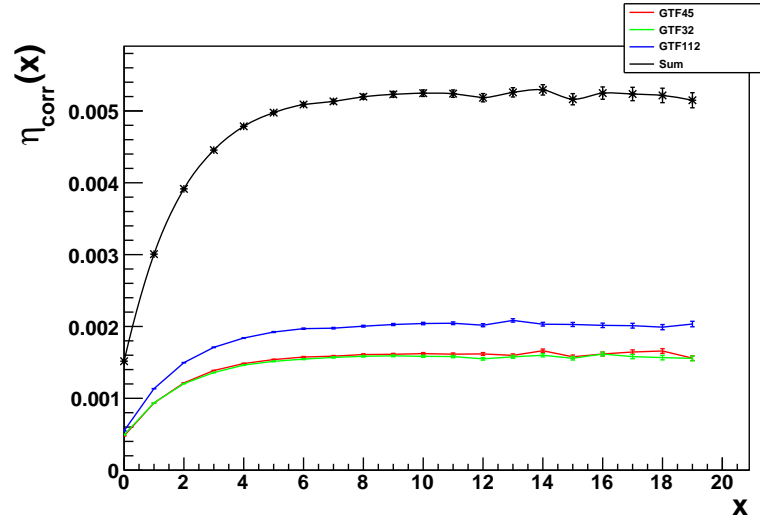


Figure 6.4 Corrected detection efficiency, $\eta_{\text{corr}}(x)$, of 1524.73 keV γ 's in the GERDA setup with respect to the parametrized volume $V(x)$ for the detectors GTF45, GTF32 and GTF112 in red, green and blue respectively and for the whole test string in black.

6.3.3 Homogeneous ^{42}K Scenarios

Homogeneous ^{42}Ar distributions were assumed and investigated first. It was quickly recognized that, given the data, a high concentration of ^{42}K in contradiction to published limits in e.g. [107] would have been observed.

Wide Homogeneous Distribution

The first investigated scenario is a homogeneous distribution of 10^9 ^{42}K decays inside a 80 cm sphere centered around the test string. This is the point of origin with a 19.5 cm offset in z in MaGe coordinates⁵. This volume is illustrated in Fig. 6.3 in red as Volume (1).

The effective volume is determined with 2142.851 which translates to 2987.13 kg of LAr. The N_{peak} , N_{BI} and $R_{p/>p}$ can be found in Tab. 6.1.

Scaling the simulated N_{peak} to a count rate results in an activity of 0.56 mBq/kg of the LAr or an ^{42}Ar concentration of $3.8 \cdot 10^{-20}$ g/g and hence, roughly an order of magnitude larger than the literature value. The $R_{p/>p}$ in the data is roughly 1 whereas the simulation shows a $R_{p/>p}$ of 17. This is either due to additional contribution of background above the peak that is not coming from ^{42}K or an enhanced β -contribution of ^{42}K . The latter favors a distribution of ^{42}K close to the detectors and motivates the next scenario.

In order to determine the peculiarities of ^{42}K decays that are detected in the HPGe, i.e. where is the ^{42}K in the LAr and where is the energy deposited in the detectors, an additional investigation has been performed. The results are shown in Fig. 6.6. It shows the vertex positions of ^{42}K decays that deposit energy in the detectors and the hit positions⁶ of events inside the detectors. The plotted positions are based on 10^9 decays simulated in the wide homogeneous distribution and are only those that are inside a 1 cm thick central slice in the x - z plane. The upper and lower subfigures denote the full sample and the full sample with an $E > 1.6$ MeV energy cut.

⁵See e.g. Fig. 4.3 for the coordinate system.

⁶A hit is an instance in which energy is deposited in the detector. An event can be composed of multiple hits e.g. multi scattering.

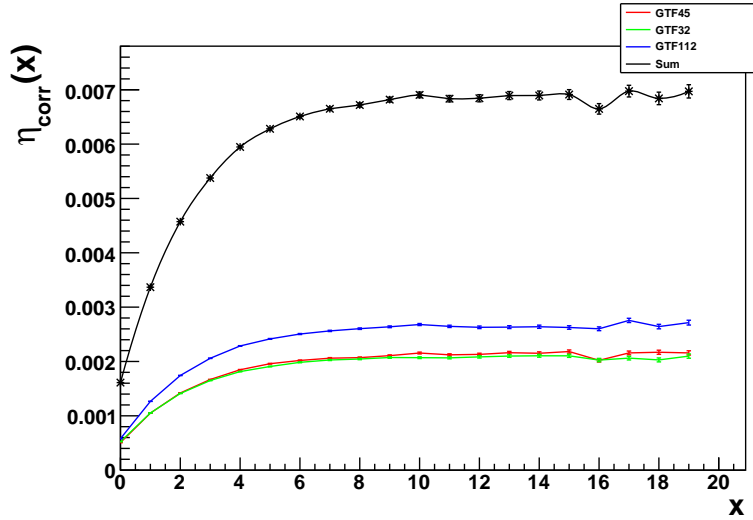


Figure 6.5 Corrected detection efficiency, $\eta_{\text{corr}}(x)$, of 2424.09 keV γ 's in the GERDA setup with respect to the parametrized volume $V(x)$ for the detectors GTF45, GTF32 and GTF112 in red, green and blue respectively and for the whole test string in black.

The visualization is rather qualitative but shows that the majority of detected decays are close to the thin DL surfaces, i.e. the top and inside the bore hole (see Fig. 4.6). The energy deposition in the full sample does not depend on DL thickness of the surface and is biggest just below any surface. This is different for the energy cut sample; the energy deposition is largest close to the thin DL surfaces and strongly indicates the penetration of β 's through the thin DL's.

Close Homogeneous Distribution

This scenario is investigated in order to account for the big discrepancy between data and MC in $R_{p/>p}$. 10^9 primary ^{42}K decays are simulated in a cylindrical volume with the dimensions $R = 10$ cm and $H = 50$ cm and an offset of 19.5 cm in z from the point of origin. This volume is shown in Fig. 6.3 in yellow as Volume (2) and has an effective size of 14.231 or 19.8 kg of LAr.

The results are presented in Tab. 6.1 and describe the data ($R_{p/>p} \approx 1$) slightly better with an approximate $R_{p/>p}$ of 8.

Close Homogeneous Distribution Without Bore Hole

Investigation show that in a homogeneously sampled MC roughly 75% of events above the peak are due to β 's [112] and that these β 's have a higher chance of penetrating the DL inside the bore hole where the DL are only 0.001 mm thick (see Fig. 4.6). In reality, the access to the bore hole is narrow and practically restricted for charged ions which would stick to the surface before entering. This motivated the exclusion of the bore hole as part of the sampling volume for ^{42}K in the MC.

The implementation of excluding the bore hole is rather cumbersome in coding and CPU time and the quick and highly simplifying approach of filling the bore hole with detector germanium is used. This changes the weight and efficiency of the detectors which has to be taken into account by comparing the results; however, the effect on γ 's is expected to be small.

The sampling volume is further reduced to a cylinder of $R = 5$ cm and $H = 50$ cm with the

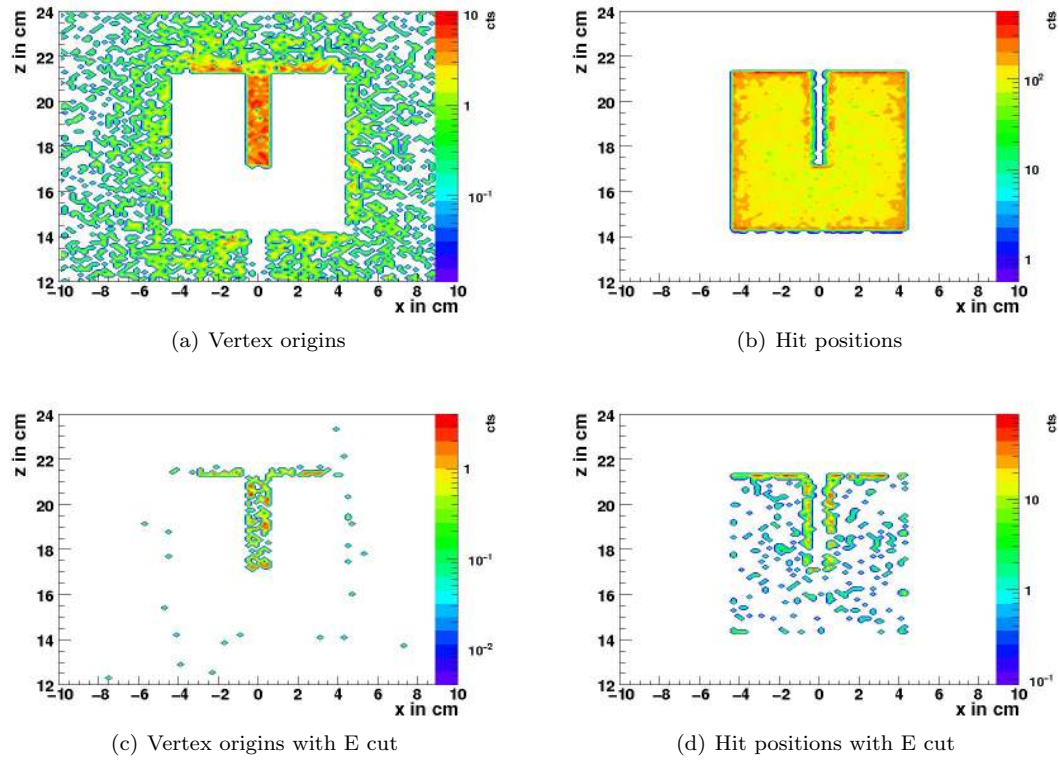


Figure 6.6 Illustration of MC primary vertex origins and hit positions for 10^9 events homogeneously distributed in Volume (1) (see Fig. 6.3). The vertex origins are drawn if they are in a 1 cm thick central slice in the x-z plane and (a) deposit any energy in the detector or (c) deposit an energy above 1.6 MeV. Hit positions are drawn if the hits are in a 1 cm thick central slice in the x-z plane and (b) deposit energy in the detector or (d) deposited a total energy of above 1.6 MeV in the detector. Note that one event, i.e. one primary vertex may result in multiple hits inside the detector with e.g. multiple Compton scattering for γ 's or multi scattering for β 's.

standard offset. It can be seen in Fig. 6.3 in black as Volume (3) and has an effective size of 2.431 or 3.39 kg of LAr. In this scenario the $R_{p/>p}$ is roughly 4 and therefore agrees with the experimental data up to a factor of four.

6.3.4 Inhomogeneous ^{42}K Scenarios

In the process of understanding the origin of the larger than expected background contribution from ^{42}K , various small runs with different high voltage, HV, configurations have been proposed and done. The HV was applied to the Rn shroud and the mini shroud whereas the latter was especially installed to provide the possibility to have a potential close to the detectors and to shield ^{42}K ion propagation mechanically. In one run it was tried to attract the ions towards the detector, i.e. the mini shroud; in another run it was tried to repel them from the detector, i.e. attract them towards the Rn shroud and eventually test the hypothesis of charge collection.

All the runs can be described with ^{42}K decays being attracted towards either the Rn shroud or the mini shroud. Therefore, two distinct MC scenarios with the two position samplings are sufficient. They can later be scaled to reality i.e. to the assumed charge collecting volume, depending on the HV applied. Those two scenarios are detailed in the following sections.

Radon Shroud Position

The Rn shroud is a 0.03 mm thin copper foil [81] that physically prevents the propagation of Rn from the outside of the cryostat towards the detectors. The cylindrical form of the shroud has a height of 193 cm and a radius of 38 cm and is not implemented in MaGe as a physical volume. It can be seen in Fig. 6.3 in blue at position (4). The distance to the detectors makes it necessary to sample 10^{10} ^{42}K decays in a 0.3 mm thick hollow cylinder at the proper shroud position.

The results are presented in Tab. 6.1 and show the lowest detection efficiency of all MC scenarios and the highest $R_{p/>p}$.

Mini Shroud Position

The mini shroud is a cylindrical form of copper foil with a height of 45 cm, a radius of 5.6 cm and a lid at the bottom. The sides of the cylinders can be seen in Fig. 6.3 as the green position (5) and the bottom lid as position (6). The shroud is not implemented in MaGe as a volume and an independent MC simulations with 10^9 decays has been performed for the cylinder side and another with 10^8 decays for the bottom lid.

The mini shroud bottom simulation has quite distinct effects on the different detectors as can be seen in the results in Tab. 6.1. Should decays at this position be significant, an independent analysis of each detector is recommended.

6.3.5 Summary and Scaling of MC Data

The summary of all MC scenarios is presented in Tab. 6.1 which contains the direct count results with respect to the simulated decays in form of the spectral characteristics defined in Sec. 6.3.1: The N_{peak} , the N_{BI} and the $R_{p/>p}$. These counts have to be scaled to physical variables in order to compare them with experimental data which will be done in Sec. 6.5. Each spectral characteristic is presented for each MC scenario and detector and for the three detector average. The rather detailed documentation is intended to enable the reader to construct its own physical scaling to different charge collecting scenarios as exemplified in Sec. 6.5 and is hoped to aid the GERDA data analysis for the ^{42}K issue. Additionally, the original MC results enable the statistical error estimation which is not done for every MC value.

The simulated spectra are presented in Fig. 6.7. They illustrate the difference in spectral forms which are seen by the detector for ^{42}K decays in different locations. The spectra are scaled in counts per keV and 10^9 simulated counts. The largest obvious difference is the ratio of the continuum below and above the peak. The area below the peak is mainly the Compton continuum from the γ -line and is therefore described by N_{peak} . The area above the peak is mainly influenced by β 's and is related to N_{peak} by $R_{p/>p}$. As expected, the ratio between the areas becomes larger for scenarios with ^{42}K decays further away from the detectors when β 's cannot reach them as e.g. in the Rn shroud (green) and mini shroud (red) scenario.

6.4 Experimental Data

GERDA is taking data since the beginning of June 2010 and a status report and data taking summary can be found in [78]. This first data consists of various short runs with quite distinct experimental configurations. All runs used the three detector test string, described in Sec. 4.2.1. Due to the testing of electronics and the mounting procedures, not all detectors were working in optimal conditions in each run. They are marked and removed from the analysis later. The data taking of the first three runs were taken only with the MCA due to problems with the FADC's. Those first runs were not considered in this thesis for consistency, since MCA and FADC data are quite distinct in handling and for instance in

Table 6.1 Raw MC results of the ^{42}K decays in different scenarios as described in Sec. 6.3.3 and 6.3.4. They are presented in form of the three variables N_{peak} , N_{BI} and $R_{\text{p}/>\text{p}}$ as defined in Sec. 6.3.1 for each detector. The three detector sum for N_{peak} and N_{BI} and the weighted average for $R_{\text{p}/>\text{p}}$ is presented in the last column.

MC Scenario	N_{sim}	GTF45	GTF32	GTF112	3-Det
Peak Count (N_{peak})					sum
Wide homogeneous distribution	10^9	$1.98 \cdot 10^4$	$1.93 \cdot 10^4$	$2.61 \cdot 10^4$	$6.52 \cdot 10^4$
Close homogeneous distribution	10^9	$1.25 \cdot 10^6$	$1.26 \cdot 10^6$	$1.52 \cdot 10^6$	$4.03 \cdot 10^6$
Cl. hom. dist. without bore hole	10^9	$2.32 \cdot 10^6$	$2.23 \cdot 10^6$	$2.63 \cdot 10^6$	$7.19 \cdot 10^6$
Rn shroud position	10^{10}	$4.51 \cdot 10^4$	$4.46 \cdot 10^4$	$6.05 \cdot 10^4$	$1.50 \cdot 10^5$
Mini shroud position sides	10^9	$1.83 \cdot 10^6$	$1.92 \cdot 10^6$	$2.25 \cdot 10^6$	$6.01 \cdot 10^6$
Mini shroud position bottom	10^8	$1.88 \cdot 10^2$	$2.96 \cdot 10^3$	$4.77 \cdot 10^5$	$4.80 \cdot 10^5$
Background Index Counts (N_{BI})					sum
Wide homogeneous distribution	10^9	102	112	99	313
Close homogeneous distribution	10^9	13,752	13,967	15,583	43,302
Cl. hom. dist. without bore hole	10^9	50,669	51,941	51,044	153,654
Rn shroud position	10^{10}	57	48	79	184
Mini shroud position sides	10^9	1,561	1,661	2,085	5,307
Mini shroud position bottom	10^8	0	3	408	411
Peak Above Peak Ratio ($R_{\text{p}/>\text{p}}$)					average
Wide homogeneous distribution	10^9	16.65	17.11	19.05	17.73
Close homogeneous distribution	10^9	8.22	8.13	8.67	8.37
Cl. hom. dist. without bore hole	10^9	4.24	3.94	4.69	4.32
Rn shroud position	10^{10}	53.70	57.83	57.93	56.61
Mini shroud position sides	10^9	50.32	49.94	47.39	49.04
Mini shroud position bottom	10^8	31.33	54.80	51.85	46.47

energy resolution. The data of the following runs since July 16 were all taken with FADC's with a resolution between 4.5..6.0 keV FWHM at the 2614 keV γ -line.

The proposed analysis chain (Sec. 4.4) was still under construction and not used since the manifold steps proved yet to be too cumbersome and complex for the test data. The data processing from FADC's was done by Bernhard Schwingenheuer and communicated to the author by ASCII files. The data is non-binned, includes a time-stamp, a float-size energy and is muon-veto and detector coincidence corrected which reduced the events by less than 10%. For the analysis in this thesis, the data is binned into histograms. The run properties are taken from [113] and [78] and feature the following conditions with the key data shown in Tab. 6.2:

Run (i)-(iii): Only MCA data and omitted in this thesis.

Run (iv): Nominal conditions.

Run (v): Rn shroud was put on -400 V to attract positive ^{42}K towards the shroud and away from the detectors.

Run (vi): Same as (v) but reducing detector voltage to +2500 V to reduce attraction of ^{42}K towards the detectors and study the ion drift.

Run (vii): Installation of the mini shroud (Sec. 6.3.4) to split the LAr volume, inhibit the ion drift and confine field lines to inside the mini shroud. The detector bias was reset to +3500 V except for GTF45 which was damaged and had to be operated at +1500 V.

Run (viii): Setting the Rn shroud to +500 V and the mini shroud to -300 V to attract ions towards the mini shroud, i.e. detectors in order to further investigate the ion drift.

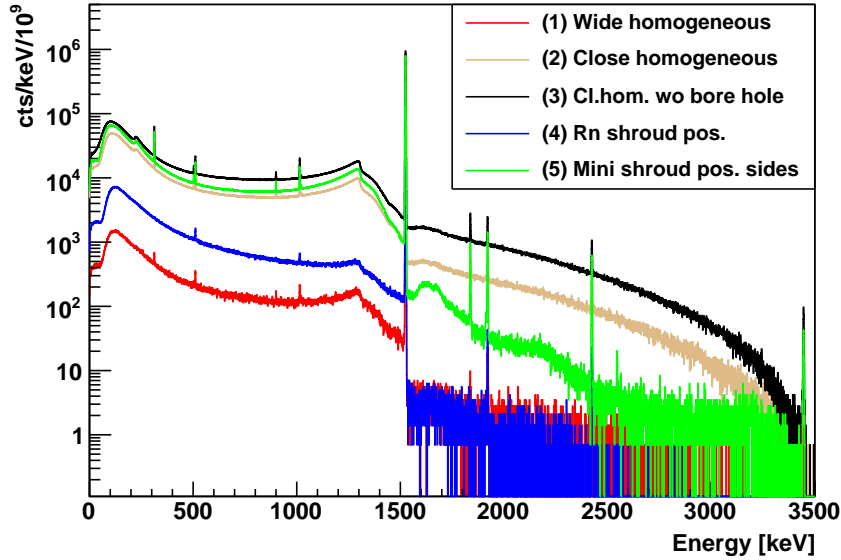


Figure 6.7 Spectral forms of different MC scenarios scaled to counts per keV and 10^9 events as seen by all three detectors. The color coding is the same as is Fig. 6.3.

Run (ixa): Setting both shrouds to ground for further drift investigation.

Run (ixb): Same as run (ixa) but GTF112 stopped working.

Run (x): Setting both shrouds on negative HV for further drift investigation. GTF112 still not operational.

Table 6.2 Properties of the first experimental runs of the GERDA experiment. Columns denote the run specifier, the date, the life time, the Rn shroud potential and the mini shroud potential.

Run	Date [dd/mm/yy]	Run time [d]	Rn shroud	Mini shroud
Without mini shroud				
(iv)	16/07/10 - 03/08/10	16.7	float	N/A
(v)	06/08/10 - 12/08/10	5.2	-400 V	N/A
(vi)	12/08/10 - 19/08/10	6.6	-400 V	N/A
Installation of mini shroud				
(vii)	25/08/10 - 17/09/10	17.9	-400 V	0 V
(viii)	17/09/10 - 28/09/10	9.5	+500 V	-300 V
(ixa)	01/10/10 - 13/10/10	12.1	0 V	0 V
(ixb)	13/10/10 - 21/10/10	7.4	0 V	0 V
(x)	22/10/10 - 09/11/10	16.3	-200 V	-400 V

A proper live time evaluation was not yet possible due to irregularities in the data taking e.g. high trigger rates and the lack of an established analysis chain. The quoted run times in Tab. 6.2 are estimations but are expected to be within 1% of the real life times.

A sum spectra of all working detectors in all runs is shown in Fig. 6.8. The data extracted from each run according to the definitions of variables in Sec. 6.3.1 is shown in Tab. 6.3. This raw data is scaled to physical values which are comparable with the MC results in the next section.

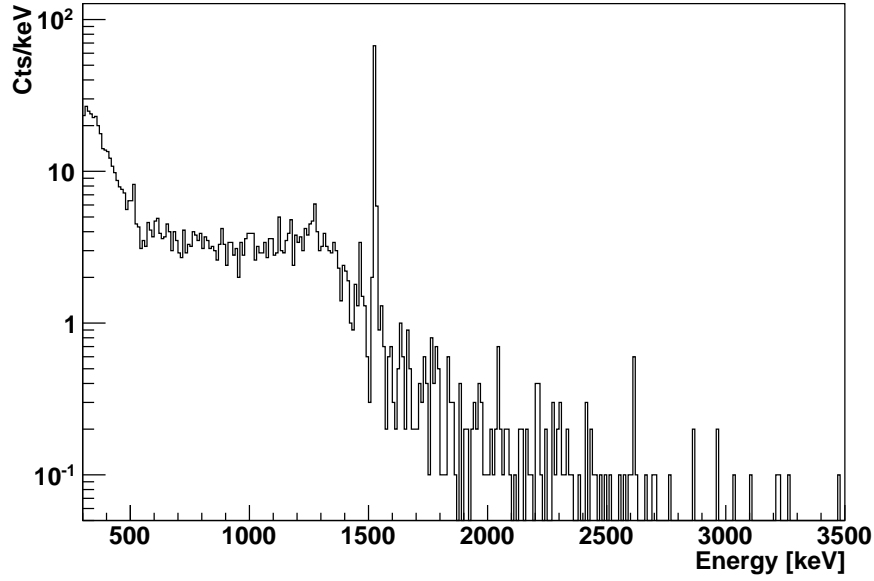


Figure 6.8 GERDA sum spectrum of detector GTF45, GTF32 and GTF112 of FADC data from run (iv) to (x) (Tab. 6.2). Note that the experimental conditions differ in between the runs and that GTF112 was not operational in run (ixb) and (x).

6.5 Analysis

The MC results from Tab. 6.1 have to be scaled to physical parameters with the ^{42}Ar concentration⁷. The concentration of $^{42}\text{Ar}/^{\text{nat}}\text{Ar} < 4.3 \cdot 10^{-21}$ g/g can be transferred in an activity per volume as

$$\frac{A}{V} = \frac{dN}{dt} \frac{1}{V} \approx \frac{\Delta N}{\Delta t} \frac{1}{V} = \frac{N_{^{42}\text{Ar}}}{V} \cdot \frac{\ln 2}{T_{1/2}} \quad (6.7)$$

in which $N_{^{42}\text{Ar}}$ is the amount of ^{42}Ar nuclides in a volume V and $T_{1/2}$ the half life of ^{42}K . The approximation can be done if the considered time Δt is short compared to the half life of ^{42}Ar which is feeding ^{42}K ; then, the $N_{^{42}\text{Ar}}$ and A stay reasonably constant. The number density, $\frac{N_{^{42}\text{Ar}}}{V}$, can be calculated with

$$\frac{N_{^{42}\text{Ar}}}{V} = \frac{N_{^{40}\text{Ar}}}{V} \cdot c = \frac{\rho_{\text{LAr}}}{A_{\text{Ar}}} \cdot c \quad (6.8)$$

in which c is the concentration $^{42}\text{Ar}/^{\text{nat}}\text{Ar}$, ρ_{LAr} the density of LAr and A_{Ar} the atomic mass of natural argon. With the given concentration, the activity per volume $\frac{A}{V}$ of LAr is $61.2 \mu\text{Bq/l}$.

The total simulated activity, A_{sim} , is simply the product of $\frac{A}{V}$ and the simulated volume, V_{sim} . With the simulated decays, N_{sim} , it is possible to calculate an equivalent simulation time, T_{sim} , with

$$T_{\text{sim}} = \frac{N_{\text{sim}}}{\frac{A}{V} \cdot V_{\text{sim}}} = \frac{N_{\text{sim}}}{A_{\text{sim}}} \quad (6.9)$$

With T_{sim} one can transfer simulated counts, i.e. N_{peak} and N_{BI} , to count rates, R , which often include the normalization to 1 kg of detector material:

⁷The decay chain of ^{42}Ar and ^{42}K are assumed to be in secular equilibrium.

Table 6.3 Experimental data from the first GERDA test runs reduced to the variables N_{peak} , N_{BI} and $R_{\text{p}/>\text{p}}$ defined in Sec. 6.3.1. The data is presented for each detector and as the three detector sum for N_{peak} and N_{BI} and as the weighted detector average for $R_{\text{p}/>\text{p}}$. GTF112 was not operational in run (ixb) and (x) and the $R_{\text{p}/>\text{p}}$ average was calculated over two detectors for these runs. The count rate of the BI is very low and has large statistical uncertainties.

Exp Scenario	GTF45	GTF32	GTF112	3-det
Peak Count (N_{peak})				sum
(iv)	79	87	103	269
(v)	18	25	16	59
(vi)	14	34	36	84
(vii)	15	18	19	52
(viii)	22	55	78	155
(ixa)	26	10	16	52
(ixb)	17	8	N/A	25
(x)	22	19	N/A	41
Background Index Counts (N_{BI})				sum
(iv)	0	3	6	9
(v)	0	1	0	1
(vi)	0	1	0	1
(vii)	0	1	2	3
(viii)	0	1	0	1
(ixa)	1	0	2	3
(ixb)	0	1	N/A	1
(x)	0	2	N/A	2
Peak Above Peak Ratio ($R_{\text{p}/>\text{p}}$)				average
(iv)	3.95	2.90	3.43	3.43
(v)	4.50	4.17	2.29	3.54
(vi)	2.33	2.62	3.27	2.78
(vii)	3.75	2.00	2.11	2.58
(viii)	3.67	4.58	8.67	5.89
(ixa)	6.50	2.00	1.60	3.22
(ixb)	8.50	2.00	N/A	5.26
(x)	4.40	1.19	N/A	2.80

$$R = \frac{N_{\text{cts}}}{T_{\text{sim}} \cdot M_{\text{det}}}. \quad (6.10)$$

These simulated count rates can be compared to measured count rates in the experiment.

The volume V_{sim} in Eq. 6.9 is simply the sampling volume in the homogeneous scenarios. For inhomogeneous scenarios, V_{sim} is a volume out of which the ^{42}K ions are charge collected. This can be a volume of LAr inside or in between shrouds or a fraction of those. The following scenarios of charge collection for MC scenarios are considered:

- (1) **Wide homogeneous:** Whole volume (1) with 2142.851 LAr.
- (2) **Close homogeneous:** Whole volume (2) with 14.231 LAr.
- (3) **Close homogeneous without bore hole:** Whole volume (3) with 2.431 LAr.
- (4a) **Rn shroud position, volume inside:** Volume inside the Rn shroud with 874.661 LAr for scenarios with no mini shroud and strong ^{42}K attraction.

- (4b) **Rn shroud position, volume between shrouds:** Volume between the Rn and the mini shroud at the height of the mini shroud with 199.761 LAr. For a high homogeneous potential between shrouds and attraction towards the Rn shroud.
- (4c) **Rn shroud position, 30 % of volume between shrouds:** 30 % of the volume (4b) with 59.931 LAr which is a more realistic assumption according to charge collection efficiency and ion life time in LAr (inspired from [114]).
- (5a) **Mini shroud position, volume inside:** Volume inside the mini shroud.
- (5b) **Mini shroud position, volume between shrouds:** Volume between the Rn and the mini shroud at the height of the mini shroud with 199.761 LAr. For high homogeneous potential between shrouds and attraction towards the mini shroud.
- (5c) **Mini shroud position, 30 % of volume between shrouds:** 30 % of the volume (5b) with 59.931 LAr which is a more realistic assumption according to charge collection efficiency and ion life time in LAr (inspired from [114]).

N_{peak} and N_{BI} from Tab. 6.1 are scaled according to these physical scenarios to R_{peak} and BI presented in cts/(kg · d) and cts/(kg · yr · keV) respectively in Tab. 6.4.

Table 6.4 MC results of R_{peak} and BI after the scaling to different physical scenarios as defined in Sec. 6.5. The $R_{\text{p}/>\text{p}}$ is not dependent on the scaling scenario and listed only for completeness since it is the same as in Tab. 6.1.

MC scenario	GTF45	GTF32	GTF112	3-det	Corresponding exp run
Peak count rate, R_{peak} [cts/(kg · d)]					
(1)	$9.6 \cdot 10^{-2}$	$9.4 \cdot 10^{-2}$	$1.0 \cdot 10^{-1}$	$9.7 \cdot 10^{-2}$	(iv),(ix)
(2)	$4.0 \cdot 10^{-2}$	$4.1 \cdot 10^{-2}$	$3.9 \cdot 10^{-2}$	$4.0 \cdot 10^{-2}$	(iv),(ix)
(3)	$1.3 \cdot 10^{-2}$	$1.2 \cdot 10^{-2}$	$1.1 \cdot 10^{-2}$	$1.2 \cdot 10^{-2}$	(iv),(ix)
(4a)	$8.9 \cdot 10^{-3}$	$8.9 \cdot 10^{-3}$	$9.4 \cdot 10^{-3}$	$9.1 \cdot 10^{-3}$	(v),(vi),(vii)
(4b)	$2.0 \cdot 10^{-3}$	$2.0 \cdot 10^{-3}$	$2.2 \cdot 10^{-3}$	$2.1 \cdot 10^{-3}$	(v),(vi),(vii)
(4c)	$6.1 \cdot 10^{-4}$	$6.1 \cdot 10^{-4}$	$6.5 \cdot 10^{-4}$	$6.2 \cdot 10^{-4}$	(v),(vi),(vii)
(5a)	$1.2 \cdot 10^{-2}$	$1.3 \cdot 10^{-2}$	$1.2 \cdot 10^{-2}$	$1.2 \cdot 10^{-2}$	(viii),(ix),(x)
(5b)	$8.3 \cdot 10^{-1}$	$8.8 \cdot 10^{-1}$	$8.0 \cdot 10^{-1}$	$8.3 \cdot 10^{-1}$	(viii),(x)
(5c)	$2.5 \cdot 10^{-1}$	$2.6 \cdot 10^{-1}$	$2.4 \cdot 10^{-1}$	$2.5 \cdot 10^{-1}$	(viii),(x)
Background index, BI [cts/(kg · yr · keV)]					
(1)	$1.8 \cdot 10^{-3}$	$2.0 \cdot 10^{-3}$	$1.4 \cdot 10^{-3}$	$1.7 \cdot 10^{-3}$	(iv),(ix)
(2)	$1.6 \cdot 10^{-3}$	$1.7 \cdot 10^{-3}$	$1.4 \cdot 10^{-3}$	$1.6 \cdot 10^{-3}$	(iv),(ix)
(3)	$1.0 \cdot 10^{-3}$	$1.1 \cdot 10^{-3}$	$8.1 \cdot 10^{-4}$	$9.5 \cdot 10^{-4}$	(iv),(ix)
(4a)	$4.1 \cdot 10^{-5}$	$3.5 \cdot 10^{-5}$	$4.5 \cdot 10^{-5}$	$4.1 \cdot 10^{-5}$	(v),(vi),(vii)
(4b)	$9.4 \cdot 10^{-6}$	$8.0 \cdot 10^{-6}$	$1.0 \cdot 10^{-5}$	$9.3 \cdot 10^{-6}$	(v),(vi),(vii)
(4c)	$2.8 \cdot 10^{-6}$	$2.4 \cdot 10^{-6}$	$3.1 \cdot 10^{-6}$	$2.8 \cdot 10^{-6}$	(v),(vi),(vii)
(5a)	$3.8 \cdot 10^{-5}$	$4.1 \cdot 10^{-5}$	$4.0 \cdot 10^{-5}$	$4.0 \cdot 10^{-5}$	(viii),(ix),(x)
(5b)	$2.6 \cdot 10^{-3}$	$2.8 \cdot 10^{-3}$	$2.7 \cdot 10^{-3}$	$2.7 \cdot 10^{-3}$	(viii),(x)
(5c)	$7.7 \cdot 10^{-4}$	$8.3 \cdot 10^{-4}$	$8.1 \cdot 10^{-4}$	$8.1 \cdot 10^{-4}$	(viii),(x)
Peak Above Peak Ratio ($R_{\text{p}/>\text{p}}$)					
Wide homogeneous distribution	16.65	17.11	19.05	17.73	
Close homogeneous distribution	8.22	8.13	8.67	8.37	
Cl. hom. dist. without bore hole	4.24	3.94	4.69	4.32	
Rn shroud position	53.70	57.83	57.93	56.61	
Mini shroud position sides	50.32	49.94	47.39	49.04	
Mini shroud position bottom	31.33	54.80	51.85	46.47	

The count rates for the experimental data was simply calculated from the counts in Tab. 6.3 with the run times in Tab. 6.2 and the detector masses and are presented in Tab. 6.5.

Table 6.5 Experimental results of R_{peak} . The BI is not presented for experimental data since the statistical errors are too large. The $R_{\text{p}/>\text{p}}$ is the same as in Tab. 6.3 and listed only for completeness. The * denotes the average over two detectors.

Experimental run	GTF45	GTF32	GTF112	3-det average	Corresponding MC scenario
Peak count rate, R_{peak} [cts/(kg · d)]					
(iv)	2.03 ± 0.23	2.24 ± 0.24	2.08 ± 0.20	2.11 ± 0.13	(1),(2),(3)
(v)	1.48 ± 0.35	2.07 ± 0.41	1.04 ± 0.26	1.49 ± 0.19	(4)
(vi)	0.91 ± 0.24	2.22 ± 0.38	1.84 ± 0.31	1.67 ± 0.18	(4)
(vii)	0.36 ± 0.09	0.43 ± 0.10	0.36 ± 0.08	0.38 ± 0.05	(5)
(viii)	0.99 ± 0.21	2.49 ± 0.34	2.77 ± 0.31	2.14 ± 0.17	(5)
(ixa)	0.92 ± 0.18	0.36 ± 0.11	0.45 ± 0.11	0.56 ± 0.08	(1),(2),(3),(4a)
(ixb)	0.99 ± 0.24	0.47 ± 0.16	N/A	$0.73 \pm 0.15^*$	(1),(2),(3),(4a)
(x)	0.58 ± 0.12	0.50 ± 0.12	N/A	$0.54 \pm 0.08^*$	(5)
Peak above peak ratio ($R_{\text{p}/>\text{p}}$)					
(iv)	3.95	2.90	3.43	3.43	(1),(2),(3)
(v)	4.50	4.17	2.29	3.54	(4)
(vi)	2.33	2.62	3.27	2.78	(4)
(vii)	3.75	2.00	2.11	2.58	(5)
(viii)	3.67	4.58	8.67	5.89	(5)
(ixa)	6.50	2.00	1.60	3.22	(1),(2),(3),(4a)
(ixb)	8.50	2.00	N/A	5.26^*	(1),(2),(3),(4a)
(x)	4.40	1.19	N/A	2.80^*	(5)

Tab. 6.4 and 6.5 can now be directly compared to each other. A detailed discussion of the results shall not be given in this thesis since it is still work in progress of the whole GERDA collaboration. However, it is obvious that a homogeneous distribution as in MC scenario (1) cannot account for the peak count rate in the experimental runs with a concentration of $< 4.3 \cdot 10^{-21}$ g/g for $^{42}\text{Ar}/^{\text{nat}}\text{Ar}$. The difference is a factor of 20 to run (iv) in normal conditions which could be only explained with an ^{42}Ar concentration of $9 \cdot 10^{-20}$ g/g, i.e. an activity of $1200 \mu\text{Bq/l}$ or with charge collection of the ^{42}K ions. The factor of 4 difference in $R_{\text{p}/>\text{p}}$ between (1) and (iv) indicates charge collection close to the detectors with increases the amount of events above the peak coming from β 's. For the experimental data, however, these values have to be treated carefully because other background than ^{42}K might influence the area above the peak.

The MC scenarios (2) and (3) come closer in explaining the $R_{\text{p}/>\text{p}}$ in the data but fail to explain the peak count rate with the given homogeneous concentration. In addition, they are somehow constructed and not expected to describe the real physical situation.

The MC scenarios at the shroud positions, (4abc) and (5abc), differ even more in $R_{\text{p}/>\text{p}}$, but the mini shroud scenarios (5abc) explain slightly better the peak count rate. This is, however, not surprising since the collecting volume was chosen for quite extrem cases. Scenarios (4c) and (5c) with a charge collecting volume that is based on extensive ion drift simulations in [114] do not explain the data very well either.

In general, the experimental runs in different conditions do not alter the results as significantly as in the different MC scenarios. This is of course expected since the MC scenarios describe idealized conditions of decay sampling and charge collection whereas the experimental data most likely incorporates superpositions of different physical processes. Additionally, the different experimental runs are rather short-term and had some initial electronic difficulties. The errors in Tab. 6.5 are only statistically, but the difference in count rates between

the detectors indicate to non negligible systematical uncertainties.

6.6 Conclusion & Perspectives

The recent $^{42}\text{Ar}/^{42}\text{K}$ issue and the accompanying MC study to the first test data runs of the GERDA experiment was documented in this chapter. Different MC scenarios with various homogeneous and discrete ^{42}K distributions were presented and scaled to different idealized physical scenarios. Additionally, the first experimental GERDA data was presented for direct comparison to the MC data.

The purpose of this chapter was the documentation of the MC study for ^{42}K and a detailed discussion was omitted on purpose. It has to be based not only on ^{42}K decay simulations but also on other investigations as e.g. the ion drift in LAr and the charge value of the ^{42}K .

The original goal of the study was to answer the main questions: Where do the ^{42}K nuclei decay and what concentration of ^{42}Ar has the LAr in GERDA. The answer is not possible with the experimental and MC data at hand and is in general a complex one. The ^{42}K distribution is neither discrete nor homogeneous and will be a complex density field determined by the complex electric field configuration in the GERDA setup. With increasing effort it might be possible to superpose different MC scenarios and include other physic processes but it is doubtful that a specific concentration can be determined in this way. The study, however, showed strong implications that the ^{42}K concentration is not homogeneous as initially assumed in the planning of the GERDA experiment.

Chapter 7

New Limits for DBD's of Pd into Excited States

This chapter presents the analysis of DBD's in two palladium isotopes into excited states. Chemical and physical properties of Pd as well as former limits on $2\nu\beta\beta$ and theoretical predictions are shown in Sec. 7.1. Three measurements were performed in the Niederneiveaumesslabor¹ Felsenkeller and after an initial analysis, the Pd was commercially purified.

The measurement setup, calibration and cleaning process is presented in Sec. 7.2. An extensive analysis was done in order to extract lower limits for the half-lives of the respective decays using various statistical methods. This analysis is the subject of Sec. 7.3 followed by prospective improvements of the experiment in Sec. 7.4.

7.1 Introduction

Pd is a rare silvery-white metal with the atomic number of 46 and is chemically associated with the platinum group. The elements of this group, ruthenium, rhodium, osmium, iridium, platinum and palladium, share some common chemical properties such as high thermal stability, mechanical resilience and a good catalytic behavior. These elements often occur together in natural deposits and it can be assumed that they are difficult to separate chemically.

Pd has six stable isotopes of which two are considered DBD isotopes; ^{102}Pd is decaying into ^{102}Ru and ^{110}Pd into ^{110}Cd (see Tab. 7.1).

Table 7.1 Abundance of stable Pd isotopes in natural Pd [27].

Isotope	^{102}Pd	^{104}Pd	^{105}Pd	^{106}Pd	^{108}Pd	^{110}Pd
Abundance [%]	1.02	11.14	22.33	27.33	26.46	11.72

The excitation schemes of the daughter nuclides of ^{102}Pd and ^{110}Pd are shown in Fig. 7.1 and 7.2 respectively. Decays into 0^+ excited states will be favored so that the dominant decay modes include a two γ -cascade for both DBD isotopes. Hence, the experimental signature consists of four γ -lines in total. The Q-values and the energy of the two causally bound γ -lines of each decay are shown in Tab. 7.2.

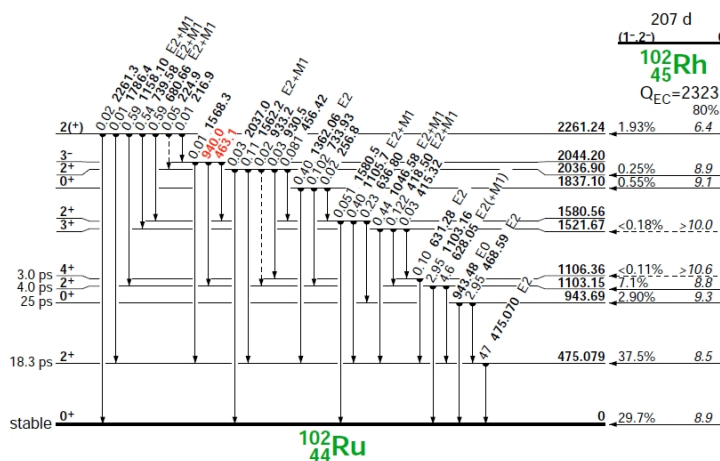
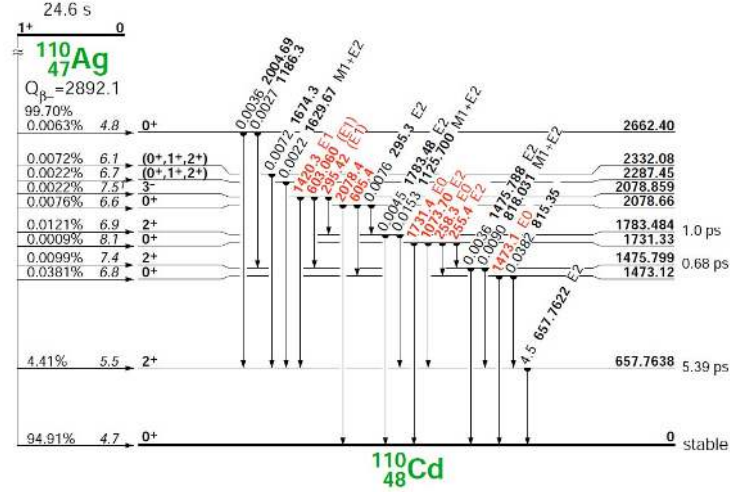


Figure 7.1 Excitation scheme of ^{102}Ru . From [27].

¹low background laboratory

Figure 7.2 Excitation scheme of ^{110}Cd . From [27].Table 7.2 Q-value and de-excitation γ 's in ^{102}Pd and ^{110}Pd .

Transition	^{102}Pd	^{110}Pd
Q-value	1172.5 keV [27]	2017 keV [115]
$0^+ \rightarrow 2^+$	468.59 keV	815.35 keV
$2^+ \rightarrow 0^+(\text{GS})$	475.07 keV	657.76 keV

7.1.1 Historic Measurements of DBD's in Pd

Pd has not been attractive for DBD research until now. It is not easily usable as a detector in an on-source approach and the characteristics of its two DBD isotopes make it not competitive in off-source experiments compared to other DBD nuclides. The only publication of a half-life limit for ^{110}Pd has been done by Rolf G. Winter in 1951 [116]. He installed 248.5 g of Pd foil in a cloud chamber and analyzed 10,097 photographs of which one showed a possible signal; two electrons emerging from the same point in the Pd foil. He stated that this signal could also be produced by cosmic muons with an expected occurrence of 0.6 events in the whole experiment. Winter quoted a lower limit for the half-life of ^{110}Pd of $6 \cdot 10^{17}$ yr. He also considered the decay of ^{108}Pd into ^{108}Cd not knowing that ^{108}Cd has a higher Q-value; therefore, his results should be taken with care.

Apart from this historic paper, no other publication is known to exist. That means that there is no experimental lower limit for the half-life of $2\nu\text{ECEC}$ or $2\nu\text{EC}\beta^+$ decays of ^{102}Pd into the ground state nor for the half-lives of ^{102}Pd or ^{110}Pd decays into excited states. There are also no limits for neutrinoless decay modes in either isotope.

7.1.2 Theoretical Prediction

Theoretically predicted half-lives for the $2\nu\beta\beta$ decay can be found in [117]. Tab. 7.3 shows different half-lives for ^{110}Pd according to different theoretical models and different axial-vector couplings g_A (Sec. 2.4.1). The dawn of new limits for DBD of Pd within this thesis triggered new calculation for matrix elements and half-lives for the ground state transitions. A new QRPA calculation using the Single State Dominance Hypothesis estimates a half-life for $2\nu\beta\beta$ in ^{110}Pd of $1.2 \cdot 10^{20}$ yr with $g_A = 1.25$ [118]. The half-life for the $0\nu\beta\beta$ transition into the ground state was calculated with the projected-Hartree-Fock-Bogoliubov model and an effective Majorana neutrino mass of $|m_{ee}| = 50$ meV to $1.09_{-0.15}^{+0.18} \cdot 10^{26}$ yr with $g_A = 1.254$

and to $2.22_{-0.31}^{+0.40} \cdot 10^{26}$ yr with $g_A = 1.0$ [119]. With the Interactive Boson Model, the matrix elements for the $0\nu\beta\beta$ decay in ^{110}Pd were calculated to be 3.623 for the ground state and 1.599 for the first excited 0^+ state [120].

Table 7.3 Theoretically predicted half-lives of ^{110}Pd $2\nu\beta\beta$ [117] for different models: Projected Hartree-Fock-Bogoliubov (PHFB), Single State Dominance Hypothesis (SSDH), Second Random-Phase Approximation (SRPA), Operator Expansion Method (OEM) and Quasiparticle Random Phase Approximation (QRPA).

Theory	g_A	$T_{1/2}$ [yr]
PHFB	1.25	$1.41 \cdot 10^{20}$
PHFB	1.00	$3.44 \cdot 10^{20}$
SSDH	1.25	$7.0 \cdot 10^{19}$
SSDH	1.00	$1.7 \cdot 10^{20}$
SRPA(W.S)	1.25	$1.186 \cdot 10^{21}$
SRPA(W.S)	1.00	$2.896 \cdot 10^{21}$
OEM		$1.24 \cdot 10^{21}$
QRPA		$1.116 \cdot 10^{19}$

7.2 Measurements & Cleaning

The measurement and analysis of $2\nu\beta\beta$ decays into excited states was done with Pd from unknown origin. The Pd was formed in a 807.1 g cylindrical solid block that fitted into a standard form (D6) with a diameter of 70 cm and a height of 21 cm (see Fig. 7.3, left). The block had some holes that appeared to result from welding or the original forming process. After an initial measurement in order to determine possible radioactive impurities, the Pd was commercially purified (Sec. 7.2.7) and returned in 802.35 g of small non-uniform $1\text{ cm} \times 1\text{ cm} \times 1\text{ mm}$ plates that were piled up into the same standard form (see Fig. 7.3, right).

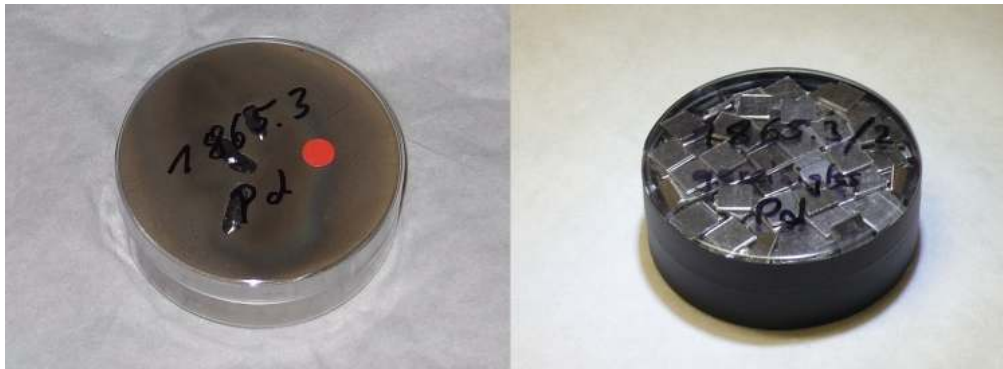


Figure 7.3 Pd block in standard form D6 before cleaning (left) and after cleaning (right).

Three measurements were performed in the Niederniveaumesslabor Felsenkeller in Dresden (Sec. 3.2.2) with a HPGe detector. Details of the measurements can be found in Tab. 7.4.

7.2.1 Experimental Setup

The experimental setup is placed inside measuring chamber 2 in the Felsenkeller laboratory. All data was taken with a low-level γ -spectrometry system that is shown in Fig. 7.4. The 1.9 kg HPGe detector, shown on the left side, is placed inside a shielding with a composit

Table 7.4 Properties of different measurements of Pd performed in the Niederniveaumesslabor Felsenkeller

No.	Starting date (time) [dd/mm/yy (hh:mm:ss)]	Life time [s (d)]	Dead time [s]	Purpose
1	14/09/09 (10:28:00)	754983 (8.7)	7	Identifying impurities
2	26/06/10 (13:35:42)	156136 (1.8)	2	Cleaning validation
3	19/07/10 (12:00:31)	1403893 (16.2)	596	Final long-term measurement

layer of 5 cm pure Cu on the inside, 5 cm pure Pb with 2.7 ± 0.6 Bq/kg (^{210}Pd) in the middle and 10 cm van Gahlen Pb [121] with 33 ± 4 Bq/kg on the outside which is shown on the right side of Fig. 7.4. The material close to the HPGe is mainly Al and Cu, but there is also some Pb used to corner the Ge crystal inside the Al holder which directly touches the crystal.

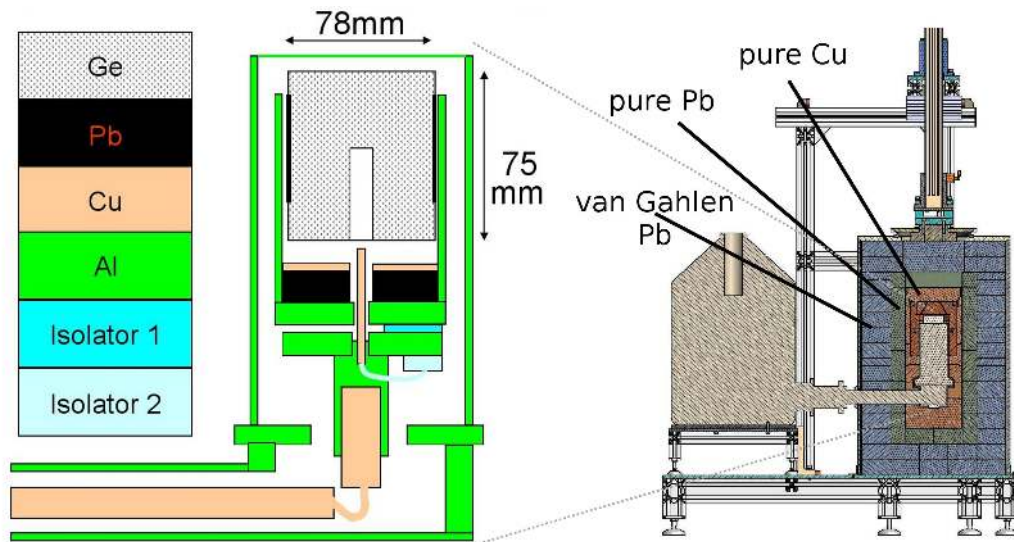


Figure 7.4 Low-level γ -spectrometry system in the Felsenkeller laboratory. The whole setup with lead castle and cryostat is shown on the right and an enlarged illustration of the detector on the left. From [57].

The HPGe detector itself has a dead layer of $50 \mu\text{m}$. The window to the sample place on top of the crystal consists of 1.6 mm thick Al. In order to estimate the detector efficiencies, the whole setup was simulated (Sec. 7.2.5).

The data was taken with an ORTEC MCA, was communicated by `spe` ASCII files and then converted to and analyzed with the ROOT framework.

7.2.2 Energy Calibration

The energy calibration of the detectors is routinely done by the Felsenkeller staff and parametrized in `spe` files in a first order polynomial:

$$E(\text{channel}) = \text{offset} + f_1 \cdot \text{channel}. \quad (7.1)$$

An available second order polynomial calibration that corrects for minor non-linearities in the detector was omitted for simplicity since it would result in histograms with non-uniform

bin widths. Both parametrizations were checked with the data and no apparent difference was observed.

The spectrum was recorded with 8192 channels and the calibration parameters are summarized in the Tab. 7.5. A slight miscalibration can be seen in Fig. D.6 in the Appendix at the 2614.53 keV ^{208}Tl peak for the spectrum of the third measurement. This has been investigated and found to be not significant for the ROI's in this thesis.

Table 7.5 Linear energy calibration according to Eq. 7.1 of different Pd measurements. The last column denotes the energy of the last bin, i.e. the maximal energy of the spectra.

Measurement	offset [keV]	f_1 [keV/channel]	Maximal energy [keV]
1, 2	-4.199327	0.342739	2803.52
3	-4.337734	0.342746	2803.44

7.2.3 Calibration of Energy Resolution

The energy resolution was calibrated by the Felsenkeller staff, parametrized in a second order polynomial and communicated as `spe` files:

$$\text{FWHM}(\text{channel}) = \text{offset} + f_1 \cdot \text{channel} + f_2 \cdot \text{channel}^2. \quad (7.2)$$

For the third measurement, the offset is 3.092977, the linear term, f_1 , is $7.347568 \cdot 10^{-4}$ and the quadratic term, f_2 , is $-2.776150 \cdot 10^{-8}$. The energy resolution calibration is not done for the measurements 1 and 2 since they were not used for peak fitting. The FWHM in channels has to be translated into energy using the linear term, f_1 , of the energy calibration in Eq. 7.1 and calculated into σ according to

$$\sigma = \text{FWHM} \cdot \frac{1}{2 \cdot \sqrt{2 \cdot \ln 2}} = \text{FWHM} \cdot \frac{1}{2.3548}. \quad (7.3)$$

The energy resolutions in FWHM and σ for the four energies of interest, EOI, are calculated in Tab. 7.6.

Table 7.6 Energy resolution in FWHM and σ for EOI.

Energy [keV]	468.59	475.07	657.76	815.35
FWHM [keV]	1.3895	1.3937	1.5111	1.6080
σ [keV]	0.5901	0.5919	0.6417	0.6828

7.2.4 Efficiency Calibration

The overall strategy is to calibrate the experimental detector efficiency, η_{exp} , with a SiO_2 sample and then to simulate the difference in self absorption between SiO_2 and Pd. Finally, the correction of self absorption, r_η , is cross checked in situ with prominent background peaks from the measured Pd spectrum.

The η_{exp} is calibrated with 17 out of 20 measured efficiencies of eight radioactive nuclides that cover the energy range from 47 keV to 2614 keV. The nuclides and data are shown in Tab. 7.7. The calibration sources are natural decay chains in a SiO_2 sample that fits a D6 standard form like the Pd (Fig. 7.4). All conditions for the calibration sources and the

Pd measurements were the same which should eliminate any geometric effect. However, there remains the difference in self absorption between Pd and SiO₂ which is investigated in Sec. 7.2.5. In order to interpolate the efficiency to the EOI, a purely empirical function is used that has no physical base since the dependencies are complex including cross section effects, geometric effects and solid state effects. There is a multitude of complex parametrizations that include the typical knee at roughly 100 keV in a HPGe efficiency plot but, since this energy range is not considered in this analysis, only the last 17 γ -lines in Tab. 7.7 above 200 keV are used for the fit. A combination of two exponential functions proved to fit the measured values above the knee quite well:

$$\eta_{\text{exp}} = p_0 \cdot e^{p_1 \cdot E} + p_2 \cdot e^{p_3 \cdot E}. \quad (7.4)$$

Table 7.7 Calibration sources in the SiO₂ sample and the 20 measured detector efficiencies. The first three peak efficiencies are omitted.

E_γ [keV]	Nuclide	η_{exp}
46.51	²¹⁰ Pb	$1.0729 \cdot 10^1$
63.28	²³⁴ Th	$1.3306 \cdot 10^1$
92.58	²³⁴ Th	$1.4196 \cdot 10^1$
238.63	²¹² Pb	$1.0695 \cdot 10^1$
241.98	²¹⁴ Pb	$1.0471 \cdot 10^1$
295.21	²¹⁴ Pb	$9.2681 \cdot 10^2$
338.32	²²⁸ Ac	$7.9793 \cdot 10^2$
351.92	²¹⁴ Pb	$8.2562 \cdot 10^2$
583.19	²⁰⁸ Tl	$4.3772 \cdot 10^2$
609.32	²¹⁴ Bi	$4.4445 \cdot 10^2$
860.56	²⁰⁸ Tl	$4.0035 \cdot 10^2$
911.20	²²⁸ Ac	$4.0591 \cdot 10^2$
968.97	²²⁸ Ac	$3.9227 \cdot 10^2$
1001.03	²³⁴ Th	$4.1431 \cdot 10^2$
1120.29	²¹⁴ Bi	$2.9391 \cdot 10^2$
1238.11	²¹⁴ Bi	$2.7428 \cdot 10^2$
1377.67	²¹⁴ Bi	$3.5113 \cdot 10^2$
1460.83	⁴⁰ K	$3.0814 \cdot 10^2$
1764.49	²¹⁴ Bi	$2.7575 \cdot 10^2$
2614.35	²⁰⁸ Tl	$1.4298 \cdot 10^2$

Errors for the measured efficiencies consist of a statistical component, an uncertainty for the calibration source activity and a component of sum coincidence effects². Without a detailed investigation, the total error is assumed to be smaller than 7%. The measuring time is chosen to achieve a statistical error of less than 1% and the systematical uncertainty of the calibration source activities is less than 6%. The measured efficiencies were fit with Eq. 7.4 resulting in the fit values shown in Tab. 7.8.

The fit function and the measured values are visualized in Fig. 7.5 and the interpolated efficiencies for the EOI are shown in Tab. 7.9.

Spectra shown in this chapter are plotted in counts or counts per second and refer to the original number of events counted by the detector. Efficiencies are only defined for full energy peaks and are not included in any spectrum. They are used in order to calculate the actual number of decayed nuclei from the number of counts in a peak at a specific energy.

²The efficiency of nuclides with multiple γ -lines can be underestimated if the cascading photons coincide inside the detector; summed energies are not counted in the single energy peaks.

Table 7.8 Efficiency calibration fit results with Eq. 7.4.

Parameter	Value	Error
p0	-3.04	0.15
p1	$-3.13 \cdot 10^{-4}$	$1.09 \cdot 10^{-4}$
p2	-1.31	0.28
p3	$-5.93 \cdot 10^{-3}$	$1.21 \cdot 10^{-3}$

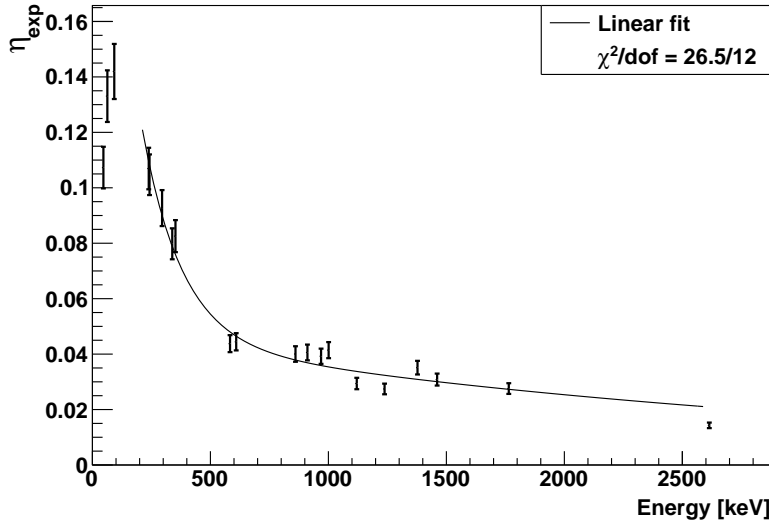


Figure 7.5 Efficiency fit of calibration source peaks in Tab. 7.7.

7.2.5 Correction of Efficiency Calibration

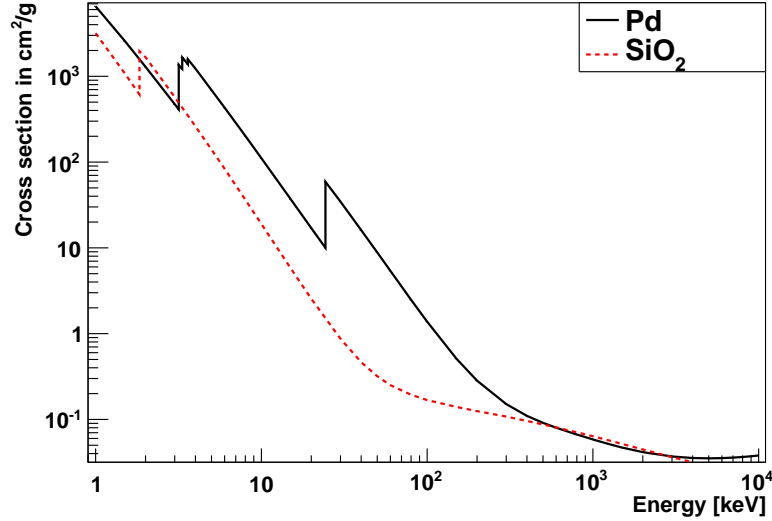
The effect of self absorption differs between Pd and SiO₂ as a function of energy which is due to different photonic cross sections resulting from different effective atomic numbers, Z . A visualization of the photonic cross sections in Pd and SiO₂ can be seen in Figure 7.6 with data from [122]. It is essential to perform a simulation of the detector in order to quantify the correction for η_{exp} , r_η . This is done with the AMOS [123] code and the help of Dorothea Sommer from the radiation group of the IKTP at the TU-Dresden. A sufficient number of photons is simulated for each EOI and sampled inside the D6 standard form filled with Pd and SiO₂ respectively. The amount of events is chosen to achieve a statistical error smaller than 0.1 % in the full energy peak which is counted and compared between the Pd and SiO₂ scenario.

The simulation includes coupled photon electron transport with photons down to 1 keV and electrons down to 10 keV, atomic excitations and de-excitations and single scattering algorithms for electrons. The density for SiO₂ is taken to be 2.4 g/cm³ and for Pd 10.2 g/cm³. The latter is estimated assuming the mass of the Pd (802.35 g) homogeneously distributed in the volume of the standard form (78.5 cm³). This density differs to the one of solid Pd with 12 g/cm³ and is expected to represent an approximately homogeneous distribution despite of the small Pd plates with air pockets in between.

The simulated spectra can be seen exemplarily in Fig. 7.7 for a single 657.76 keV γ -line and in Fig. D.1 till D.3 in the Appendix for the other EOI's; black denotes the Pd spectrum and red the SiO₂ spectrum. Some spectral features are visible such as the full energy peak, the

Table 7.9 Efficiencies for EOI's determined by interpolation of calibration source peaks in SiO₂.

Energy [keV]	468.59	475.07	657.76	815.35
η_{exp} in SiO ₂	0.0577	0.0570	0.0440	0.0389

Figure 7.6 Photon cross sections for Pd (black solid line) and SiO₂ (red dotted line) with data from [122].

Compton edge, the Compton continuum, the backscattered full energy peak and some lead X-ray lines. The full energy peak results from events where the photon deposits its whole energy in the detector. The Compton edge is the maximum energy that can be transferred from a photon to an electron via Compton scattering with a scattering angle of 180 deg. The Compton continuum is shaped by photons scattering in an angle lower than 180 deg and denotes the range in the spectrum from zero keV to the Compton edge. The backscattered full energy peak is formed by photons that are scattered 180 deg outside the detector prior to their complete absorption inside the detector. The X-ray lines at around 80 keV result from excited lead atoms in the holding structure of the crystal which are highlighted in Fig. 7.4.

The simulation yields the efficiencies for the EOI's in Pd, $\eta_{\text{sim}}(\text{Pd})$, in SiO₂, $\eta_{\text{sim}}(\text{SiO}_2)$, and their ratio $r_\eta = \eta_{\text{sim}}(\text{Pd})/\eta_{\text{sim}}(\text{SiO}_2)$ which are presented in Tab. 7.10.

Table 7.10 Simulated efficiencies, η_{sim} , and efficiency ratios, r_η , for single photons in Pd and SiO₂ with the EOI's.

Energy [keV]	468.59	475.07	657.76	815.35
$\eta_{\text{sim}}(\text{Pd})$	0.0376	0.0375	0.0338	0.0314
$\eta_{\text{sim}}(\text{SiO}_2)$	0.0651	0.0645	0.0528	0.0463
r_η	0.578	0.581	0.641	0.677

Comparing the values for SiO₂ in Tab. 7.9 and 7.10, it can be seen that the measured and simulated efficiency, η_{exp} and η_{sim} agree only up to 13% and that the simulation overestimates. If one explains the difference merely with an inaccurate simulation of the geometric setup,

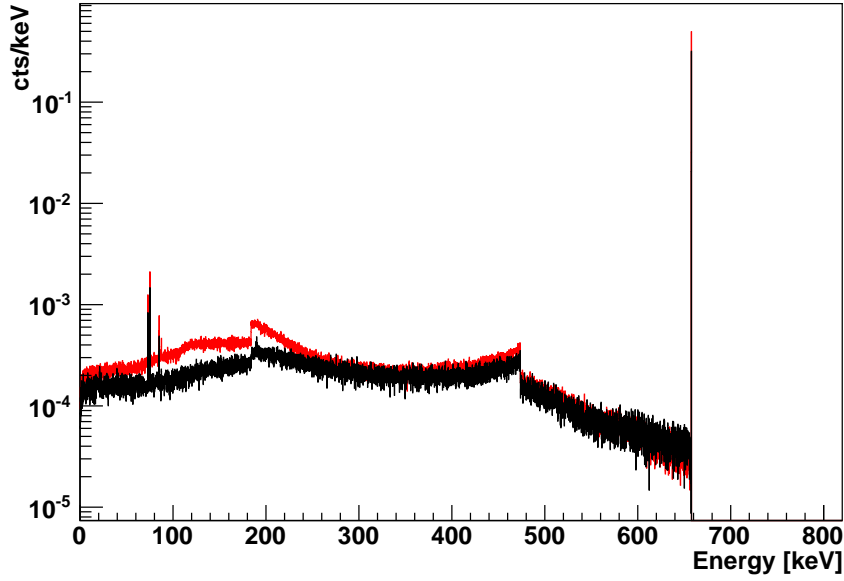


Figure 7.7 Energy spectrum of a simulated source of 657.76 keV photons homogeneously distributed in a D6 standard form consisting of $\rho = 10.22 \text{ g/cm}^3$ Pd (black) and SiO_2 (red).

which could easily explain such a discrepancy, it would mostly be canceled in the ratio of the simulated efficiency. Since there exists a reasonable experimental efficiency calibration for SiO_2 , r_η is the sole value of interest and the difference between simulation and experiment is not of further interest in this thesis.

There is no need to parametrize r_η for the final analysis since it was specifically simulated for the EOI; however, for validation purposes in Sec. 7.2.6, the r_η at energies of various background peaks is needed. For that purpose a linear interpolation of the values in Tab. 7.10 is assumed which is a rather simplified approach since it is evident that the photonic cross sections of Pd and SiO_2 do not follow linear dependencies at energies between 100 and 1000 keV (see Fig. 7.6).

7.2.6 Validation Checks

It is challenging to validate the calibration “in situ” in a low background environment. Especially after the cleaning process, hardly any γ -line with sufficient statistics can be found (see Fig. D.4, D.5 and D.6 in the Appendix); however, some prominent background peaks can be selected and investigated in order to check the energy and efficiency calibration. The selection is based on Tab. A.1, A.2 and A.3 in the Appendix and includes criteria such as a high line efficiency, an energy around the EOI, the visibility in the spectrum and the occurrence in an equilibrated part of a primordial decay chain. Since the recent cleaning process certainly broke the equilibrium, the latter criterion reduced the choice of nuclides to sections in the decay chains with small connecting half-lives; that are nuclides chronologically decaying between ^{226}Ra and ^{214}Bi in the ^{238}U decay chain and between ^{228}Th and ^{208}Pb in the ^{232}Th decay chain. Tab. 7.11 shows the selected nuclides and peak energies, E_γ , of which the ones highlighted with a star proved suitable to fit.

A Gaussian plus a constant are used for fitting the background peaks in a range of $\pm 15 \text{ keV}$ around the peak energy. The mean of the Gaussian is constrained to $E_\gamma \pm 0.5 \text{ keV}$ and the σ to the value interpolated with Eq. 7.3 at the respective peak energy $\pm 0.01 \text{ keV}$. The peak area and the constant term are left unconstrained. It is taken care that the fitted mean

Table 7.11 Selected background peaks for in situ validation of efficiency calibration for the primordial decay chains of ^{238}U and ^{232}Th . Columns denote the nuclide, the peak energy and the γ -line efficiency with respect to the whole decay chain. Peaks highlighted with a * proved suitable to fit.

Decay chain/ nuclide	E_γ [keV]	ϵ_{line} [%] in respect to chain
^{238}U chain		
^{226}Ra	186.10	3.51
^{214}Pb	241.98	7.12
	295.21*	18.15
^{214}Bi	351.92*	35.1
	609.32*	44.6
	1120.29	14.7
^{232}Th chain		
^{212}Pb	238.63*	43.5
^{208}Tl	583.19*	30.6
	860.56	4.5
^{212}Bi	727.33	6.7

does not touch the boundaries of the constrains whereas no such condition is applied to σ since it proved difficult to achieve a good fit on that parameter for peaks with low statistics. Tab. 7.12 shows the fit results of five peaks that are reasonably to fit. The columns show in sequence the nuclide, the respective peak energy, the difference between the peak energy and the mean energy obtained by the fit, the experimental efficiency, η_{exp} , obtained by Eq. 7.4, the correction to the efficiency, r_η , according to a linear interpolation described in Sec. 7.2.5 and the calculated expected activity of the respective decay chain in decays during the whole measurement time. The latter is calculated with:

$$A_{\text{chain}} = \frac{N_{\text{cnt}}}{\eta_{\text{exp}} \cdot r_\eta \cdot \epsilon_{\text{line}}}, \quad (7.5)$$

where N_{cnt} denotes the counts in the peak area and ϵ_{line} the line efficiency of the nuclei with respect to the decay chain.

The calculated activity should have the same value for each peak in an equilibrated part of a decay chain and can be used to validate the efficiency calibration. Furthermore, comparing these values with and without correction for self absorption can check whether the r_η -correction is useful. However, this method only probes the difference of r_η at given E_γ 's and does not justify the absolute r_η which is the crucial variable for the further analysis. The difference in r_η is expected to be small at similar energies which makes this method not very sensitive as a test of the MC simulation but is nonetheless the only possibility to test the efficiency calibration in situ. The test is shown in Fig. 7.8 in which A_{chain} is drawn for the ^{238}U chain in the left plots and for the ^{232}Th chain in the right plots. The first row of plots shows A_{chain}^* calculated without r_η in Eq. 7.5, whereas the second line shows A_{chain} with r_η according to Eq. 7.5 for comparison. Also shown are the errors of the fitted N_{cnt} and the constant fit function of A_{chain} . The test yields the goodness' of the fits for A_{chain}^* and A_{chain} for each of the two decay chains. The χ^2 and the degree of freedom, dof, of the fits are presented in Tab. 7.13.

The plots in Fig. 7.8 and the fit results show that the correction for self absorption greatly enhances the consistency of the two ^{232}Th decay chain nuclides. The ^{238}U decay chain nuclides, however, seem to become slightly less consistent because of the 295.21 keV ^{214}Pb

Table 7.12 Fitted in situ background peaks for validation checks. The columns denote the nuclide, the peak energy, E_γ , the difference between peak energy and fitted peak energy, E_{fit} , the experimental efficiency for the SiO₂ calibration, the correction for self absorption between SiO₂ and Pd and the calculated decays per decay chain within the measuring time.

Decay chain nuclide	E_γ [keV]	$E_\gamma - E_{\text{fit}}$ [keV]	η_{exp}	r_η	A_{chain} [T_{meas}^{-1}]
²³⁸ U chain					
²¹⁴ Pb	295.21	-0.32	0.090	0.529	31.62 ± 6.47
	351.92	-0.30	0.076	0.546	23.91 ± 3.84
²¹⁴ Bi	609.32	0.00	0.046	0.621	24.39 ± 4.09
²³² Th chain					
²¹² Pb	238.63	-0.15	0.109	0.513	14.63 ± 2.54
²⁰⁸ Tl	583.19	-0.10	0.048	0.613	21.16 ± 4.36

Table 7.13 Goodness' of in situ fits for prominent peak counts of the primordial decay chains ²³⁸U and ²³²Th with (A_{chain}) and without (A_{chain}^*) the correction for self absorption between SiO₂ and Pd.

χ^2 of fits	²³⁸ U	²³² Th
A_{chain}^*	0.96	3.38
A_{chain}	1.13	1.68
dof	2	1

peak. The criticism of this technique is clearly the linear approximation of r_η which becomes more inconsistent with energies further away from the four simulated EOI's. This is especially true for the 295.21 keV peak. The low count rates and possible contributions of other background nuclides could additionally compromise this test.

However, the energy dependence of r_η is not needed for the further analysis since it is exactly known for the four simulated EOI's. It was merely used as a validation of the calibration mechanisms with low statistics background peaks which is working for four out of five peaks and is therefore found to be valid.

7.2.7 Cleaning

The first Pd spectrum (red spectrum in Fig. D.4, D.5 and D.6 in the Appendix) shows a significant contamination of ²⁴¹Am at 59.54 keV and other less significant peaks of primordial decay chain nuclides. Since ²⁴¹Am with a half life of 432.2 yr is not part of a primordial decay chain and the Pd is of unknown origin, it was controversial whether it could be used for DBD investigation.

There were two options to proceed: A chemical cleaning in order to refine the Pd or the purchase of new ultra pure Pd. The latter option was quickly ruled out with a Pd price of more than €100 per gram³ [124]. The cleaning option was pursued and the German company C. HAFNER GmbH + Co. KG was found to be suitable. The price for cleaning the Pd sample was €633.91 and it was guaranteed to have a purity higher than 99.95%. The exact chemical cleaning process is confidential but the basic principle is to dissolve the Pd

³10 m of 99.99+ % Pd wire with 2.36 g/m cost €2392.

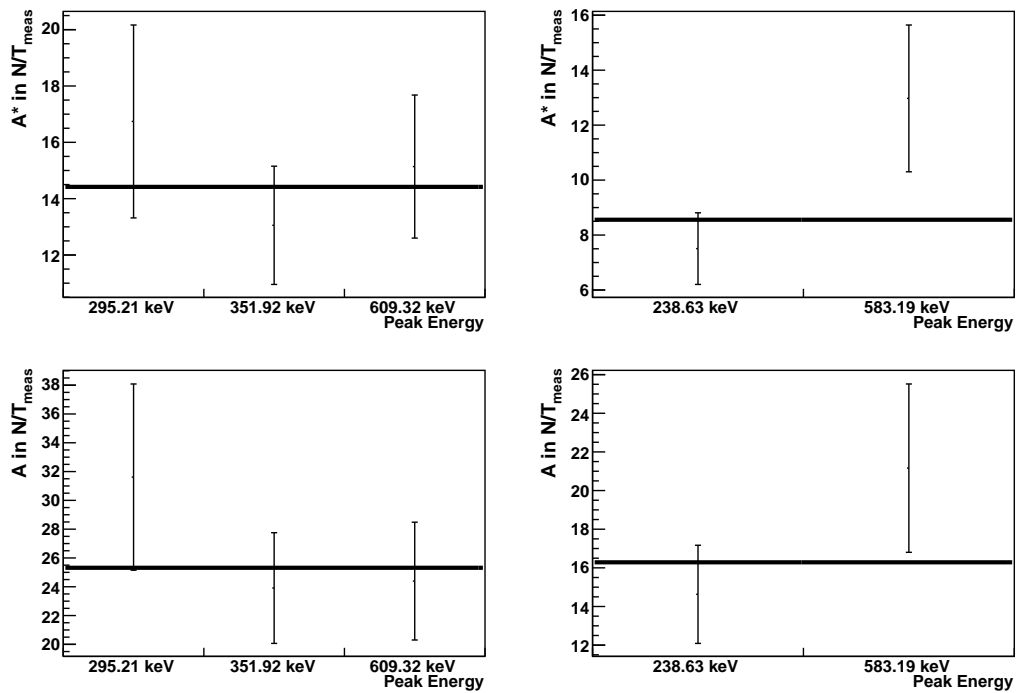


Figure 7.8 In situ test of calibration with prominent background nuclides. A_{chain}^* denotes the expected decays per decay chain without the correction for self absorption whereas A_{chain} includes it. The left plots show the ^{238}U decay chain nuclides and the right plots the ^{232}Th decay chain nuclides. The decays per decay chain should be independent of the γ -line characteristics and a constant is used to fit the value (solid line).

in an acid which precipitates some impurities and then to filtrate the remains. This is done sequentially with various acids that are sensitive to different impurities. Finally, the resulting salt is returned to metallic Pd with a reducing agent.

The time line of the cleaning process is recorded in Tab. 7.14 in order to consider cosmic activation in the future. During the cleaning, the Pd weight was reduced from 807.1 g to 802.35 g.

Table 7.14 Time line of Pd cleaning process for cosmic activation record. The abbreviations denote: FK - Felsenkeller, TU - Technical University Dresden, CH - C. HAFNER GmbH.

Logistic action	Date
FK → TU	12/03/10
TU → CH	16/03/10
CH reception	19/03/10
Arrival of account	29/03/10
CH → TU	31/03/10
TU → FK	01/04/10

7.3 Spectral Analysis

The background spectrum under investigation is shown in Fig. D.4, D.5 and D.6 in the Appendix for measurement 1, before the cleaning (red), and measurement 3, after the cleaning (black). The enlargements at the four ROI's is shown on the left sides in Fig. 7.9 and Fig. D.7, D.8 and D.9 in the Appendix. The counts vary strongly between the bins and the background estimation is highly sensitive to the size and position of the side bands. The measurements show some prominent background peaks mainly from decay chain nuclides. Those and some anthropogenic peaks are discussed in Sec. 7.3.1. The area around the EOI's and possible γ -line contributions from background nuclides are analyzed in Sec. 7.3.2. The construction of a background model is done in Sec. 7.3.3 and the extraction of upper limits for the counts at the EOI's is done in Sec. 7.3.4. These upper count limits are eventually used in Sec. 7.3.5 to calculate the half-lives of Pd DBD modes.

7.3.1 Background Peak Before and After Cleaning

The measured spectrum in Fig. D.4, D.5 and D.6 in the Appendix show some background peaks. They mostly originate from primordial decay chain nuclides. The following peaks and nuclides have been identified:

^{238}U decay chain: ^{234m}Pa with 1001.03 keV, ^{226}Ra with 186.10 keV, ^{214}Pb with 295.21 keV and 351.92 keV, ^{214}Bi with 609.32 keV, 1120.29 keV and 1764.49 keV and ^{110}Pb with 46.54 keV.

^{232}Th decay chain: ^{228}Ac with 911.21 keV and 968.97 keV, ^{212}Pb with 238.63 keV, ^{212}Bi with 727.33 keV and ^{208}Tl with 583.19 keV and 2614.53 keV.

^{235}U decay chain: ^{235}U with 185.72 keV.

Other prominent peaks are at 1460.83 keV from ^{40}K , the annihilation peak at 511 keV and the Pb X-ray lines between 70 and 80 keV. Anthropogenic background is found at 59.54 keV which belongs to ^{241}Am .

After the chemical cleaning, many of the former background peaks vanished or decreased in intensity. The ^{241}Am peak vanished beyond recognition. All of the primordial decay chain peaks decreased tremendously which becomes especially apparent in the 2614.53 keV ^{208}Tl peak. The 511 keV annihilation peak did not change significantly and the ^{40}K peak even seems to have increased after the cleaning. The X-ray lines between 70 and 80 keV did not change which supports the thesis that they originate in the detector holding structure.

The quantitative evaluation of the primordial decay chain peaks has not been done in this thesis and would be difficult to interpret since the breaking of equilibria in the history of the Pd sample. The breaking points are at the time of the mining which is unknown, at the time of the last melting, which is unknown, and at the time of the chemical cleaning. All these processes have changed the ratio of decay chain nuclides differently and, depending on the elapsed time, parts of the chain will have returned into secular equilibrium.

The main result of this investigation is the confirmation that the background can be modeled around the EOI's as a continuum and does not need the consideration of specific background peaks. Apart from the ^{40}K impurification, the chemical cleaning process performed well.

7.3.2 Area around Pd Peaks

The areas around each of the four Pd peaks were investigated for background γ -lines that could contribute to the signal regions. Tab. D.1 in the Appendix shows an exhaustive list

of all known γ -lines within ± 5 keV of the EOI's that have a progeny nuclide with a half-life of more than a year [106]. The only nuclide with a close γ -line that has a significant intensity is ^{137}Cs with 661.66 keV and 85.1% intensity. There are, however, the intermediate nuclides between the DBD nuclides and their progenies, i.e. ^{102}Rh ($T_{1/2} = 207$ d), ^{110}Ag ($T_{1/2} = 24.6$ s), ^{102m}Rh ($T_{1/2} = 2.9$ yr) and ^{110m}Ag ($T_{1/2} = 249.79$ d), which have intrinsically decay modes in exactly the same excited states of the progenies. Hence, this contributes to the indistinguishable background of the Pd γ -lines.

A way to estimate the impact of background peaks with similar energies to the ROI's is to look for other γ -lines of the respective background nuclides. This is done visually since most of these nuclides have γ -lines of higher intensity than the ones under suspect or γ -lines at higher energies which makes them easier to spot due to less background.

^{102}Rh has no reasonable γ -lines to check. The γ -line with the highest efficiency is the ^{102}Pd γ -line of the $2^+ \rightarrow 0^+$ (GS) transition with 475.07 keV. No peak was spotted there which means that there is no background expected from ^{102}Rh at the ^{102}Pd $0^+ \rightarrow 2^+$ γ -line at 468.59 keV.

^{102m}Rh has multiple high intensity γ -lines at higher energies e.g. 631.28 keV with 56%, 697.49 keV with 44% or 1112.84 keV with 19%. With a visual inspection one can interpret low count rate peaks at those energies but this would have to be tested with proper statistical analysis. Since the results for the Pd peaks do not yield a significant peak (Sec. 7.3.4), the additional background is not considered in the final analysis and remains a prospect for further studies.

^{110}Ag has a short half life of $T_{1/2} = 24.6$ s and does not need to be considered.

^{110m}Ag has multiple high intensity γ -lines at higher energies e.g. 657.76 keV with 94%, 1384.3 keV with 24.12% or 1505.04 keV with 12.95%. There was no peak found with a visual inspection at neither of those energies.

^{137}Cs with a 661.66 keV line is 3.9 keV above the ^{110}Pd $0^+ \rightarrow 2^+$ γ -line and cannot be seen visually in the spectrum. Therefore, it can be assumed that it does not contribute to the respective peak.

The γ -line selection in Tab. D.1 in the Appendix is created with a simple cut on the half-life of the progenitors of the corresponding background nuclides. A more complete analysis could include short lived progenitors that are fed by long lived pre-progenitor earlier along in a possible decay chain. This, however, would increase the complexity of the analysis beyond the scope of this thesis.

7.3.3 Background Model

The background has a wide distribution and is difficult to estimate with a simple fit. An appropriate fit function could be a constant, a linear or an exponential function, depending on the energy of the peak⁴. A study has shown that the resulting background in the peak areas are highly dependent on the range of the side bands that are used for the background fits. For this reason, a rather unusual method is used to estimate the background and its uncertainty.

In a range of ± 30 keV around the peak, the amount of bins with specific entries are plotted in a histogram of entries per bin. The area of ± 5 keV around the peak is not included⁵. For

⁴The background in γ -ray spectroscopy tends to flatten at higher energies. At lower energies the background falls steeply and can be approximated with an exponential.

⁵Not using the ROI for the background estimation is not crucial in cases where the signal is expected to be minute compared to the background; it is, however, bad practice in an epistemological sense.

a purely statistical background this distribution of entries per bin should be either Poisson in case of low count rates or Gaussian otherwise. The fit of this distribution of either function results in the mean and the width of the background. The advantage of this method is the yield of a proper uncertainty and the possibility to control the background for irregularities, e.g. background peaks or non-statistical behavior which would result in a distortion of the Gaussian or Poisson distribution. In case of a sloping background e.g. in a low energy region or a large side band area, the entries per bin distribution would simply widen and result in a more conservative estimate.

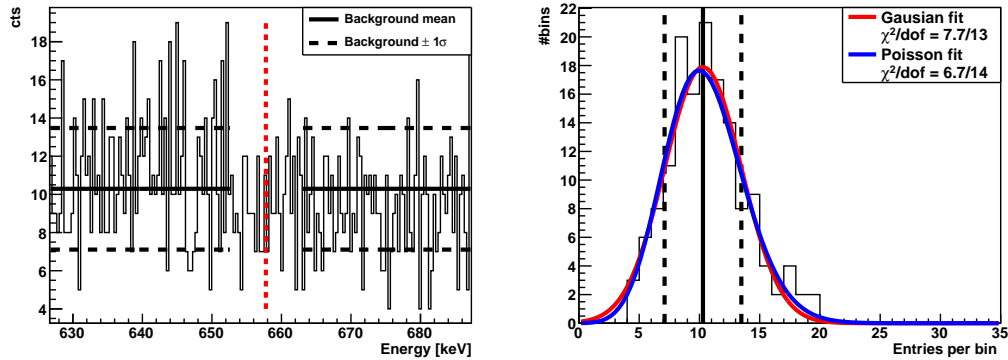


Figure 7.9 Modeling of the background around the 657.76 keV γ -line. The right plot shows the entry per bin distribution fitted with a Gaussian (red curve) and a Poisson (blue curve). The left plot shows the spectrum in a ± 30 keV area around the expected peak (red dotted vertical line) with the area used for the background modeling. In both plots, the black solid lines is the background mean and the black dotted lines are the Gaussian background 1σ uncertainties.

The area around the ROI and the entry per bin distribution is shown exemplary in Fig. 7.9 for the 657.76 keV peak of ^{110}Pd and in Fig. D.7, D.8 and D.9 in the Appendix for the three other Pd peaks. The right plots show the distribution of entries per bin fitted with a Gaussian (red) and a Poisson (blue). The left plots show the spectra around the ROI's with the illustration of the side bands used for the background estimation. The black solid lines denote the background means and the black dotted lines denote their Gaussian 1σ variances. The red vertical lines show the positions of the expected Pd peaks.

It was decided to use a Poisson fit for each peak of interest for the sake of consistency even though the mean count rate exceeded 15 counts at the lower energetic ^{102}Pd γ -lines. The fit results are shown on Tab. 7.15.

Table 7.15 Results of a Poisson and a Gaussian fit on the background distribution in Fig. 7.9 and Fig. D.7, D.8 and D.9 in the Appendix.

Energy [keV]	468.59	475.07	657.76	815.35
Poisson mean	17.147	17.132	10.481	8.444
Gaussian mean	17.007	16.881	10.292	8.340
Gaussian sigma	3.939	5.009	3.185	2.793

7.3.4 Extracting Count Limits

The binning of the data requires a binned approach (Sec. 3.4.6). The statistical method for extracting an upper limit of the signal is used binwise for 15 different bins and the resulting

15 limits are weighted with the expected signal contribution in the specific bin (Eq. 3.15). The signal contribution is acquired with the integration of a normalized Gaussian with the width from Tab. 7.6. With 15 bins and a bin width of 0.343 keV, the integrated bins cover always more than 99.98 % of the whole Gaussian signal.

The high variation of the background makes it feasible to use a profiled likelihood approach (Sec. 3.4.5). The ROOT class `TRolke` is used with a Poisson distributed background (Tab. 7.15). The results can be seen in Tab. 7.16.

The different statistical approach of Feldman and Cousins is used in a similar manner. Its implementation in the `TFeldmanCousins` class in ROOT is used with the assumption of a constant background, i.e. the simple mean of the background distribution. The results are presented in Tab. 7.16.

The Unified Approach (Feldman and Cousins) and the profiled likelihood method use different constructions of the confidence intervals where the Feldman and Cousins method is expected to be more conservative at low signal count rates. For comparison between the two techniques, a third limit is extracted with the `TRolke` class. This time, the background is assumed to be Gaussian with a zero width⁶, which, naively, should provide the same conditions for both ROOT classes. This result can be seen in Tab. 7.16 and can be compared to the Feldman and Cousins results.

Table 7.16 Upper limits on signal counts with two profiled likelihood methods (`TRolke`), Poisson distributed and constant background, and the Feldman-Cousins method (`TFeldmanCousins`) for 95 % CL.

Energy [keV]	468.59	475.07	657.76	815.35
<code>TRolke</code> Poisson	19.75	28.77	23.05	17.94
<code>TFeldmanCousins</code>	17.49	22.80	18.66	15.33
<code>TRolke</code> constant	13.67	21.39	16.77	13.13

As expected, the Unified Approach is more conservative in a constant background scenario than the profiled likelihood method, which in this case is just the classical method with a simple likelihood (see Fig. 3.7). On the other hand, the profiled likelihood yields higher upper count limits if the background uncertainty is included. This confirms the prior assumption that the background uncertainty is in fact not negligible and that the Feldman and Cousins method is not the ideal choice in this scenario (see discussion in 3.4.5). The MLE or the best value for the signal count cannot be retrieved with the method described. A simple likelihood fit with a Gaussian and a constant background showed that the MLE is negative in three out of four ROI's; therefore, it is not stated and the analysis is continued with the upper limit.

7.3.5 Calculating Half-Lives

The most conservative upper signal limit of the profiled likelihood method with a Poisson distributed background is used for calculating the half-lives of the Pd DBD modes with Eq. 3.4. In this equation, T denotes the total measuring live time (Tab. 7.4), $\eta = \eta_{\text{exp}} \cdot r_{\eta}$ the corrected detection efficiency (Tab. 7.10), ϵ_{line} the γ -line efficiency and N_0^{iso} the total number of the respective DBD nuclei. ϵ_{line} is 100 % with respect to each other [27] and N_0^{iso} can be simply calculated with Eq. 3.5 in which M is the total mass of Pd, 802.35 g, A the atomic mass of elemental Pd, 106.42 u, and f_{iso} the isotopic abundance (Tab. 7.1). The

⁶The width, σ , is set to a small number instead of zero ($\sigma = 0.001$ keV) in order to avoid computational clashes.

number of ^{102}Pd nuclei was calculated with $4.63 \cdot 10^{22}$ and the number of ^{110}Pd nuclei with $5.32 \cdot 10^{23}$. This results with Eq. 3.4 and the upper signal limits, N_{cts} , in Tab. 7.16 to the half-lives presented in Tab. 7.17.

Table 7.17 Lower limit of half-life acquired with the profiled likelihood method and a Poisson distributed background for the four Pd DBD into excited states at 95 % CL.

Nuclide	^{102}Pd	^{102}Pd	^{110}Pd	^{110}Pd
Transition	$0^+ \rightarrow 2^+$	$2^+ \rightarrow 0^+(\text{GS})$	$2^+ \rightarrow 0^+(\text{GS})$	$0^+ \rightarrow 2^+$
Energy [keV]	468.59	475.07	657.76	815.35
$T_{1/2}$ [yr]	$2.54 \cdot 10^{18}$	$1.73 \cdot 10^{18}$	$2.14 \cdot 10^{19}$	$2.54 \cdot 10^{19}$

If the DBD decay modes in the first excited 0^+ states are the only transitions into excited states, the half-lives according to the $0^+ \rightarrow 2^+$ and $2^+ \rightarrow 0^+(\text{GS})$ γ -lines should be the same since they are 100 % causally linked. If there are decays into the first excited 2^+ state, then the $2^+ \rightarrow 0^+(\text{GS})$ γ 's should occur more frequently. The results in Tab. 7.17 naively suggest the latter since the $T_{1/2}$ of the $2^+ \rightarrow 0^+(\text{GS})$ modes are smaller than the ones of the respective $0^+ \rightarrow 2^+$ transitions. This is true even though the $2^+ \rightarrow 0^+(\text{GS})$ γ -line is the more energetic one in ^{110}Pd and the less energetic one in ^{102}Pd which is an argument against the effect being caused by overall background levels that differ between higher and lower energies. However, this effect can also be by chance due to the strongly fluctuating background and the difference in upper count limits for the two γ -lines is not used to improve the limit on the decay modes into the 2^+ states⁷. The physical result of this measurement is the upper limit for the half-lives of ^{110}Pd and ^{102}Pd decaying into the first excited 0^+ and 2^+ state. Since the analysis only considers de-excitation γ 's, the half-life limits are also valid for every other DBD mode into the same excited states, especially for the $0\nu\beta\beta$ modes.

7.4 Conclusion & Perspectives

The two DBD isotopes in Pd, ^{102}Pd and ^{110}Pd , have been investigated with a rather simple and low cost standard γ -ray spectroscopy experiment in the Felsenkeller laboratory. Three state of the art Frequentist statistical methods were used to extract upper limits from a count spectrum. The most conservative of these results were used in a straight forward calculation of lower limits on the half-lives. The experiment yields the world first lower half-life limit on the $2\nu\beta^-\beta^-$ and $0\nu\beta^-\beta^-$ decay of ^{110}Pd into the first excited 0^+ state with a half-life larger than $2.54 \cdot 10^{19}$ yr (95 % CL) and the world first limit on the $2\nu\text{ECEC}$ and $0\nu\text{ECEC}$ decay of ^{102}Pd into the first excited 0^+ state with a half-life larger than $2.54 \cdot 10^{18}$ yr (95 % CL). Furthermore, the 2ν and 0ν decay modes into the first excited 2^+ state were analyzed with a lower half-life limit of $2.14 \cdot 10^{19}$ yr and $1.73 \cdot 10^{18}$ yr in ^{110}Pd and ^{102}Pd respectively. The difference in sensitivity between the two DBD nuclides is largely determined by the difference in isotopic abundance between the two isotopes.

The analysis of the current data can be improved with a more thorough investigation on possible background contributions in the ROI's including possible decay chains. With the argument of additional background, the effective count rate will decrease and the half-life limit increase. A future analysis can also investigate summation peaks of the two γ -lines and possible X-ray lines from $2\nu\text{ECEC}$ decay in ^{102}Pd . The detection of the latter can be enhanced with a low energy germanium detector with a thin low absorbing window and the sampling of the Pd tiles close to and around the detector. Investigating the 511 keV peak

⁷In principle one could argue that the counts from Pd 0_1^+ transitions should contribute to the counts from Pd 2_1^+ transitions and that the difference between both γ -line counts is in fact the signal for the Pd 2_1^+ transition, which would be much smaller and the half-life limit much larger; however, this argument is only true for MLE's and not for the stated upper limits.

for a possible contribution of the $2\nu\beta^+\text{EC}$ is difficult since it requires the precise knowledge of the background.

The irregular nature of the background makes it less promising to continue the experiment with a simply longer exposure since the sensitivity, i.e. half-life limit, is expected to increase only with the square root of the measuring time (Eq. 3.2). However, serious enhancements can be expected from setup improvements as e.g. the use of real coincidence between the two γ -lines in either Pd DBD isotope. Multiple HPGe detectors can be used to increase the solid angle coverage and additionally reject the background with a coincidence veto. The arrangement of the Pd in a thin layer around the detector will minimize self absorption and increase the detection efficiency.

Chapter 8

GERDA ^{36}Ar Analysis

The novel technique of operating an array of bare HPGe detectors in a large amount of LAr provides the opportunity to investigate argon isotopes. This chapter contains an analysis of the radiative ^{36}Ar $0\nu\text{ECEC}$ decay with the first GERDA data.

Sec. 8.1 introduces the ^{36}Ar $0\nu\text{ECEC}$ decay, Sec. 8.2 describes the experimental data and Sec. 8.3 presents a MC study for determining the detection efficiency in the GERDA cryostat. The background model and the analysis is shown in Sec. 8.4 and the chapter is concluded in Sec. 8.5.

8.1 Introduction

In the GERDA concept, liquid argon is serving as a cooling medium for the HPGe detectors and as a passive shielding against external radiation. The GERDA cryostat (Sec. 4.2.2) contains 64 m^3 or 89.2 t of natural LAr with an array of HPGe detectors in its center. The isotopic abundance of ^{36}Ar in natural Ar is 0.336% [27] which sums up to 300 kg in the whole cryostat.

^{36}Ar is expected to be unstable undergoing double electron capture into ^{36}S with a Q-value of 433.5 keV [27] (see Fig. 8.1). The low Q-value energetically excludes decay modes with β^+ and decays into excited states of ^{36}S . The two-neutrino EC decay modes are discussed in Sec. 2.3.1 and the neutrinoless EC decay modes in Sec. 2.3.2. The analysis in this chapter investigates the radiative $0^+ \rightarrow 0^+$ $0\nu\text{ECEC}$ into the ground state with three photons in the final state; two X-rays coming from the two atomic shell de-excitations and one γ transporting the rest of the decay energy. The two X-rays are bound to origin from different shells, most likely the K and the L shell, and have energies of $E_K = 2.47\text{ keV}$ and $E_L = 0.23\text{ keV}$. This leaves $E_\gamma = 430.8\text{ keV}$ for the γ . The experimental signature is solely the 430.8 keV γ -line since the GERDA HPGe detectors are not designed for low energy measurements.

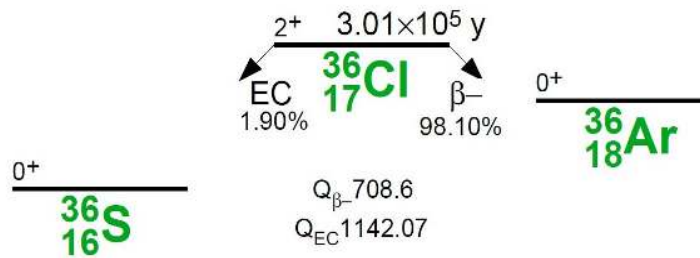


Figure 8.1 Part of the mass parabola of $A=36$ nuclides illustrating the ^{36}Ar decay into ^{36}S . From [27].

The $0\nu\text{ECEC}$ decay mode has the preliminary theoretically estimated half-life of 10^{35} yr (private communication within [125] without stated $|m_{ee}|$) whereas the $2\nu\text{ECEC}$ decay mode is calculated with a half-life of 10^{29} yr [126].

There exists only one experimental half-life limit for the radiative ^{36}Ar $0\nu\text{ECEC}$ of $1.9 \cdot 10^{18}\text{ yr}$ (68% C.L.) [125] which was measured with LArGe, the liquid argon test facility for GERDA.

8.2 Experimental Data

The experimental data is the same as being used for the ^{42}K investigation in Sec. 6.4. The different runs with the three detector test string (Sec. 4.2.1) are presented in Tab. 6.2. The GTF112 detector was not working during the runs (ixb) and (x) which were excluded from the final analysis for simplicity. This results in a total exposure of 68.0d with all three detectors. 25.4d of two detector exposure is omitted. The different experimental situations, e.g. the installation of the mini shroud, different high voltages on the shrouds or on the detectors are assumed to have no effect on ^{36}Ar decays; the ^{36}Ar concentration is not influenced by electric fields and the 430.8 keV γ -line is not significantly shielded by the 0.03 mm thick shroud foils.

The calibration is done sporadically with a manual operated ^{228}Th source and a preliminary analysis framework independently of the background runs. The energy calibration was already applied by Bernhard Schwingenheuer. For the resolution calibration four peaks are fitted to each spectra with the equation

$$\text{FWHM}[\text{keV}] = \sqrt{a^2 + b^2 \cdot E[\text{keV}]}, \quad (8.1)$$

which translates into a Gaussian σ with $\sigma = 1/2.35 \text{FWHM}$, where a and b are two fit parameters. The calibration data and fitting was taken from the preliminary calibration web interface [127] and the resulting resolutions for each detector and calibration run at 430.8 keV are presented in Tab. 8.1. The average of all individual resolutions are calculated to a FWHM of 4.01 keV or a σ of 1.70 keV. Data from detectors GTF45 and GTF112 at August 5, 2010 were not included due to a not reasonable fit.

Table 8.1 GERDA detector resolution from sporadic calibration runs at 430.8 keV.

Resolution [keV]	GTF45	GTF32	GTF112
03/07/10			
FWHM	3.12 ± 0.05	3.58 ± 0.06	3.69 ± 0.10
σ	1.32 ± 0.02	1.52 ± 0.02	1.57 ± 0.04
05/08/10			
FWHM	4.17 ± 0.06	6.81 ± 33.25	7.06 ± 20.76
σ	1.77 ± 0.03	2.89 ± 14.12	3.00 ± 8.82
10/08/10			
FWHM	3.50 ± 0.18	4.97 ± 0.10	4.08 ± 0.21
σ	1.49 ± 0.07	2.11 ± 0.04	1.73 ± 0.09
12/08/10			
FWHM	3.42 ± 0.19	4.92 ± 0.10	4.15 ± 0.15
σ	1.45 ± 0.08	2.09 ± 0.04	1.76 ± 0.06

8.3 MC Study of Detection Efficiency

The 430.8 keV γ -line has only a limited range in LAr which makes it necessary to restrict the volume of LAr to be used for the calculation. The basic problem is to determine the size of a volume that does not underestimate the γ -line efficiency; i.e. there should be no contributions to the 430.8 keV γ -line which comes from decays outside the considered volume. The approach is to simulate 430.8 keV photons homogeneously and isotropically in different sized volumes and calculate the detection efficiency scaled to an equal activity of

the LAr¹. This MC study is essentially the same as for the ^{42}K γ -lines which is thoroughly described in Sec. 6.3.2. The result is presented in Fig. 8.2 and shows a plot of the detection efficiency at different sized volumes that are parametrized with x (Eq. 6.1 - 6.3). If the detection efficiency does not change with increasing volume, there are no increasing contributions to the ^{36}Ar peak. This is found to be at $x = 4$ which translates into a cylindrical volume with $R(4) = 50$ cm and $H(4) = 130$ cm and into an effective LAr volume² of 1.019 m³.

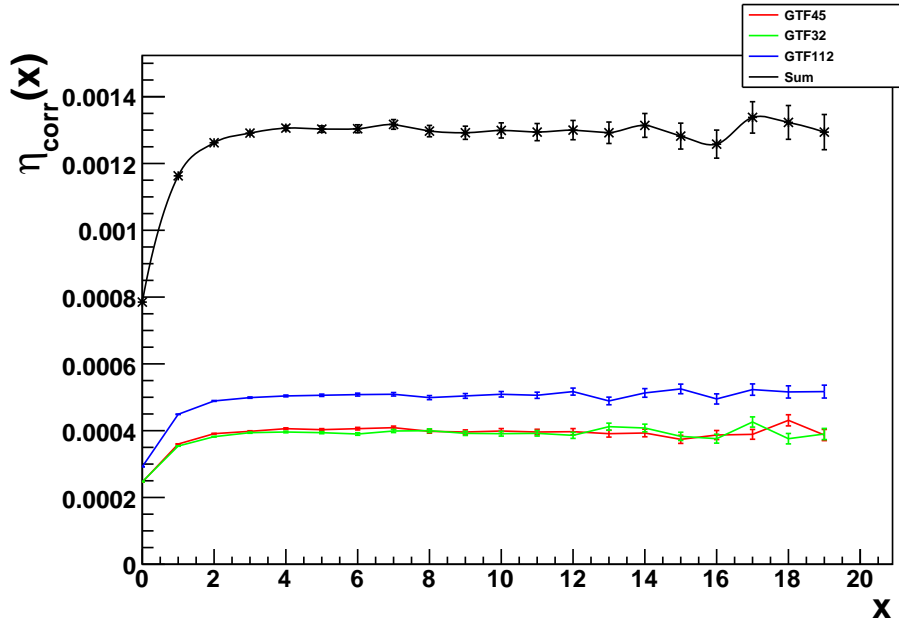


Figure 8.2 Corrected detection efficiency, $\eta_{\text{corr}}(x)$, of 430.8 keV γ 's in the GERDA setup with respect to the parametrized volume $V(x)$ for the detectors GTF45, GTF32 and GTF112 in red, green and blue respectively and for the whole test string in black.

This volume is used to simulate the detection efficiencies, η , for each detector. 10^9 of 430.8 keV γ 's are sampled homogeneously and isotropically inside the volume and the resulting events in the full energy peak and the calculated η are shown in Tab. 8.2. The statistical errors calculated from the peak counts are less than 0.2%.

Table 8.2 Detection efficiencies of a 430.8 keV γ -line with the GERDA test string and a cylindrical LAr volume with $R(4) = 50$ cm and $H(4) = 130$ cm. The left column denotes the detector events out of 10^9 simulated events and the right column denotes the detection efficiency η .

Detector	Peak counts	η
GTF45	283431	$2.83 \cdot 10^{-4}$
GTF32	276025	$2.76 \cdot 10^{-4}$
GTF112	354899	$3.55 \cdot 10^{-4}$
Sum	914355	$9.14 \cdot 10^{-4}$

¹This is basically done with the scaling to a constant density of simulated decays per unit volume.

²The effective volume is the parametrized cylindrical volume without the volume of detectors and support structures.

8.4 Analysis

The strategy to derive the half-life limit for the ^{36}Ar decay is to construct a background model in order to estimate the expected background in the ROI (Sec. 8.4.1), then to extract an upper count limit at the position of the expected peak (Sec. 8.4.2) and to calculate the half-life limit with the simulated efficiency (Sec. 8.4.3).

8.4.1 Background Model

The GERDA experiment is optimized for a low background around the ^{76}Ge Q-value of 2039 keV. The background at lower energies, especially around 430.8 keV is significantly higher. The detector intrinsic background below the Q-value is dominated by the $2\nu\beta\beta$ decay but there is additional outside background as e.g. coming from ^{39}Ar . This is a β^- -decay with a Q-value and β -endpoint at 565 keV. It was simulated within [128] that the maximum of the ^{39}Ar spectrum is at around 100 keV with a rate of 330 cts/(kg · yr · keV). This and additional background components are not further pursued so that it was not possible to construct a MC background model.

Instead, a simple linear function was used for fitting the background ± 60 keV around the peak³. The area of ± 5 keV around the peak was excluded from the fit.

The fitting area and the fitting function is shown in Fig. 8.3 and described by

$$y[\text{counts/bin}] = a + b \cdot E[\text{keV}] \quad (8.2)$$

with the parameters fitted to $a = 39.065$ and $b = -0.0722$. The background at 430.8 keV is calculated to be 7.96 counts/bin and assumed to be constant in the whole peak area.

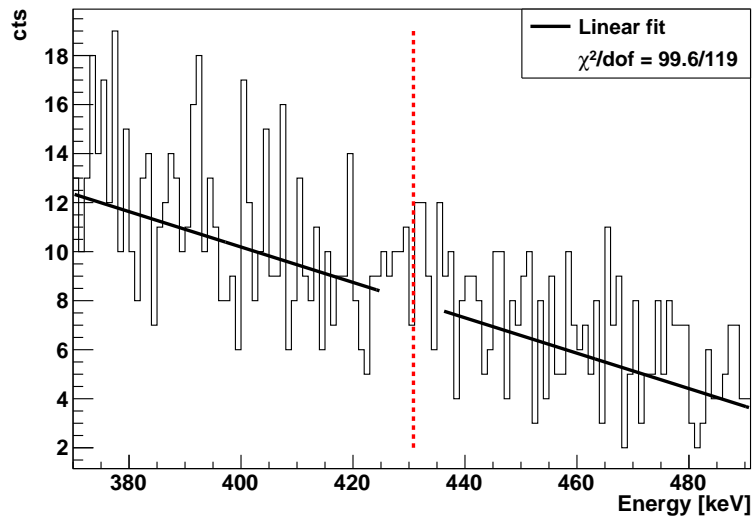


Figure 8.3 Linear background fit around the peak area. The solid line denotes the fit function in the area used for fitting and the dashed line the expected peak position.

³A better method to retrieve the background and consider its uncertainties as described in Sec. 7.3.3 did not prove feasible since the background is on a slope in this energy range; this would induce a higher uncertainty, i.e. a wider entry per bin distribution, than the simple linear fit applied here (see Sec. 7.3.3 for more information).

8.4.2 Extracting Count Limits

The extraction of the upper count limits for the signal is done with the Unified Approach of Feldman and Cousins (Sec. 3.4.4) and with the profiled likelihood method (Sec. 3.4.5) and is closely related to the analysis of Pd in Sec. 7.3.4. The binning of the data is treated according to the method described in Sec. 3.4.6. Nine bins with a bin width of 1 keV are used for sampling the Gaussian peak at 430.8 keV with a σ of 1.70 keV which accounts for 99.18 % of the peak area.

The simple linear background fit does not consider the background variations per bin. This can be taken into account with a nuisance parameter in the profiled likelihood method which is assumed to follow a Poisson distribution with the mean of the background 7.96 counts/bin (Sec. 8.4.1). The upper count limits for the signal calculated with `TRolke` and `TFeldmanCousins` are presented in Tab. 8.3. Additionally, `TRolke` is used for a calculation without a background uncertainty for direct comparison with the Unified Approach.

Table 8.3 Upper limits on signal counts with two profiled likelihood methods (`TRolke`), Poisson distributed and constant background, and the Feldman-Cousins method (`TFeldmanCousins`) for 95 % CL.

Stat. method	Signal upper limit
<code>TRolke</code> Poisson	11.61
<code>TFeldmanCousins</code>	9.83
<code>TRolke</code> constant	9.51

The profiled likelihood method with constant background and the Unified Approach show good agreement with a slightly more conservative limit of the latter. The difference between the methods is, however, not as large as in the Pd analysis in Sec. 7.3.4 and the influence of the background uncertainty on the upper limit is lower.

8.4.3 Calculating Half-Lives

The most conservative upper limit of the profiled likelihood method with a Poisson distributed background is used for the half-life calculation of the radiative ^{36}Ar $0\nu\text{ECEC}$ decay mode. Eq. 3.4 is used to calculate $T_{1/2}$ in which T is total measuring time with all three detectors, 68.0 d (Sec. 8.2), η the three detector efficiency, $9.14 \cdot 10^{-4}$ (Tab. 8.2), $\epsilon_{\text{line}} = 100\%$ for this decay mode, N_{cts} the upper count limit (Tab. 8.3) and N_0 the total amount of ^{36}Ar nuclei inside the considered volume. The latter can be calculated according to Eq. 3.5. The source mass, M , is calculated with the volume of 1.019 m^3 (Sec. 8.3) and the LAr density of 1394 kg/m^3 to 1420.49 kg, the atomic mass, A , of elemental argon is 39.948 u and the isotopic abundance is 0.336 %, which results in $N_0 = 7.195 \cdot 10^{25}$.

With these values, the lower limit of the half-life is calculated to $7.32 \cdot 10^{20}$ yr with 95 % CL.

This result has to be considered preliminary since the first background runs were rather unstable and can include some non negligible systematic uncertainties which are not considered; however, the expected limit will be at least two orders of magnitude better than the current one from LArGe.

8.5 Conclusions & Perspectives

In this chapter, the first data runs of the GERDA experiment were used to retrieve a lower half-life limit for the radiative ^{36}Ar $0\nu\text{ECEC}$. The detection efficiency for the test string setup was simulated and the energy resolution was roughly averaged over available preliminary calibration runs. The spectrum was analyzed with different statistical methods and a conservative preliminary lower limit of $7.32 \cdot 10^{20}$ yr (95 % CL) was retrieved with a profiled likelihood approach with Poisson distributed background. This result is more than two orders of magnitude better than the current limit of $1.9 \cdot 10^{18}$ yr (68 % CL), but still 14 orders of magnitude below the preliminary theoretical prediction of 10^{35} yr.

The analysis in this chapter showed that the GERDA setup is suitable to be used for ^{36}Ar $0\nu\text{ECEC}$ investigation and can provide improved lower half-life limits. The installation of Phase I with 12 detectors and considerably longer and more stable background runs are expected to significantly increase the sensitivity for this decay mode; however, the background increases for enriched detectors because of the $2\nu\beta\beta$ decay of ^{76}Ge .

Chapter 9

Conclusions & Perspectives

This thesis featured four different and independent studies and analyses of DBD experiments with the emphasis on excited state transitions; the study of coincidence analysis for the $2\nu\beta\beta$ decay of ^{76}Ge into the first excited 0^+ state with the state of the art GERDA experiment, the $^{42}\text{Ar}/^{42}\text{K}$ background study for GERDA, the analysis of excited state transitions in ^{110}Pd and ^{102}Pd with a low cost γ -spectroscopy setup and the analysis of the radiative $0\nu\text{ECEC}$ decay in ^{36}Ar with first GERDA data.

A rather extensive introduction in the physics of DBD and the review of the current experimental situation and challenges in the field was presented in the first chapters in order to reconcile the different topics and experimental approaches in this theses.

The study of a coincidence analysis in Chap. 5 was done for the nominal 14 detector GERDA Phase I array with the fictional starting date of 01/07/10 and the run time of one year. A detailed background model was developed that treats each detector individually, is easily adaptable to different array geometries and different run times and may serve as the base for data analysis in the future. Different cuts have been developed and tested for the specific requirements of the final state particles of the $2\nu\beta\beta$ decay into the first excited 0^+ state of ^{76}Se . The presumably best cut was found to be a two detector cut with one final state γ fully detected in one detector. The study predicted the survival of 2.15 background events and 24.29 signal events after the cut for the total Phase I with an assumed signal decay half-life of 10^{23} yr which covers most of the theoretical predictions. This is a promising factor 10 excess of signal over background. Considered was mainly internal cosmic activated background and primordial decay chains in the detector holders. The examination of additional background contributions is encouraged as e.g. the unexpected large $^{42}\text{Ar}/^{42}\text{K}$ component. The study can be continued with the calculation of the combined background rejection efficiency of all background processes and the weighted combined analysis of the different cuts.

The $^{42}\text{Ar}/^{42}\text{K}$ study was presented and compared with the first experimental data of the GERDA experiment in Chap. 6. The detailed description and presentation of results is hoped to facilitate the efforts of data analysis in the GERDA collaboration. There were no direct results of the MC study other than strong implication towards an inhomogeneous distribution of ^{42}K in the LAr that could be explained by charge collection. The investigation of the $^{42}\text{Ar}/^{42}\text{K}$ issue is ongoing and a detailed discussion was omitted on purpose.

The analysis of an 802.35 g Pd sample for DBD transitions of ^{110}Pd and ^{102}Pd into the first excited 0^+ states was presented in Chap. 7. 13 kg · d exposure were used to extract lower half-life limits of $2.54 \cdot 10^{19}$ yr for $2\nu\beta^-\beta^-$ and $0\nu\beta^-\beta^-$ in ^{110}Pd and $2.54 \cdot 10^{18}$ yr for $2\nu\text{ECEC}$ and $0\nu\text{ECEC}$ in ^{102}Pd (95 % CL) with a profiled likelihood and a Poisson background distribution. The limits for the same transitions into the first excited 2^+ state were found to be $2.14 \cdot 10^{19}$ yr for ^{110}Pd and $1.73 \cdot 10^{18}$ yr for ^{102}Pd . These are the first limits for decays into excited states in the two Pd isotopes. Future improvements of these limits are possible with a longer measuring time but are expected to be more efficient with a different experimental setup; the composition of the small Pd tiles around the detector would reduce the self absorption and enable the analysis of low energetic X-ray lines for a better understanding of the $2\nu\text{ECEC}$ transition in ^{102}Pd . The 511 keV γ -line could be analysed in order to investigate the $2\nu\text{EC}\beta^+$ decay mode. The utilization of two HPGe detectors on either side of the sample would increase the detection efficiency and enables the possibility of a coincidence analysis which would tremendously reduce the background. However, all these suggestions increase the effort of calibration and simulation as well as the financial demands and would outclass the analysis presented within this thesis.

Chap. 8 featured a preliminary analysis of the radiative $0\nu\text{ECEC}$ decay of ^{36}Ar and demonstrated the utilization of the GERDA experiment for the investigation of this decay mode. With 96,500 kg · d exposure of the first data, a lower half-life limit of $7.32 \cdot 10^{20}$ yr (95 % CL) was retrieved with the profiled likelihood method and a Poisson background distribution. This is two orders of magnitude larger than the current limit but well below the theoretically estimated 10^{35} yr. The stated limit is preliminary for the test data but a substantial

increase of exposure and detection efficiency can be expected from the proper background runs of GERDA Phase I.

All four investigations of this thesis are encouraged to be improved on the analysis level. The statistical method of combining Feldman-Cousins or profiled likelihood limits on a bin by bin base is expected to overcover which makes the results in this thesis more conservative. The combination of MLE's on the likelihood level would increase the predictability of the experiments and enables to properly combine data of different runs with different experimental situations. This would help the coincidence analysis in Chap. 5 with combining different cuts and the ^{36}Ar analysis with combining runs with a different detection efficiency.

The investigation of excited state transitions improves NME calculations which are imperative to retrieve an effective Majorana neutrino mass. This is especially interesting for ^{76}Ge with the pending claim of evidence for $0\nu\beta\beta$, which would facilitate other experiments the validation of that claim with different DBD nuclides.

Appendix A

General Considerations

Table A.1 Primordial decay chain of ^{238}U . The half-life of the respective nuclide is shown in the first column. The second column denotes the nuclide with the kind of decay and with the branching ratios in case of multiple decay possibilities. The last three columns show the most prominent α 's, β 's and γ 's respectively. Values are taken from [129] unless marked with a star; marked values are taken from [106].

Half-life $T_{1/2}$	Nuclide (decay) Branch	α -decay energy [MeV(branch%)]	β -decay energy [MeV(branch%)]	γ -emission energy [keV(branch%)]
$4.468 \cdot 10^9$ a	^{238}U (α)	4.197(77) 4.147(23)		49.55(0.062)
24.1 d	^{234}Th (β)		0.199(72.5) 0.104(17.8) 0.060(7.1)	92.37(2.42) 63.28(4.1) 92.79(2.39)
1.175 m	^{234m}Pa (β)		2.29(98.4) 1.53(0.62) 1.25(0.74)	766.37(0.316) 1001.03(0.839)
$2.45 \cdot 10^5$ a	^{234}U (α)	4.775(72.5) 4.723(27.5)		53.20(0.123)
$7.538 \cdot 10^4$ a	^{230}Th (α)	4.688(76.3) 4.621(23.4)		67.67(0.38)
1600 a	^{226}Ra (α)			
2.8235 d	^{222}Rn (α)	5.490(99.9) 4.987(0.08)		
3.05 m	^{218}Po (α/β)	6.002(100)		
2 s 26.8 m	0.018 % ^{218}At (α) 99.98 % ^{214}Pb (β)		0.73(40.5) 0.67(46)	295.21(18.15) 241.98(7.12) 351.92(35.1)
19.9 m	^{214}Bi (α/β)		3.275(19.9) 1.88(7.18) 1.542* 1.424* 1.51(16.9) 1.02(16.9)	609.32(44.6) 768.36(4.76) 1120.29(14.7) 1238.11(5.78) 1764.49(15.1) 2204.21(4.98)
1.3 m $164.3 \mu\text{s}$	0.021 % ^{210}Tl (α) 99.979 % ^{214}Po (β)	7.687(100)		
22.3 a	^{210}Pb (β)		0.063(19) 0.017(99)	46.54(4.24)
5.013 d	^{210}Bi (β)		1.161(99)	
138.4 d	^{210}Po (α)	5.305(99)		
stable	^{206}Pb			

Table A.2 Primordial decay chain of ^{232}Th . The half-life of the respective nuclide is shown in the first column. The second column denotes the nuclide with the kind of decay and with the branching ratios in case of multiple decay possibilities. The last three columns show the most prominent α 's, β 's and γ 's respectively. Values are taken from [129] unless marked with a star; marked values are taken from [106].

Half-life $T_{1/2}$	Nuclide (decay) Branch	α -decay energy [MeV(branch%)]	β -decay energy [MeV(branch%)]	γ -emission energy [keV(branch%)]
$1.405 \cdot 10^{10}$ a	^{232}Th (α)	4.012(77.9) 3.954(22.1)		63.81(0.27)
5.75 a	^{228}Ra (β)		0.039(60) 0.015(40)	
6.15 h	^{228}Ac (β)		2.18(10) 1.70(11.6) 1.11(31.0)	338.32(11.3) 968.97(16.2) 911.21(26.6)
1.9131 a	^{228}Th (α)	5.423(71.1) 5.340(28.2) 5.221(0.44)		84.37(1.22) 215.99(0.28)
3.664 d	^{224}Ra (α)	5.685(94.9) 5.449(5.1)		240.99(4.4)
55.6 s	^{220}Rn (α)	6.288(99.9) 5.747(0.11)		549.73(0.11)
0.145 s	^{216}Po (α)	6.778(100)		
10.64 h	^{212}Pb (β)		0.569(12) 0.331(83) 0.159(5)	300.09(3.25) 238.63(43.5)
60.55 m	^{212}Bi (α/β)	6.089(27.1) 6.050(69.9)	2.248(86.6) 1.521(6.8)	1620.74(1.5) 727.33(6.7)
3.053 m	35.94% ^{208}Tl (β)		1.80(51) 1.52(21.7) 1.29(22.8) 1.52(3.1)	583.19(30.6) 860.56(4.5) 510.77(8.2) 2614.53(35.8)
0.298 μs	64.06% ^{212}Po (α)	8.785(100)		
stable	^{208}Pb			

Table A.3 Primordial decay chain of ^{235}U . The half-life of the respective nuclide is shown in the first column. The second column denotes the nuclide with the kind of decay and with the branching ratios in case of multiple decay possibilities. The last three columns show the most prominent α 's, β 's and γ 's respectively. Values are taken from [129] unless marked with a star; marked values are taken from [106].

Half-life $T_{1/2}$	Nuclide (decay) Branch	α -decay energy [MeV(branch%)]	β -decay energy [MeV(branch%)]	γ -emission energy [keV(branch%)]
$7.037 \cdot 10^8$ a	^{235}U (α)	4.400(55) 4.364(17)		185.72(57.2) 143.76(10.96)
25.52 h	^{231}Th (β)		0.305(35) 0.218(37) 0.134(12.8) 0.090(12)	25.64(14.6) 84.21(6.71) 81.24(0.89)
$3.276 \cdot 10^4$ a	^{231}Pa (α)	5.058(11.0) 5.012(24.5) 5.029(20) 4.951(22.8) 4.737(8.4)		27.36(10.3) 300.07(2.47) 302.67(2.2)
21.773 a	^{227}Ac (α/β)	4.951(47) 4.938(40)	0.046(54)	
21.8 m 18.718 d	1.38 % ^{223}Fr (β) 98.62 % ^{227}Th (α)	6.038(24.0) 5.978(23.4) 5.757(20.3) 5.709(8.2)		50.13(7.9) 235.97(12.1) 256.5(7.0)
11.435 d	^{223}Ra (α)	5.748(9.1) 5.717(53.7) 5.608(24.2) 5.540(9.1)		154.21(5.62) 269.46(13.7) 323.87(3.93) 338.28(2.79)
3.96 s	^{219}Rn (α)	6.819(81.0) 6.553(11.5) 6.425(7.5)		271.23(10.8) 401.81(6.4)
1.8 ms	^{215}Po (α)	7.386(99)		
36.1 m	^{211}Pb (β)		1.355(92) 0.951(1.8) 0.525(5.3)	404.85(3.78) 832.01(3.52)
2.17 m	^{211}Bi (α/β)	6.623(84) 6.279(16)		351.07(12.91)
0.52 s 4.77 m	0.32 % ^{211}Po (α) 99.68 % ^{207}Tl (β)		1.442(99.76)	897.83(0.24)
stable	^{207}Pb			

Table A.4 Double β^- decaying nuclides. Columns denote the nuclide, the decay mode¹, the isotopic abundance and the Q-value of the decay. Values are taken from [28] and [106].

Nuclide	Decay mode	Abundance in %	Q-value
⁴⁶ Ca	$\beta^- \beta^-$	0.004	988.35 keV
⁴⁸ Ca	$\beta^- \beta^-$	0.187	4273.6 keV
⁷⁰ Zn	$\beta^- \beta^-$	0.631	998.46 keV
⁷⁶ Ge	$\beta^- \beta^-$	7.83	2039 keV
⁸⁰ Se	$\beta^- \beta^-$	49.61	132.56 keV
⁸² Se	$\beta^- \beta^-$	8.73	2995.5 keV
⁸⁶ Kr	$\beta^- \beta^-$	17.279	1258.01 keV
⁹⁴ Zr	$\beta^- \beta^-$	17.38	1142.87 keV
⁹⁶ Zr	$\beta^- \beta^-$	2.8	3347.7 keV
⁹⁸ Mo	$\beta^- \beta^-$	24.19	112.75 keV
¹⁰⁰ Mo	$\beta^- \beta^-$	9.67	3034.68 keV
¹⁰⁴ Ru	$\beta^- \beta^-$	18.62	1301.17 keV
¹¹⁰ Pd	$\beta^- \beta^-$	11.72	2003.8 keV
¹¹⁴ Cd	$\beta^- \beta^-$	28.73	539.96 keV
¹¹⁶ Cd	$\beta^- \beta^-$	7.49	2808.7 keV
¹²² Sn	$\beta^- \beta^-$	4.63	368.08 keV
¹²⁴ Sn	$\beta^- \beta^-$	5.79	2287.81 keV
¹²⁸ Te	$\beta^- \beta^-$	31.74	867.95 keV
¹³⁰ Te	$\beta^- \beta^-$	34.08	2530.3 keV
¹³⁴ Xe	$\beta^- \beta^-$	10.4357	825.38 keV
¹³⁶ Xe	$\beta^- \beta^-$	8.8573	2461.8 keV
¹⁴² Ce	$\beta^- \beta^-$	11.114	1416.72 keV
¹⁴⁶ Nd	$\beta^- \beta^-$	17.2	70.83 keV
¹⁴⁸ Nd	$\beta^- \beta^-$	5.7	1928.77 keV
¹⁵⁰ Nd	$\beta^- \beta^-$	5.6	3367.68 keV
¹⁵⁴ Sm	$\beta^- \beta^-$	22.75	1251.62 keV
¹⁶⁰ Gd	$\beta^- \beta^-$	21.86	1729.44 keV
¹⁷⁰ Er	$\beta^- \beta^-$	14.91	654.35 keV
¹⁷⁶ Yb	$\beta^- \beta^-$	12.76	1083.38 keV
¹⁸⁶ W	$\beta^- \beta^-$	28.43	489.94 keV
¹⁹² Os	$\beta^- \beta^-$	40.78	412.36 keV
¹⁹⁸ Pt	$\beta^- \beta^-$	7.163	1046.77 keV
²⁰⁴ Hg	$\beta^- \beta^-$	6.87	419.49 keV
²³² Th	$\beta^- \beta^-$	100	837.57 keV
²³⁸ U	$\beta^- \beta^-$	99.2742	1144.2 keV

¹All nuclides that are listed are expected to decay via $\beta^- \beta^-$ and the only reason of this column is for consistency with Tab. A.6. Nuclides with large atomic masses may decay with additional modes as e.g. ²³⁸U.

Table A.6 Double electron capture nuclides. Columns denote the nuclide, the possible decay modes, the isotopic abundance and the Q-value of the decay. All listed nuclides decay via $\epsilon\epsilon$ - double electron capture and, depending on their Q-value (Sec. 2.3.1), may additionally decay via $\epsilon\beta^+$ - combined electron capture and β^+ decay or $\beta^+\beta^+$ - double β^+ decay. Values are taken from [28] and [106].

Nuclide	Decay mode	Abundance in %	Q-value
³⁶ Ar	$\epsilon\epsilon$	0.3365	433.5 keV
⁴⁰ Ca	$\epsilon\epsilon$	96.94	193.78 keV
⁵⁰ Cr	$\epsilon\epsilon, \epsilon\beta^+$	4.345	1171.4 keV
⁵⁴ Fe	$\epsilon\epsilon$	5.845	679.9 keV
⁵⁸ Ni	$\epsilon\epsilon, \epsilon\beta^+$	68.0769	1925.8 keV
⁶⁴ Zn	$\epsilon\epsilon, \epsilon\beta^+$	48.63	1096.4 keV
⁷⁴ Se	$\epsilon\epsilon, \epsilon\beta^+$	0.89	1209.4 keV
⁷⁸ Kr	$\epsilon\epsilon, \epsilon\beta^+, \beta^+\beta^+$	0.35	2866 keV
⁸⁴ Sr	$\epsilon\epsilon, \epsilon\beta^+$	0.56	1786.8 keV
⁹² Mo	$\epsilon\epsilon, \epsilon\beta^+$	14.84	1649.1 keV
⁹⁶ Ru	$\epsilon\epsilon, \epsilon\beta^+, \beta^+\beta^+$	5.54	2719 keV
¹⁰² Pd	$\epsilon\epsilon, \epsilon\beta^+$	1.02	1172.0 keV
¹⁰⁶ Cd	$\epsilon\epsilon, \epsilon\beta^+, \beta^+\beta^+$	1.25	2771 keV
¹⁰⁸ Cd	$\epsilon\epsilon$	0.89	269 keV
¹¹² Sn	$\epsilon\epsilon, \epsilon\beta^+$	0.97	1922 keV
¹²⁰ Te	$\epsilon\epsilon, \epsilon\beta^+$	0.09	1698 keV
¹²⁴ Xe	$\epsilon\epsilon, \epsilon\beta^+, \beta^+\beta^+$	0.09	2865.6 keV
¹²⁶ Xe	$\epsilon\epsilon$	0.09	897 keV
¹³⁰ Ba	$\epsilon\epsilon, \epsilon\beta^+, \beta^+\beta^+$	0.106	2611 keV
¹³² Ba	$\epsilon\epsilon$	0.101	839.9 keV
¹³⁶ Ce	$\epsilon\epsilon, \epsilon\beta^+, \beta^+\beta^+$	0.185	2400 keV
¹³⁸ Ce	$\epsilon\epsilon$	0.251	693 keV
¹⁴⁴ Sm	$\epsilon\epsilon, \epsilon\beta^+$	3.07	1781.1 keV
¹⁵² Gd	$\epsilon\epsilon$	0.20	55.6 keV
¹⁵⁶ Dy	$\epsilon\epsilon, \epsilon\beta^+$	0.06	2011 keV
¹⁵⁸ Dy	$\epsilon\epsilon$	0.10	283.3 keV
¹⁶² Er	$\epsilon\epsilon, \epsilon\beta^+$	0.14	1844.5 keV
¹⁶⁴ Er	$\epsilon\epsilon$	1.61	24.1 keV
¹⁶⁸ Yb	$\epsilon\epsilon, \epsilon\beta^+$	0.13	1422.1 keV
¹⁷⁴ Hf	$\epsilon\epsilon, \epsilon\beta^+$	0.16	1101.1 keV
¹⁸⁰ W	$\epsilon\epsilon$	0.12	146 keV
¹⁸⁴ Os	$\epsilon\epsilon, \epsilon\beta^+$	0.02	1451.5 keV
¹⁹⁰ Pt	$\epsilon\epsilon, \epsilon\beta^+$	0.014	1383 keV
¹⁹⁶ Hg	$\epsilon\epsilon$	0.15	819.7 keV

Appendix B

Example MaGe Macro

Define manager:

```
Choose seed for random generator  
/MG/manager/heprandomseed 1294414100  
Choose verbosity  
/MG/manager/mglog trace
```

Define geometry:

```
/MG/geometry/detector GerdaArray  
/MG/geometry/database false  
Choose geometry definition of detectors  
/MG/geometry/detector/geometryfile geometry.dat  
Choose geometry of array e.g. Phase I  
/MG/geometry/detector/matrixfile matrix_phase.i.dat
```

Define processes:

```
#/MG/processes/optical true  
#/MG/processes/lowenergy true  
/MG/processes/realm BBdecay
```

Define eventactions:

```
Choose verbosity  
/MG/eventaction/reportingfrequency 10000  
Choose output scheme and file name  
/MG/eventaction/rootschema GerdaArray  
/MG/eventaction/rootfilename MR.Co60.Crystal.geometry1_12.p1.10e6_00.root
```

Initialisation:

```
/run/initialize
```

Define generator:

```
/MG/generator/select decay0  
Choose sampling method and sampling volume  
/MG/generator/confine volume  
/MG/generator/volume Crystal.geometry1.12  
Choose input file for DECAY0  
/MG/generator/decay0/filename D0.Co60.1e6  
/grdm/fBeta true
```

Define run:

```
/tracking/verbose 0  
Choose number of decays to be processed  
/run/beamOn 1000000
```


Appendix C

GERDA Coincidence Analysis

Table C.1 Exposure history of GERDA Phase I detectors since 2006 with data taken from [76]. Detailed exposure times are grouped if in close proximity. Time to start denotes the elapsed time till the fictional Phase I start at 01/07/10.

Detector	Date [dd/mm/yy]	Exposure time [d]	Time to start [d]
ANG1	26/08/06	98.8	1405
	27/10/08	50	612
ANG2	30/11/06	25.2	1309
	24/01/07	7.7	1254
	20/04/07	28.9	1168
	11/07/08	44.7	720
ANG3	30/11/06	25.2	1309
	25/01/07	7.7	1253
	20/04/07	28.9	1168
	11/07/08	37.2	720
	27/10/08	50	612
ANG4	23/11/06	23.3	1316
	25/01/07	15.4	1253
	19/04/07	21.2	1169
	25/06/08	15.1	736
	06/08/08	22.5	694
ANG5	30/11/06	25.2	1309
	25/01/07	7.7	1253
	20/04/07	28.9	1168
	19/06/08	15	742
	06/08/08	22.5	694
RG1	23/11/06	23.3	1316
	24/01/07	15.4	1254
	11/07/08	44.7	720
RG2	23/11/06	23.3	1316
	24/01/07	15.4	1254
	25/06/08	25.8	736
	06/08/08	22.5	694
RG3	21/11/06	66.2	1318
	27/10/08	57.9	612
GTF32	20/12/06	39.9	1289
	19/04/07	12.6	1169
	11/07/08	29.5	720
GTF42	23/01/07	48	1255
	11/04/07	5.8	1177
	22/10/07	32.3	983
GTF44	23/11/06	23.3	1316
	18/04/07	16.5	1170
	22/10/07	32.3	983
GTF45	23/01/07	42.6	1255
	25/06/08	27.6	736
	06/08/08	22.5	694
GTF110	23/11/06	23.3	1316
Continued on next page...			

Table C.1 ...continued from previous page

Detector	Date [dd/mm/yy]	Exposure time [d]	Time to start [d]
	13/02/07	11.7	1234
	19/04/07	20.1	1169
	06/08/08	22.5	694
GTF112	24/01/07	42.7	1254
	19/04/07	12.6	1169
	11/07/08	29.5	720

Table C.2 Normalization between detectors in the GERDA Phase I background model for each background nuclide. The detector with 1.000 has the highest background activity and all other detectors are scaled according to their activity. Out of 10^6 simulated events per detector and nuclide, SimEv/Det, only the respective fraction according to the normalization was selected. This results in an individual total amount of simulated events for each background nuclide, TotSimEv. See Sec. 5.2 for more details.

Det	^{68}Ga	^{60}Co	^{65}Zn	^{58}Co	^{57}Co	^{54}Mn	$^{76}\text{Ge}(\text{GS})$	$^{76}\text{Ge}(\text{Sig})$
GTF42	0.416	0.819	0.484	0.036	0.527	0.396	0.078	0.078
GTF112	0.868	0.666	0.900	0.461	0.920	0.647	0.094	0.094
GTF32	0.659	0.734	0.680	0.360	0.694	0.488	0.074	0.074
GTF44	0.371	0.686	0.427	0.035	0.462	0.345	0.078	0.078
GTF110	0.775	0.620	0.803	0.466	0.823	0.580	0.097	0.097
GTF45	1.000	0.592	1.000	0.641	1.000	0.684	0.074	0.074
ANG1	0.085	0.368	0.175	0.318	0.132	0.283	0.336	0.336
ANG4	0.127	0.616	0.276	0.231	0.213	0.470	0.836	0.836
RG3	0.208	0.999	0.423	0.802	0.313	0.660	0.745	0.745
RG1	0.115	0.679	0.246	0.218	0.188	0.407	0.753	0.753
RG2	0.128	0.515	0.273	0.256	0.207	0.448	0.773	0.773
ANG5	0.148	0.727	0.324	0.263	0.250	0.552	0.960	0.960
ANG2	0.172	0.810	0.374	0.295	0.288	0.634	1.000	1.000
ANG3	0.311	1.000	0.638	1.000	0.474	1.000	0.861	0.861
Sum	6.037	9.824	7.676	5.137	6.943	7.534	6.759	6.759
SimEv/Det	10^6	10^6	10^6	10^6	10^6	10^6	10^6	10^6
TotSimEv	5383524	9830642	7024283	5382423	6492482	7594982	6758674	6758674

Table C.3 Scaling of simulated decays, TotSimEv, (see Tab. C.2) to expected decays from the GERDA Phase I background model, TotExpEv. See Sec. 5.2 for more details.

	^{68}Ga	^{60}Co	^{65}Zn	^{58}Co	^{57}Co	^{54}Mn	$^{76}\text{Ge}(\text{GS})$	$^{76}\text{Ge}(\text{Sig})$
TotExpEv	$1.72 \cdot 10^2$	$6.26 \cdot 10^1$	$2.63 \cdot 10^2$	$5.12 \cdot 10^1$	$3.62 \cdot 10^1$	$5.53 \cdot 10^1$	$5.85 \cdot 10^4$	$9.07 \cdot 10^2$
TotSimEv	$5.38 \cdot 10^6$	$9.83 \cdot 10^6$	$7.02 \cdot 10^6$	$5.38 \cdot 10^6$	$6.49 \cdot 10^6$	$7.59 \cdot 10^6$	$6.76 \cdot 10^6$	$6.76 \cdot 10^6$
Scaling	$3.19 \cdot 10^{-5}$	$6.37 \cdot 10^{-6}$	$3.74 \cdot 10^{-5}$	$9.51 \cdot 10^{-8}$	$5.58 \cdot 10^{-6}$	$7.27 \cdot 10^{-6}$	$8.66 \cdot 10^{-3}$	$1.34 \cdot 10^{-4}$

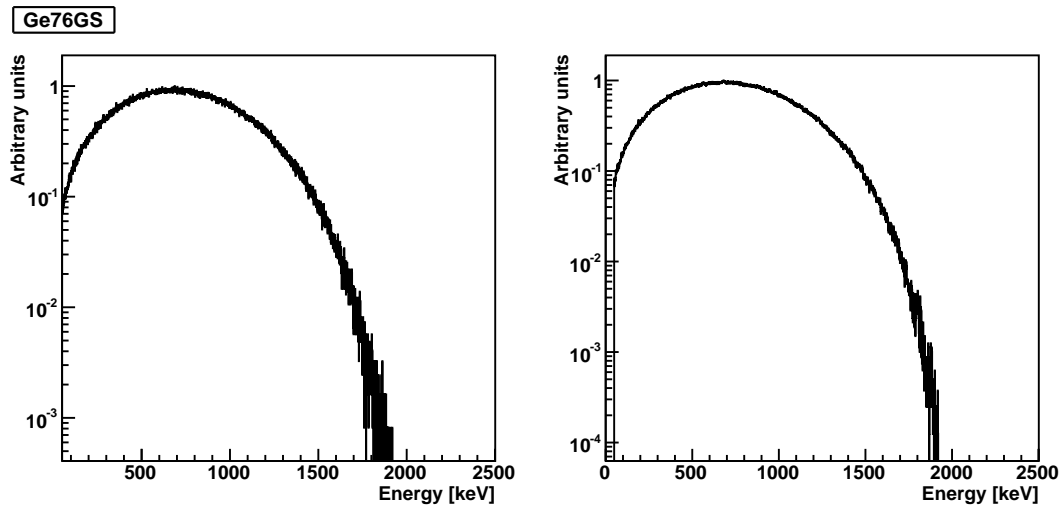


Figure C.1 Spectral shape of the ^{76}Ge $2\nu\beta\beta$ decay into the ground state as seen in ANG2 without any coincidence cuts (left) and in the whole GERDA Phase I setup, i.e. sum of all detector energies (right). The spectra are shown in arbitrary units normalized to their maximum bin entry.

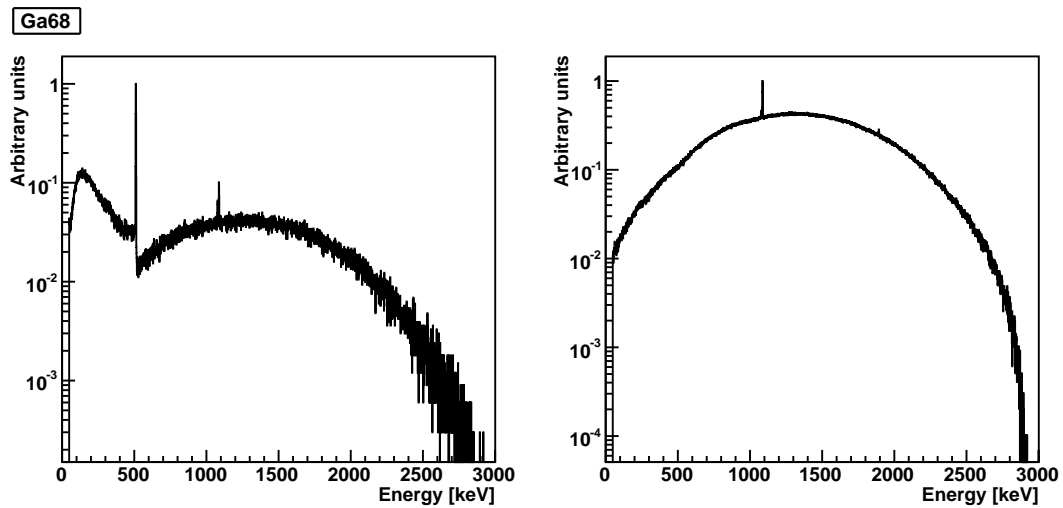


Figure C.2 Spectral shape of ^{68}Ga decays inside the detectors as seen in ANG2 without any coincidence cuts (left) and in the whole GERDA Phase I setup, i.e. sum of all detector energies (right). The spectra are shown in arbitrary units normalized to their maximum bin entry.

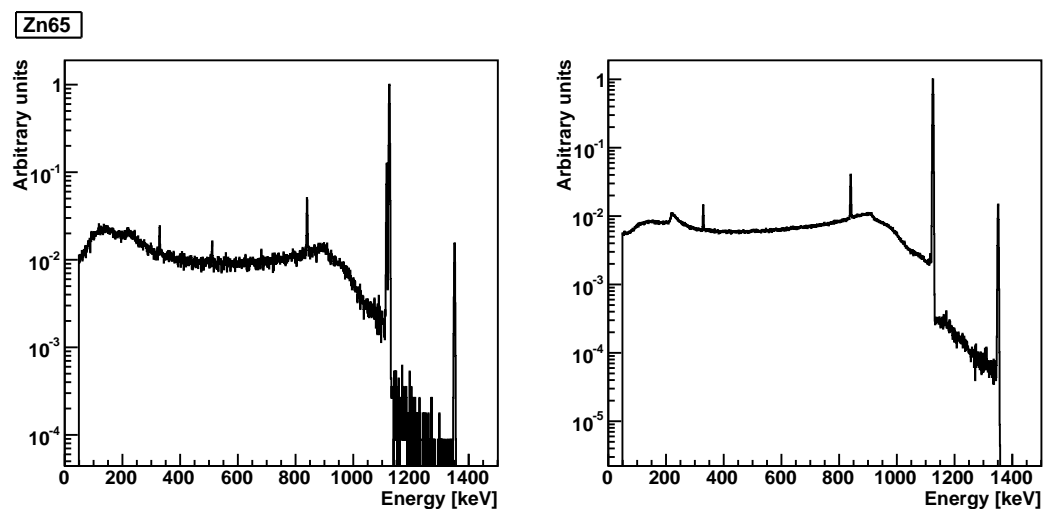


Figure C.3 Spectral shape of ^{65}Zn decays inside the detectors as seen in ANG2 without any coincidence cuts (left) and in the whole GERDA Phase I setup, i.e. sum of all detector energies (right). The spectra are shown in arbitrary units normalized to their maximum bin entry.

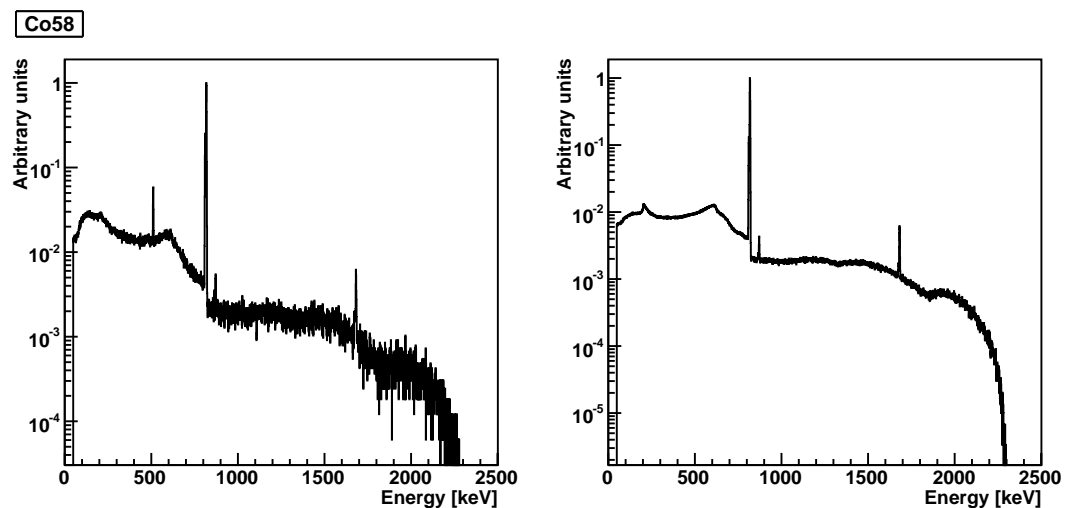


Figure C.4 Spectral shape of ^{58}Co decays inside the detectors as seen in ANG2 without any coincidence cuts (left) and in the whole GERDA Phase I setup, i.e. sum of all detector energies (right). The spectra are shown in arbitrary units normalized to their maximum bin entry.

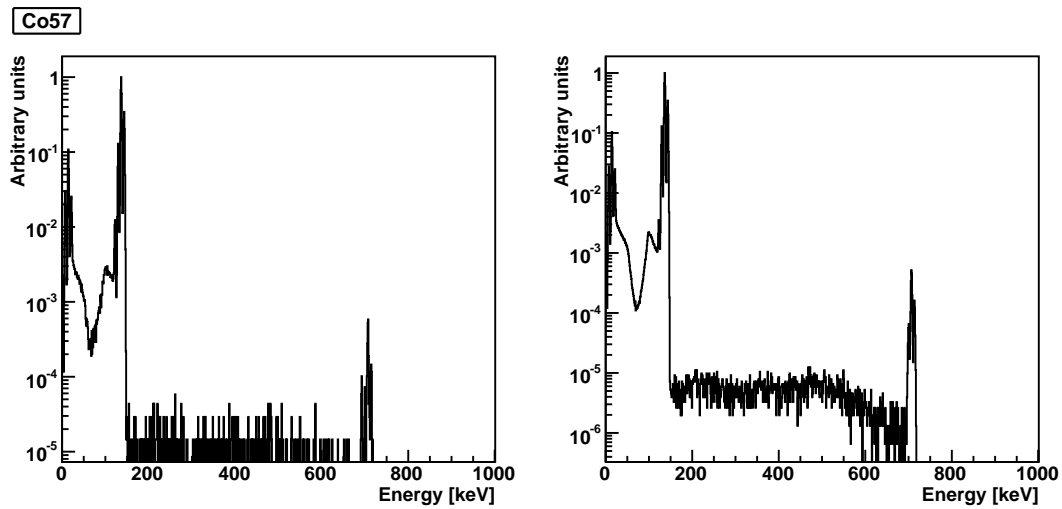


Figure C.5 Spectral shape of ^{57}Co decays inside the detectors as seen in ANG2 without any coincidence cuts (left) and in the whole GERDA Phase I setup, i.e. sum of all detector energies (right). The spectra are shown in arbitrary units normalized to their maximum bin entry.

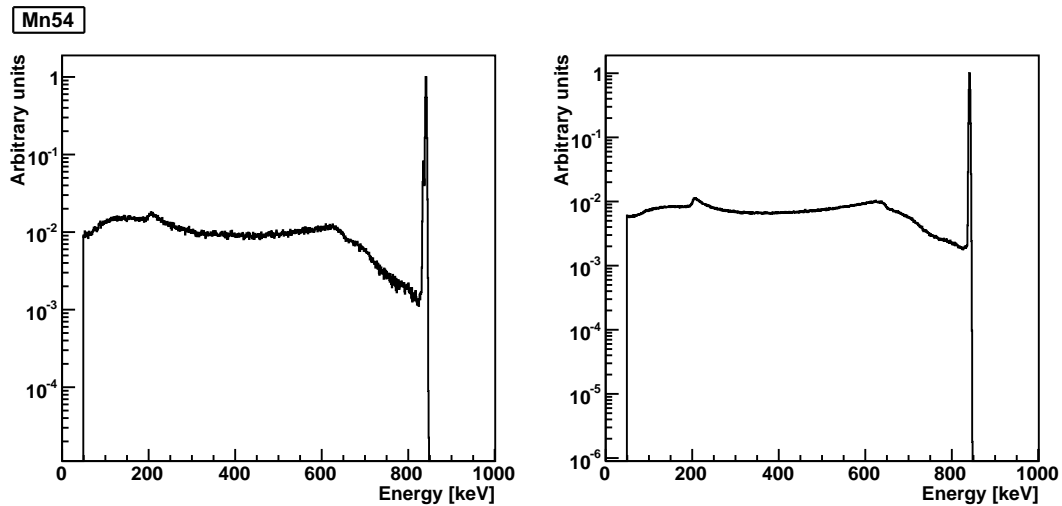


Figure C.6 Spectral shape of ^{54}Mn decays inside the detectors as seen in ANG2 without any coincidence cuts (left) and in the whole GERDA Phase I setup, i.e. sum of all detector energies (right). The spectra are shown in arbitrary units normalized to their maximum bin entry.

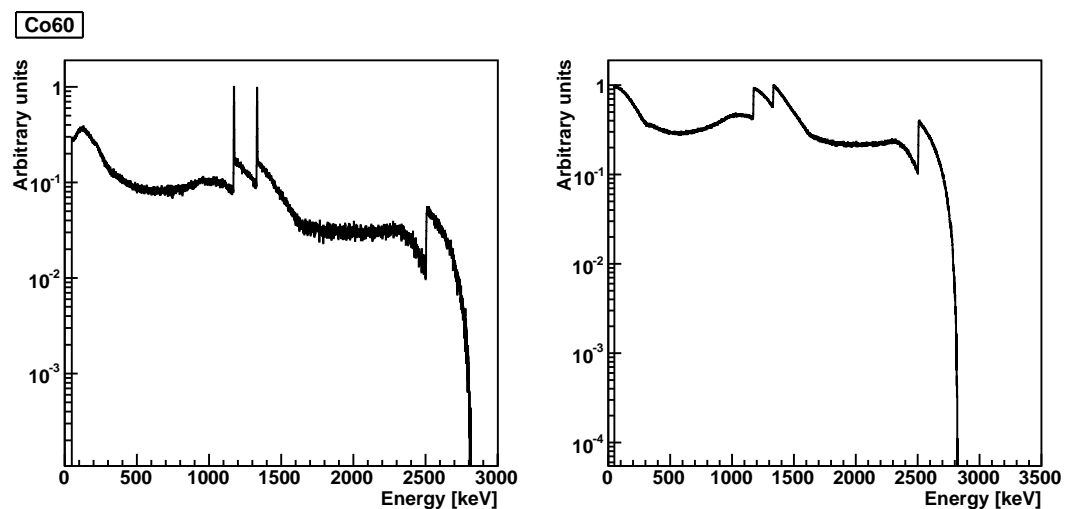


Figure C.7 Spectral shape of ^{60}Co decays inside the detectors as seen in ANG2 without any coincidence cuts (left) and in the whole GERDA Phase I setup, i.e. sum of all detector energies (right). The spectra are shown in arbitrary units normalized to their maximum bin entry.

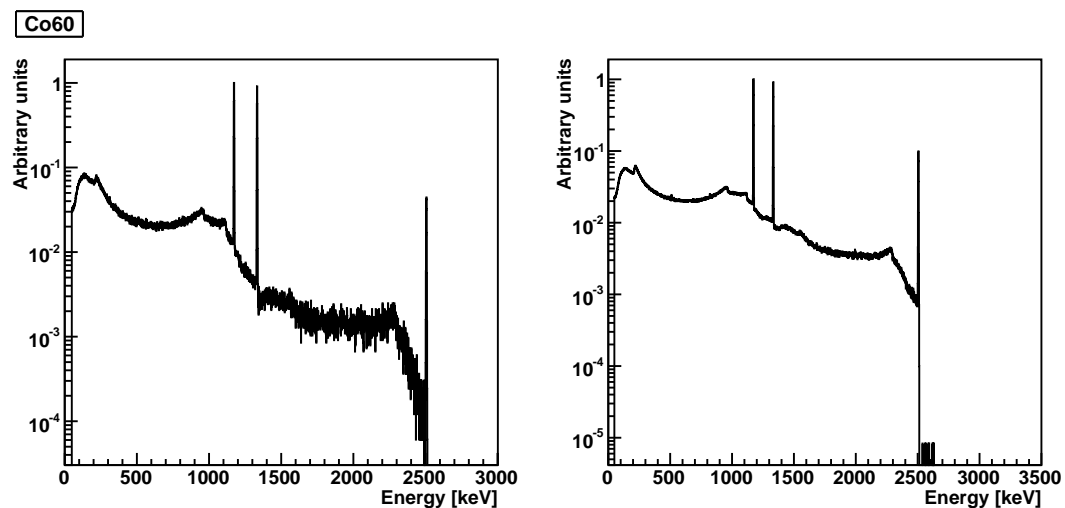


Figure C.8 Spectral shape of ^{60}Co decays inside the holders as seen in ANG2 without any coincidence cuts (left) and in the whole GERDA Phase I setup, i.e. sum of all detector energies (right). The spectra are shown in arbitrary units normalized to their maximum bin entry.

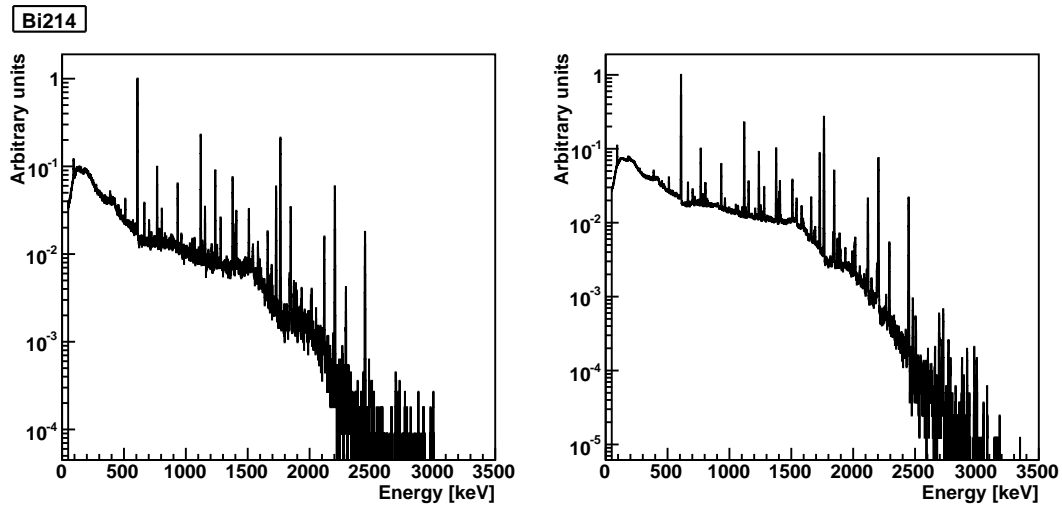


Figure C.9 Spectral shape of ^{214}Bi decays inside the holders as seen in ANG2 without any coincidence cuts (left) and in the whole GERDA Phase I setup, i.e. sum of all detector energies (right). The spectra are shown in arbitrary units normalized to their maximum bin entry.

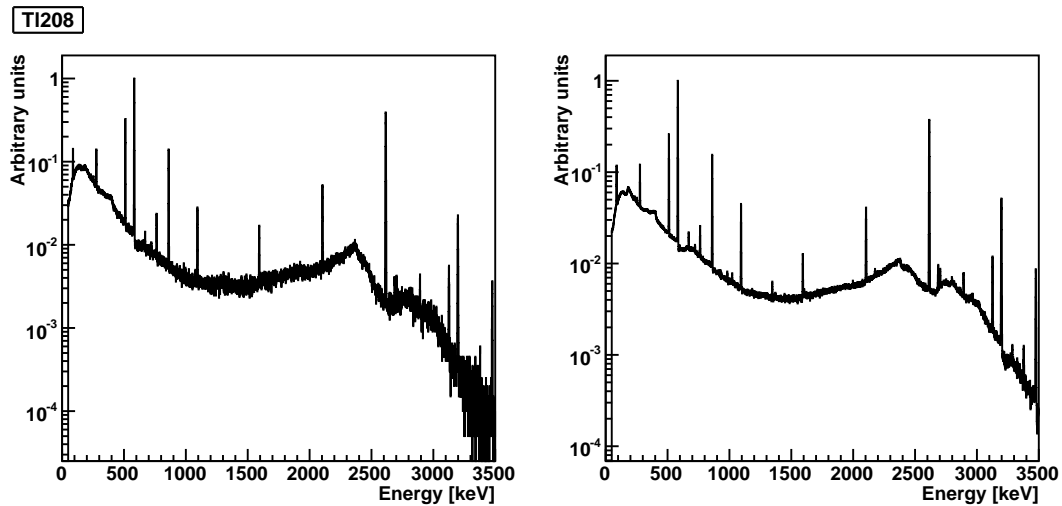


Figure C.10 Spectral shape of ^{208}Tl decays inside the holders as seen in ANG2 without any coincidence cuts (left) and in the whole GERDA Phase I setup, i.e. sum of all detector energies (right). The spectra are shown in arbitrary units normalized to their maximum bin entry.

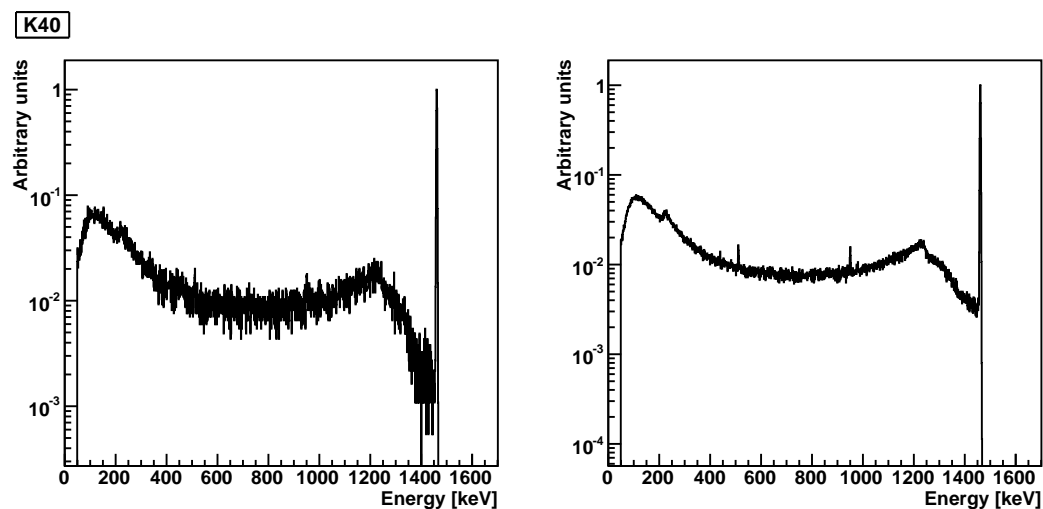


Figure C.11 Spectral shape of ^{40}K decays inside the holders as seen in ANG2 without any coincidence cuts (left) and in the whole GERDA Phase I setup, i.e. sum of all detector energies (right). The spectra are shown in arbitrary units normalized to their maximum bin entry.

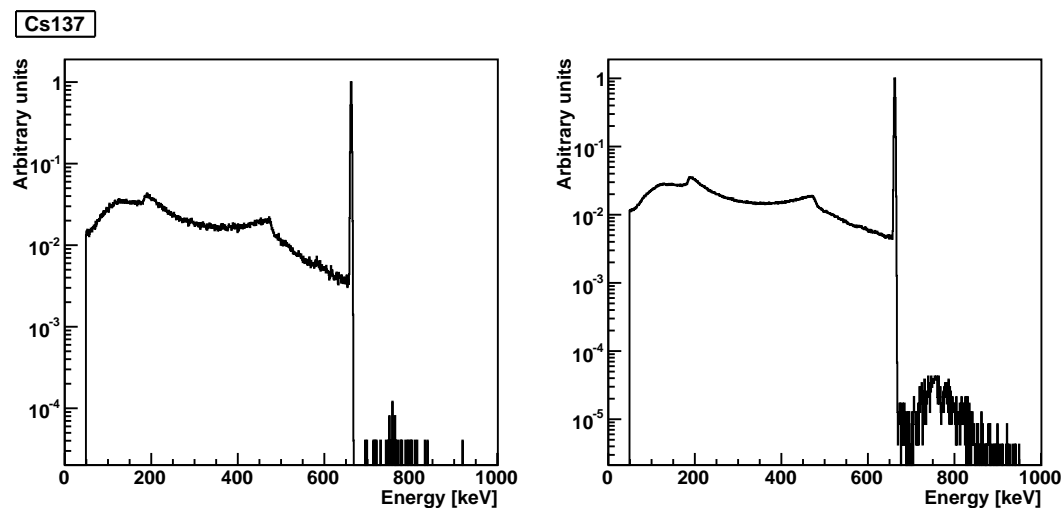


Figure C.12 Spectral shape of ^{137}Cs decays inside the holders as seen in ANG2 without any coincidence cuts (left) and in the whole GERDA Phase I setup, i.e. sum of all detector energies (right). The spectra are shown in arbitrary units normalized to their maximum bin entry.

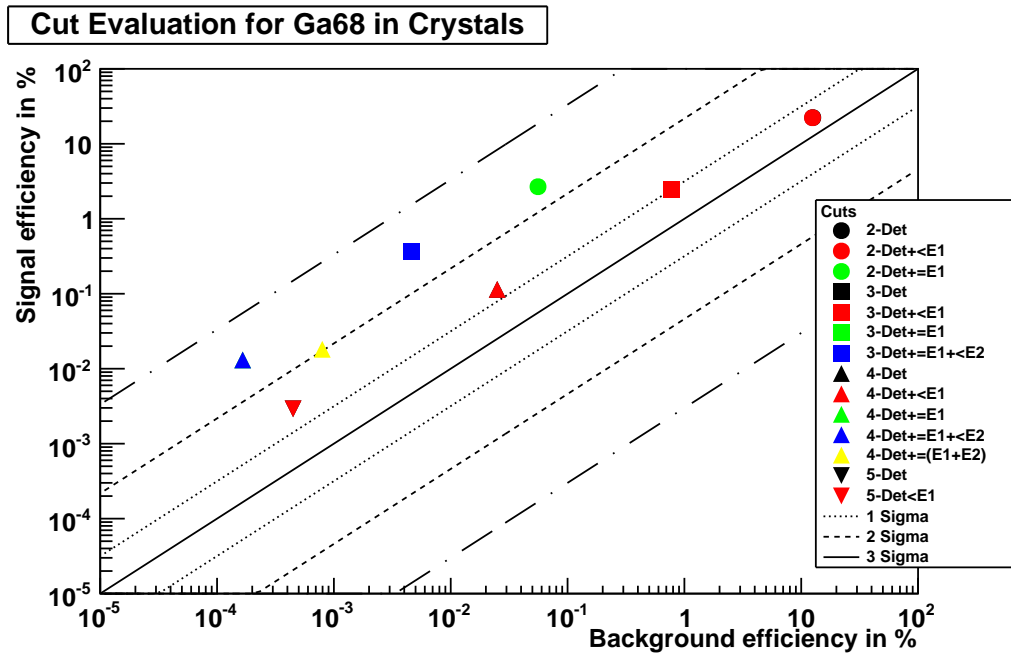


Figure C.13 Cut evaluation for the signal decay of ^{76}Ge into the first excited 0^+ state compared to the background decay of ^{68}Ga inside the detectors. See description in Sec. 5.4.2 for more information on the cuts.

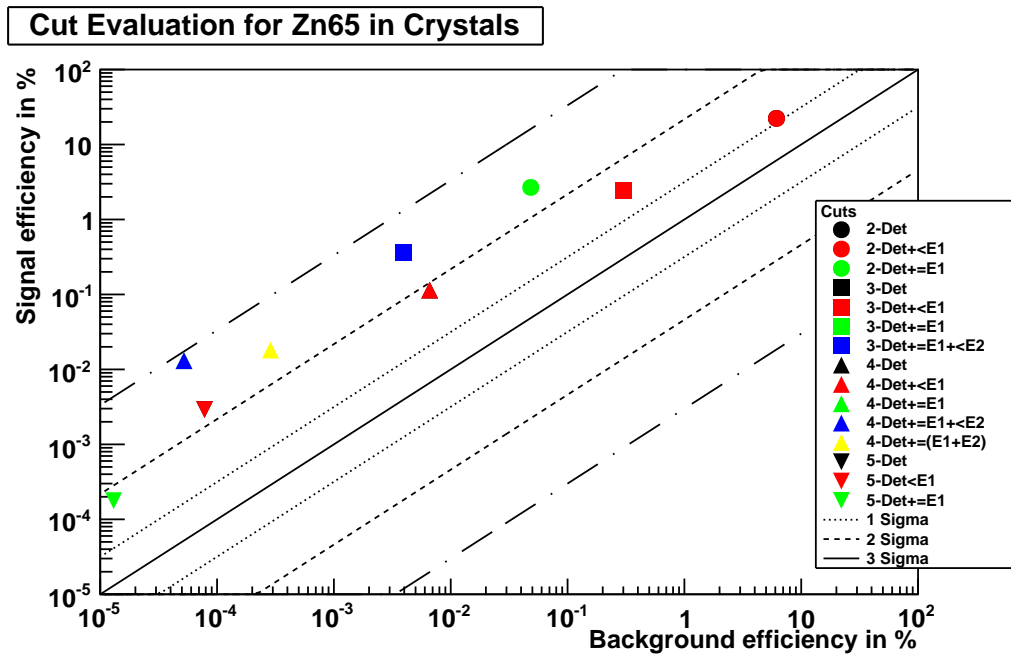


Figure C.14 Cut evaluation for the signal decay of ^{76}Ge into the first excited 0^+ state compared to the background decay of ^{65}Zn inside the detectors. See description in Sec. 5.4.2 for more information on the cuts.

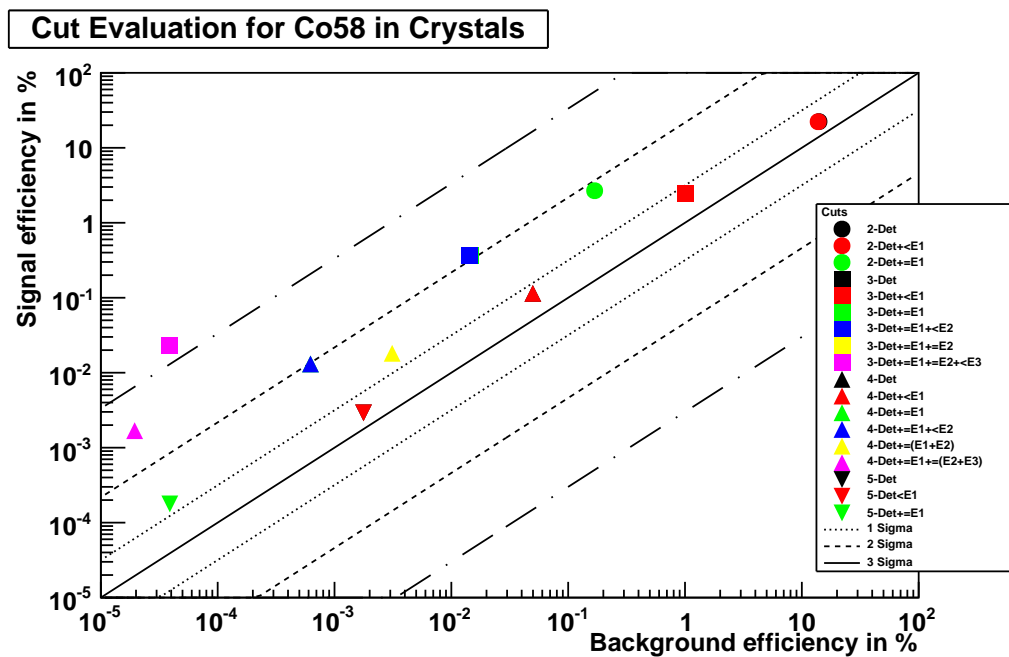


Figure C.15 Cut evaluation for the signal decay of ^{76}Ge into the first excited 0^+ state compared to the background decay of ^{58}Co inside the detectors. See description in Sec. 5.4.2 for more information on the cuts.

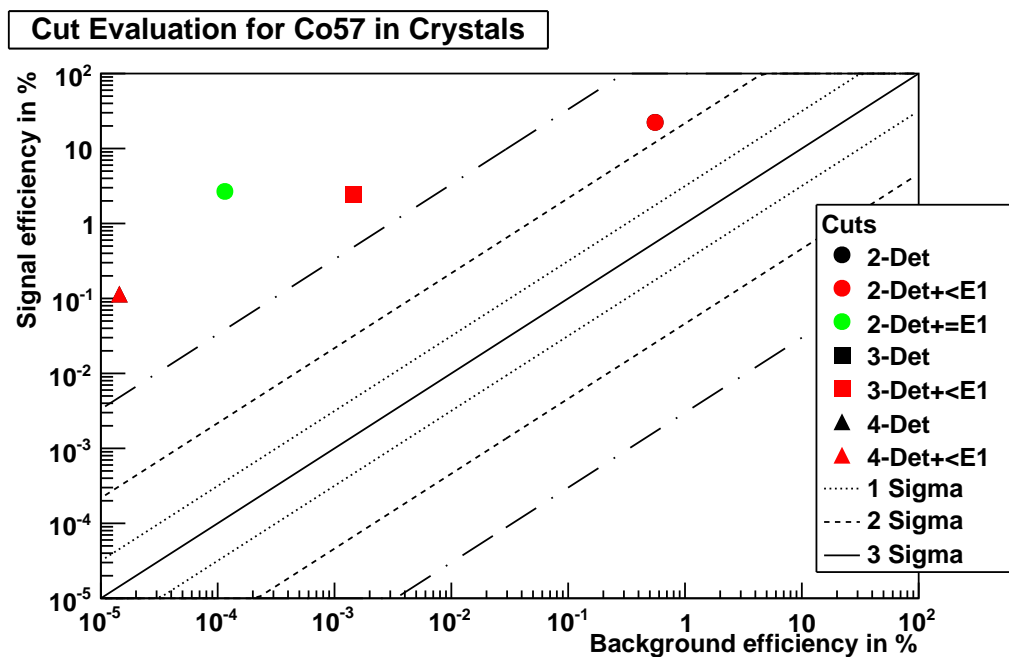


Figure C.16 Cut evaluation for the signal decay of ^{76}Ge into the first excited 0^+ state compared to the background decay of ^{57}Co inside the detectors. See description in Sec. 5.4.2 for more information on the cuts.

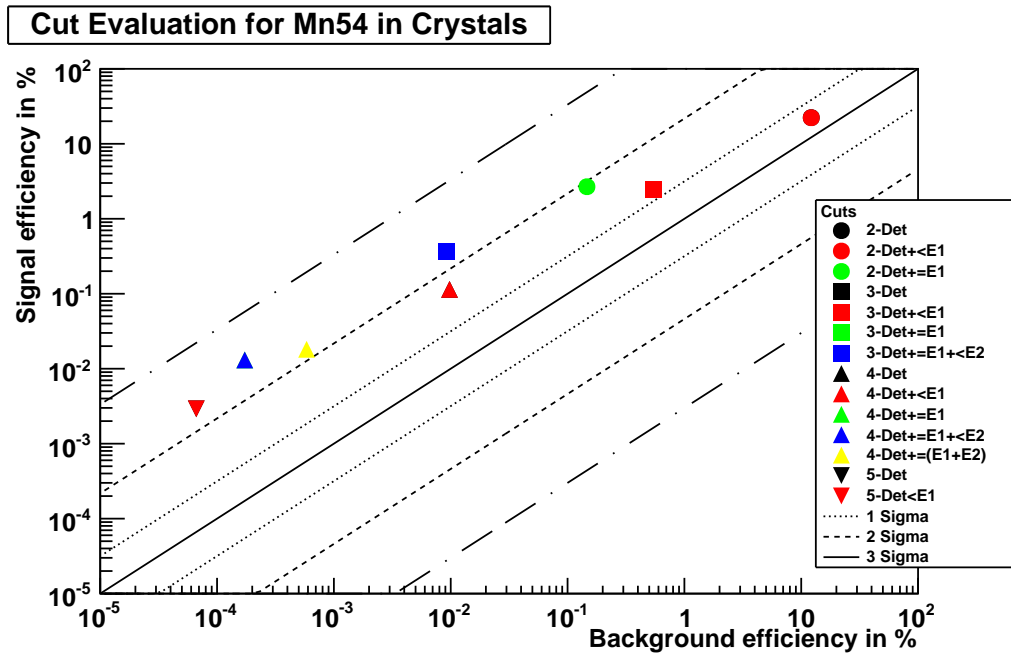


Figure C.17 Cut evaluation for the signal decay of ^{76}Ge into the first excited 0^+ state compared to the background decay of ^{54}Mn inside the detectors. See description in Sec. 5.4.2 for more information on the cuts.

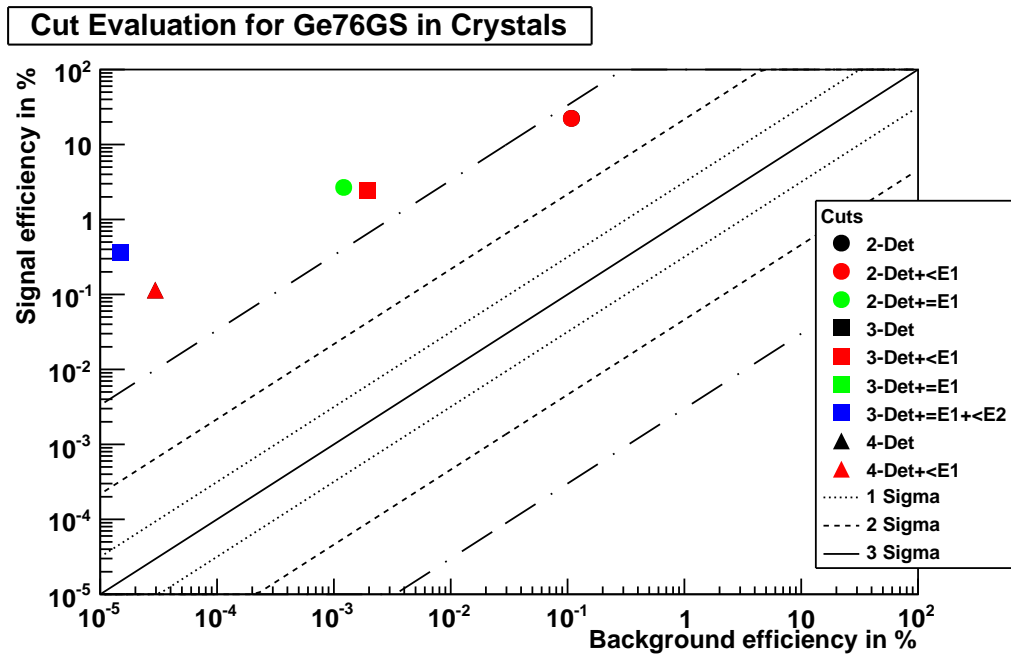


Figure C.18 Cut evaluation for the signal decay of ^{76}Ge into the first excited 0^+ state compared to the background decay of ^{76}Ge into the ground state inside the detectors. See description in Sec. 5.4.2 for more information on the cuts.

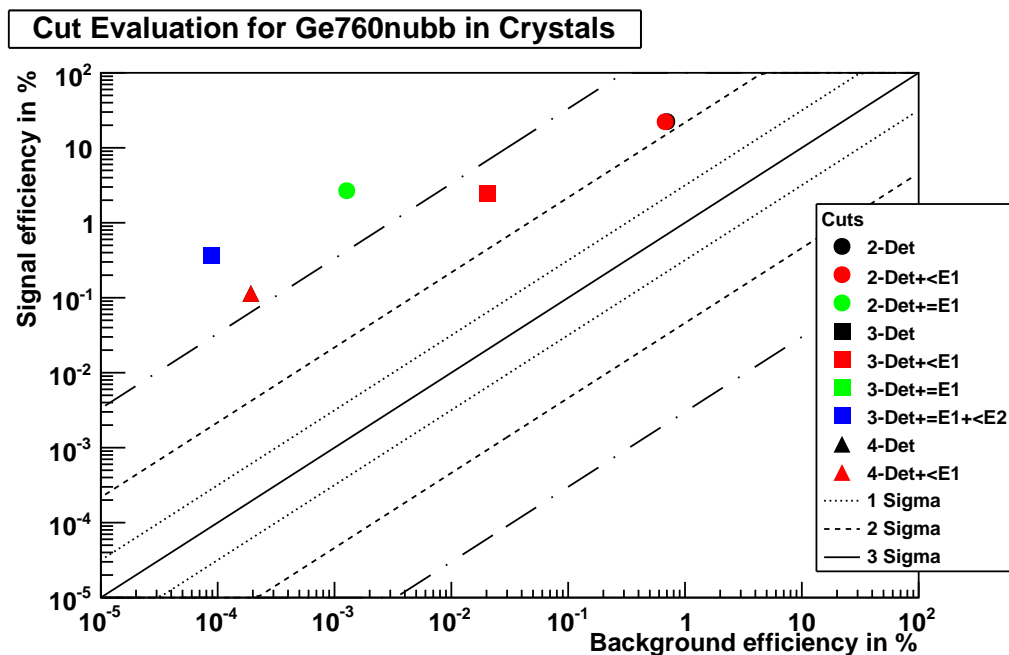


Figure C.19 Cut evaluation for the signal decay of ^{76}Ge into the first excited 0^+ state compared to the $0\nu\beta\beta$ decay of ^{76}Ge into the ground state inside the detectors. See description in Sec. 5.4.2 for more information on the cuts.

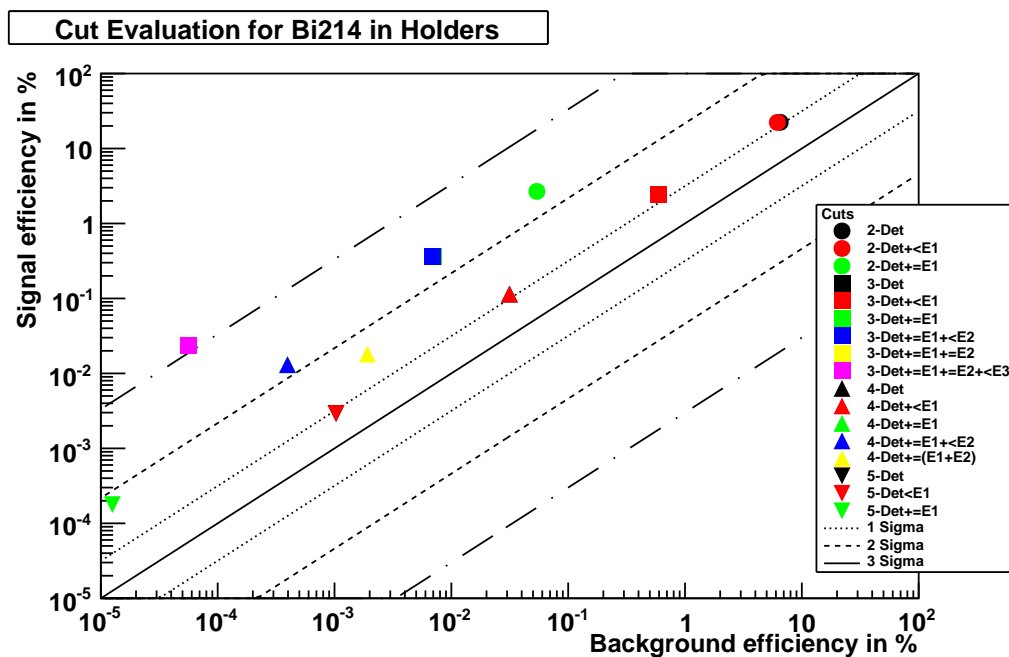


Figure C.20 Cut evaluation for the signal decay of ^{76}Ge into the first excited 0^+ state compared to the background decay of ^{214}Bi inside the holders. See description in Sec. 5.4.2 for more information on the cuts.

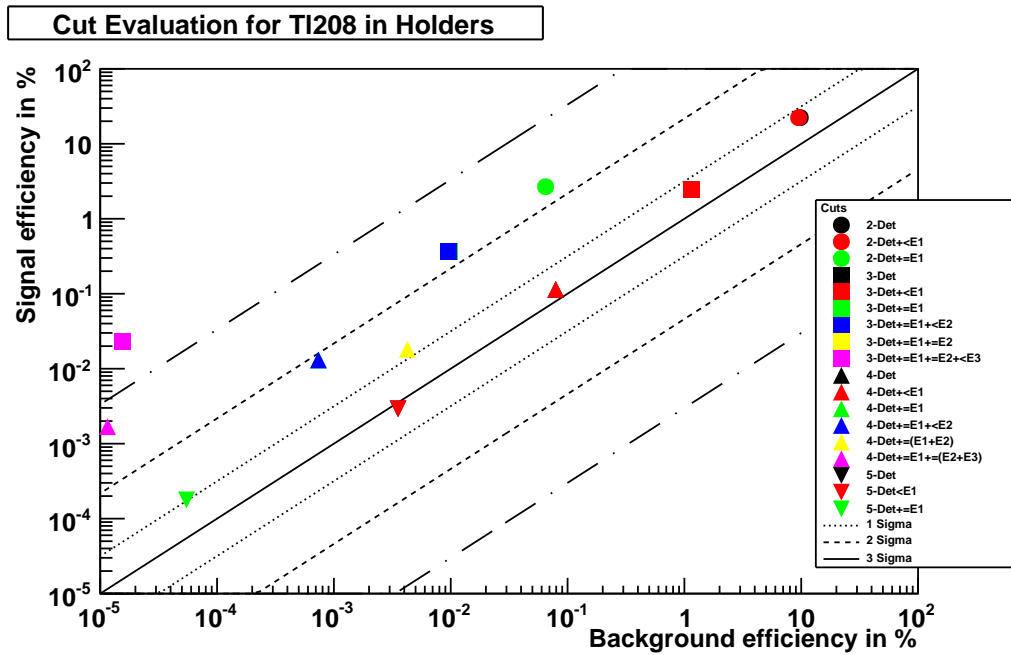


Figure C.21 Cut evaluation for the signal decay of ^{76}Ge into the first excited 0^+ state compared to the background decay of ^{208}Tl inside the holders. See description in Sec. 5.4.2 for more information on the cuts.

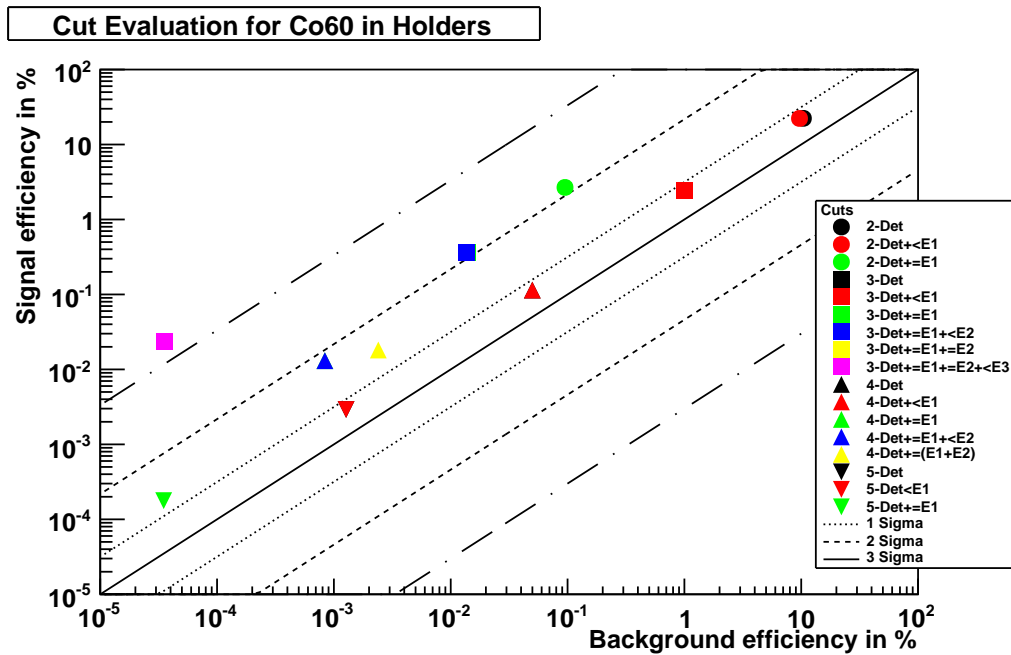


Figure C.22 Cut evaluation for the signal decay of ^{76}Ge into the first excited 0^+ state compared to the background decay of ^{60}Co inside the holders. See description in Sec. 5.4.2 for more information on the cuts.

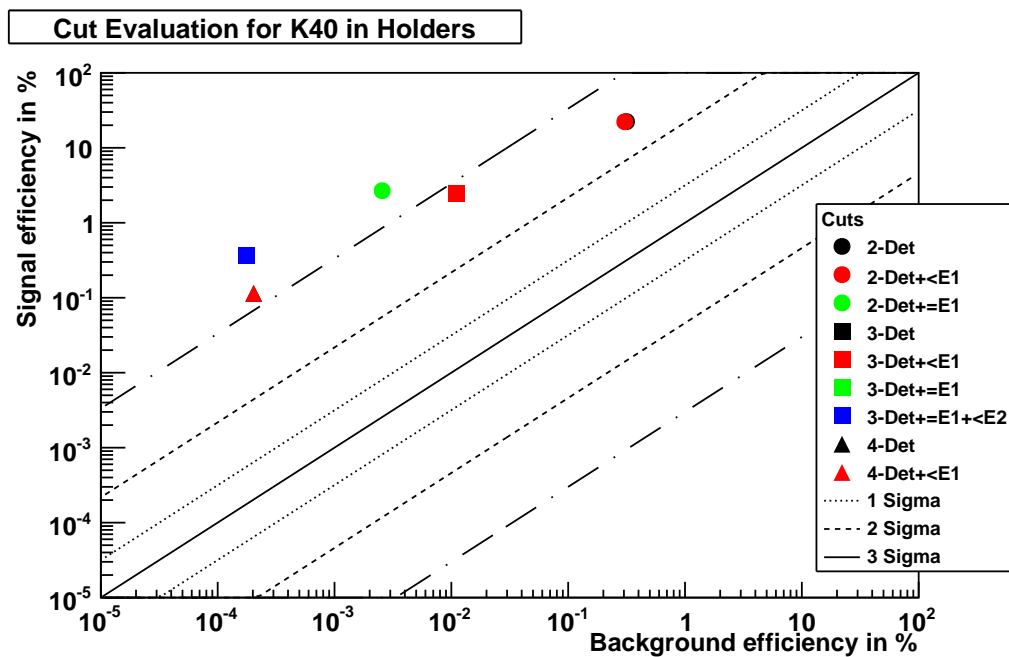


Figure C.23 Cut evaluation for the signal decay of ^{76}Ge into the first excited 0^+ state compared to the background decay of ^{40}K inside the holders. See description in Sec. 5.4.2 for more information on the cuts.

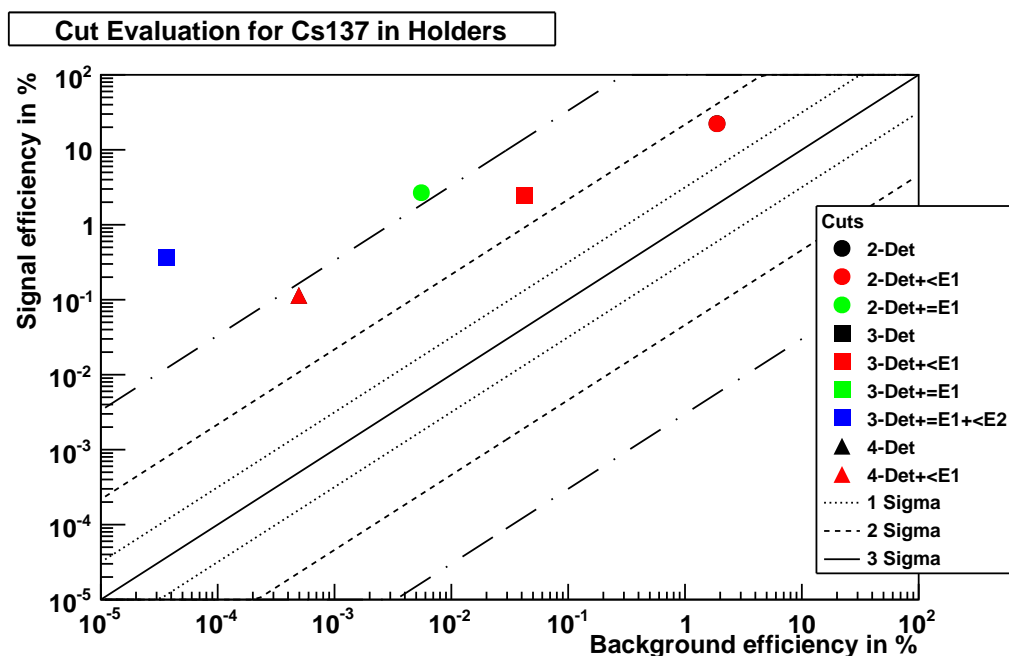


Figure C.24 Cut evaluation for the signal decay of ^{76}Ge into the first excited 0^+ state compared to the background decay of ^{137}Cs inside the holders. See description in Sec. 5.4.2 for more information on the cuts.

Appendix D

Excited States in Palladium

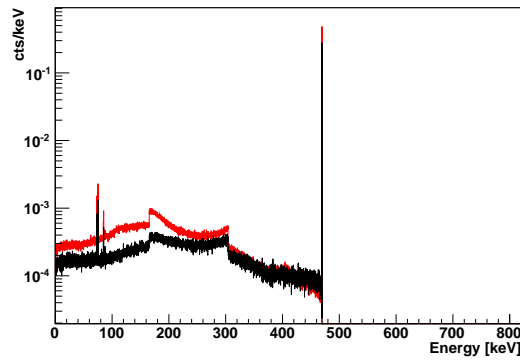


Figure D.1 Energy spectrum of a simulated source of 468.59 keV photons homogeneously distributed in a D6 standard form consisting of $\rho = 10.22 \text{ g/cm}^3$ palladium (black) and SiO_2 (red).

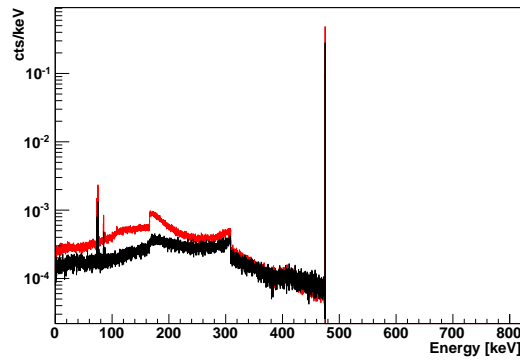


Figure D.2 Energy spectrum of a simulated source of 475.07 keV photons homogeneously distributed in a D6 standard form consisting of $\rho = 10.22 \text{ g/cm}^3$ palladium (black) and SiO_2 (red).

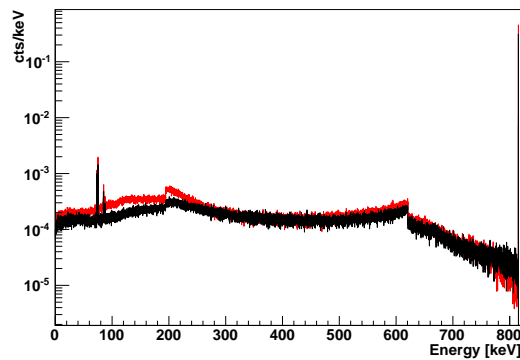


Figure D.3 Energy spectrum of a simulated source of 815.35 keV photons homogeneously distributed in a D6 standard form consisting of $\rho = 10.22 \text{ g/cm}^3$ palladium (black) and SiO_2 (red).

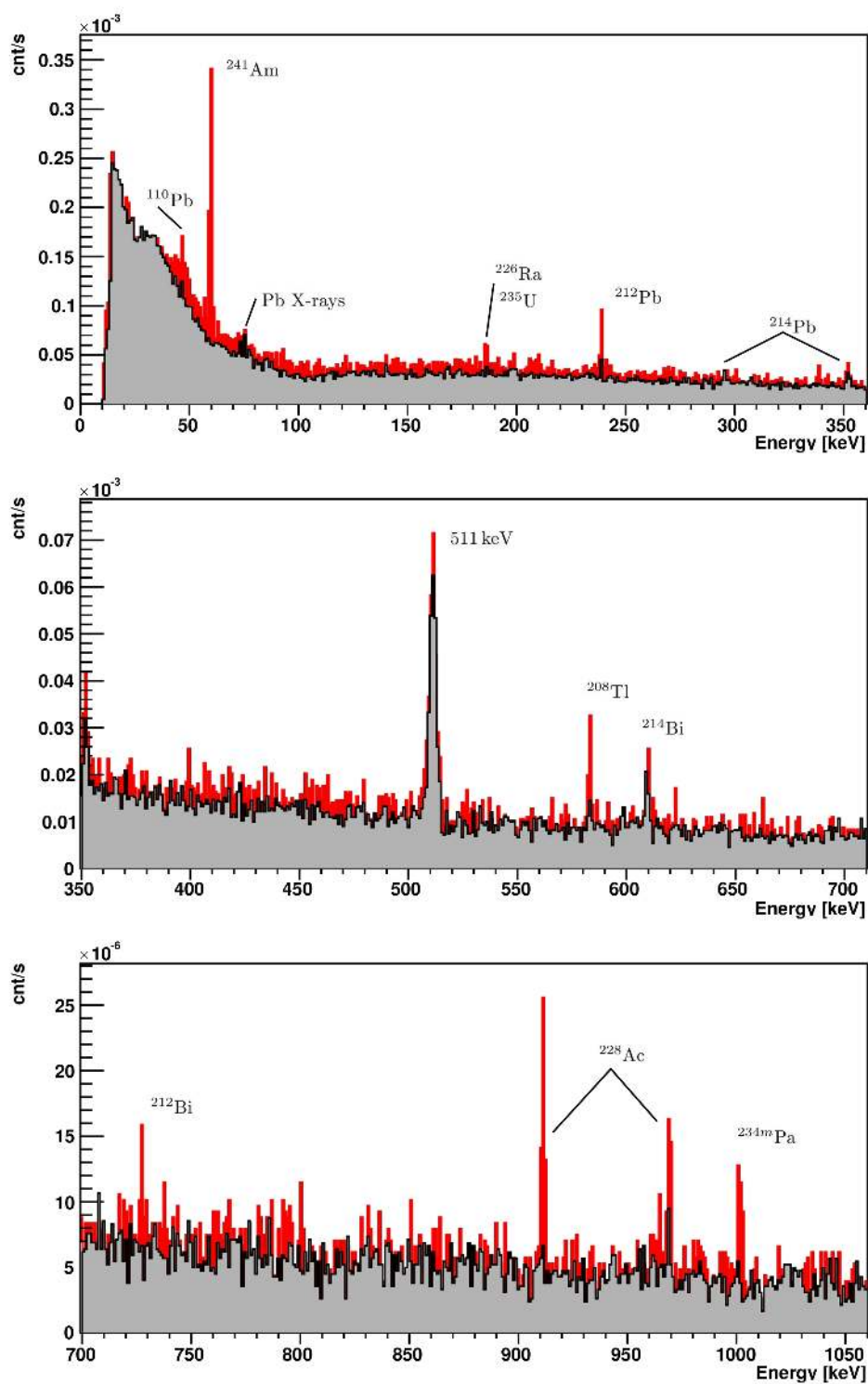


Figure D.4 Pre and post cleaning palladium spectra from 0 to 1600 keV; red - original Pd (measurement 1), grey - cleaned Pd (measurement 3), see Section 7.2.

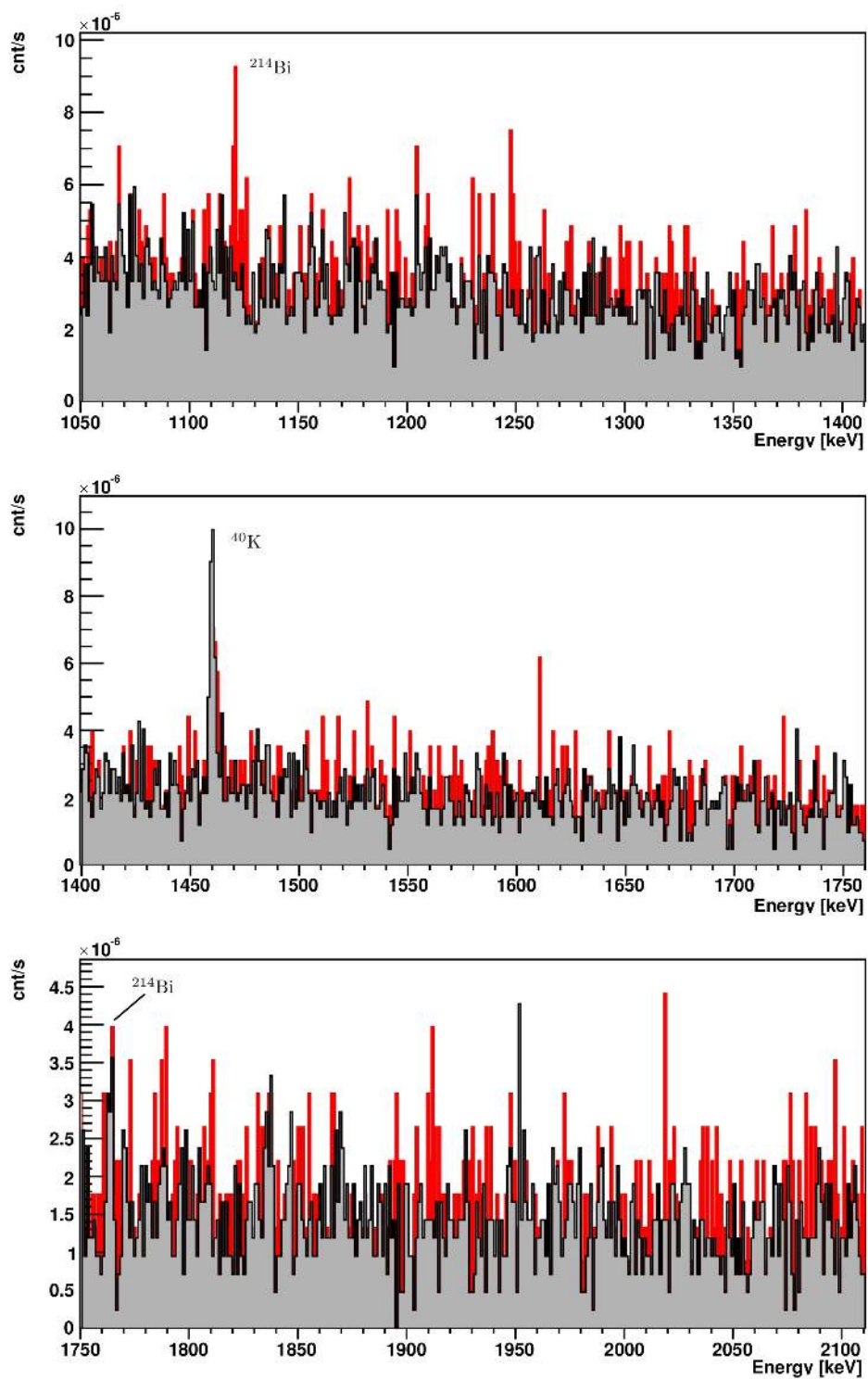


Figure D.5 Pre and post cleaning palladium spectra from 1050 keV to 2010 keV; red - original Pd (measurement 1), grey - cleaned Pd (measurement 3), see Section 7.2.

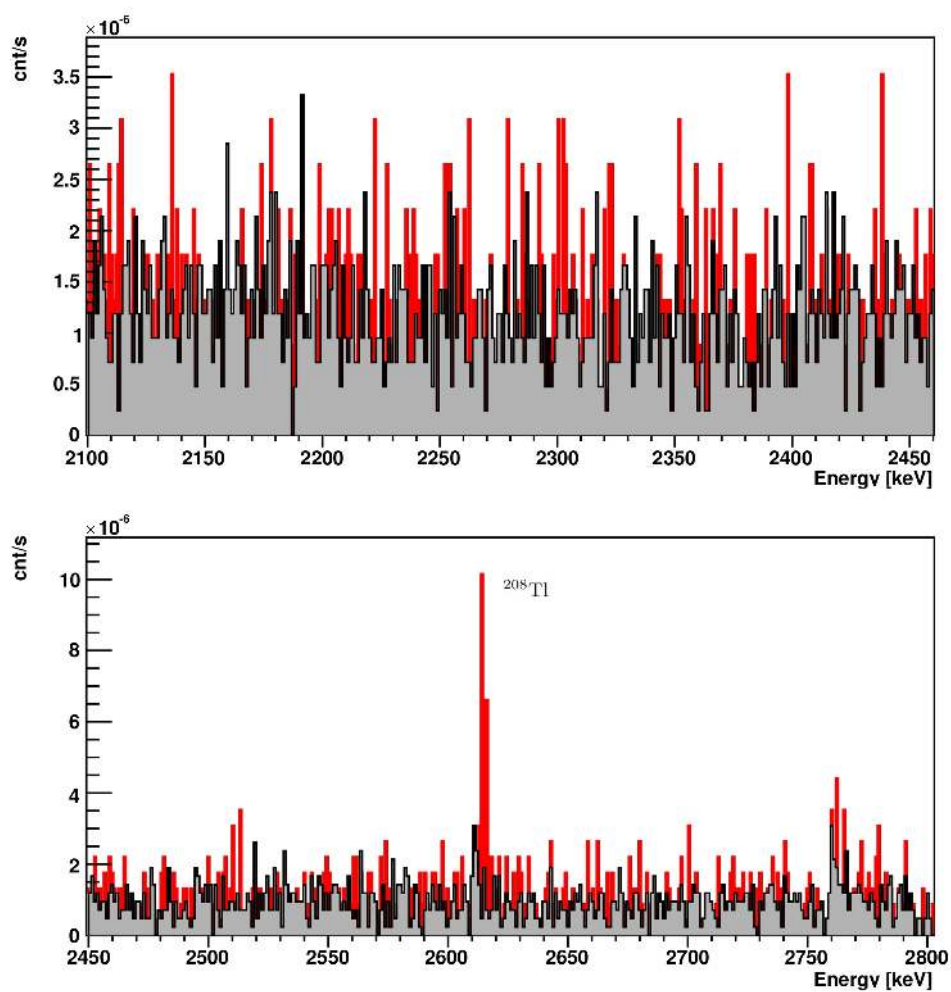


Figure D.6 Pre and post cleaning palladium spectra from 2100 keV to 2803 keV; red - original Pd (measurement 1), grey - cleaned Pd (measurement 3), see Section 7.2.

Table D.1 Known γ -lines that are within ± 5 keV of the expected Pd γ -lines at 468.59 keV, 475.07 keV, 657.76 keV and 815.35 keV and have a half-life of longer than 356 d. Listed are the energy, the emission probability, the decay mode, the half-life and the nuclide. ^{102}Ru , ^{102m}Ru , ^{110}Ag and ^{110m}Ag are emphasized and listed separately since they have exactly the same γ -lines as ^{102}Pd and ^{110}Pd respectively. The selection was done with [106].

Energy [keV]	Intensity in %	Decay mode	$T_{1/2}$	Nuclide
468.59 \pm 5 keV				
468.58	2.42	e+b+	207 d	102Rh
463.71	0.00000028	a	24110 yr	239Pu
463.9	0.00429	b-	8.593 yr	154Eu
464.11	0.08	e+b+	36.9 yr	150Eu
464.11	0.38	e+b+	36.9 yr	150Eu
464.797	1.212	b-	1.20E3 yr	166mHo
467.84	0.0609	b-	8.593 yr	154Eu
468.12	0.00000288	a	432.2 yr	241Am
469.8	N/A	a	29.1 yr	243Cm
471.1	0.000014	a	1.592E+5 yr	233U
475.07 \pm 5 keV				
475.10	95.4	e+b+	2.9 yr	102mRh
475.10	38.4	e+b+	207 d	102Rh
471.1	0.000014	a	1.592E+5 yr	233U
474.300	5.40E-08	a	24110 yr	239Pu
474.498	0.145	e+b+	36.9 yr	150Eu
475.365	1.486	b-	2.0648 yr	134Cs
476.37	0.0363	b-	1.20E3 yr	166mHo
476.89	0.018	e+b+	36.9 yr	150Eu
478.27	0.2263	b-	8.593 yr	154Eu
478.40	0.0000014	a	68.9 yr	232U
478.6	0.000014	a	1.592E+5 yr	233U
657.76 \pm 5 keV				
657.7622	4.5	b-	24.6 s	110Ag
657.7622	94.0	b-	249.79 d	110mAg
653.02	0.0000377	a	432.2 yr	241Am
654.81	0.00000225	a	24110 yr	239Pu
656.487	0.1448	e+b+	13.537 yr	152Eu
657.0	0.0000028	a	1.592E+5 yr	233U
658.28	0.053	e+b+	36.9 yr	150Eu
658.860	0.0000097	a	24110 yr	239Pu
661.657	85.1	b-	30.07 yr	137Cs
662.24	0.0012	a	7370 yr	243Am
662.40	0.000364	a	432.2 yr	241Am
662.66	0.015	e+b+	36.9 yr	150Eu
815.35 \pm 5 keV				
815.35	0.0382	b-	24.6 s	110Ag
818.031	7.29	b-	249.79 d	110mAg
810.451	0.320	e+b+	13.537 yr	152Eu
812.01	0.00000061	a	432.2 yr	241Am
813.504	4.50E-08	a	24110 yr	239Pu
815.507	0.516	b-	8.593 yr	154Eu
816.0	2.40E-08	a	24110 yr	239Pu
816.44	0.049	e+b+	36.9 yr	150Eu
816.62	0.0000008	a	68.9 yr	232U
817.89	0.000064	a	18.10 yr	244Cm
818.10	0.75	e+b+	471.7 d	252Es
819.0	0.00000040	a	432.2 yr	241Am

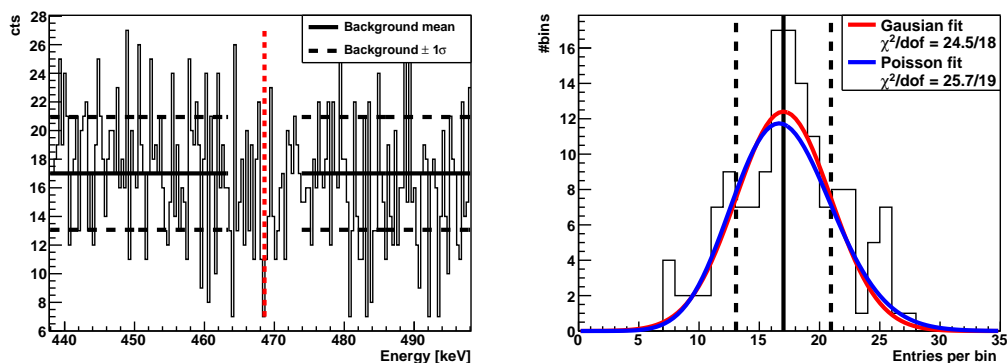


Figure D.7 Modeling of the background around the 468.59 keV γ -line. The right plot shows the entry per bin distribution fitted with a Gaussian (red curve) and a Poisson (blue curve). The left plot shows the spectrum in a ± 30 keV area around the expected peak (red dotted vertical line) with the area used for the background modeling. In both plots, the black solid lines is the background mean and the black dotted lines are the Gaussian background 1σ uncertainties.

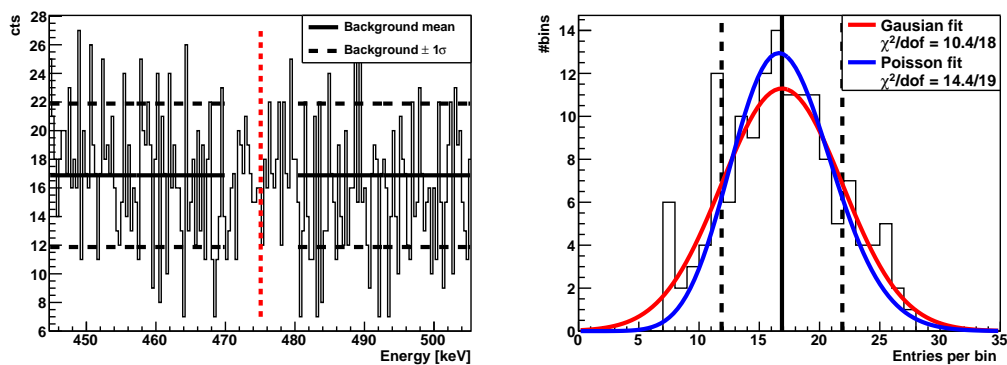


Figure D.8 Modeling of the background around the 475.07 keV γ -line. The right plot shows the entry per bin distribution fitted with a Gaussian (red curve) and a Poisson (blue curve). The left plot shows the spectrum in a ± 30 keV area around the expected peak (red dotted vertical line) with the area used for the background modeling. In both plots, the black solid lines is the background mean and the black dotted lines are the Gaussian background 1σ uncertainties.

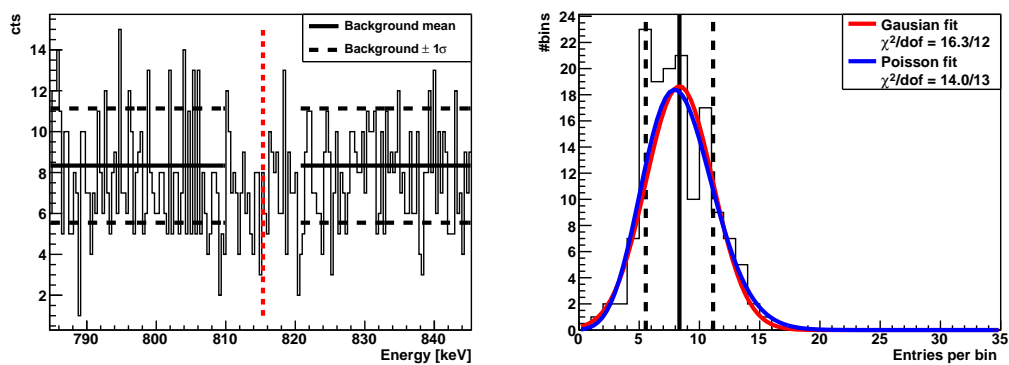


Figure D.9 Modeling of the background around the 815.35 keV γ -line. The right plot shows the entry per bin distribution fitted with a Gaussian (red curve) and a Poisson (blue curve). The left plot shows the spectrum in a ± 30 keV area around the expected peak (red dotted vertical line) with the area used for the background modeling. In both plots, the black solid lines is the background mean and the black dotted lines are the Gaussian background 1σ uncertainties.

Appendix E

List of Acronyms

This is a list of frequently used acronyms in order to avoid confusions with possible different definitions in various literature

DBD Double Beta Decay: All $0\nu\beta\beta$ and $2\nu\beta\beta$ decays.

$2\nu\beta\beta$ Neutrino accompanied double beta decay including $2\nu\beta^-\beta^-$, $2\nu\beta^+\beta^+$, $2\nu\text{ECEC}$ and $2\nu\text{EC}\beta^+$.

$0\nu\beta\beta$ Neutrinoless double beta decay including $0\nu\beta^-\beta^-$, $0\nu\beta^+\beta^+$, $0\nu\text{ECEC}$ and $0\nu\text{EC}\beta^+$.

$\beta^-\beta^-$ Double beta minus decay.

$\beta^+\beta^+$ Double beta plus decay.

ECEC Double electron capture.

$\text{EC}\beta^+$ Combined electron capture and beta plus decay.

$T_{1/2}$ Half-life of a nuclide. Also used as the half-life of one specific decay mode.

ADC Analog Digital Converter.

ANG Anriched GERDA detectors from the HDM experiment

BEGe Broad Energy Germanium detector.

BI Background Index.

CI Confidence Interval.

CL Confidence Level.

CP Charge and Parity symmetry.

DAQ Data Acquisition.

DL Dead Layer.

dof Degrees of Freedom for a fit.

EOI Energy of Interest.

FADC Fast/Flash ADC.

FWHM Full Width at Half Maximum.

GERDA GERmanium Detector Array.

GPS General Particle Source event generator.

GS Ground State.

GTF Natural GERDA detectors from the GENIUS experiment

HDM Heidelberg-Moscow experiment.

HPGe High Purity Germanium Detector.

LAr Liquid Argon

LNGS Laboratori Nazionali del Gran Sasso.

MaGe Majorana GERDA MC framework.

MC Monte Carlo.

MCA Multichannel Analyzer.

MLE Maximum Likelihood Estimate.

MSE Multi-Site Event.

NME Nuclear Matrix Element.

PMT Photomultiplier.

RG Enriched GERDA detectors from the IGEX experiment

ROI Region of Interest.

SM Standard Model.

SSE Single-Site Event.

TPC Time Projection Chamber.

Bibliography

- [1] E. Fermi, “An attempt of a theory of beta radiation,” *Z. Phys.*, vol. 88, pp. 161–177, 1934.
- [2] C. L. Cowan, F. Reines, F. B. Harrison, H. W. Kruse, and A. D. McGuire, “Detection of the Free Neutrino: a Confirmation,” *Science*, vol. 124, no. 3212, pp. 103–104, 1956.
- [3] M. G. Inghram and J. H. Reynolds, “Double Beta-Decay of ^{130}Te ,” *Phys. Rev.*, vol. 78, pp. 822–823, Jun 1950.
- [4] S. R. Elliott, A. A. Hahn, and M. K. Moe, “Direct evidence for two-neutrino double-beta decay in ^{82}Se ,” *Phys. Rev. Lett.*, vol. 59, pp. 2020–2023, Nov 1987.
- [5] W. H. Furry, “On Transition Probabilities in Double Beta-Disintegration,” *Phys. Rev.*, vol. 56, pp. 1184–1193, Dec 1939.
- [6] H. V. Klapdor-Kleingrothaus, A. Dietz, H. L. Harney, and I. V. Krivosheina, “Evidence for Neutrinoless Double Beta Decay,” *Mod. Phys. Lett.*, vol. A16, pp. 2409–2420, 2001.
- [7] Y. Fukuda *et al.*, “Measurements of the solar neutrino flux from Super-Kamiokande’s first 300 days,” *Phys. Rev. Lett.*, vol. 81, pp. 1158–1162, 1998.
- [8] A. S. Barabash *et al.*, “Two neutrino double-beta decay of ^{100}Mo to the first excited 0^+ state in ^{100}Ru ,” *Physics Letters B*, vol. 345, no. 4, pp. 408–413, 1995.
- [9] S. L. Glashow, “Partial Symmetries of Weak Interactions,” *Nucl. Phys.*, vol. 22, pp. 579–588, 1961.
- [10] ALEPH Collaboration, “Precision electroweak measurements on the Z resonance,” *Phys. Rept.*, vol. 427, pp. 257–454, 2006.
- [11] K. Zuber, *Neutrino Physics (Series in High Energy Physics, Cosmology and Gravitation)*. Taylor & Francis, 1 ed., 11 2003.
- [12] “Particle Data Group website.” <http://pdg.lbl.gov/index.html>, Jan 2011.
- [13] N. Schmitz, *Neutrino Physik*. Teubner Verlag, Jun 1997.
- [14] C. Cohen-Tannoudji, B. Diu, and F. Laloe, *Quantum Mechanics (2 vol. set)*. Wiley-Interscience, Oct 2006.
- [15] Z. Maki, M. Nakagawa, and S. Sakata, “Remarks on the Unified Model of Elementary Particles,” *Progress of Theoretical Physics*, vol. 28, no. 5, pp. 870–880, 1962.
- [16] V. Gribov and B. Pontecorvo, “Neutrino astronomy and lepton charge,” *Physics Letters B*, vol. 28, no. 7, pp. 493–496, 1969.
- [17] A. Strumia and F. Vissani, “Neutrino masses and mixings and...,” 2006.
- [18] M. C. Gonzalez-Garcia and Y. Nir, “Developments in neutrino physics,” *Rev. Mod. Phys.*, vol. 75, pp. 345–402, 2003.

- [19] J. Bouchez, M. Cribier, W. Hampel, J. Rich, M. Spiro, and D. Vignaud, “Matter effects for solar neutrino oscillations,” *Zeitschrift für Physik C Particles and Fields*, vol. 32, pp. 499–511, 1986.
- [20] C. Weinheimer *et al.*, “High precision measurement of the tritium beta spectrum near its endpoint and upper limit on the neutrino mass,” *Phys. Lett.*, vol. B460, pp. 219–226, 1999.
- [21] V. M. Lobashev *et al.*, “Direct search for mass of neutrino and anomaly in the tritium beta-spectrum,” *Phys. Lett.*, vol. B460, pp. 227–235, 1999.
- [22] A. Osipowicz *et al.*, “KATRIN: A next generation tritium beta decay experiment with sub-eV sensitivity for the electron neutrino mass,” *ArXiv:hep-ex/0109033*, 2001.
- [23] A. Monfardini *et al.*, “The microcalorimeter arrays for a rhenium experiment (MARE): A next-generation calorimetric neutrino mass experiment,” *Prog. Part. Nucl. Phys.*, vol. 57, pp. 68–70, 2006.
- [24] H. V. Klapdor-Kleingrothaus and I. V. Krivosheina, “The Evidence for the Observation of $0\nu\beta\beta$ Decay: The Identification of $0\nu\beta\beta$ Events from the Full Spectra,” *Modern Physics Letters A*, vol. 21, pp. 1547–1566, 2006.
- [25] A. Faessler *et al.*, “QRPA uncertainties and their correlations in the analysis of neutrinoless double beta decay,” *Phys. Rev.*, vol. D79, p. 053001, 2009.
- [26] “PLANCK mission website.” <http://www.sciops.esa.int/index.php?project=PLANCK>, Jan 2011.
- [27] R. B. Firestone, C. M. Baglin, and S. Y. F. Chu, *Table of Isotopes, 8th Edition*. Wiley-Interscience, 8 ed., Jul 1999.
- [28] V. I. TRETYAK and Y. G. ZDESENKO, “TABLES OF DOUBLE BETA DECAY DATA—AN UPDATE,” *Atomic Data and Nuclear Data Tables*, vol. 80, no. 1, pp. 83–116, 2002.
- [29] S. R. Elliott and P. Vogel, “Double beta decay,” *Ann. Rev. Nucl. Part. Sci.*, vol. 52, pp. 115–151, 2002.
- [30] K. Zuber, “Summary of the workshop on ‘Matrix elements for neutrinoless double beta decay’,” *ArXiv:nucl-ex/0511009*, 2005.
- [31] A. Barabash, F. Hubert, P. Hubert, and V. Umatov, “Double beta decay of ^{150}Nd to the First 0^+ excited state of ^{150}Sm ,” *JETP Letters*, vol. 79, pp. 10–12, 2004.
- [32] M. Doi and T. Kotani, “Neutrinoless Modes of Double Beta Decay,” *Progress of Theoretical Physics*, vol. 89, no. 1, pp. 139–159, 1993.
- [33] J. J. Gomez-Cadenas *et al.*, “Sense and sensitivity of double beta decay experiments,” *ArXiv:hep-ex/1010.5112v3*, 2010.
- [34] K. Zuber, “Long term prospects for double beta decay,” *ArXiv:nucl-ex/1002.4313*, 2010.
- [35] “SNO+ Collaboration Website.” <http://snoplus.phy.queensu.ca/Home.html>, Jan 2011.
- [36] G. Heusser, “Low-radioactivity background techniques,” *Ann. Rev. Nucl. Part. Sci.*, vol. 45, pp. 543–590, 1995.
- [37] S. Schönert, “Neutrinoless double beta decay,” *Journal of Physics: Conference Series*, vol. 203, no. 1, p. 012014, 2010.
- [38] F. Piquemal, “Double beta decay review,” *Journal of Physics: Conference Series*, vol. 120, no. 5, p. 052004, 2008.

- [39] “CUORICINO Collaboration Website.” <http://crio.mib.infn.it/wig/Cuoricinopage/CUORICINO.php>, Jan 2011.
- [40] “NEMO Collaboration Website.” <http://nemo.in2p3.fr/nemow3/>, Jan 2011.
- [41] “CUORE Collaboration Website.” <http://crio.mib.infn.it/wig/Cuorepage/CUORE.php>, Jan 2011.
- [42] “EXO Collaboration Website.” <http://www-project.slac.stanford.edu/exo/>, Jan 2011.
- [43] “GERDA Collaboration Website.” <http://www.mpi-hd.mpg.de/gerda/>, Jan 2011.
- [44] A. Terashima, Y. Takemoto, E. Yonezawa, H. Watanabe, S. Abe, and M. Nakamura, “R&D for possible future improvements of KamLAND,” *Journal of Physics: Conference Series*, vol. 120, no. 5, p. 052029, 2008.
- [45] “Majorana Collaboration Website.” <http://majorana.npl.washington.edu/>, Jan 2011.
- [46] Y. Hirano, T. Kishimoto, I. Ogawa, R. Hazama, S. Umehara, K. Matsuoka, G. Ito, Y. Tsubota, and the CANDLES Collaboration, “Study of double beta decay of ^{48}Ca with CANDLES,” *Journal of Physics: Conference Series*, vol. 120, no. 5, p. 052053, 2008.
- [47] “COBRA Collaboration Website.” <http://www.cobra-experiment.org/>, Jan 2011.
- [48] J. Díaz *et al.*, “The NEXT experiment,” *Journal of Physics: Conference Series*, vol. 179, no. 1, p. 012005, 2009.
- [49] H. Ohsumi, the NEMO, and S. Collaboration, “SuperNEMO project,” *Journal of Physics: Conference Series*, vol. 120, no. 5, p. 052054, 2008.
- [50] Y. Zdesenko, F. Avignone III, V. Brudanin, F. Danevich, V. Kobychyev, B. Kropivyan-sky, S. Nagorny, V. Tretyak, and T. Vylov, “CARVEL experiment with $^{48}\text{CaWO}_4$ crystal scintillators for the double β decay study of ^{48}Ca ,” *Astroparticle Physics*, vol. 23, no. 2, pp. 249–263, 2005.
- [51] N. Ishihara *et al.*, “The DCBA experiment for studying neutrinoless double beta-decay,” *Journal of Physics: Conference Series*, vol. 203, no. 1, p. 012071, 2010.
- [52] M. Nomachi *et al.*, “MOON (Mo Observatory Of Neutrinos) for double beta decay,” *Nuclear Physics B - Proceedings Supplements*, vol. 138, pp. 221–223, 2005. Proceedings of the Eighth International Workshop on Topics in Astroparticle and Underground Physics.
- [53] A. Giuliani, “Highlights in Double Beta Decay,” *The International Student Workshop 2010 on Neutrinoless Double Beta Decay*, Nov 2010. <http://www.pit.physik.uni-tuebingen.de/grabmayr/workshop/agenda.htm>,
- [54] “DUSEL Website.” <http://www.dusel.org/>, Jan 2011.
- [55] A. Bettini, “The world underground scientific facilities. A compendium,” *ArXiv:hep-ex/0712.1051*, 2007.
- [56] “LNGS Website.” <http://www.lngs.infn.it/>, Jan 2011.
- [57] D. Degering and M. Köhler, “Low-level γ -ray spectrometry in the medium deep underground laboratory Felsenkeller/Dresden,” in *IEEE Nuclear Science Symposium Dresden*, 2008.
- [58] J. F. Ziegler, “Terrestrial cosmic ray intensities,” *IBM Journal of Research and Development*, vol. 42, pp. 117–140, Jan. 1998.

- [59] W. Preuße, *Höhenstrahlungsinduziertes Nulleffektspektrum von Gammastrahlungsdetektoren*. PhD thesis, TU Dresden, 1993.
- [60] S. Cebrián, “The Problem of Cosmogenic Activation in Double Beta Decay Experiments,” *Revista de la Academia de Ciencias Exactas, Físicas, Químicas y Naturales de Zaragoza*, vol. 59 (Serie 2a), pp. 7–46, 2004.
- [61] “ROOT Website.” <http://root.cern.ch/drupal>, Jan 2011.
- [62] G. Cowan, *Statistical Data Analysis (Oxford Science Publications)*. Oxford University Press, USA, Jun 1998.
- [63] G. J. Feldman and R. D. Cousins, “Unified approach to the classical statistical analysis of small signals,” *Phys. Rev. D*, vol. 57, pp. 3873–3889, Apr 1998.
- [64] J. Neyman, “Outline of a Theory of Statistical Estimation Based on the Classical Theory of Probability,” *Royal Society of London Philosophical Transactions Series A*, vol. 236, pp. 333–380, Aug 1937.
- [65] “TFeldmanCousins on ROOT Website.” <http://root.cern.ch/root/html/TFeldmanCousins.html>, Jan 2011.
- [66] W. A. Rolke, A. M. López, and J. Conrad, “Limits and confidence intervals in the presence of nuisance parameters,” *Nuclear Instruments and Methods in Physics Research A*, vol. 551, pp. 493–503, Oct 2005.
- [67] G. Cowan and E. Gross, “Discovery significance with statistical uncertainty in the background estimate,” *ATLAS Statistics Forum*, May 2008.
- [68] A. Stuart and K. Ord, *Kendall’s Advanced Theory of Statistics, Volume 1: Distribution Theory*. Wiley, 6 ed., Apr 2009.
- [69] “TRolke on ROOT Website.” <http://root.cern.ch/root/html/TRolke.html>, Jan 2011.
- [70] G. Cowan, “Statistics for peak finding,” *COBRA note*, 2005.
- [71] “A New ^{76}Ge Double Beta Decay Experiment at LNGS,” 2004. GERDA Letter of Intent.
- [72] K. Kröninger, L. Pandola, and V. Tretyak, “Feasibility study of the observation of the neutrino accompanied double beta-decay of Ge-76 to the $0+(1)$ excited state of Se-76 using segmented germanium detectors,” *ArXiv:nucl-ex/0702030*, Feb 2007.
- [73] H. V. Klapdor-Kleingrothaus *et al.*, “GENIUS-TF: A test facility for the GENIUS project,” *Nucl. Instrum. Meth.*, vol. A481, pp. 149–159, 2002.
- [74] C. E. Aalseth *et al.*, “Recent results of the IGEX Ge-76 double-beta decay experiment,” *Phys. Atom. Nucl.*, vol. 63, pp. 1225–1228, 2000.
- [75] A. Caldwell, B. A. Majorovits, and J. Schubert, “Proposal for Occupation Schemes of the Detector Array,” tech. rep. GSTR-08-026.
- [76] “GERDA Wiki TG1.” <http://www.mpi-hd.mpg.de/gerda/>, Jan 2011.
- [77] M. Barnabé Heider, *Performance and stability tests of bare high purity germanium detectors in liquid argon for the GERDA experiment*. PhD thesis, MPI Heidelberg, 2009.
- [78] GERDA Collaboration, “Status report from the commissioning of GERDA,” tech. rep. GSTR-10-004.
- [79] J. Schubert, “Simulation of 2.6MeV Photons in the Inner Wall of the GERDA Cryostat,” tech. rep., 2008. GSTR-08-015.

- [80] GERDA Collaboration, “Progress Report to the LNGS Scientific Committee - April 2007,” tech. rep.
- [81] L. Pandola, K. Knoepfle, S. Schönert, and B. Schwingenheuer, “Background from radon emanation in the GERDA cryostat,” tech. rep. GSTR-09-001.
- [82] GERDA Collaboration, “Progress Report to the LNGS Scientific Committee - March 2006,” tech. rep.
- [83] B. K. Freund, F. Ritter and P. Grabmayr, “Update on the Muon Veto — installation of the DAQ,” tech. rep. GSTR-10-003.
- [84] M. Shirchenko, F. Ritter, V. Egorov, D. Zinatulina, J. Jochum, P. Grabmayr, M. Knapp, G. Meierhofer, K.-T. Knoepfle, and M. Junker, “Testing and transportation of muon-veto panels to LNGS,” tech. rep. GSTR-08-016.
- [85] Y. Chan *et al.*, “MaGe - a Geant4-based Monte Carlo framework for low-background experiments,” *ArXiv:nucl-ex/0802.0860*, Feb. 2008.
- [86] “GEANT4 Website.” <http://geant4.cern.ch/>, Jan 2011.
- [87] L. Pandola, M. Knapp, K. Kröniger, D. Lenz, L. Jing, X. Liu, J. Schubert, and M. Jelen, *MaGe - the GERDA/Majorana Monte Carlo Framework - Userguide*, 2009.
- [88] O. A. Ponkratenko, V. I. Tretyak, and Y. G. Zdesenko, “The Event generator DECAY4 for simulation of double beta processes and decay of radioactive nuclei,” *Phys. Atom. Nucl.*, vol. 63, pp. 1282–1287, 2000.
- [89] A. S. Barabash, A. V. Derbin, L. A. Popeko, and V. I. Umatov, “Search for $\beta\beta$ decay of ^{76}Ge to the excited states in ^{76}Se ,” *Zeitschrift für Physik A Hadrons and Nuclei*, vol. 352, pp. 231–233, Jun 1995.
- [90] W. C. Haxton and G. J. Stephenson, “Double beta Decay,” *Prog. Part. Nucl. Phys.*, vol. 12, pp. 409–479, 1984.
- [91] S. K. Dhiman and P. K. Raina, “Two-neutrino double-beta decay matrix elements for ground and excited states of ^{76}Ge and ^{82}Se nuclei,” *Phys. Rev. C*, vol. 50, pp. R2660–R2663, Dec 1994.
- [92] O. Civitarese and J. Suhonen, “Two-neutrino double-beta decay to excited one- and two-phonon states,” *Nuclear Physics A*, vol. 575, no. 2, pp. 251–268, 1994.
- [93] S. Stoica and I. Mihut, “Nuclear structure calculations of two-neutrino double-beta decay transitions to excited final states,” *Nuclear Physics A*, vol. 602, no. 2, pp. 197–210, 1996.
- [94] M. Aunola and J. Suhonen, “Systematic study of beta and double beta decay to excited final states,” *Nuclear Physics A*, vol. 602, no. 2, pp. 133–166, 1996.
- [95] J. Toivanen and J. Suhonen, “Study of several double-beta-decaying nuclei using the renormalized proton-neutron quasiparticle random-phase approximation,” *Phys. Rev. C*, vol. 55, pp. 2314–2323, May 1997.
- [96] J. Schwieger, F. Simkovic, A. Faessler, and W. A. Kaminski, “Double β decay to excited states of several medium-heavy nuclei within the renormalized quasiparticle random phase approximation,” *Phys. Rev. C*, vol. 57, pp. 1738–1743, Apr 1998.
- [97] S. I. Vasilev, A. A. Klimenko, S. B. Osetrov, and A. A. Smolnikov, “New Bound to the Probability of $\text{Ge}76$ $\beta\beta$ Decay to the 0^+ $\text{Se}76$ Level,” *JETP Letters*, vol. V. 72, p. 279, September 2000.
- [98] K. Kröniger and L. Pandola, “Feasibility study for the measurement of the neutrino accompanied double beta decay of Ge-76 to excited states of Se-76 with the GERDA experiment,” tech. rep. GSTR-06-003.

- [99] K. Kroeninger and X. Liu, “Initial Results From The Gerda Monte Carlo Simulation,” tech. rep. GSTR-05-004.
- [100] S. Schönert, “Active background suppression techniques in DBD decay experiments,” *The International Student Workshop 2010 on Neutrinoless Double Beta Decay*, Nov 2010. <http://www.pit.physik.uni-tuebingen.de/grabmayr/workshop/agenda.htm>.
- [101] S. Cebrián, “The Problem of Cosmogenic Activation in Double Beta Decay Experiments,” *Revista de la Academia de Ciencias Exactas, Físicas, Químicas y Naturales de Zaragoza*, vol. 59 (Serie 2a), 2004.
- [102] S. Cebrián *et al.*, “Cosmogenic activation in germanium double beta decay experiments,” *Journal of Physics: Conference Series*, vol. 39, no. 1, p. 344, 2006.
- [103] B. Schwingenheuer, “Intrinsic contaminations of Germanium diodes from Th-228 and Ra-226,” tech. rep. GSTR-05-022.
- [104] C. Buck, F. X. Hartmann, T. Lasserre, D. Motta, S. Schonert, U. Schwana, and H. Simgen, “The LENS project,” *Nuclear Physics B - Proceedings Supplements*, vol. 118, pp. 450–450, 2003. Proceedings of the XXth International Conference on Neutrino Physics and Astrophysics.
- [105] H. V. Klapdor-Kleingrothaus *et al.*, “Latest Results from the Heidelberg-Moscow Double Beta Decay Experiment,” *Eur. Phys. J.*, vol. A12, pp. 147–154, 2001.
- [106] “The Lund/LBNL Nuclear Data Search.” <http://nucleardata.nuclear.lu.se/nucleardata/toi/>, Jan 2011.
- [107] V. D. Ashitkov *et al.*, “Liquid argon ionization detector for double beta decay studies,” *ArXiv:nucl-ex/0309001*, 2003.
- [108] G. Heusser, “Ar42 and other nobel gas radionuclides in the atmosphere,” <http://www.mpi-hd.mpg.de/gerda/meetings.html>, Jul 2010.
- [109] A. J. Peurrung, T. W. Bowyer, R. A. Craig, and P. L. Reeder, “Expected atmospheric concentration of ^{42}Ar ,” *Nuclear Instruments and Methods in Physics Research Section A: Accelerators, Spectrometers, Detectors and Associated Equipment*, vol. 396, no. 3, pp. 425–426, 1997.
- [110] V. D. Ashitkov *et al.*, “New experimental limit on the ^{42}Ar content in the Earth’s atmosphere,” *Nuclear Instruments and Methods in Physics Research Section A: Accelerators, Spectrometers, Detectors and Associated Equipment*, vol. 416, no. 1, pp. 179–181, 1998.
- [111] L. GLENDENIN, “Determination of the energy of beta particles and photons by absorption,” *Nucleonics*, vol. 2, no. 1, pp. 12–32, 1948.
- [112] B. Lehnert, “MC Simulation of K42 Decays,” <http://www.mpi-hd.mpg.de/gerda/meetings.html>, Jul 2010.
- [113] B. Schwingenheuer, “Status data in GERDA,” <http://www.mpi-hd.mpg.de/gerda/meetings.html>, Nov 2010.
- [114] K. Pelczar, “E-field & drift simulations,” <http://www.mpi-hd.mpg.de/gerda/meetings.html>, Nov 2010.
- [115] “Private Communication with Kai Zuber.”
- [116] R. G. Winter, “A Search for Double Beta-Decay in Palladium,” *Phys. Rev.*, vol. 85, p. 687, Feb 1952.

- [117] R. Chandra, J. Singh, P. K. Rath, P. K. Raina, and J. G. Hirsch, “Two-neutrino double β -decay of $94 \leq A \leq 110$ nuclei for the $0^+ - 0^+$ transition,” *Eur. Phys. J. A*, vol. 23, no. 2, pp. 223–234, 2005.
- [118] “Private Communication with Fedor Šimkovic.”
- [119] P. K. Rath, R. Chandra, K. Chaturvedi, P. K. Raina, and J. G. Hirsch, “Uncertainties in nuclear transition matrix elements for neutrinoless $\beta\beta$ decay within the projected-Hartree-Fock-Bogoliubov model,” *Phys. Rev. C*, vol. 82, p. 064310, Dec 2010.
- [120] “Private Communication with Francesco Iachello.”
- [121] “Von Gahlen International Inc.” <http://www.vongahlen.nl/profile/>, Jan 2011.
- [122] “XCOM: Photon Cross Sections Database.” <http://www.nist.gov/pml/data/xcom/index.cfm>, Jan 2011.
- [123] U. Reichelt and J. Henniger, “Application of Advanced Monte Carlo Methods in Numerical Dosimetry,” in *Radiat. Protect. Dosim. 119*, proceedings of 14th Int. Conf. on Solid State Dosimetry, pp. 479–482, 2006.
- [124] “Alfa Aesar.” <http://www.alfa.com/>, Jan 2011.
- [125] O. Chkvorets, *Search for Double Beta Decay with HPGe Detectors at the Gran Sasso Underground Laboratory*. PhD thesis, MPI Heidelberg, 2008.
- [126] H. Nakada, T. Sebe, and K. Muto, “Realistic shell-model calculations of the $2\nu\beta\beta$ nuclear matrix elements and the role of the shell structure in intermediate states,” *Nuclear Physics A*, vol. 607, no. 3, pp. 235–249, 1996.
- [127] “GERDA Preliminary Calibration Web Interface.” <http://www.physik.unizh.ch/groups/groupbaudis/gerda/restricted/lngsonlinedisplay/main.html>, Jan 2011.
- [128] H. Simgen, “Ar39 background for bare germanium p-type detectors in LAr and LN2,” tech. rep., 2006. GSTR-06-020.
- [129] W. Wahl, *Radionuclide Handbook for Laboratory Workers*. INSTITUTE FOR SPECTROMETRY AND RADIATION PROTECTION.

Acknowledgments

Many people contributed to this thesis in a technical or non-technical way in form of advising, tutoring, inspiring, helping and with moral support.

First, i would like to thank my supervisor Kai Zuber for his guidance, inspiration, his plentiful ideas and his personal association in the group and i would also like to thank Arno Straessner for accepting the second reviewing of my thesis.

This work would not be the same without Belina von Krosigk who spent an immense amount of her time on thorough technical, semantical and orthographical corrections and prevented numerous mistakes and some serious errors. Thank you!

Data analysis is only the end of a long chain of efforts that have been started by many people a long time ago. I would like to thank the whole GERDA collaboration and everyone who contributed to the building of this impressive experiment. I am specifically grateful to Luciano Pandola, Bernhard Schwingenheuer, Marik Barnabé-Heider, Dušan Budjáš and Assunta Di Vacri who all supervised, tutored or worked with me in some kind and to Alexander Domula and Matthias Allardt, the local GERDA group. I would like to thank the Felsenkeller staff with special thanks to Detlev Degering and Felix Krüger for providing the data and help for analyzing the palladium. I also want to mention and thank Dorothea Sommer from the Strahlenphysik for providing the MC simulation of the Felsenkeller detector.

The importance of the daily working life and the people there cannot be appreciated enough. I would like to thank all the group members that made the time of my thesis fruitful, interesting, enjoyable, fun and not routine - in all facets. Special thanks goes to the crew of E14, to Wiebke Tenner, Marcel Heine, Philipp Schrock, Arnd Sörensen and Tobias Reinhardt, and to all others with whom I could spent lunch and coffee breaks. I am also grateful for the institute's social and technical activities especially for the soccer play, the computing café and the occasional pub night.

Eventually, i want to thank my fellow students and close friends Heike Pfau and Sarah Röttinger with whom i had a great time in Dresden and always someone to turn to in physics and personal confusions. I am also very grateful to my parents who always supported me unconditionally in all these years. Finally, i want to thank Tine, who was always there in the last month and steadily coped with my pre dead line antics.

I would like to dedicated this thesis to the memory of Alexander Lankau with whom i studied, discussed and philosophized many issues and shared endless adventures in the mountains, the pubs and the library. He was an important part in an important episode of my life.

Plagiatserklärung

”Hiermit erkläre ich gemäß §21, Absatz 8 der Diplomprüfungsordnung für den Studiengang Physik der Technischen Universität Dresden, dass ich die am heutigen Tage eingereichte Diplomarbeit zum Thema *Analysis of Double Beta Decays in Germanium, Palladium and Argon* selbstständig verfasst, keine anderen als die angegebenen Quellen und Hilfsmittel benutzt habe sowie Leistungen anderer nicht als meine eigenen ausgegeben habe.”

Dresden, den 14. Februar 2011

Björn Lehnert